UNIVERSITY OF SOUTHAMPTON

FACULTY OF NATURAL AND ENVIRONMENTAL SCIENCES

School of Ocean and Earth Sciences

Middle Eocene Greenhouse Climate Instability

by

Wendy E. C. Kordesch

Thesis for the degree of Doctor of Philosophy

AUGUST 2016

UNIVERSITY OF SOUTHAMPTON

ABSTRACT

FACULTY OF NATURAL AND ENVIRONMENTAL SCIENCES

Doctor of Philosophy

Thesis for the degree of Doctor of Philosophy

MIDDLE EOCENE GREENHOUSE INSTABILITY

By Wendy Elaine Chee Kordesch

Understanding warm climate states is increasingly important as projections of anthropogenic climate change indicate atmospheric carbon dioxide concentrations in the coming century not previously seen on Earth for tens of millions of years. The Eocene (~56-34 Ma) is a critical period in the long-term Cenozoic climate evolution, encompassing the transition from widespread greenhouse warmth and high atmospheric carbon dioxide levels pervasive during the early Eocene to an icehouse world with major Antarctic ice sheets and cooler temperatures. Increasingly, it has become apparent that global climate during this transition was not gradual; the middle Eocene is characterized by significant short-term climate variability with recent findings including both transient warming and cooling events. However, the timing, and nature of many of the climate fluctuations during this interval are poorly constrained. To this end, this thesis aims to better characterize the long-term background trends and investigate the nature of short-term transient perturbations during the greenhouse climate of the middle Eocene.

In Chapter 2, new nine million year long benthic foraminiferal stable isotope records (~46 to 38 Ma) generated from recently drilled equatorial Pacific sediments with excellent age control are presented. These are the first records to document that the seven enigmatic equatorial Pacific Carbon Accumulation Events (CAEs) are not associated with transient global cooling and/or glaciation events, as previously hypothesized. Further, new carbonate accumulation records in Chapter 3 provide the first robust evidence for the presence of CAEs 3 and 4 in the Atlantic basin. Together, these findings constrain the feasibility of potential CAE forcing mechanisms and imply that there are only two viable mechanisms; (1) solute flux from continental weathering, and (2) increased organic carbon burial from marine assemblage changes.

A new compilation (including new and published records) of carbonate accumulation records from a paleodepth transect (2-4 km) in the Atlantic and Pacific basins provides the first multi-basin look at deep-sea carbonate burial at high temporal resolution across the Middle Eocene Climatic Optimum global warming event (~40 Ma). New CCD and lysocline interpretations reveal for the first time that multiple rapid fluctuations (<100 kyrs) and extreme lysocline shoaling (reaching >2 km water depth) are superimposed on long-term trends. This finding implies multiple pulses of carbon input to the ocean–atmosphere system during the MECO and provides critical time constraints to potential forcing mechanisms, which have so far remained elusive.

In the final Chapter 4, new lithological and geochemical data from the Atlantic and Pacific Basins are presented which reveal the global nature of the transient 'C19r event' (~41.5 Ma) and confirm that the event meets the criteria to be defined as a 'hyperthermal'. Further, analyses of the stable isotope datasets suggests that the C19r event was not exceptional and is one (albeit the most extreme) of a large number of transient 'warming' events throughout the middle Eocene, adding to the growing body of data implying that hyperthermal occurrence is pervasive outside of the very warm late Paleocene and early Eocene.

Table of Contents

List of Tables

List of Appendix Tables

List of Figures

List of Supplemental Figures

DECLARATION OF AUTHORSHIP

I, **Wendy Elaine Chee Kordesch** declare that this thesis and the work presented in it are my own and has been generated by me as the result of my own original research.

MIDDLE EOCENE GREENHOUSE INSTABILITY

I confirm that:

1. This work was done wholly or mainly while in candidature for a research degree at this University;
2. Where any part of this thesis has previously been submitted for a degree or any other qualification at this University or any other institution, this has been clearly stated;
3. Where I have consulted the published work of others, this is always clearly attributed;
4. Where I have quoted from the work of others, the source is always given. With the exception of such quotations, this thesis is entirely my own work;
5. I have acknowledged all main sources of help;
6. Where the thesis is based on work done by myself jointly with others, I have made clear exactly what was done by others and what I have contributed myself;
7. None of this work has been published before submission.

Signed: .....

Date: .....

Acknowledgements

First and foremost, I would like to sincerely thank my team of supervisors (in order of accrual): Paul Wilson, Heiko Pälike, Kirsty Edgar, and Steve Bohaty. Your expertise and guidance are the reason this PhD exists. Thanks to Paul for a fateful conversation at the Paris Post Cruise meeting that resulted in my move to the UK, and whose advice and direction have kept me on track. Thanks to Heiko for on-going encouragement, and whose say 'yes' attitude led to new opportunities I would not have otherwise pursued. Thanks to Kirsty whose guidance and mentorship (and willingness to Skype) at times kept me going. Thanks to Steve for patient discussions about the MECO, and for always supporting 'just *one* last run' of samples from 'just *one* more site'.

Thanks also to examiners Phil Sexton and Gavin Foster for helpful discussions of this thesis, and to my Panel Chair Alan Kemp.

I am fortunate to have a number of collaborators to thank: Thomas Westerhold and Ursula Röhl for patiently teaching me XRF scanning techniques, for support during my stay in Bremen, and for on-going productive discussions throughout this work. Claudia Agnini for detailed discussions on MECO age models, which somehow always managed to include laughter. The ship and shore based researchers from IODP Exp. 320 and 342 for productive discussions about early versions of this work that proved key in developing this research.

I am indebted to a number of people whose support in the lab was instrumental in processing thousands of samples: Yuxi, Emmeline, Denise, Grant, Gemma, Jack, and Alex. A huge thank you to Megan Spencer, whose meticulous attention to detail I admire. I could not have completed this thesis without her good humour and constant willingness to help.

Thanks are in order to those at NOCS: To the paleoclimate research group for valuable scientific discussions, and also for perhaps equally crucial non-scientific discussions during endless hours in the sediment preparation lab. In particular, I would like to express my gratitude for office mates in 784/15, which was my 'home away from home'. Tom and Rosie continue to faithfully translate British culture and offer friendship, support, and 'office meetings' when I need it most regardless of subject matter or time zone. To Anieke and Richard for stepping into their shoes. To Carolyn, Anya, Diederik, and 'paleodragon' for their friendship and encouragement.

Thanks to mentors Peggy Delaney and Howie Scher, for continued support and advice and for encouraging me to pursue a PhD.

Finally, thanks to my family and to J Zac Stein, who make it all worthwhile.

Definitions and Abbreviations

Yr	Years
Kyr	Thousands of years
Myr	Millions of years
Ma	Millions of years ago
$\delta^{18}O$	Oxygen isotope signature: $^{18}O/^{16}O$ relative to VPDB standard
$\delta^{13}C$	Carbon isotopic signature: $^{13}C/^{12}C$ relative to VPDB standard
CIE	Carbon isotope excursion
‰	Parts per million
VPDB	Vienna Pee Dee Belemnite
pCO_2	Atmospheric carbon dioxide concentrations
CCD	Carbonate Compensation Depth
XRF	X-ray fluorescence
Fe	Iron
Ba	Barium
$CaCO_3$	Calcium carbonate
CAR	Carbonate mass accumulation rate
MAR	Mass accumulation rate
DIC	Dissolved inorganic carbon
SEM	Scanning electron microscopy
MECO	Middle Eocene Climatic Optimum
PETM	Paleocene-Eocene Thermal Maximum
ETM-2	Eocene Thermal Maximum-2
EECO	Early Eocene Climatic Optimum
EOT	Eocene-Oligocene Transition
CAE	Carbonate Accumulation Events 1-7
DSDP	Deep Sea Drilling Program
ODP	Ocean Drilling Program
IODP	Integrated Ocean Drilling Program
PEAT	Pacific Equatorial Age Transect (IODP Exp. 320, 321)
ESIC	Eocene Stable Isotope Consortium (IODP Exp. 342)
mbsf	Metres below sea floor. This is depth each drilled core is based on the actual length of the recovered core and the drillers depth
mcd	Metres composite depth. This is the shipboard depth scale of the spliced section.
rmcd	Revised metres composite depth. This is the post cruise revised shipboard depth scale of the spliced section
adj rmcd	Adjusted revised metres composite depth, revised composite core depth below seafloor (revised CCSF-A), or ‘adjusted rmcd’ for short. This is the revised the shipboard spliced composite section for Exp. 320 and 321 that includes depths outside of the splice.

Chapter 1: Introduction

Contents

1.1 Why study the Eocene?

If current rates of anthropogenic carbon dioxide emissions continue at their current rate, by the end of this century Earth may experience atmospheric temperatures and greenhouse gas concentrations not previously recorded since the Eocene [56-34 million years ago, Ma; *IPCC*, 2013; *Pagani*, 2005]. This drastic forecast highlights the necessity to improve our understanding of ancient climates; particularly those with higher temperatures and greenhouse gases than modern day to better understand how Earth systems function in warmer climates. Understanding past climate and environmental changes not only contextualizes modern trends, it is one of the only ways to investigate and test carbon cycle and climatic changes over long timescales.

The Eocene encompasses both the warmest temperatures recorded in the past 65 Ma and an extremely dynamic climate (**Figure 1-1**) [*Zachos et al.*, 2001a]. In particular a series of carbon-cycle led rapid (<100 thousand years; kyr) warming events or 'hyperthermals' that interrupt the climate trend during the Eocene can be investigated to provide vital clues to understanding how warm climates respond to changing greenhouse gas forcing. However, climate dynamics during the Eocene are still poorly constrained due to a general scarcity of high-resolution data sets. Without detailed records of past climate and carbon cycle variability we cannot fully understand how climate functions in a warmer world and the implications it may have for the future.

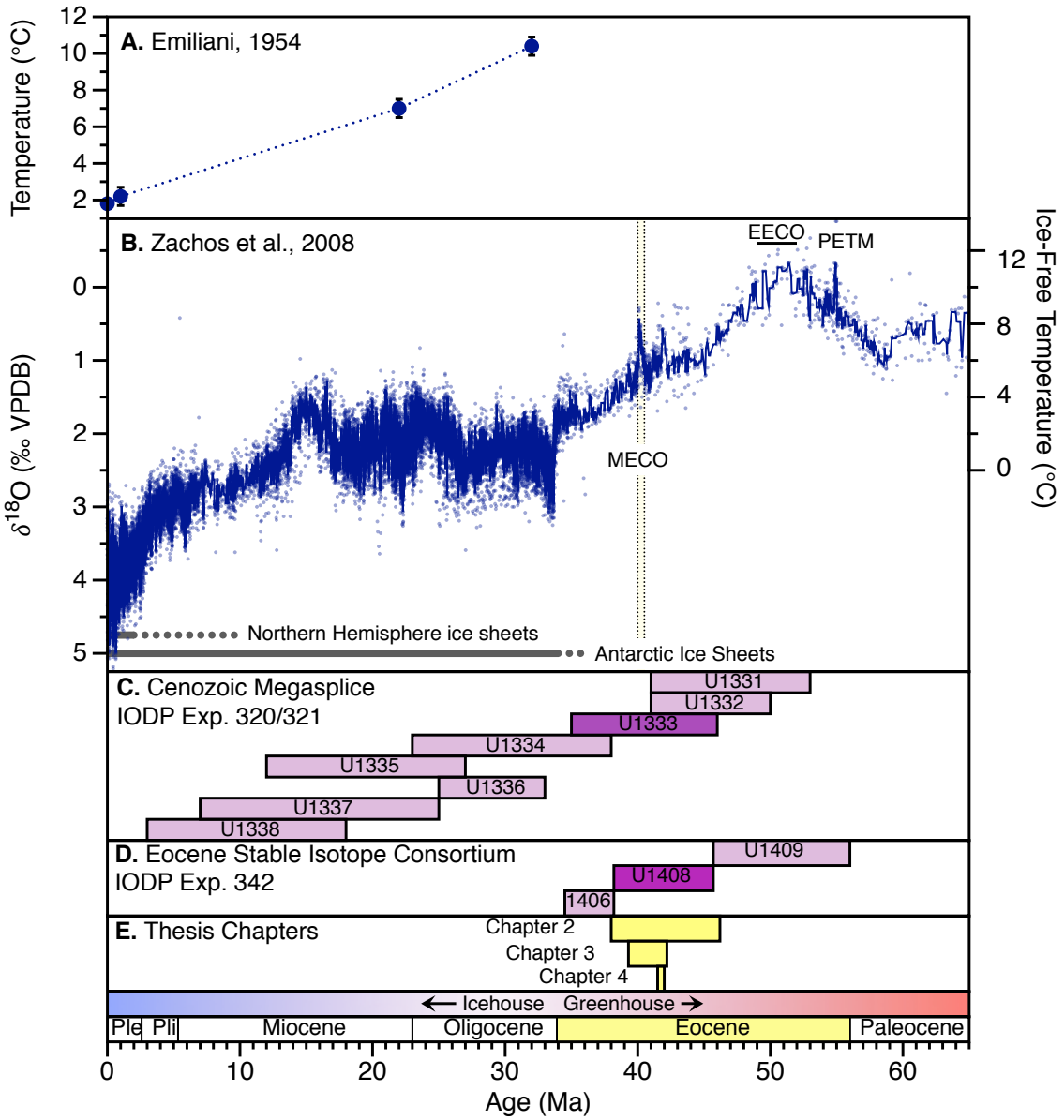

Figure 1-1 Cenozoic climate records and recently recovered sediments spanning the Eocene employed in this thesis.
Benthic foraminiferal oxygen isotope records showing (a) the first Cenozoic temperature record [Emiliani, 1954; with updated ages from Pearson, 2012] and (b) a recent global composite spanning the Cenozoic with > 17,500 measurements [Zachos et al., 2008]. Solid Horizontal black bars in (b) show a standard qualitative representation of large-scale permanent ice sheets and dashed bars indicate partial or ephemeral ice sheets. MECO = Middle Eocene Climatic Optimum. EECO = Early Eocene Climatic Optimum. PETM = Paleocene-Eocene Thermal Maximum. (c) Time intervals recovered by Integrated Ocean Drilling Program (IODP) Expeditions 320 and 321 for the "Cenozoic Megasplice" (IODP Sites U1331-U1338). Site U1333 utilized here in dark purple. (d) Time intervals and sites included in the "Eocene Stable Isotope Consortium" (IODP Exp. 342 Sites U1406, U1408 and U1409). Site U1408 utilized here in dark purple. (e) Time intervals for which new data are presented in this thesis.

1.2 Oxygen isotopes and Eocene Climate

1.2.1 Oxygen isotope systematics

Stable oxygen isotopes ($\delta^{18}O$) are one of the oldest and most widely measured proxies used in paleoclimate research as a recorder of both ocean temperature and global ice volume [e.g. *Pearson*, 2012 and references therein]. In particular, the measurement of oxygen isotopes in foraminiferal calcite has been instrumental in developing our understanding of global climate over the past ~100 Ma. Because foraminifera (unicellular protists) are ubiquitous in the world ocean, large numbers of their calcitic shells can be found in marine sediments that span long time intervals (many millions of years) allowing for the generation of high-resolution paleoclimate records.

Stable oxygen isotope paleoclimatology is fundamentally possible because seawater contains a mixture of several species of water differing in molecular weight due to stable isotopes of oxygen. The two most abundant forms of oxygen are the 'light' isotope ^{16}O, and the 'heavy' isotope ^{18}O (with abundances of 99.757 % and 0.205 %, respectively) [*Rosman and Taylor*, 1998]. The slight difference in mass between these two isotopes imposes differences in chemical properties where molecular bonds between light isotopes are less strong than heavy isotopes. The result is a fractionation effect, where evaporation preferentially selects molecules of water containing the light isotope of oxygen ($H_2{}^{16}O$) and condensation preferentially selects 'heavy' oxygen ($H_2{}^{18}O$). Thus, as water vapour forms and is transported pole-ward within the hydrological cycle most heavy-^{18}O is precipitated out along the way and glacial ice is a reservoir of ^{18}O-depleted oxygen. This temperature/ice dependency in the ratio of seawater $^{18}O/^{16}O$ is the basis for the oxygen isotope proxy because relatively enriched ^{18}O seawater can indicate colder climates and or increased ice volume. The isotope ratio of $^{18}O/^{16}O$ is expressed using delta notation ($\delta^{18}O$) as per mil (‰) relative to an international standard (**Equation 1-1**). A positive $\delta^{18}O$ value indicates enrichment of the heavy isotope relative to

the standard while a negative $\delta^{18}O$ value indicates depletion of the heavy isotope relative to the standard. The most commonly used standard for carbonate samples is the Vienna PeeDee Belemnite (VPDB; $\delta^{18}O = 0$) [*Epstein et al.*, 1953].

Equation 1-1 $$\delta^{18}O = \frac{(^{18}O/^{16}O)_{Sample} - (^{18}O/^{16}O)_{Standard}}{(^{18}O/^{16}O)_{Standard}} \times 1000$$

The most common measurement of $\delta^{18}O$ is from fossil carbonates of foraminiferal calcite tests ($CaCO_3$). Foraminiferal calcite ($CaCO_3$) is advantageous because test carbonate precipitates from seawater (**Equation 1-2**) and reflects the oxygen isotopic composition of ions dissolved in seawater in which the organism lived. Therefore, the isotopic fractionation (fractionation factor, α; **Equation 1-3**) of $^{18}O/^{16}O$ between carbonate and water is temperature dependent. This relationship was first shown empirically by *McCrea [1950*] and subsequently empirically derived by studies with analyses from cultured organism tests and inorganic carbonate [*Epstein et al.*, 1953; *O'Neil et al.*, 1969; *Erez and Luz*, 1983; *Kim and O'Neil*, 1997; *Bemis et al.*, 1998]. These studies have revised the paleotemperature equation and relate the $\delta^{18}O$ of foraminiferal carbonate to environmental conditions a basic quadratic equation (**Equation 1-4**) [comprehensive table in *Pearson et al.* 2012] where the coefficients *a*, *b*, and *c* are experimentally derived, $\delta^{18}O_c$ is the measured calcite value, and $\delta^{18}O_{sw}$ is the isotope ratio of seawater. The overall effect of this equation is a ~0.25 ‰ decrease in $\delta^{18}O$ equivalent to a ~1°C change in temperature. In this thesis the $\delta^{18}O$ of foraminiferal carbonate is converted to temperature using *Kim and O'Neil* [1997] as modified by *Bemis et al.* [1998] and using an ice-free $\delta^{18}O_{sw}$ of -1.27 ‰ (VPDB) (**Equation 1-5**).

Equation 1-2 $$Ca^{2+} + 2HCO_3^- \leftrightarrow CaCO_3 + CO_2 + H_2O$$

Equation 1-3 $$\alpha = \frac{(^{18}O/^{16}O)_{calcite}}{(^{18}O/^{16}O)_{water}}$$

Equation 1-4 $$T\ (℃) = a + b\left(\delta^{18}O_c - \delta^{18}O_{sw}\right) + c(\delta^{18}O_c - \delta^{18}O_{sw})^2$$

Equation 1-5 $$T\ (℃) = 16.1 + (-4.64)\left(\delta^{18}O_c - (-1.27)\right) + 0.09(\delta^{18}O_c - (-1.27))^2$$

However, the use of $\delta^{18}O$ from foraminiferal calcite is an indirect method of measuring temperature and ice volume and there are other important factors that must be accounted for when interpreting $\delta^{18}O$ records. These include biological factors (vital effects), factors from the environment that influence the $\delta^{18}O_{sw}$, and factors from the environment that influence preservation in sediments. These factors and their effects on $\delta^{18}O$ records are described in the following paragraphs.

Vital effects from foraminifera were discovered early on, as studies found offsets of +1-2 °C due to some species of foraminifera that calcify out of equilibrium with seawater [i.e. *Shackleton et al.*, 1973] that leads to carbonate ion concentrations and pH local to foraminifera tests [Spero 1992; Spero and Lea 1993; Spero et al., 2007]. This effect is equivalent to a theoretical decrease in $\delta^{18}O$ of ~1.42 ‰ per unit of pH increase [Zeebe 2001]. In planktic foraminifera the most significant offsets arise from the presence of photosymbionts that lower pH and raise carbonate ion concentrations [e.g. *Rink et al.*, 1998]. Photosymbionts are rare in benthic foraminifera due to their habitats below the photic zone. However, $\delta^{18}O$ analyses from benthic foraminiferal calcite can be influenced by shell growth-rate changes throughout the organism's life cycle where small specimens tend to have more negative $\delta^{18}O$ values [i.e. Erez 2003]. Benthic foraminifera also have consistent species offsets [*Duplessey et al.*, 1970; *Shackleton and Opdyke*, 1973] due to habitat/depth variation (e.g. epifaunal vs. infaunal). To avoid the issues that arise from vital effects, it is necessary to account for the specific ecology of the foraminifera. A common benthic species to correct to is *Cibicidoides* (a practice that is utilized throughout this thesis) because *Cibicidoides* values are closer to equilibrium with seawater [*Kim and O'Neil* 1997]. Another strategy is to analyse foraminifera from a narrow size fraction to account for the negative offsets that can arise from small/young specimens.

Environmental factors that influence $\delta^{18}O$ records (other than temperature) include those that affect $\delta^{18}O_{sw}$ both globally and regionally. Global $\delta^{18}O_{sw}$ varies mostly by changes in the total volume of continental ice sheets globally, which varies over time depending on the conditions of climate and geography that determine the $\delta^{18}O$ value of glacial ice sheets [see discussion in *Ravelo and Hillaire-Marcel* 2007]. Ice volume affects the global $\delta^{18}O_{sw}$ signal because ice sheet growth/decline timescales (~10-100 kyr) are much longer than the timescales of ocean ventilation (~1 kyr) and the ocean is well mixed on longer timescales. Ice volume estimations can be deconvolved from temperature signals by the combined use of $\delta^{18}O$ with other methods of estimating temperature (e.g. Mg/Ca ratios). This thesis focuses on the middle Eocene time interval where it is common to assume ice-free conditions (making ice volume estimations unnecessary) represented by a 1 ‰ difference between the $\delta^{18}O_{sw}$ between modern and ice free worlds [e.g. Shackleton and Kennett, 1975; Zachos et al., 1994; Miller et al., 2005]. Regional differences in $\delta^{18}O_{sw}$ can result from a number of environmental factors. The largest signal comes from the 'salinity effect' where variations in evaporation, precipitation, and vapour transport patterns results in higher $\delta^{18}O$ values in regions with net evaporation and lower $\delta^{18}O$ values in regions with net precipitation equivalent to ~0.5 ‰ per unit salinity [*Rohling and Cooke,* 1999]. Regional differences in the $\delta^{18}O_{sw}$ are also affected by the formation area (water source basin/region) and circulation history of deep-water masses, which can both impose large signals. Deep-water formation occurs in surface waters at high latitudes and imposes properties on water masses that remain as long as the water mass is transported out of contact with the surface. This effect can be significant, for example, modern ocean variability of surface water $\delta^{18}O_{sw}$ ranges ± 1.5 ‰, equivalent to a ± 5 °C temperature difference [*Schmidt et al.*, 1999; *LeGrande and Schmidt*, 2006].

Along with effects that influence $\delta^{18}O$ records biologically and in the water column are effects that occur after the deposition of foraminiferal tests on the seafloor by diagenetic processes. Calcite dissolution occurs because the remineralization of organic matter in sediments can lower porewater pH and dissolve foraminifera tests [*Jahnke et al.*, 1997]. This leads to dissolution and then reprecipitation of calcite can alter the primary $\delta^{18}O_{sw}$ values [e.g. *Pearson*

et al., 2001; *Wilson and Norris*, 2001; *Sexton et al.*, 2006]. The effects of recrystallization can be visible through inspection via scanning electron microscope and it is common practice to inspect for opaqueness under reflective light, infilling, and test wall structure. Though this is a more significant issue with planktic foraminifera because benthics have denser wall structures [*Pearson et al.*, 2001; *Sexton et al.*, 2006; *Edgar et al.*, 2013], recrystallization of foraminiferal calcite occurs in most pelagic carbonate oozes.

Along with oxygen isotopes, stable carbon isotopes ($\delta^{13}C$) have been used for decades as a paleoceanographic tool for understanding the functioning of the carbon cycle between the two main carbon reservoirs: organic matter and sediment. The stable isotopes of carbon are ^{12}C and ^{13}C (with abundances of 98.89 % and 1.11 % respectively) [*Faure*, 1977]. The mass difference between the two isotopes creates a fractionation effect where molecules of carbon dioxide containing the light isotope of carbon ($^{12}CO_2$) are preferentially fixed during photosynthesis [*Park and Epstein*, 1960]. Thus, organic matter is a reservoir of ^{13}C-depleted carbon and if more carbon is stored in organic carbon globally, reservoirs (e.g. the ocean) can become enriched in ^{13}C. The ratio of $^{13}C/^{12}C$ in a sample is expressed using delta notation (**Equation 1-6**) and the $\delta^{13}C$ of foraminiferal calcite reflects the carbon isotopic composition of dissolved organic carbon (DIC) in seawater in which the shell calcifies.

Equation 1-6

$$\delta^{13}C = \frac{\left(^{13}C/^{12}C\right)_{Sample} - \left(^{13}C/^{12}C\right)_{Standard}}{\left(^{13}C/^{12}C\right)_{Standard}} \times 1000$$

1.2.2 Oxygen isotope trends

Some of the first $\delta^{18}O$ measurements ever made utilizing the calcite in benthic (deep-sea dwelling) foraminiferal tests span the Oligocene to modern (~34 million year; Myr) and comprise the first discrete inferred ocean temperature/ice record showing the well-known but not previously quantified cooling trend across the Cenozoic (**Figure 1-1a**) [the past 65 Ma; *Emiliani*, 1954; *Pearson*, 2012]. Though this first estimate overestimated temperature changes by excluding the changes in seawater $\delta^{18}O$, since the mid-1950s

scientists have been continually improving and expanding Cenozoic stable isotope records by extending them farther into the past and generating higher-resolution and more stratigraphically continuous records. Much of this research was made possible by sediments recovered by the Integrated Ocean Drilling Program (IODP) and its predecessors. The first global compilation of Cenozoic benthic foraminiferal oxygen isotopes was comprised of data from eight records with a ~0.6 Myr resolution [*Miller et al.*, 1987]. In contrast, one of the most recent (and heavily used) compilations contains >40 records incorporating >17,500 analyses (**Figure 1-1b**) [*Zachos et al.*, 2008].

The reconstruction of past climate from oxygen isotope data combined with other paleoceanographic proxies has revealed that the Cenozoic cooling trend represents a major shift from widespread global warmth with only minor or non-existent ice sheets to cooler temperatures and the eventual development of bi-polar glaciation [*Zachos et al.*, 2001a]. This pattern of change is frequently referred to as the shift from "greenhouse" to "icehouse" climate regimes and the Eocene in particular marks the key transitional period when the most fundamental of these changes began.

Climate during the Eocene was warm, with deep sea temperatures ~10°C higher than at the present day [*Zachos et al.*, 2001a]. Surface water temperatures in the Arctic reached ~18°C [*Sluijs et al.*, 2006], warm enough to support crocodiles and species of palm [*Greenwood and Wing*, 1995; *Markwick*, 1998]. In fact, the highest atmospheric carbon dioxide concentrations (pCO_2) and temperatures for the entire Cenozoic occur in the Eocene during the Early Eocene Climatic Optimum (EECO; 52-50 Ma; **Figure 1-1**) [*Anagnostou et al.*, 2016; *Beerling and Royer*, 2011; *Greenwood and Wing*, 1995; *Pearson and Palmer*, 2000; *Pearson et al.*, 2001]. The thermal gradient between the equator and the poles during the EECO was half that of modern day with both warmer equatorial waters and much higher mid- and high-latitude sea surface temperatures [*Bijl et al.*, 2010; *Shackleton and Kennett*, 1975; *Stott et al.*, 1990; *Tripati et al.*, 2003]. The end of the EECO marks the onset of long-term cooling (~5°C lower deep sea temperatures by the end of the Eocene) that continues for the rest of the Cenozoic [*Inglis et al.*, 2015; *Zachos et al.*, 2001a]. Finally, the Eocene-Oligocene transition (EOT; ~34 Ma) coincides with rapid step-wise cooling and the dramatic expansion of Antarctic ice sheets [*Coxall et*

al., 2005; *Katz et al.*, 2008; *Lear et al.*, 2008; *Miller et al.*, 1991; *Zachos et al.*, 1992], demarking the transition from the end of the greenhouse and start of the icehouse climate state.

While the multi-million year climate patterns of the Eocene are generally well known, the details of shorter-term fluctuations (< 500 kyr) remain poorly constrained. High resolution studies have revealed significant shorter-term climate variability superimposed on the Cenozoic cooling trend and the number of rapid global warming events or 'hyperthermals' has increased with the creation of new higher resolution records and increased spatial coverage [e.g. *Edgar et al.*, 2007; *Lauretano et al.*, 2015; *Littler et al.*, 2014; *Sexton et al.*, 2011]. The largest and most severe of the known hyperthermal events, the Paleocene Eocene Thermal Maximum (PETM; 56 Ma) defines the start of the Eocene Epoch and is associated with 5-7˚C warming of sea surface temperatures and a coeval global Carbon Isotope Excursion (CIE) of roughly –3.0 ‰ in deep-sea sediments [*Kennett and Stott*, 1991; *E Thomas and Shackleton*, 1996; *Zachos et al.*, 2003]. The PETM is also associated with widespread deep-sea carbonate dissolution, indicating a 2 kilometre (km) shoaling of the Carbonate Compensation Depth (CCD) over ~10 kyr [*Zachos et al.*, 2005]. Following the PETM were a number of similar but less extreme hyperthermal events in the early to middle Eocene [*Edgar et al.*, 2007; *Lourens et al.*, 2005; *Sexton et al.*, 2011; *E Thomas and Zachos*, 2000] as well as recent evidence for a transient cooling event at ~37 Ma, the Priabonian Oxygen Isotope Maximum [*Scher et al.*, 2014]. In the Pacific during middle Eocene a series of seven Carbonate Accumulation Events (CAEs) between 46 and 34 Ma correspond to large (~500-1000 m) fluctuations in the CCD, increased biogenic silica accumulation, and organic carbon burial [*Lyle et al.*, 2002a; *Lyle et al.*, 2005; *Olivarez Lyle and Lyle*, 2005; 2006; *Pälike et al.*, 2012]. The largest of the middle Eocene CCD shifts occurs at the termination of CAE-3 at ~40 Ma when the CCD shoaled by > 1 km across the onset of the Middle Eocene Climatic Optimum global warming event (MECO) [*Pälike et al.*, 2012], that sustained 4-5˚C warmer deep-sea temperatures for ~500 kyr [*Bohaty and Zachos*, 2003; *Bohaty et al.*, 2009], significantly longer than the earlier late Paleocene to early Eocene hyperthermals.

Stable oxygen and carbon ($\delta^{18}O$ and $\delta^{13}C$) isotope records and clay horizons were primarily used to identify many of the transient Eocene climate

events, however the events need to be tested by comprehensive interrogation of geological datasets—a challenge that will require construction of a diverse set of high-resolution multi-proxy datasets from sites around the globe. A number of so-called hyperthermal events have, thus far, been identified at only a single location [Edgar et al., 2007; Littler et al., 2014; Sexton et al., 2011] and details regarding their global extent, duration, magnitude, and forcing mechanisms still remain largely unknown. Additionally, it is unclear if these events are exceptional or related to each other through cyclical forcing of Earth's orbit [*DeConto et al.*, 2012; *Galeotti et al.*, 2010; *Kirtland Turner et al.*, 2014; *Littler et al.*, 2014].

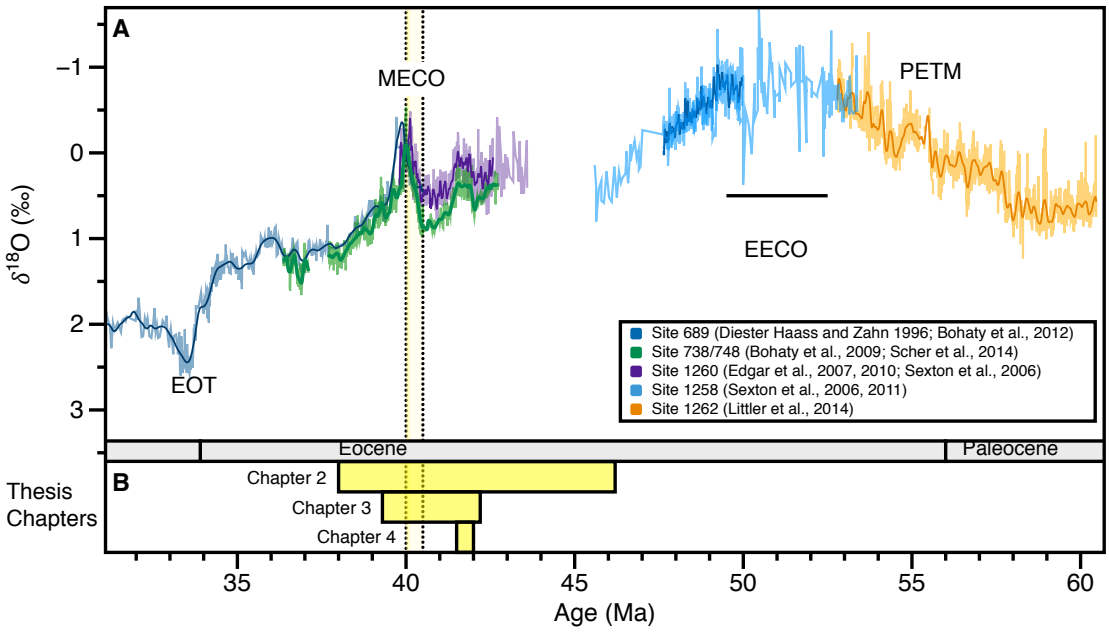

Figure 1-2 Existing high-resolution benthic stable isotope records across the late Paleocene to early Oligocene interval.
Benthic foraminiferal $\delta^{18}O$ from Site 689 [*Bohaty et al.*, 2012; *Diester-Haass and Zahn*, 1996], Site 738 and 748 [*Bohaty et al.*, 2009; *Scher et al.*, 2014], Site 1260 data [*Edgar et al.*, 2007; *Edgar et al.*, 2010; *Sexton et al.*, 2006a], Site 1258 [*Sexton et al.*, 2006a; *Sexton et al.*, 2011], and Site 1262 [*Littler et al.*, 2014]. Shaded bars in b) indicate time intervals for which new data are presented in this thesis. EOT = Eocene-Oligocene Transition. MECO = Middle Eocene Climatic Optimum. EECO = Early Eocene Climatic Optimum. PETM = Paleocene-Eocene Thermal Maximum. Ages for Sites 1262 and 1258 are as published; Ages for other sites have been converted to the PEAT timescale of *Westerhold et al.* [2014]. Shaded region marks the MECO event as defined in *Bohaty et al.* [2009].

Stable isotope compilations have immensely improved our understanding of the Cenozoic, however there are still several problematic issues that necessitate improved records. For instance, compilation records generated from multiple ocean basins across an array of latitudes may introduce systematic error resulting from local variations like regional water temperature differences [*Sexton et al.*, 2006a]. This is further complicated by records generated on different benthic foraminiferal species or single analyses made on samples comprising multiple benthic foraminiferal species, which can introduce error from differing foraminiferal vital effects [*Erez*, 1978; *Grossman*, 1987; *Sexton et al.*, 2006a]. Third, errors can arise from the correlation of numerous stable isotope records from multiple sites with varying age model quality.

A limitation to the study of Eocene climates is the low density of stable isotope data prior to ~34 Ma (**Figure 1-2**), partly due to a shallow CCD and resulting low carbonate burial during the time hindering the preservation of carbonate microfossils [*Pälike et al.*, 2012]. In fact, the lack of suitable high-resolution well-dated sediments in this interval has created an "Eocene gap" between ~42-53 Ma in the astronomically calibrated geologic timescale, which is the only time interval of the last 65 Ma without a detailed orbital age calibration [*Pälike and Hilgen*, 2008]. This not only leads to less accurate dating in the Eocene it also hinders the extension of astronomically anchored timescales into the Paleocene, which must instead rely on ages from floating time scales based on cyclostratigraphy [e.g. *Westerhold and Röhl*, 2013]. A more accurate timescale for the middle Eocene is an 'urgent' priority within Earth science and climate modelling communities because the exact duration of extreme events can crucially help to narrow down plausible forcing and feedback mechanisms [*Pälike and Hilgen*, 2008].

To this end, recent Integrated Ocean Drilling Program (IODP) Expeditions 320/321 and 342 [*Norris et al.*, 2014c; *Pälike et al.*, 2010] in the equatorial Pacific and northern Atlantic, respectively have targeted expanded Eocene sediment sequences to fill the gap and enable investigation in the middle Eocene at unprecedented detail. Together, a collection of benthic stable

isotope records from eight proximal sites located in the equatorial Pacific from IODP Exp. 320/321 will comprise the first ever continuous, single-location, well resolved Cenozoic compilation colloquially termed the "Cenozoic Megasplice" (**Figure 1-1**). Work from ~34 to ~56 Ma is also underway to develop a compilation of even higher-resolution continuous, single-location, well resolved records from three proximal sites (Sites U1406, U1408, U1409) in the North Atlantic which span the entirety of the Eocene, termed the "Eocene Stable Isotope Consortium" (ESIC; **Figure 1-1**). Upon completion the Cenozoic Megasplice and ESIC records will comprise the highest resolution Eocene benthic stable isotope data generated to date, and specifically target both the problems in long-term stable isotope compilations and filling the interval of the "Eocene gap" with an astronomically calibrated timescale from both the Pacific and Atlantic ocean basins.

The overarching goal of this thesis is to better understand the fine-scale timing and nature of both long and short-term time climate trends and events in the middle Eocene. While each of the research chapters has its own clear objectives and goals, the records generated in Chapters 2 and 4 also contribute directly to the Cenozoic Megasplice and ESIC projects, respectively that are aimed at achieving the larger goals of the paleoceanographic community.

1.3 Thesis outline and aims:

The aim of this thesis is to generate new stable carbon and oxygen isotope and physical property records to constrain the nature and timing of Eocene climate events, with particular focus on the poorly resolved middle Eocene (**Chapter 2**), the MECO (**Chapters 2** and **Chapter 3**) and the magnetochron C19r hyperthermal event (**Chapter 4**; **Figure 1-1e**). The specific aims of Chapters 2 through 4 are as follows.

1.3.1 Chapter 2: Middle Eocene greenhouse climate instability in the equatorial Pacific (IODP Site U1333)

A series of Eocene Carbonate Accumulation Events (CAEs) between ~46 and 35 Ma observed in the equatorial Pacific are associated with large fluctuations in the CCD, increased biogenic silica accumulation, and organic carbon burial [*Lyle et al.*, 2002a; *Lyle et al.*, 2005; *Olivarez Lyle and Lyle*, 2002; 2005; 2006; *Pälike et al.*, 2012]. The CAEs are also thought to be precursor cooling [and possible ice-building; *Tripati et al.*, 2005] events to the dramatic cooling at the start of the Oligocene (~34 Ma) when large permanent ice sheets formed on Antarctica [*Coxall and Wilson*, 2011; *Coxall et al.*, 2005; *Kennett and Stott*, 1991; *Shackleton and Kennett*, 1975; *Zachos et al.*, 2001a], however this hypothesis has never been directly verified. In **Chapter 2** this hypothesis is tested by investigating the pattern and timing of Eocene CAEs and whether they correspond to changes in environmental conditions (i.e., temperature and/or carbon cycling and storage). To this end, a long (~8 Myr), single-site, monospecific benthic foraminiferal stable isotope record spanning the middle Eocene at IODP Exp. 320 Site U1333 has been generated encompassing all seven CAEs and the MECO for the first time. This new record also fills a critical (high resolution) stable isotope data gap in the middle Eocene between ~46 and 42.5 Ma (**Figure 1-2**), at a site with excellent age control and at higher resolution than available published long-term records to date [*Edgar et al.*, 2007; *Edgar et al.*, 2010; *Sexton et al.*, 2006a; *Sexton et al.*, 2011]. Further, this new record from Site U1333 comprises the oldest portion of the 'Cenozoic Megasplice', providing an essential test of the veracity of the 'classic' Cenozoic

stable isotope composite curve [*Cramer et al.*, 2009; *Zachos et al.*, 2001b] from a single location in high resolution (**Figure 1-1c**).

1.3.2 Chapter 3: Dynamic, large-magnitude Carbonate Compensation Depth changes during the Middle Eocene Climatic Optimum

The MECO global warming event (~40 Ma) is characterized a by rise in atmospheric pCO_2 concentrations, gradual ~4 °C warming of both the surface and deep ocean over ~500 kyr, and prolonged carbonate dissolution in the deep ocean [*Bijl et al.*, 2010; *Bohaty and Zachos*, 2003; *Bohaty et al.*, 2009; *Edgar et al.*, 2010]. However, together the duration of warming and prolonged carbonate dissolution suggests that the prevailing theory for the origin of the MECO (e.g., a gradual increase in pCO_2 due to volcanic degassing) is in conflict with basic carbon cycle theory. This so-called 'carbon-cycle conundrum' [*Sluijs et al.*, 2013] is a major problem because on long timescales (>500 kyr) carbon input and warming should theoretically increase silicate weathering rates, which would lead to carbonate accumulation [*Berner et al.*, 1983; *Walker et al.*, 1981]. This discrepancy is at least partially exacerbated by the current scarcity of carbon cycle and environmental data with which to test key hypotheses and inform modelling studies. To this end, the focus of **Chapter 3** (**Figure 1-1e**) is to generate the first detailed reconstruction of the CCD and lysocline history in both the Atlantic and Pacific basins across the MECO using high-resolution records of sediment carbonate content and a suite of other sedimentological records (e.g., fragmentation) to augment published high-resolution equatorial Pacific carbonate records [*Lyle et al.*, 2005; *Pälike et al.*, 2012]. Critically, new sites expand the existing depth transect in higher resolution and capture full CCD behaviour globally for the first time. Together, this new compilation helps to identify carbon cycle behaviour to constrain plausible mechanisms for carbon release that drove this enigmatic global warming event.

1.3.3 Chapter 4: Evidence for hyperthermals in the middle Eocene: the magnetochron C19r event

The long-term global climate transition from Greenhouse to Icehouse conditions through the Eocene is punctuated by several transient warming events, including the short-lived (<200 kyr) magnetochron C19r 'hyperthermal'

event at ~41.5 Ma [*Edgar et al.*, 2007; *Westerhold and Röhl*, 2013]. The C19r event was first identified at ODP Site 1260 in the equatorial Atlantic [*Edgar et al.*, 2007], but a dissolution horizon at the peak of the event hindered accurate determination of both its duration and magnitude and therefore its origin. Research within this interval of the middle Eocene has typically been hindered by recovery of stratigraphically discontinuous sediments and this event could have been easily missed by low-resolution stratigraphies available at sites elsewhere [*Dawber and Tripati*, 2011a; b; *Lear et al.*, 2004; *Tripati et al.*, 2005], thus the extent of this short-lived event has yet to be corroborated as global or even basin-wide. However, the event suggests a considerable perturbation to the carbon cycle and climate occurs more than six Myr after the hyperthermal events of the late Paleocene and early Eocene (and well outside of the EECO). In **Chapter 4** (**Figure 1-2**), new stable isotope ($\delta^{13}C$ and $\delta^{18}O$) and sedimentological records from ODP Sites 702 (subantarctic South Atlantic), 929 (equatorial Atlantic), and U1408 (north Atlantic) were generated to test if the C19r event is present outside of ODP Site 1260 and ultimately better constrain changes in the magnitude, timing, and drivers of this little known event.

**The chapters in this thesis were written with the aim of being individually submitted as manuscripts for publication. Thus, chapters may contain unavoidable repetition.*

Chapter 2: Middle Eocene greenhouse climate instability in the equatorial Pacific (IODP Site U1333)

Contents

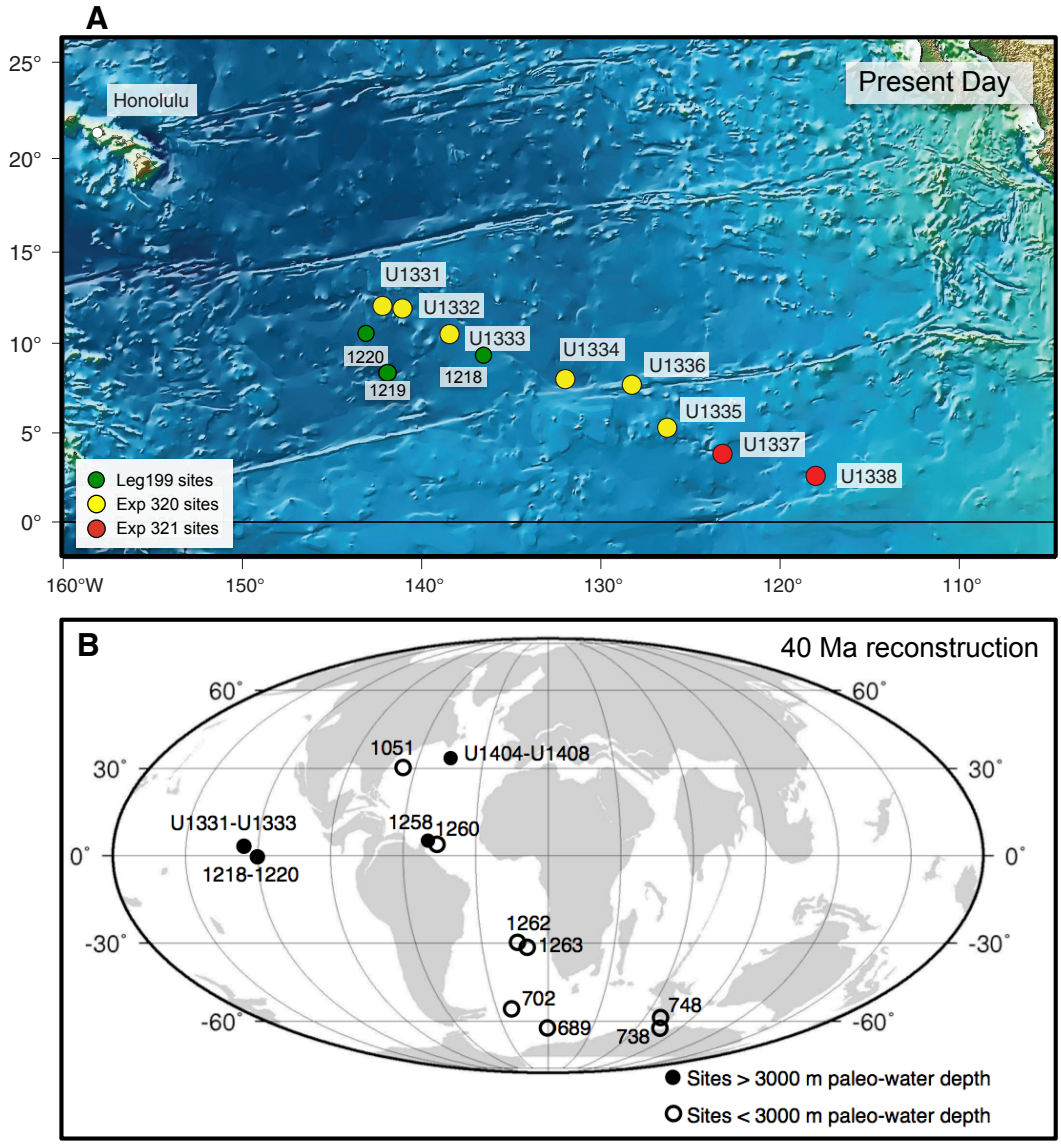

Figure 2-1 DSDP, ODP and IODP site location map of middle Eocene sections included in this study.
(a) Present day location of equatorial Pacific sites and IODP Site U1333 (modified from *Pälike et al.* [2012]) and (b) additional IODP/ODP/DSDP sites mentioned in this study. Approximate positions on ~40 Ma paleogeography from [*Hay et al.*, 1999; *ODSN*, 2011]. Solid circles are deep water sites (paleodepth >3000 m) and unfilled circles are shallow (paleodepth <3000 m).

2.1 Introduction

The Eocene Epoch (~56-34 millions years ago, Ma) is a critical interval in the long-term global climate evolution of the Cenozoic, encompassing the transition from widespread greenhouse warmth in the early Eocene to an icehouse world characterized by large Antarctic ice sheets and cooler temperatures [*Zachos et al.*, 2001a]. Geological records from both marine and terrestrial environments show that there is significant short-term climate instability superimposed on this long-term gradual cooling trend, including numerous transient global warming events during the early middle Eocene [*Cramer et al.*, 2009; *Kennett and Stott*, 1991; *Lourens et al.*, 2005; *Sexton et al.*, 2011; *E Thomas and Shackleton*, 1996; *Zachos et al.*, 2003] and middle Eocene [*Bohaty and Zachos*, 2003; *Bohaty et al.*, 2009; *Edgar et al.*, 2007]. Continental-scale and 'permanent' ice sheets in the Cenozoic first developed across the Eocene-Oligocene Transition (EOT) at ~34 Ma [*Coxall and Wilson*, 2011; *Coxall et al.*, 2005; *Kennett and Stott*, 1991; *Shackleton and Kennett*, 1975; *Zachos et al.*, 2001a], with the inception of a large Antarctic ice sheet. Initiation of glaciation in the Northern Hemisphere glaciation occurred later at ~11-5 Ma [*Bailey et al.*, 2013; *Holbourn et al.*, 2005; *Lear et al.*, 2000; *Miller et al.*, 1991; *Zachos et al.*, 2001a]. A number of lines of evidence suggest the presence of transient cooling episodes [*Lyle et al.*, 2005; *Pascher et al.*, 2015; *Scher et al.*, 2014] and development of the ephemeral ice much earlier than ~34 Ma. For instance, there is sedimentological and/or paleontological evidence for winter sea-ice in the Arctic as early as ~45 Ma [*Moran et al.*, 2006; *St John*, 2008] and isolated alpine glaciers in east Greenland from ~38 Ma [*Eldrett et al.*, 2007]. However, there is also speculation based on deep-sea proxy records and sea-level studies that large ice-sheets existed in Antarctica and even the Northern Hemisphere in the middle and late Eocene [*Dawber and Tripati*, 2011b; *Dawber et al.*, 2011; *Tripati et al.*, 2005].

Table 2-1 Comparison of modelled scenarios proposed for CAEs and their viability in light of new data presented in this thesis

	Modelled Scenario	*Pälike et al., 2012*		*This Study*		Records needed
		Conclusion	Reasoning	Conclusion	New Evidence	
1	Organic carbon surface export rain ratio changes	Unlikely	Modelled CCD variations are too small	-	-	-
2	Changes in shelf-basin fractionation	Unlikely	Requires repeated large changes in sea level during the Eocene, for which there is no evidence. Yet to be empirically resolved.	Not plausible	No correlation between cooler temperatures and CAEs; no evidence for large-scale ice mass	-
3	Deep ocean ventilation source change from Southern Ocean to the North Pacific	Unlikely; Plausible if CCD is globally asynchronous	Model results in asynchronous CCD changes in different ocean basins. Yet to be empirically resolved.	Unlikely	CCD shoaling during the MECO was synchronous in the Atlantic and Pacific.** Preliminary signs of CAE presence in the North Atlantic*	Detailed CCD records from the Atlantic Basin
4	Changes in deep-sea temperature and concentration of Mg or Ca of seawater	Unlikely	Modelled CCD variations are too small	-	-	-
5	Changes in solute flux into the deep ocean from increased continental weathering	Plausible if CCD is globally synchronous	Model results in equatorial Pacific CCD deepening of ~100–1000 m. Requires globally synchronous changes in CCD. Yet to be empirically resolved.	Plausible	CCD shoaling during the MECO was synchronous in the Atlantic and Pacific.** Preliminary signs of CAE presence in the North Atlantic*	Detailed CCD records from the Atlantic Basin; records of weathering
6a	Increased C_{org} burial from: changes in organisms' basal metabolic rates	Plausible	Model results in CCD changes of ~300–600 m are possible for a 2–4-fold change in the initial fraction of sediment labile organic matter	Unlikely	No consistent cooler temperature response with CAEs to slow metabolism	-
6b	Increased C_{org} burial from: changes in marine plankton assemblages			Plausible		Detailed productivity records across all CAEs; Surface signal

**Norris et al., 2014*

***Chapter 3 of this thesis*

In drillcores recovered during Ocean Drilling Program (ODP) Leg 199, seven fluctuations in equatorial Pacific deep-sea carbonate accumulation (Carbonate Accumulation Events, CAEs, numbered 1-7) were discovered in sediments at Sites 1218 and 1219 (**Figure 2-1**) between ~46 – 34 Ma. These CAEs varied in magnitude [*Lyle et al.*, 2002a] and are separated from one another by carbonate-poor intervals (**Figure 2-1**). Preliminary studies suggested that the CAEs represented temporary deepening of the Carbonate Compensation Depth (CCD; a sediment property that occurs at the oceanic depth where the downward flux of carbonate rain delivered from calcifying organisms is balanced by dissolution on the seafloor). The largest of the equatorial Pacific CAEs, CAE-3, occurs between ~42.0 and 40.5 Ma and is accompanied by positive $\delta^{18}O$ shifts in both bulk sediment and benthic foraminifera [*Lyle et al.*, 2005]. Similarly, limited data across the peaks of CAEs 2 and 4 also indicated relatively high bulk sediment $\delta^{18}O$ values (although no background data were collected for context). Taken together, inferences from these data and the similarity of isotopic changes and CCD response to events at the EOT suggests that the CAEs are associated with transient cooling and/or glaciation [*Burgess et al.*, 2008; *Dawber and Tripati*, 2011b; *Lyle et al.*, 2002a; *Lyle et al.*, 2005; *Olivarez Lyle and Lyle*, 2005; 2006; *Tripati et al.*, 2005]. However, carbonate accumulation rates in pelagic sediments are controlled not only by preservation (carbonate saturation state of deep water) but also productivity (abundance of calcifying organisms and available nutrients) [*Lyle et al.*, 2008; *Van Andel*, 1975]. Subsequent studies have shown that at least the youngest CAEs (3-7) [~34.5 to 42 Ma] also correspond to intervals of increased biogenic silica accumulation, organic carbon burial, and export production [*Griffith et al.*, 2010; *Lyle et al.*, 2005; *Olivarez Lyle and Lyle*, 2005] implying a potentially important role for productivity in driving these events. CAEs 3 and 4 are also interrupted at ~40.5 Ma by a well-documented global warming event, the Middle Eocene Climatic Optimum (MECO) [*Bohaty and Zachos*, 2003; *Bohaty et al.*, 2009; *Edgar et al.*, 2010]. However, placement of further constraints on the nature of changes in the climate and CCD across the middle Eocene from ODP Leg 199 sediments was limited because the main objective of this leg was to obtain a paleolatitude transect; thus, Eocene strata have low carbonate content and the sites span a limited water depth transect (three sites between ~3.6 to 4.4 km paleodepth; **Figure 2-1**).

Integrated Ocean Drilling Program (IODP) Exps. 320 and 321 returned to the equatorial Pacific in 2009 and drilled eight new sites. One primary objective of these expeditions was to obtain a flow line transect of high-resolution carbonate accumulation records across an array of paleodepths (~3–5 km) to more fully constrain the position of the CCD through the Eocene (**Figure 2-1**) [*Pälike et al.*, 2010; *Pälike et al.*, 2012]. The resulting new CCD reconstruction brings together carbonate data from all available Deep Sea Drilling Program (DSDP) and (Integrated) Ocean Drilling Program sites in the equatorial Pacific to create the most highly constrained Cenozoic CCD curve to date (**Figure 2-2**) [*Pälike et al.*, 2012]. This record confirms the presence of at least seven CCD fluctuations of up to ~1 km in the equatorial Pacific between ~46 and 34 Ma that correspond to the CAEs originally identified.

Pälike et al. [2012] tested several different possible driving mechanisms for the Eocene CCD fluctuations in the equatorial Pacific using the GENIE 3-D model of intermediate complexity [*Panchuk et al.*, 2008; *Ridgwell and Schmidt*, 2010] and the LOSCAR geochemical box model [*Zeebe*, 2012]. Model output hypotheses considered less plausible to explain CCD dynamics include: (1) changes in the rain ratio (reconstructed CCD fluctuations are too small); (2) changes in shelf-basin fractionation (requiring large-scale oscillations in ice mass for which no convincing evidence currently exists [*Bohaty et al.*, 2009; *Edgar et al.*, 2007]), (3) changes in deep-sea temperature and oceanic [Mg] and [Ca]; and (4) switches in the dominant deep-water source between the Southern Ocean and North Pacific leading to opposite CCD behaviour in different ocean basins [*Pälike et al.*, 2012]. Model outputs indicate that the CAEs could plausibly be caused by changes in (5) Changes in solute flux into the deep ocean from increased continental weathering through time and/or (6) the amount and type (refractory vs. labile) of organic carbon supplied to the seafloor (**Table 2-1**). A current lack of similar records from other areas of the oceans limits the ability to fully test the viability of the various proposed mechanisms and ultimately confirm if CAEs are indeed global, which may also help to further constrain the mechanism. One additional key piece of missing information is a detailed understanding of the relationship between climate and the CCD through the Eocene. Middle Eocene benthic foraminiferal $\delta^{18}O$ records from the equatorial Pacific are incomplete and currently are only available across CAE-3 [*Lear et al.*, 2004; *Lyle et al.*, 2005; *Tripati et al.*, 2005].

Furthermore, there are no high-resolution equatorial Pacific environmental or climatic records spanning CAEs 1 and 2 (~42.5–45.5 Ma) from the equatorial Pacific or any ocean basin.

For this study, new high-resolution (~4–10 kyr sample spacing), stratigraphically continuous, monospecific benthic foraminiferal oxygen and carbon stable isotope records ($\delta^{18}O$ and $\delta^{13}C$) were developed from IODP Site U1333 spanning CAEs 1–7 (~38–46 Ma). These data are combined with existing benthic foraminiferal oxygen and carbon stable isotope records for the ~34.5–38 Ma interval [*Sghibartz et al.*, unpublished] and high-resolution carbonate records [*Westerhold et al.*, 2014] from the same site. These records are used to test, for the first time, the relationship between environmental change and carbonate accumulation in the equatorial Pacific throughout the middle and late Eocene and to evaluate hypothesized driving mechanisms. In addition, these new datasets provide the first detailed record of the MECO event from the Pacific Ocean, which was incompletely recovered during Leg 199, as well as new insights on the important, but understudied, time interval between ~43 and 46 Ma.

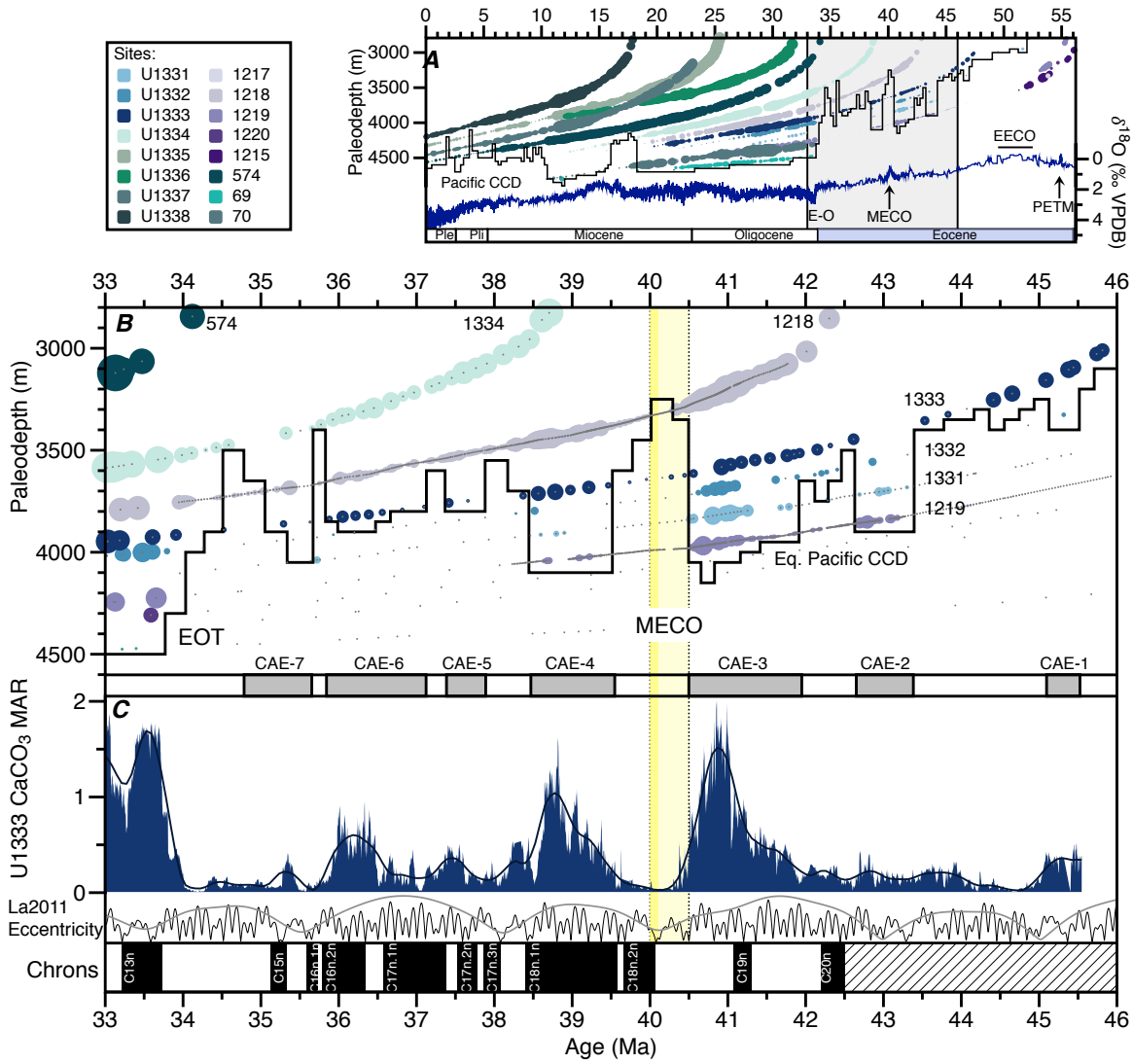

Figure 2-2 CCD and carbonate accumulation rate reconstruction from a depth transect in the equatorial Pacific region.
(a) Cenozoic and (b) Eocene as a function of backtracked age and paleodepth from *Pälike et al.* [2012]. Circle area is scaled by CAR (filled circles). A solid black line indicates the position of the CCD. Grey bars highlight intervals of high $CaCO_3$ MAR from equatorial Pacific sites representing the regional compilation of Carbonate Accumulation Events (ages of CAEs are used hereafter). (c) High resolution $CaCO_3$ MAR at Site U1333 calculated in this study from XRF $CaCO_3$ (wt %) from *Westerhold et al.* [2014]. Eccentricity orbital solution is from La2011 [*Laskar et al.*, 2011a; *Laskar et al.*, 2004] with the filter showing eccentricity amplitude modulation occurring approximately every ~2.4 Myr. $CaCO_3$ MAR data from *Pälike et al.* [2012] are from discrete carbonate measurements in *Pälike et al.* [2010]. $CaCO_3$ MAR data from *Westerhold et al.* [2014] are calculated from NMS Ca counts normalized to $CaCO_3$ (wt %). Ages in (a) are calculated from the PEAT timescale magnetochron boundaries in *Westerhold et al.* [2014] and ages in (b) are calculated from tuning tie-points in *Westerhold et al.* [2014] from 33 Ma until ~42.5 Ma where ages are linearly interpolated from calcareous nannofossil datums in *Pälike et al.* [2010]. Shaded region marks MECO warming (light yellow) and peak-MECO CIE (darker yellow) as defined in *Bohaty et al.* [2009].

2.2 Materials and Methods

2.2.1 Site Selection

IODP Site U1333 is located north of the equator on the East Pacific Rise ridge crest (0°30.996′N, 138°25.159′W; **Figure 2-1**) at 4853 meters below sea level (mbsl) and well below the modern lysocline [*Pälike et al.*, 2010]. The site comprises the shallowest middle Eocene sediments recovered by the "Pacific Equatorial Age Transect" during IODP Exp. 320 and 321 and contains a ~183 m-thick sediment sequence spanning the middle Eocene to lower Miocene that is complete to the biozone and magnetochron level [*Pälike et al.*, 2010]. Three holes, U1333A–C were drilled at the site and a revised composite splice was constructed at decimetre-scale resolution via correlation of magnetic susceptibility, gamma ray attenuation bulk density, natural remnant magnetization data, and core images [*Westerhold et al.*, 2011]. Thus, the spliced composite section at Site U1333 comprises the first continuous sequence of sediments spanning the entirety of the middle Eocene and with carbonate present throughout nearly the entire interval. Here, we focus on the middle Eocene interval between 150.67 and 204.29 m adjusted rmcd (revised composite depth rmcd [m revised CCSF-A] or 'adjusted rmcd' [*Westerhold et al.*, 2011]) when Site U1333 was located between ~3100 and 3500 m paleodepth and within the equatorial high productivity zone (paleoposition ± 2° latitude of the equator until ~35 Ma [*Pälike et al.*, 2010]). Sedimentation rates are ~0.5 cm/Kyr and are composed of pale brown to dark brown nannofossil ooze and radiolarian clay with highly variable carbonate content throughout (~0 to 95 wt %; [*Pälike et al.*, 2010]). Benthic foraminifera occur nearly continuously throughout the sequence but the vast majority of samples are barren of planktic foraminifera [*Pälike et al.*, 2010].

2.2.2 Carbon and oxygen isotope analysis of bulk sediment and benthic foraminifera

In total 1,071 samples were taken at ~5 cm spacing from Site U1333 between 150.67 and 204.29 m adjusted rmcd (equivalent to ~ 4 -10 kyr resolution). These samples were predominantly from Hole U1333B with core gaps filled from Holes U1333A and U1333C along the revised splice [*Westerhold et al.*, 2011] (**Supplemental Figure 2-7g,h**). Bulk sediment samples were dried in an oven at 50 ºC, disaggregated in a solution of deionized water and sodium hexametaphosphate overnight, and then washed over a 63-μm size mesh sieve and oven dried. All sample preparation was carried out at the University of Southampton National Oceanography Centre, Southampton, UK (NOCS).

In total 957 samples contained sufficient individuals of the epifaunal benthic foraminifer *Nuttallides truempyi* for isotopic analysis. Between eight to twelve specimens were picked from the 180-250 μm size fraction and analysed in each sample; however in low carbonate intervals where foraminifera were rare, as few as three specimens were used to obtain a measurement. Samples were considered 'barren' of foraminifera after the entirety of the 180-250 μm size fraction was inspected by light microscopic analyses and fewer than 2 whole test specimens were found (**Supplemental Figure 2-7**). Bulk isotopes ($\delta^{18}O$ and $\delta^{13}C$) were also measured from a small sub-set (n=30) of samples across the MECO interval (where no benthic foraminifera were available) however more than a third of samples failed on the mass spectrometer because the carbonate content was too low for analysis (**Appendix Table 5-2**).

All bulk and most (~67 %) benthic foraminiferal samples were measured on a Finnigan MAT 253 gas isotope ratio mass spectrometer connected to a Kiel IV automated carbonate preparation device at the Zentrum für Marine Tropenökologie ZMT at the University of Bremen and are calibrated against an in-house standard (Solnhofen limestone). Analytical precision based on replicates of Solnhofen limestone (1σ) was ±0.08 ‰ for $\delta^{18}O$ and ±0.02 ‰ for $\delta^{13}C$. The remaining (~33 %) benthic foraminiferal stable isotopes analyses were conducted at NOCS using a GEO 20-20 mass spectrometer where samples were reacted with phosphoric acid at 70˚C using the Carbonate Automatic

Preparation System (CAPS) in line with the mass spectrometer, with an external analytical precision of better than ±0.07 ‰ for $\delta^{18}O$ and ±0.03 ‰ for $\delta^{13}C$ based on replicate analysis of an in-house standard calibrated to NBS-19. An inter-laboratory offset in benthic foraminiferal $\delta^{18}O$ and $\delta^{13}C$ values is corrected for by Gaussian interpolation of the means of the datasets using a 0.5 m step and 3 m filter window (**Equation 2-1**, **Equation 2-2**; **Supplemental Figure 2-1**, where 'Bremen' are measurements made at the University of Bremen and 'NOCS' are measurements made at the University of Southampton National Oceanography Centre). All benthic isotope data are corrected relative to those obtained from the University of Bremen values where the majority of the data was produced. All results are standardized relative to the Vienna Pee Dee Belemnite (VPDB) standard after calibration to the reference material NBS 19. Stable isotopes were corrected for isotopic disequilibrium with seawater as follows: benthic $\delta^{18}O$ of *N. truempyi* (Nutt) were adjusted to *Cibicidoides* (CIB) values (**Equation 2-3**;[*Katz et al.*, 2003]) and converted to temperature using *Kim and O'Neil* [1997] as modified by *Bemis et al.* [1998] and using an ice-free $\delta^{18}O_{sw}$ of -1.2 ‰ (VPDB). Benthic $\delta^{13}C$ values were adjusted to *Cibicidoides* values (**Equation 2-4**;[*Katz et al.*, 2003]).

Equation 2-1 $$\delta^{18}O_{Bremen} = [0.764 * \delta^{18}O_{NOCS}] - 0.091$$

Equation 2-2 $$\delta^{13}C_{Bremen} = [0.828 * \delta^{13}C_{NOCS}] - 0.1517$$

Equation 2-3 $$\delta^{18}O_{CIB} = \left[{(\delta 18O_{Nutt} + 0.10)}/{0.89}\right]$$

Equation 2-4 $$\delta^{13}C_{CIB} = [\delta^{18}O_{Nutt} + 0.34]$$

2.2.3 Coarse fraction and sediment carbonate content

Coarse fraction (wt %) data are commonly used as a proxy for carbonate dissolution in deep marine sediments [e.g. *Kelly et al.*, 2005]. Coarse fraction wt % is calculated by dividing the amount of sample (in grams) in the >63 μm

size fraction after sediment washing by the total initial dry bulk sediment weight (in grams) and then multiplying by 100.

To ensure that the capture of the carbonate signal across the MECO was fully documented, high-resolution XRF-calibrated carbonate estimates [*Westerhold et al.*, 2014] were augmented with bulk sediment weight % $CaCO_3$ measurements. Discrete sample splits (20–30 mg; n = 73) between 163.5 and 175.8 m adjusted rmcd were first dried and then homogenized using an agate mortar and pestle. Carbonate content was measured by high-precision coulometry on a UIC CM5015 CO_2 Coulometer at NOCS equipped with an automated preparation device in which samples are reacted in acid using a carousel system. A calibration was generated from a powdered Carrera marble standard on samples between ~1 - 8 mg at the beginning and end of each sample run and a consistency standard of pure calcium carbonate was included after every 10 samples within a run. The limit of detection was 1.19 ± 0.21 wt % $CaCO_3$.

In order to determine carbonate accumulation rates ($CaCO_3$MAR; g cm^{-2} kyr^{-1}) from XRF-derived $CaCO_3$ wt % records from Site U1333, [*Westerhold et al.*, 2014], linear sedimentation rates (LSR; cm kyr^{-1}) were calculated using all age-depth tiepoints (see below) and estimated dry bulk density (DBD; g cm^{-3}) for all sample intervals using a calibration between shipboard measurements of gamma ray attenuation bulk density (GRA; g/cc) and discrete shipboard measurements of dry bulk density (DBD; g cm^{-3}) ($y= 0.5213x + 0.6821$, $r^2=0.697$; **Supplemental Figure 2-2**; [*Pälike et al.*, 2010]). Carbonate accumulation rates ($CaCO_3$ MAR; g cm^{-2} kyr^{-1}) were calculated as the product between wt % $CaCO_3$ (g $CaCO_3$ g bulk $sediment^{-1}$), LSR (cm kyr^{-1}), and DBD (g bulk sediment cm^{-3}).

2.2.4 Age model, filtering, and spectral analysis

Ages in this study use the cyclostratigraphic, astronomically calibrated age model developed for the middle Eocene through Oligocene (~31- 42.5 Ma) from XRF core scanning data, magnetostratigraphic datum, and bulk stable isotopes [*Westerhold et al.*, 2014]. The orbitally tuned stratigraphy does not extend in sediments older than ~42.5 Ma because of poor age control due to

an absence of magnetostratigraphic data and few biostratigraphic datums, as well as stratigraphic issues including core gaps and a possible hiatus at ~189 m adjusted rmcd (i.e. inconsistent magnetic susceptibility data between all three holes A, B, and C; **Supplemental Figure 2-7d**). Thus, for sediments older than ~42.5 Ma, the ages are based on the shipboard nannofossil stratigraphy [*Pälike et al.*, 2010] (**Supplemental Figure 2-3**).

Spectral analysis was performed on new benthic foraminiferal stable isotope records in both the depth and age domains to identify dominant cyclicity and test the existing orbital stratigraphy. The records were resampled in the depth domain at 5 cm intervals, in the age domain at 5 kyr intervals, and were linearly detrended using a Gaussian notch filter ($\delta^{13}C$ depth frequency = 0.01, bandwidth = 1; $\delta^{18}O$ age frequency = 0.01; bandwidth = 1). Stable isotope data were then filtered to establish the dominant cyclicity in both the depth and age domains using band pass filtering in Analyseries 2.0 [*Paillard et al.*, 1996]. Band pass filtering was conducted in the age domain for the 405-kyr eccentricity at 2.47 cycles/Myr, 100-kyr eccentricity at 10 cycles/Myr, and 1.2 Myr obliquity at 0.83 cycles/Myr. MTM power spectra was generated using the kSpectra Toolkit using three tapers and a resolution of 2, where confidence intervals of 90, 95, and 99% are based on a red noise estimation [*Mann and Lees*, 1996].

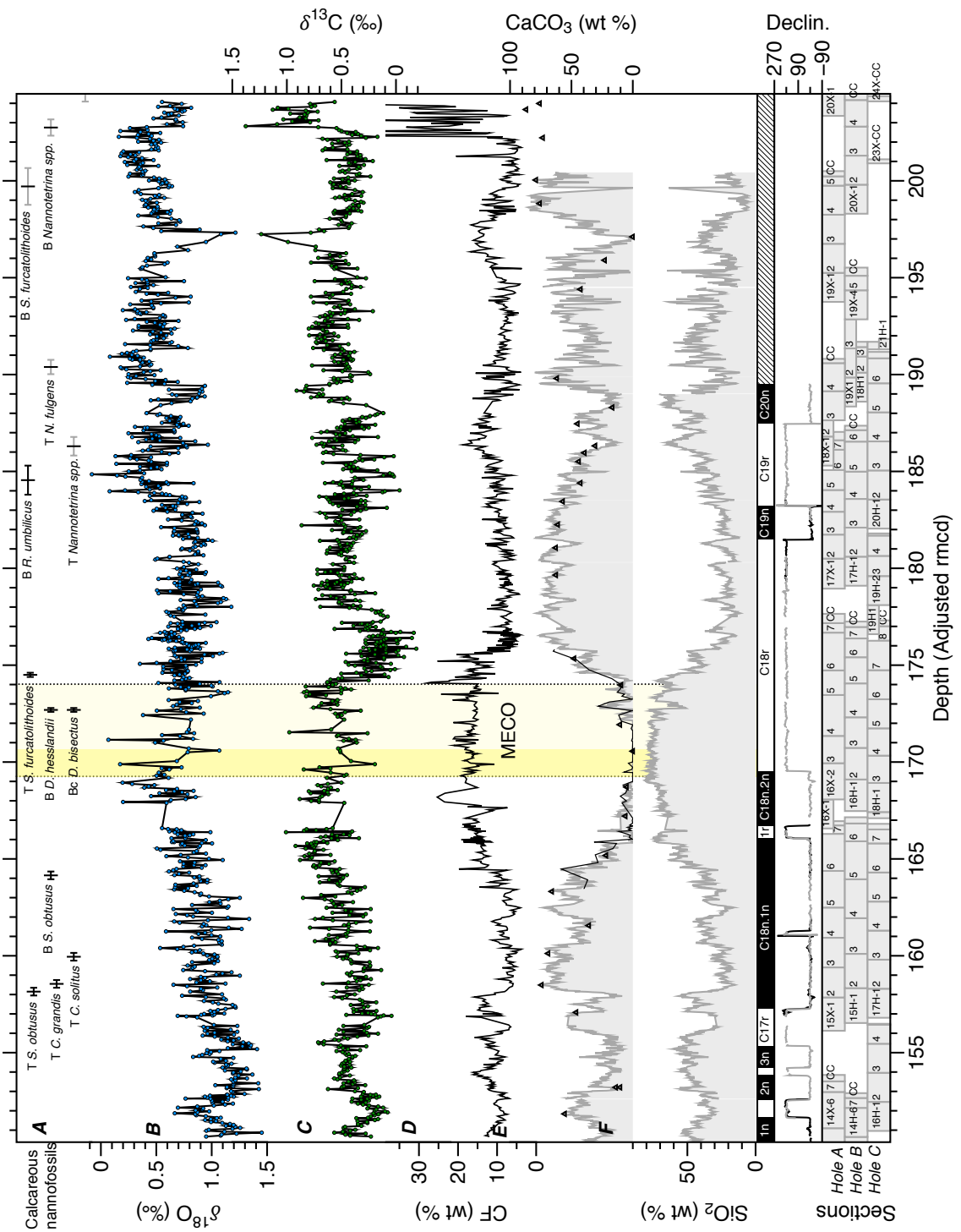

Figure 2-3 IODP Site U1333 benthic foraminiferal stable isotope and sedimentological data versus depth across study interval.
(a) Calcareous nannofossil datums [*Pälike et al.*, 2010; *Toffanin et al.*, 2013], new benthic foraminiferal (b) $\delta^{18}O$ and (c) $\delta^{13}C$ from *N. truempyi*, (d) coarse fraction (wt %), (e) Normalized median scaled (NMS) Ca counts expressed as $CaCO_3$ (wt %; solid gray line) [*Westerhold et al.*, 2014], shipboard $CaCO_3$ (wt %; triangles) [*Pälike et al.*, 2012], and new $CaCO_3$ (wt %; solid black line). (f) NMS Si counts expressed as SiO^2 (wt %) [*Westerhold et al.*, 2014]. Also shown is Site U1333 magnetostratigraphy and declination data [*Westerhold et al.*, 2014], and core recovery from Holes U1333A-C [*Pälike et al.*, 2012].

2.3 Results

2.3.1 Foraminiferal preservation and coarse fraction records

To constrain changes in carbonate preservation that might be associated with the CAEs and the minima in carbonate accumulation between the CAEs the benthic foraminiferal taphonomy was assessed in all samples. Benthic foraminifera are present throughout the study interval except in a few samples where $CaCO_3$ falls below ~5 wt % (**Figure 2-3f**). These intervals coincide with darker-coloured sediment dominated by clay reflecting carbonate dissolution, but with the exception of barren samples no obvious changes in the foraminiferal preservation state are observed across the study interval [*Pälike et al.*, 2010]. Samples are completely barren of foraminifera within the MECO interval between 170.07 and 170.48 m adjusted rmcd (10 consecutive samples in the most severely dissolved interval; **Supplemental Figure 2-7**). Where present, *N. truempyi* is 'moderately' preserved and all specimens are 'frosty' [sensu *Sexton et al.*, 2006b] reflecting micron-scale recrystallization of the test wall. This is further evidenced by SEM analysis, which reveals the absence of vertical pore channels in wall cross sections and inorganic calcite 'overgrowths' on the interior test wall (**Supplemental Figure 2-4**).

Coarse fraction values range between ~4 and 35 wt %, with long-term trends co-varying with wt % biogenic silica and $\delta^{13}C$ (**Figure 2-3**). Typically, in deep sea sediments higher coarse fraction values result from an increased proportion of foraminifer tests, and conversely a decline in coarse-fraction values corresponds to increased test fragmentation by dissolution (or increased current intensity and winnowing) [*Broecker and Clark*, 1999; *Hancock and Dickens*, 2006; *Kelly et al.*, 2005]. However, at Site U1333 the % coarse fraction increases as carbonate content decreases (e.g. across the MECO interval). This is because the >63 μm size fraction at Site U1333 is predominantly composed of the biosiliceous radiolaria [*Pälike et al.*, 2010].

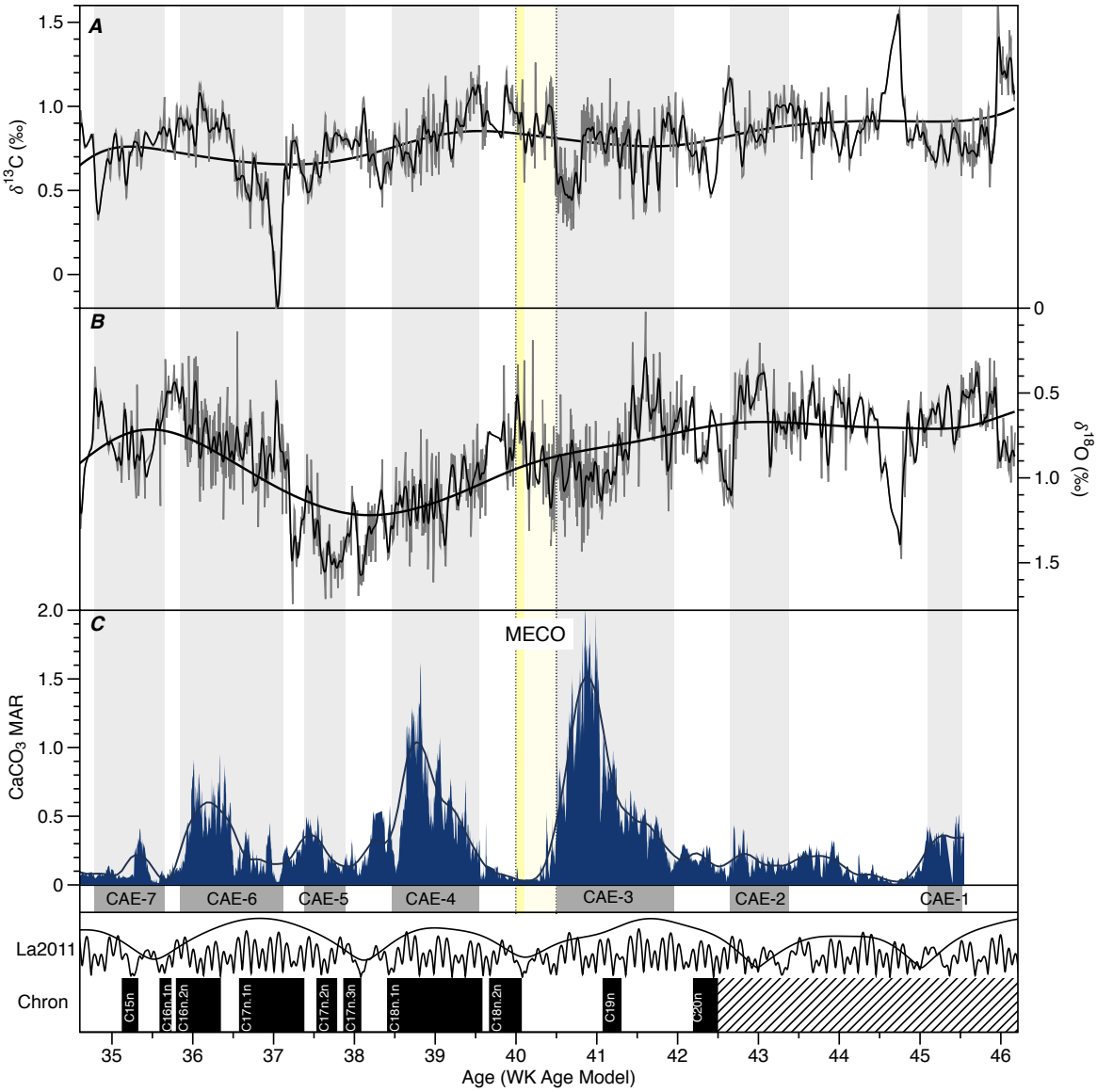

Figure 2-4 IODP Site U1333 benthic foraminiferal stable isotope and sedimentological data versus age across study interval.
Benthic foraminiferal (a) $\delta^{13}C$ and (b) $\delta^{18}O$ (grey lines) with long-term data trends calculated using a LOESS smoothing with 5 kyr and 2 Myr windows (black lines). (c) $CaCO_3$ MAR at Site U1333 calculated in this study using $CaCO_3$ (wt %) [*Westerhold et al.*, 2014]. Labels are as defined in **Figure 2-2**. $\delta^{13}C$ and $\delta^{18}O$ prior to ~37 Ma are from *Sghibartz et al.* [unpublished].

2.3.2 Site U1333 benthic foraminiferal $\delta^{18}O$ and $\delta^{13}C$ records

The new Site U1333 benthic foraminiferal (*N. truempyi*) stable isotope data generated in this study spans a continuous ~9-Myr long interval (~46 to 37.2 Ma; **Figure 2-3**). This is the longest, most highly resolved, and stratigraphically complete benthic $\delta^{18}O$ and $\delta^{13}C$ dataset for the middle Eocene to date. Combined with benthic foraminiferal $\delta^{18}O$ and $\delta^{13}C$ records (*Cibicidoides grimsdalei*) from *Sghibartz et al.* [unpublished] for the interval between ~37.2 – 34.5 Ma the resulting record is the first to span all seven CAEs, which substantially increases data coverage for this time interval and fills a critical gap in existing datasets between 43 – 46 Ma (**Figure 2-4**). The relative timing and pattern of benthic foraminiferal $\delta^{18}O$ and $\delta^{13}C$ trends are generally consistent with published composite records [*Cramer et al.*, 2009; *Zachos et al.*, 2008; *Zachos et al.*, 2001a], e.g., they exhibit the well-known long-term $\delta^{18}O$ increase from ~0.7 ‰ in the oldest samples at the base of the section (~46 Ma) to ~1.25 ‰ in the late Eocene (~37 Ma) which is interpreted to record long-term Eocene cooling (**Figure 2-5**). Benthic foraminiferal $\delta^{13}C$ values vary between ~0.2 and 1.2 ‰ throughout the record. Superimposed on the long-term $\delta^{18}O$ trend is a multi million-year (~10 m) long quasi-cyclical $\delta^{18}O$ trend with shifts of ± 0.5 ‰ reflecting warm/cool alternations of ~2 to 3 ˚C on near eccentricity timescales (~2.4 Myr; **Figure 2-4**). One of these is coincident with the MECO event at ~40 Ma (**Figure 2-4**, vertical yellow bar). The modulation of climate by eccentricity is a common feature of Eocene (and Oligocene) stable isotope records [e.g. *Westerhold and Röhl*, 2013], however there is no consistent isotopic signal corresponding to low amplitude nodes predicted by the Laskar 2011 model (**Figure 2-4**) [*Laskar et al.*, 2011a; *Laskar et al.*, 2011b]. Notably, during the MECO $\delta^{18}O$ values increase by ~0.5 ‰ and $\delta^{13}C$ decreases by ~0.3 ‰ without evidence for a negative $\delta^{13}C$ excursion. The lowest observed $\delta^{18}O$ values in the record occur at ~41.5 Ma ($\delta^{18}O$ = ~0.0 ‰) and precede a prominent ~500 kyr $\delta^{13}C$ minimum ($\delta^{13}C$ = ~0.7 ‰ centred at ~40.7 Ma) that occurs just after the peak of CAE-3 (immediately prior to the MECO) and the highest observed carbonate accumulation rates at this site in the middle Eocene.

Figure 2-5 High-resolution benthic foraminiferal stable isotopes across the late Paleocene and Eocene Interval.
Benthic foraminiferal (a) $\delta^{18}O$ and (b) $\delta^{13}C$ from Site U1333 in the equatorial Pacific (this study; <37 Ma from *Sghibartz et al.* [unpublished]), ODP Site 1260 in the equatorial Atlantic [*Edgar et al.*, 2007; *Edgar et al.*, 2010; *Sexton et al.*, 2006a], ODP Site 689 in the Southern Ocean [*Diester-Haass and Zahn*, 1996] and Sites 738/748 [*Bohaty et al.*, 2009; *Scher et al.*, 2014] in the Southern Ocean, ODP Site 1258 in tropical western Atlantic [*Sexton et al.*, 2011], and ODP Site 1262 in the South-eastern Atlantic [*Littler et al.*, 2014]. Enlarged late to middle Eocene interval in (c) and (d) shows increased detail and highlights short-term climate events. Labels are as defined in **Figure 2-2**. Ages for Sites 1262 and 1258 are as published; Ages for all other sites have been converted to the PEAT timescale of *Westerhold et al.* [2014].

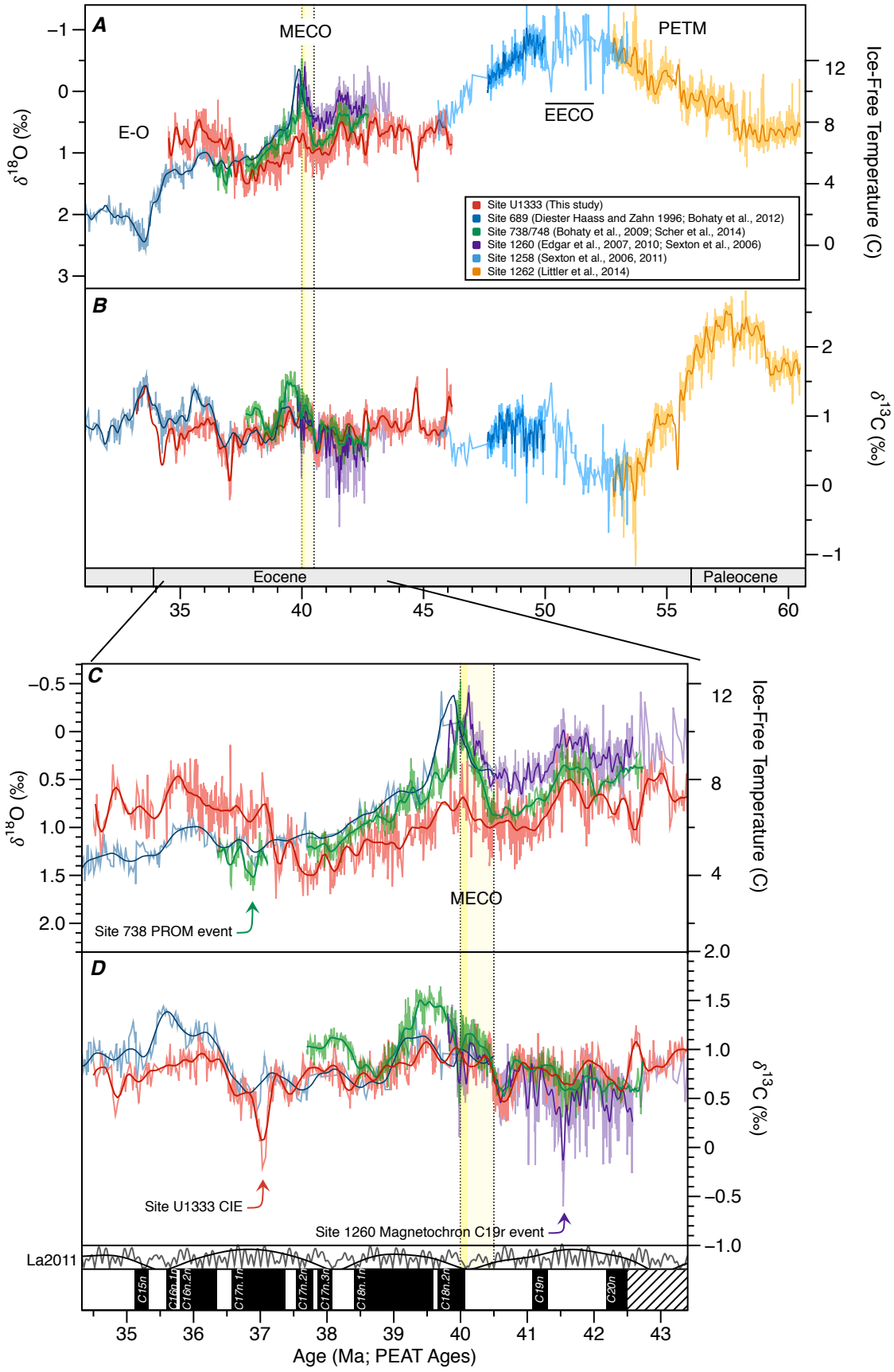
A
MECO
PETM
E-O
EECO
Site U1333 (This study)
Site 689 (Diester Haass and Zahn 1996; Bohaty et al., 2012)
Site 738/748 (Bohaty et al., 2009; Scher et al., 2014)
Site 1260 (Edgar et al., 2007, 2010; Sexton et al., 2006)
Site 1258 (Sexton et al., 2006, 2011)
Site 1262 (Littler et al., 2014)
δ18O (‰)
Ice-Free Temperature (C)
B
δ13C (‰)
Eocene
Paleocene
C
MECO
Site 738 PROM event
D
Site U1333 CIE
Site 1260 Magnetochron C19r event
La2011
C15n
C16n.1n
C16n.2n
C17n.1n
C17n.2n
C17n.3n
C18n.1n
C18n.2n
C19n
C20n
Age (Ma; PEAT Ages)

Comparison of the benthic foraminiferal isotope record with $CaCO_3$ MARs at Site U1333 allows us to test for the first time whether the CAEs are consistently associated with shifts to higher $\delta^{18}O$ values implying cooling and/or ice growth as hypothesized (**Figure 2-4**) [*Lear et al.*, 2004; *Lyle et al.*, 2005; *Tripati et al.*, 2005]. It is evident that the relationship between CAEs and $\delta^{18}O$ values is not as simple as proposed in previous studies. Only CAE-3 is clearly associated with a shift to higher benthic foraminiferal $\delta^{18}O$ values (i.e., inferred cooling). If anything, CAEs-1, 2, and 4 are more strongly coupled with a shift to lower benthic foraminiferal $\delta^{18}O$ values (i.e., inferred warming). The relationship with CAEs-5, 6, and 7 is less clear.

Comparison between available benthic stable isotope records for other sites within the middle to late Eocene interval highlights key similarities and differences between records from different ocean basins (**Figure 2-5c, d**). With the exception of the MECO, trends in $\delta^{18}O$ between ~37.5 and 42.5 Ma from Equatorial Atlantic ODP Site 1260 [*Edgar et al.*, 2007; *Edgar et al.*, 2010; *Sexton et al.*, 2006a] and Southern Ocean Sites 738 and 748 [*Bohaty and Zachos*, 2003; *Bohaty et al.*, 2009] show close correlation with trends from U1333 in magnitude and pattern. The Atlantic Ocean consistently exhibits the lowest $\delta^{18}O$ values (warmest temperatures and/or least saline waters), followed by the Southern, and then Pacific Ocean with offsets of +0.3 ‰ (~1.3 ˚C) between the Atlantic Ocean and Southern Ocean and +0.25 ‰ (~1.1 ˚C) between the Southern Ocean and Pacific Ocean. While records at Site 1260 do not extend post-MECO because of a hiatus, the lower resolution benthic $\delta^{18}O$ records from Southern Ocean Sites 689 [*Diester-Haass and Zahn*, 1996], 738, and 748 continue to have a consistent offset with the Pacific until ~37.5 Ma when the offset between Pacific Ocean and Southern Ocean benthic $\delta^{18}O$ records switch, with Pacific Ocean exhibiting the lowest $\delta^{18}O$ values. Also occurring at ~37.5 is a short-lived prominent negative $\delta^{13}C$ excursion (~0.7 ‰) along with the highest background $\delta^{18}O$ values of the entire record (~1.7 ‰; **Figure 2-5**).

One unexpected feature of the Site U1333 benthic stable isotope record is the discovery of a pronounced transient +0.7 ‰ $\delta^{13}C$ and $\delta^{18}O$ shift between 196.4 to 197.5 m adjusted rmcd (~44.7 Ma; **Figure 2-7**). Precise dating of this interval is difficult because it lies stratigraphically below the astronomically

tuned portion of the record. However, the first occurrence of the calcareous nannofossil *Sphenolithus furcatolithoides* (199.7 m adjusted rmcd, **Supplemental Figure 2-3**; [*Pälike et al.*, 2010]), occurs ~2 m below the event near the base of calcareous nannofossil Zone CNE10 (CP13b, NP15) [*Agnini et al.*, 2014]. The excursion (herein referred to as the 'Biozone CNE10 event') falls within CNE10 and magnetochron C20r, is ~400 kyrs in duration with an approximate age of ~44.7 Ma (maximum age of ~45.42 Ma [*Agnini et al.*, 2014]). Coincident with the isotopic excursion is a discrete clay layer associated with a decrease in bulk carbonate from ~80 wt % to near-zero values [*Pälike et al.*, 2010; *Westerhold et al.*, 2014]. This isotopic excursion is also evident in published low-resolution bulk sediment $\delta^{18}O$ records (+1.1 ‰) (**Figure 2-7**) [*Leon-Rodriguez and Dickens*, 2013] and associated with pronounced chemical changes including decreases in barium (from ~1 to 0 wt % BaO) and manganese (from ~1.5 to 0 wt % MnO), but little change in iron or silicon [*Westerhold et al.*, 2014].

2.3.3 Cyclicity in benthic foraminiferal stable isotope records

Multi-Taper Method (MTM) power spectrum and band-pass filtering analysis of the benthic $\delta^{18}O$ and $\delta^{13}C$ records in the depth domain reveals significant power at several periods (**Figure 2-6**). In the depth domain, the strongest peaks (i.e., statistically significant above the 99% confidence interval level) are detected at 6.43 m, 3.7 m, and 2.56 m in $\delta^{18}O$ and 4.42 m, 2.5 m, and 0.146 m in $\delta^{13}C$. When the same analyses are repeated in the age domain these frequencies are not found to correspond strongly to eccentricity cycles of ~100 and 405 kyr, which would be consistent with published XRF derived-elemental data at this site that exhibit strong 100-kyr and 405-kyr cyclicities in the depth/age domains, particularly in the Normalized Mean Scaled (NMS) Si, Fe, and Ca intensity data (expressed as SiO_2, Fe_2O_3 and $CaCO_3$ wt % data, respectively) [*Westerhold et al.*, 2014]. There is some evidence for power at frequencies relating to precession (at 19, 21 and 23 kyrs), but these are not considered due to the corrections for measurements from two institutions (see Methods).

Ideally the orbital signal in these new benthic foraminiferal stable isotope records would be sufficiently powerful to permit extension of the orbitally

tuned age model at the site below 42.5 Ma. However, further age model work was not considered at this site due to the necessary corrections for measurements from two institutions (see Methods) as they likely introduced error and the orbital signals are not very strong. It is possible, however, to use the identified longer cyclicities in the stable isotope records to independently test the robustness of the current age model (<42.5 Ma; [*Westerhold et al.*, 2014]) that is based solely on sediment properties other than stable isotopes (including from bulk sediment in this interval). Based on cycle counting from stable isotope records the total duration of our records should be 8.97 Myr according to the ages used in this study (a combination of the age model of *Westerhold et al.* [2014] <42.5 Ma and nannofossils datums thereafter; **Supplemental Figure 2-3**). The $\delta^{13}C$ record exhibits n=20.5 405-kyr cycles indicating an 8.3 Myr duration, while the $\delta^{18}O$ record exhibits 22 clear cycles and a duration of 8.9 Myr. Though these calculations inherently rely on the accuracy of the hole-to-hole correlations (splice), $\delta^{18}O$ cycle-counting results in a close approximation of the record duration estimated from the published age model and confirms that calcareous nannofossil datums used in this study are reasonably well constrained.

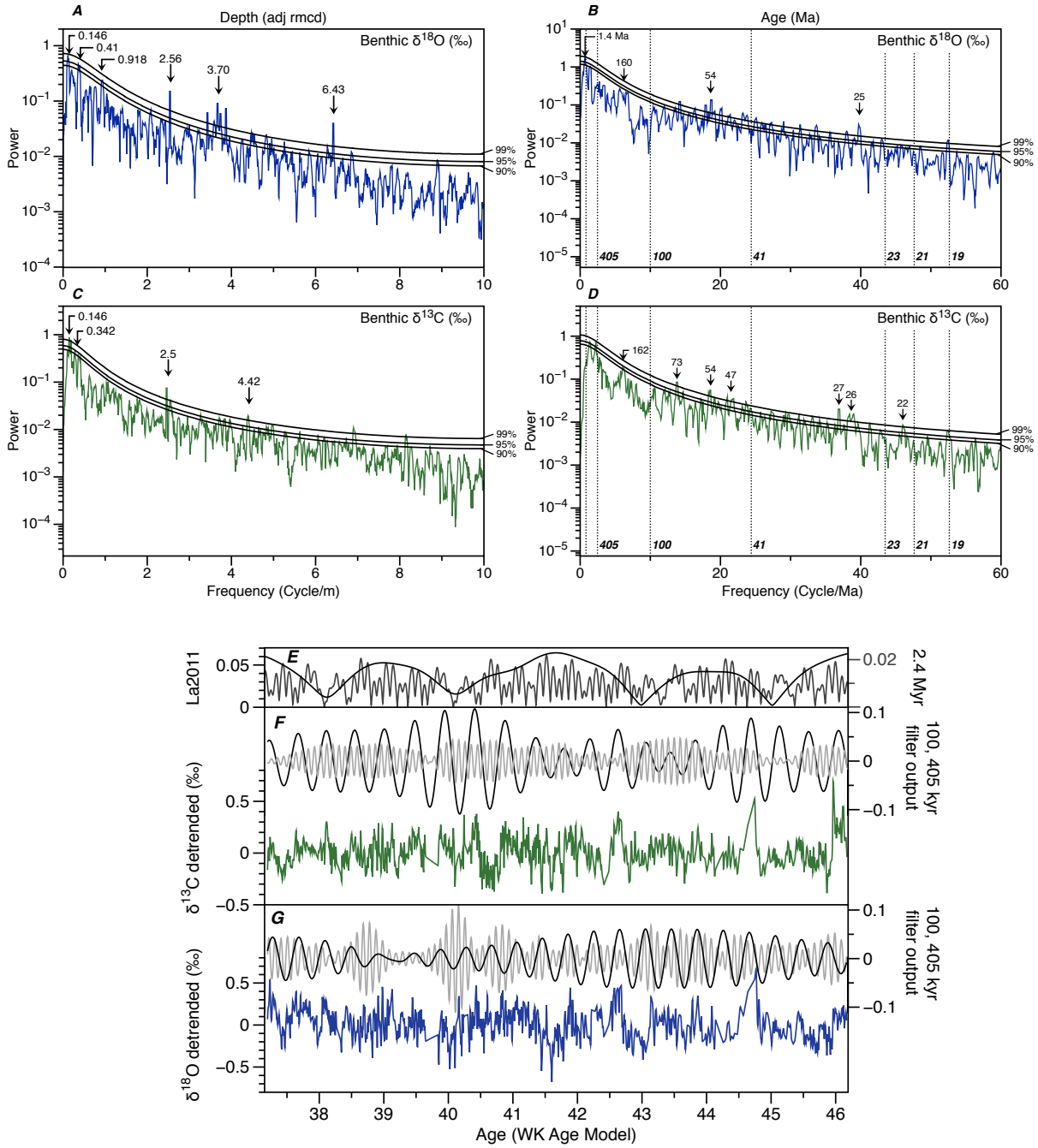

Figure 2-6 Spectral Analysis of Site U1333 benthic isotope data.
MTM power spectra of benthic foraminiferal (a, b) $\delta^{18}O$ and (c, d) $\delta^{13}C$ data in the depth and age domain calculated by the kSpectra Toolkit using 3 tapers. Confidence intervals (90%, 95%, 99%) are based on a robust red noise estimation [*M E Mann and J Lees*, 1996]. Prior to analysis outliers and the long-term trend were both removed and the time series linearly resampled at 5-m and 5-kyr intervals. (e) Eccentricity orbital solution from La2011 [*Laskar et al.*, 2011a; *Laskar et al.*, 2004] with filter showing eccentricity amplitude modulation occurring approximately every ~2.4 Myr. Filter outputs for (f) $\delta^{13}C$ and (g) $\delta^{18}O$ for 405 kyr (black) and 100 kyr (grey) plotted against detrended benthic stable isotopes.

2.4 Discussion

2.4.1 Testing the feasibility of hypothesized mechanisms of CAEs

The Eocene CCD is shallow (<4000 m) and extremely dynamic compared to the rest of the Cenozoic (**Figure 2-2**) [*Lyle et al.*, 2002a; *Pälike et al.*, 2012; *Van Andel*, 1975]. Recent numerical modelling studies have focused on testing multiple mechanisms invoked to explain these large-scale changes in the CCD in the Eocene equatorial Pacific [*Hain et al.*, 2015; *Pälike et al.*, 2012]. Regardless of the mechanism invoked, the Eocene CCD is highly sensitive to carbon cycle perturbations because the CCD is much shallower than at any other time in the Cenozoic and thus has a smaller carbonate buffering capacity [*Pälike et al.*, 2012]. Also, Eocene seawater [Ca] was higher, meaning that seawater was poorly buffered and susceptible to abrupt changes [*Hain et al.*, 2015]. However, the main driver(s) of the CAEs remains uncertain.

The modelling experiments of *Pälike et al.* [2012] were undertaken for steady state conditions and identify six possible mechanisms for CCD change. Several of these hypotheses were deemed unlikely because model outputs fail to match existing observations, reconstructing CCD shifts that are too small and on timescales that are too short. These include (1) organic carbon surface export rain ratio changes, (2) changes in shelf-basin fractionation, (3) deep ocean ventilation source change from Southern Ocean to the North Pacific, and (4) changes in deep-sea temperature and concentration of Mg or Ca of seawater. The two more plausible scenarios responsible for CAEs include (5) changes in solute flux into the deep ocean from increased weathering and (6) increased organic carbon burial from changes in ecology (see summary in **Table 2-1**).

The new dataset presented in this thesis chapter provides an opportunity to revisit the feasibility of several of the hypothesized causal mechanisms. For instance, while initially considered unlikely, model scenario 2 (changes in shelf basin fractionation; **Table 2-1**) has yet to be tested empirically but can be

directly addressed with new benthic foraminiferal $\delta^{18}O$ records from Site U1333. Changes in shelf-basin fractionation necessitate large-scale sea level change via thermal expansion/contraction (on the order of a few meters) and/or continental ice volume across all CAEs. If correct, this implies a direct correlation between proxy data for temperature/ice volume (benthic foraminiferal $\delta^{18}O$ values) and $CaCO_3$ MAR should be observed. However, there is no consistent $\delta^{18}O$ response across the CAEs (**Figure 2-4**). CAE-3 is the only CAE associated with an increase in $\delta^{18}O$, and the amplitude of the $\delta^{18}O$ change does not necessitate the growth of large ice sheets or sea level change (See **Section 2.4.2**). Furthermore, if CAEs were related to the waxing and waning of continental ice sheets, we might expect long-term Eocene cooling to lead to a progressive increase in the size of CAEs through the Eocene as Earth's background climate moved closer to the threshold for ice-sheet growth. There is no such progression in $CaCO_3$ MAR across the seven CAEs. These new data therefore show that transient changes in shelf-basin fractionation should be excluded from further consideration. This likely differs from the situation at the EOT [*Armstrong McKay et al.*, 2016; *Merico et al.*, 2008] where there is convincing evidence for the development of large ice sheets on Antarctica and a permanent step-change in the system [*Coxall and Wilson*, 2011; *Coxall et al.*, 2005; *Houben et al.*, 2012].

Model scenario 3 (changes in the location of deep water formation) and scenario 5 (increased continental weathering and variations of solute input into the deep ocean) of *Pälike et al.* [2012] (**Table 2-1**) are only plausible if the pattern of CAEs between the Pacific and Atlantic basins is asynchronous or synchronous, respectively. A switch in the formation of deep water from the Southern Ocean to the Pacific necessitates that CAEs occur out of phase in the Atlantic and Pacific Oceans due to resulting water mass age differences (assuming a single source of deep water formation). Conversely, changes in continental weathering will vary solute input to the deep ocean globally, necessitating CAEs that occur in phase in the Atlantic and Pacific Oceans on the temporal resolution of our datasets. Two new lines of evidence allow us to test these scenarios. First, while empirical Atlantic CCD datasets do not currently span the entire Eocene, synchronous behaviour of the Atlantic and Pacific CCD during CAEs-3 and 4, and the Atlantic, Pacific, and Indian Oceans during the MECO [Thesis Chapter 2; *Bohaty et al.*, 2009] suggest a global

coherence in CCD fluctuations. Preliminary results from the Northwest (IODP Exp. 342) and equatorial (ODP Site 929) Atlantic also suggest that the CAEs are present here [*Norris et al.*, 2014a; supplementary info in: *Pälike et al.*, 2012] and of similar age to those from the equatorial Pacific record. Second, our new dataset shows general long-term agreement in both the pattern and amplitude of benthic $\delta^{18}O$ and $\delta^{13}C$ records between the equatorial Pacific, equatorial Atlantic [*Edgar et al.*, 2007; *Edgar et al.*, 2010], and Southern Oceans (**Figure 2-5**; [*Bohaty et al.*, 2009; *Diester-Haass and Zahn*, 1996]) implying no significant changes in either temperature or water mass age characteristics on the recurrent intervals of the CAEs. To conclusively exclude scenario 3 (asynchronous CAEs) detailed records of $CaCO_3$ MAR with paired well-dated benthic foraminiferal $\delta^{18}O$ and $\delta^{13}C$ records are needed from the Atlantic. However, the preliminarily data presented in this chapter suggest that scenario 3 is unlikely because CAEs appear synchronous in the Atlantic and Pacific, while scenario 5 remains plausible but new data explicitly recording changes in global weathering rates are required to further test this hypothesis.

Model scenario 6 (**Table 2-1**) invokes changes in the efficiency of the biological pump leading to either (6a) less efficient recycling of organic matter in the water column by changes in organism basal metabolic rate or (6b) less efficient recycling of organic matter due to changes in the composition of marine plankton assemblages. Metabolic rates are strongly temperature-dependent. This relationship is best described by the 'Q_{10}' rule where metabolic rates approximately double for every 10°C temperature increase [*Brown et al.*, 2004; *Gillooly et al.*, 2001]. Thus, cooler ocean temperatures should result in a slowdown of organismal metabolic rates and recycling of organic matter from surface waters leading to increased organic matter burial and less remineralized CO_2, decreasing carbonate ion solubility and increasing carbonate accumulation. Alternatively, slowed remineralization could be caused by a shift in plankton assemblage types to more refractory types that are less easily recycled by marine bacteria (e.g., carbonate vs. siliceous forms). These two scenarios (6a and 6b) are supported by empirical observations at Sites 1218 and 1219 which reveal that CAEs-3 and 4 correspond to increased accumulation of calcareous and biosiliceous (opal) sediment, and organic carbon [*Lyle et al.*, 2005; *Moore Jr et al.*, 2008; *Olivarez Lyle and Lyle*, 2005; 2006]. New results from IODP Exp. 320 and 321 shed light on several aspects

of these proposed scenarios. First, the metabolic hypothesis (Scenario 6a; **Table 2-1**) is based on the assumption that warm/cool temperature alternations occurred in phase with CAEs, for which there is no strong evidence in the new benthic $\delta^{18}O$ records at Site U1333 (**Figure 2-4**). Second, this scenario relies on simultaneous increased burial fluxes of calcareous and biosiliceous sediment; however, close inspection of records from Sites 1218 and 1219 spanning a longer time interval and alongside new data from Site U1333 reveals that this assumption is unwarranted (**Supplemental Figure 2-8**). Biogenic silica accumulation is indeed highest during CAEs-3 and 4 at Sites 1218 and 1219 [*Lyle et al.*, 2005], yet silica accumulation is still high between events. Also, biogenic silica MAR does not increase during CAE-3 or 4 at Site U1333 (or with clear correlation to any of the other CAEs) with the highest values occurring directly out of phase with carbonate peaks [*Westerhold et al.*, 2014] (**Supplemental Figure 2-8**). Furthermore, the carbonate and silica signals across CAEs 3 and 4 are complicated by widespread carbonate dissolution during the MECO, which is also associated with increased biosiliceous accumulation observed in the Southern Ocean and North Atlantic related to the MECO event [*Witkowski et al.*, 2012; *Witkowski et al.*, 2014]. In addition, decoupling between the magnitude of changes in $CaCO_3$ MAR and export productivity suggests that CAEs 4 and 6 are a function of both productivity and preservation (inferred from Ba; [*Griffith et al.*, 2010]).

Having revisited the six competing hypotheses for the CAEs discussed by *Pälike et al.* [2012] (**Table 2-1**), only solute flux changes via increased continental weathering (Scenario 5) and increased organic carbon burial from marine plankton assemblage changes (Scenario 6b) are capable of explaining the observed changes in both carbonate accumulation and benthic $\delta^{18}O$ and $\delta^{13}C$. However, the lack of consistent relationships between CAEs, productivity, and deep-sea temperature suggests that changes in the biological pump were not closely linked with global climatic changes, and there is currently no proposed mechanism for scenario 6b that would cause either the recovery in accumulation or the repetition of all seven CAEs. Therefore, based on the new insights of this study, the CAEs are tentatively ascribed to increased solute supply (scenario 5) resulting from increased continental weathering as discussed in *Pälike et al.* [2012]. Critically, this hypothesis assumes that the solute flux can change without any initial change in pCO_2 (and therefore

temperature), which is consistent with increased continental weathering from precipitation forced by orbital modulation of the monsoon system.

Ultimately, determining the exact operating mechanism(s) controlling CCD variations in the equatorial Pacific will require more globally extensive records to obtain a basic understanding of the geographical extent of CAEs and whether they are present in the Atlantic and Indian Ocean basins. There are also currently no existing shallow water records from the equatorial Pacific (e.g. $\delta^{18}O$ and $\delta^{13}C$ in planktic foraminifera or bulk sediment), global records of marine ecology or continental weathering rates to further test the weathering hypothesis (scenario 6b).

2.4.2 Transient middle-late Eocene climate perturbations?

Benthic foraminiferal $\delta^{18}O$ values indicate that bathyl temperatures in the equatorial Pacific during the middle Eocene were notably warmer than today, with peak temperatures ranging from ~10 ˚C prior to the MECO to ~4 ˚C immediately prior to the EOT (assuming no ice volume effect), in broad agreement with temperature reconstructions for the same time interval made on published records [*Zachos et al.*, 2008; *Zachos et al.*, 2001a] (**Figure 2-5**) Superimposed on this background warmth were several prominent isotopic excursions associated with carbonate variability. The recently recorded Priabonian oxygen isotope maximum (PrOM) event in the Southern Ocean at ~37.3 Ma is associated with a positive shift in $\delta^{18}O$ (~0.5 ‰ and inferred cooling) and evidence from Nd isotopes interpreted as the presence of small ice sheet presence on East Antarctica [*Scher et al.*, 2014]. Though recorded in the Southern Ocean, the event was speculated to coincide with CAE-5 (precise correlation was hindered by a lack of carbonate records to identify CAEs in the Southern Ocean) (**Figure 2-5**). In the new records presented here a short-lived prominent ~0.7 ‰ negative $\delta^{13}C$ excursion at ~37.25 Ma may correspond to the PrOM event (there is no published $\delta^{13}C$ data with which to compare in the Southern Ocean), however the excursion is accompanied by a negative $\delta^{18}O$ excursion (~0.5 ‰) and inferred warming. Though no transient cooling is observed at U1333, $\delta^{18}O$ values reach the highest of the entire record ~1.7 ‰ from ~37.25 to 38 Ma, approaching the ~2.0 ‰ threshold proposed for the probable existence of ice sheets [*Miller et al.*, 1987] (**Figure 2-5**).

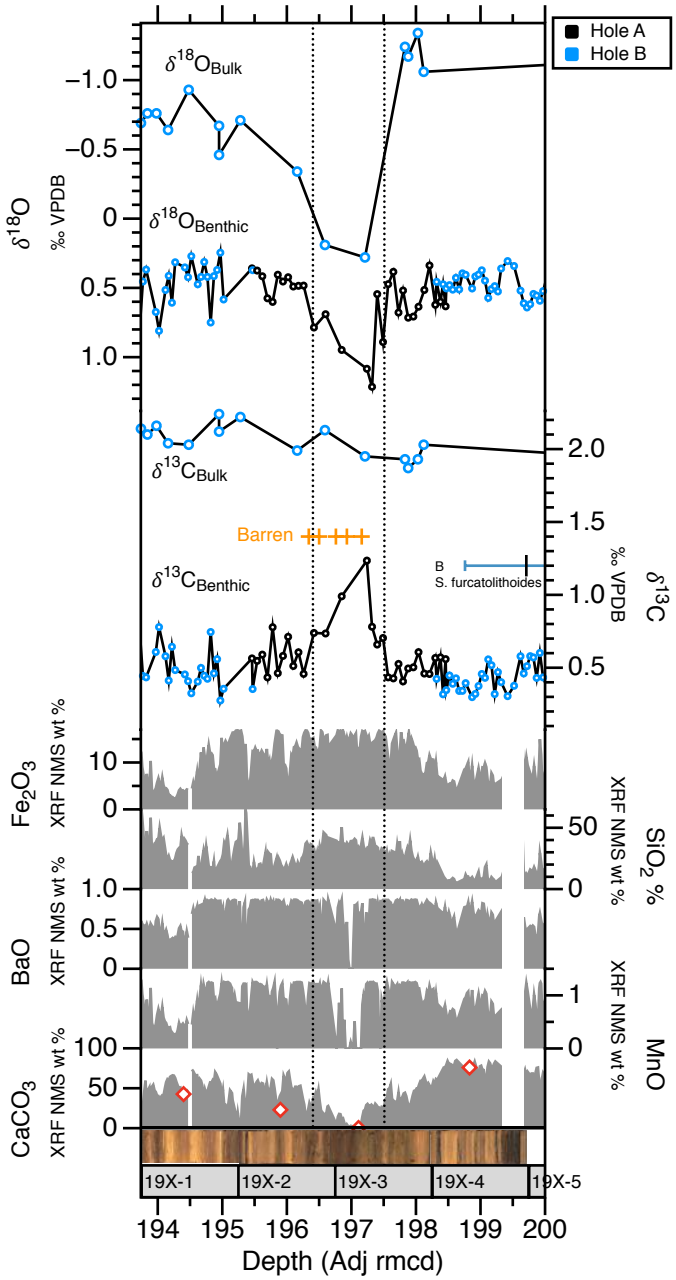

Figure 2-7 Summary of stable isotope and sediment composition across Cores U1333A 19X-1 to 5.
Benthic foraminifera and bulk sediment [*Leon-Rodriguez and Dickens*, 2013] $\delta^{18}O$ and $\delta^{13}C$ versus depth plotted with records of Normalized median scaled (NMS) Fe counts expressed as Fe_2O_3 (wt %), NMS Si counts expressed as SiO_2 (wt %), NMS Ba counts expressed as BaO (wt %), NMS Mn counts expressed as MnO (wt %), and NMS Ca counts expressed as $CaCO_3$ (wt %). Yellow crosses represent isotope coarse samples barren of benthic foraminifera. XRF data from *Westerhold et al.* [2014]. Dotted vertical lines show excursion as defined by benthic $\delta^{18}O$ and $\delta^{13}C$. Bottom occurrence of calcareous nannofossil *Sphenolithus furcatolithoides*, core photos, and core recovery from *Pälike et al.* [2010].

Further back into the Eocene the evidence for large ice sheets is deeply controversial. A large positive shift of ~1.2 ‰ in benthic foraminiferal $\delta^{18}O$ values at equatorial Pacific Site 1218 (**Figure 2-1**, **Figure 2-8**) combined with bottom water temperature estimates from Mg/Ca records, and evidence for CCD deepening was interpreted as necessitating ice growth not only on Antarctica but bipolar glaciation during CAE-3 between ~41.5 and 40.7 Ma [*Tripati et al.*, 2005]. At the time, this study was highly controversial because of poor preservation and dolomitization of carbonate in the key interval at Site 1218 [*Lyle et al.*, 2002b] which may have compromised records, and the existence of large ice sheets in the middle Eocene is at odds with contemporaneous warm polar ocean temperatures [*Lear et al.*, 2000; *Sexton et al.*, 2006a; *Zachos et al.*, 2001a] and high atmospheric CO_2 levels [*Bijl et al.*, 2010; *Pagani et al.*, 2005; *Pearson and Palmer*, 2000]. Indeed subsequent high-resolution studies from equatorial Atlantic ODP Site 1260, South Atlantic ODP Site 702 and Southern Ocean Site 738 all show a more modest increase in benthic foraminiferal $\delta^{18}O$ values over the same time interval (~0.6 ‰, 0.4 ‰, and 0.5 ‰, respectively; [*Bohaty et al.*, 2009; *Edgar et al.*, 2007]; **Figure 2-8**). Thus, calculations of estimated ice volumes with the revised benthic $\delta^{18}O$ shifts at Site 1260 resulted in a maximum of ~0.4 to 0.6 times the modern Antarctic budget [*Edgar et al.*, 2007].

Located <350 km away from Site 1218, Site U1333 provides a more continuous carbonate record across the controversial interval and thus, the opportunity to further test this competing hypotheses over environmental change in this interval. The new benthic foraminiferal $\delta^{18}O$ record presented here shows general agreement with other records in the overall pattern of change: overall warmth in magnetochron C19r and cooling during C19n and C18r with gradual cooling starting at ~41.5 Ma peaking at ~40.7 Ma. A long-term mean through the values indicates that Site U1333 registers a maximum positive shift of ~ +0.5 ‰ (~41.5 Ma) corresponding to a maximum cooling of 2.5 ˚C of bottom waters assuming ice-free conditions, significantly smaller than the magnitude previously invoked [*Tripati et al.*, 2005] (**Figure 2-8**). Furthermore, due to the close proximity of the two sites and the higher sampling resolution at Site U1333, it is not likely that a transient event is missing from this record. Ultimately, the coherence in benthic foraminiferal $\delta^{18}O$ values between ocean basins most likely implies global cooling did occur

between ~41.5 and 40.5 Ma. However, the maximum shift in $\delta^{18}O$ values is not large enough across this interval to require large bipolar ice sheets in the middle Eocene (without invoking untenably high $\delta^{18}O$ values for ice sheets or concurrent deep water warming), consistent with findings of *Edgar et al.* [2007]. Therefore, cooling during CAE-3 was not accompanied by ice sheet growth in the Northern Hemisphere, but we cannot rule out the possibility that smaller scale ephemeral ice sheets developed in Antarctica. This conclusion is consistent with high Eocene atmospheric pCO_2 estimates [*Anagnostou et al.*, 2016; *Pagani*, 2005; *Zhang et al.*, 2013] and global climate modelling indicating that the threshold for Northern Hemisphere glaciation required substantially lower CO_2 than evidenced [*DeConto et al.*, 2008].

Table 2-2 Comparison of key features characterizing transient events in the Eocene

Event type	*Δ $\delta^{18}O$*	*Δ $\delta^{13}C$*	*Age (Ma)*	*Event duration*	*Δ CaCO3 (wt %)*	*Δ CCD*	*Citation*
Biozone CNE10 event	+	+	~44.7	<500 kyr	Dissolution	Shoaling	(this study)
Early Eocene Hyperthermals	-	-	Early Eocene	<100 kyr	Dissolution	Shoaling	Kennett and Stott, 1991; Laurens et al., 2005; Sexton et al., 2011; Thomas and Shackleton 1996; Zachos et al., 2003
Eocene Oligocene transition	+	+	~34	~400 kyr	Accumulation	Deepening	Coxall and Wilson, 2011; Coxall et al., 2005; Kennett and Stott, 1991; Shackleton and Kennett, 1975; Zachos et al., 1996; Zachos et al., 2001
Priabonian oxygen isotope maximum event	+	?	~37	~140 kyr	Presumed accumulation	Presumed deepening	Scher et al., 2014
Magnetochron C19r Event	-	-	41.5	40-50 kyr	Dissolution	Shoaling	Edgar et al., 2007; Westerhold et al., 2014

2.4.3 The 'Biozone CNE10 event'?

The new Site U1333 records are the first high-resolution benthic foraminiferal $\delta^{13}C$ and $\delta^{18}O$ records to span the interval between ~42.6 and 46.2 Ma and have led to the discovery of the Biozone CNE10 event (described in **Section 2.3.2; Figure 2-7**). However, close coincidence between the isotopic excursion and pronounced lithological and chemical changes in the core

necessitate that a diagenetic origin, as opposed to a climatic one, is first evaluated. Two lines of evidence support a possible role for diagenesis. First, porcellanite is found ~80 cm below the excursion (Hole U1333A-19X-4) [*Pälike et al.*, 2010]. Second, and most compelling, MnO and BaO records both show sharp decreases at the peak of the isotopic excursion indicating the possible onset of reducing conditions during diagenesis, and trace metals remobilized above [*Calvert and Pedersen*, 1993]. However, it is atypical for Fe_2O_3 to remain steady across a dissolution interval (**Figure 2-7**); clay layers are commonly associated with an increase in iron-rich minerals [*Westerhold et al.*, 2014].

If the excursion is a real climatic signal, there are currently no analogous events known from the Eocene with positive $\delta^{13}C$ and $\delta^{18}O$ excursions and CCD shoaling, highlighting seemingly unique behaviour between temperature, carbon storage/uptake, and the carbonate system across this event. The magnitude and duration of the Biozone CNE10 Event is reminiscent of the short-lived hyperthermal events identified in the early and middle Eocene, however those events are associated with negative $\delta^{13}C$ and $\delta^{18}O$ excursions [e.g. *Edgar et al.*, 2007; *Littler et al.*, 2014; *Lourens et al.*, 2005; *Sexton et al.*, 2011] (**Table 2-2**). Whereas the PrOM event [~37.3 Ma; *Scher et al.*, 2014] and EOT are associated with a positive shift in isotopic values (however there are no available $\delta^{13}C$ or carbonate data from the PrOM event with which to compare to our records) and inferred cooling and/or ice growth [*Coxall and Wilson*, 2011; *Coxall et al.*, 2005; *Houben et al.*, 2012; *Scher et al.*, 2011]. The EOT however, corresponds to the largest CCD deepening observed in the Cenozoic [*Pälike et al.*, 2012] and does not agree with the CCD shoaling observed here.

Nearby equatorial Pacific IODP Sites U1331 and U1332, and ODP Site 1220 are much deeper that Site U1333 and thus, contain little or no carbonate [*Pälike et al.*, 2010] on which to develop high-resolution sedimentological records (e.g. stable isotope analyses, XRF core scanning) to test if the event is present. However, high-resolution bulk sediment stable isotope records from ODP Sites 702 and 1263 in the South Atlantic [*Westerhold et al.*, 2015] do not exhibit any significant $\delta^{13}C$ or $\delta^{18}O$ excursions around ~45 Ma. Additionally, high resolution XRF Fe records and core photos from ODP Site 1260 in the Equatorial Atlantic show no signs of a significant clay layer at this time [*Westerhold et al.*, 2014].

2.4.4 The MECO event in the equatorial Pacific

The MECO is by far the most studied interval in the middle Eocene, and although prominent warming and ocean acidification has been well documented globally [*Bohaty and Zachos*, 2003; *Bohaty et al.*, 2009], there are as of now no complete records across the event from the Pacific Ocean [*Dawber and Tripati*, 2011b; *Lear et al.*, 2004] and key questions remain as to the drivers behind the event [*Sluijs et al.*, 2013]. New data from Site U1333 has sedimentological characteristics typical of the MECO including: severe carbonate dissolution evidenced by a low-carbonate clay layer [*Pälike et al.*, 2010], and reduced abundance of planktic and benthic foraminifera [*Takata et al.*, 2013] and calcareous nannofossils [*Toffanin et al.*]. However, most striking is the lack of the most characteristic and prominent MECO feature in the $\delta^{18}O$ signal from the classic Southern Ocean records: gradual warming from ~40.5 Ma culminating in a pronounced $\delta^{18}O$ minimum at ~40.1 Ma (with a total shift of ~1.0 to 1.5 ‰ across the whole event) followed by abrupt cooling [*Bohaty et al.*, 2009]. Site U1333 $\delta^{18}O$ values show a gradual decrease in $\delta^{18}O$ values, representing warming from ~40.5 Ma, but prolonged negative values remain until much later 39.85 Ma (with no pronounced peak) when the recovery to higher $\delta^{18}O$ values or cooling is observed elsewhere (**Figure 2-5**, **Figure 2-8**). Explanations for this discrepancy could include: (1) MECO is incomplete at Site U1333 because of a hiatus in the section or a recovery gap, (2) MECO is complete at this site but the $\delta^{18}O$ signal is obscured by post-depositional processes, or (3) the low-magnitude $\delta^{18}O$ shift (and thus, subdued warming signal) is a true representation of the MECO in the equatorial Pacific. Each of these hypotheses is discussed in the following sections.

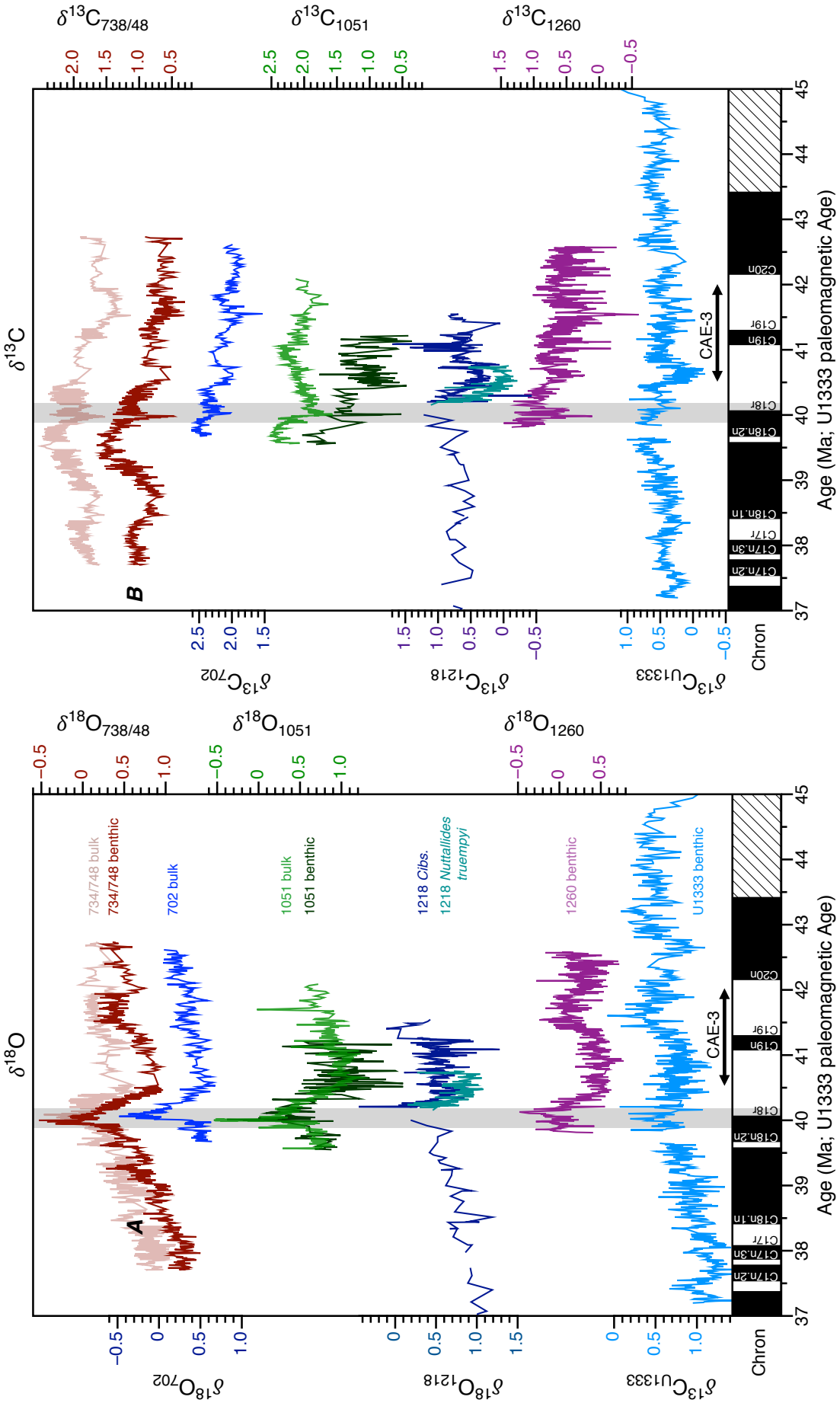
δ13C738/48
δ13C1051
δ13C1260
δ13C
B
CAE-3
δ13C702
δ13C1218
δ13CU1333
Chron
Age (Ma; U1333 paleomagnetic Age)
δ18O738/48
δ18O1051
δ18O1260
δ18O
A
734/748 bulk
734/748 benthic
702 bulk
1051 bulk
1051 benthic
1218 Cibs.
1218 Nuttallides truempyi
1260 benthic
U1333 benthic
δ18O702
δ18O1218
δ13CU1333

Figure 2-8 Compilation of stable isotope records across the MECO interval. Benthic foraminifera (dark brown) and bulk sediment (light brown) from ODP Site 738 and 748 [*Bohaty et al.*, 2009], bulk sediment from ODP Site 702 (blue) [*Bohaty et al.*, 2009], benthic foraminifera (dark green) [*Edgar et al.*, 2010]and bulk sediment (light green) [*Bohaty et al.*, 2009], from ODP Site 1051, benthic foraminifera from IODP Site 1218 [*Lear et al.*, 2004; *Tripati et al.*, 2005], benthic foraminifera from IODP Site 1260 (purple) [*Edgar et al.*, 2007; *Edgar et al.*, 2010] and benthic foraminifera from IODP Site U1333 (light blue) [this study]. Shaded interval represents the interval of lowest benthic foraminiferal $\delta^{18}O$ values at Sites U1333 and 1260. Records are shown on a revised age scale calculated according to PEAT timescale magnetostratigraphy at Site U1333 [*Westerhold et al.*, 2014].

2.4.4.1 Is the MECO event complete at Site U1333?

Accurate dating of MECO is often hindered by a weak magnetic polarity signal in key sections, particularly at the magnetochron C18r/C18n boundary due to either the presence of chert in condensation horizons related to the shallow CCD during the MECO (e.g. Sites 1218 and 1220) or high carbonate content and low number of magnetic carriers and thus, low magnetic signal (e.g. Sites 738 and 748) [see discussion in *Edgar et al.*, 2010]. Sites with both stable isotope records and a magnetostratigraphy spanning the full MECO interval only exist at ODP Sites 702 and Site 1051 in the Southern and subtropical Northern Atlantic, respectively (**Supplemental Figure 2-5**, **Supplemental Figure 2-6**) [*Bohaty et al.*, 2009; *Clement and Hailwood*, 1991; *Edgar et al.*, 2010; *Ogg and Bardot*, 2001]. The peak of the MECO event at Site 702 (defined by the lowest observed bulk sediment $\delta^{18}O$ values) spans the top of magnetochron C18r and the lower ~13% of the duration of magnetochron C18n.2n (grey shading in top panel, **Supplemental Figure 2-6**). At Site 1051 the lowest benthic (and bulk) foraminiferal $\delta^{18}O$ values occur within the lower ~20 % of magnetochron C18n.2n (grey shading in second panel, **Supplemental Figure 2-6**). Although slight differences in the timing are indicated (likely due to a combination of carbonate dissolution, uncertainty in the placement of the magnetochron boundary, and/or non-linear sedimentation rates) the onset of post-MECO cooling at both sites begins by ~39.99 Ma or ~20 % of the way through magnetochron C18n.2n ($\delta^{18}O$ panel in **Supplemental Figure 2-5**).

Site U1333 has arguably the highest quality paleomagnetic record in this interval of the Eocene recovered anywhere, with a distinctive step-like behaviour at magnetochron boundaries (including the rare C18n.2n – C18r boundary) [*Pälike et al.*, 2010; *Westerhold et al.*, 2014] (**Supplemental Figure 2-6**). Thus, the new benthic $\delta^{18}O$ record presented in this chapter can be used to help assess whether the MECO is complete at Site U1333. A splice gap due to core gaps and drilling disturbances in all three holes occurs in magnetochron C18n.2n (166.52 – 167.10 m adjusted rmcd [*Pälike et al.*, 2010]) (**Supplemental Figure 2-7**). The splice gap, however, occurs at ~39.84 Ma and declination data show that this is ~57 % of the way through magnetochron C18n.2n and is therefore unlikely to be responsible for the small magnitude of

the peak-MECO signal. Furthermore, the resulting gap between samples (~38 kyr) is insufficient to span the full warming of the MECO (~500 kyr). Consequently, the MECO interval at this site is considered stratigraphically complete.

2.4.4.2 Is the MECO at Site U1333 obscured by post-depositional processes?

The MECO coincides with a shallow CCD [*Pälike et al.*, 2010] (**Figure 2-2**) leading to extensive carbonate dissolution at Site U1333 and potentially other diagenetic effects resulting from changes in bottom or pore water conditions, and/or sedimentation rates. It is likely that corrosive bottom waters led to extremely low benthic foraminiferal abundances (<1 %) found between 174-166 m adjusted rmcd [*Takata et al.*, 2013] thus, some isotopic analyses were conducted on only a few (n=4) specimens in this interval, which could lead to increased secular variability [see discussion in *Pearson*, 2012] (location of barren samples plotted in **Supplemental Figure 2-7**). Also, despite evidence of benthic foraminiferal test recrystallization (**Supplemental Figure 2-4**), previous studies from IODP Exp. 320 and 321 sediments (including one on Oligocene benthic foraminifera at Site U1333) indicate that diagenesis has only a negligible effect on benthic foraminiferal isotope ($\delta^{18}O$ and $\delta^{13}C$) records in most circumstances [*Edgar et al.*, 2013; *Voigt et al.*].

Carbonate dissolution can lead to condensation or truncation of stable isotope records and at Site U1333 the distinct negative $\delta^{13}C$ excursion (~0.5 ‰) that characterizes the peak of the event in the Southern Ocean records [*Bohaty et al.*, 2009] and other sites is not evident (**Figure 2-8**). However, this is not uncommon; this short-lived (>50 kyr) feature is absent from many MECO records [see map in *Boscolo Galazzo et al.*, 2014]. It is plausible that a thin (<50 kyr) condensed interval in sediments at the peak of the MECO at Site U1333 is responsible for the absence of the CIE, however there are no missing orbital cycles across this interval [*Westerhold et al.*, 2014] and the longer-term trends exhibited are consistent with published $\delta^{18}O$ and $\delta^{13}C$ records.

Elevated bioturbation is another potential mechanism to consider but the plateaued MECO $\delta^{18}O$ signal at Site U1333 spans a ~5 m thick interval and there is no sedimentological evidence for large-scale mixing [*Pälike et al.*,

2010]. Furthermore, Ce records from fish teeth indicate reduced oxygen concentrations associated with warmer bottom waters in the Southern Ocean within the MECO and likely reduced bioturbation [*Moebius et al.*, 2014; *Moebius et al.*, 2015]. We therefore conclude that diagenesis and bioturbation are unlikely to have significantly modified the MECO signal at Site U1333.

2.4.4.3 A low-latitude signal?

In the absence of convincing evidence for post depositional processes or sampling artefacts, the muted $\delta^{18}O$ signal across the MECO event is likely to be a real feature reflecting modest changes in bottom water conditions at low latitudes. The $\delta^{18}O$ record from Site U1333 bears a strong resemblance to the published record from ODP Site 1260 in the equatorial Atlantic [*Edgar et al.*, 2007; *Edgar et al.*, 2010; *Sexton et al.*, 2006a]. Records from ODP Site 1260 have undergone several age model iterations due to ambiguity regarding the location of the magnetochron C18r/C18n boundary, lack of biostratigraphic constraints at the top of the section, and what was initially assumed to be an unusual benthic $\delta^{18}O$ signal which led to interpretation that the peak and recovery of the event were missing [*Edgar et al.*, 2007; *Edgar et al.*, 2010; *Sexton et al.*, 2006a; *Westerhold and Röhl*, 2013]. A recent cyclostratigraphy developed at ODP Site 1260 suggests, however, that the peak of the MECO is present, though some ambiguity remains in the shallowest portion of the record (where the recovery might be expected), which was not orbitally tuned [*Westerhold and Röhl*, 2013]. The critical C18r/C18n magnetochron boundary is suggested to have occurred just above the shallowest paleomagnetic measurements at ODP Site 1260 [44 m rmcd; *Edgar et al.*, 2010; *Suganuma and Ogg*, 2006; *Westerhold and Röhl*, 2013], which also coincides with the largest XRF Fe peak and clay layer (**Supplemental Figure 2-6**). If the C18r/C18n magnetochron boundary occurs just above 44 m rmcd, the benthic $\delta^{18}O$ signal across the MECO from Site 1260 (~0.7 ‰) shows noteworthy overall coherence with the magnitude and shape of changes recorded in the benthic $\delta^{18}O$ signal from Site U1333 (~0.7 ‰) albeit with an offset where Site 1260 is consistently ~0.5 ‰ lower than Site U1333. In fact, the two records show strong overall congruence from ~42.5 to 40 Ma (**Figure 2-5**, **Figure 2-8**), providing further evidence that the latest cyclostratigraphy age model for Site 1260 is sound and that the peak of the MECO is present at Site 1260

[*Westerhold and Röhl*, 2013]. This finding implies that the MECO benthic $\delta^{18}O$ signal is globally variable, with a negative benthic $\delta^{18}O$ excursion of ~1.0-1.5 ‰ observed in the Southern Ocean [*Bohaty et al.*, 2009] and a much smaller excursion (~0.5 to 0.7 ‰) in deep water at low latitudes.

This finding is perplexing; the Pacific is the largest ocean on Earth (even larger in the Eocene) and thus proxy records from this location should provide a global signal [*Lyle et al.*, 2008]. While an Eocene equator-to-pole surface temperature gradient is expected [*Huber and Sloan*, 2001], it is not expected in deep waters which are insulated from geographical differences in temperature and salinity and formed at high latitudes [e.g. *Zachos et al.*, 2001b]. However, differences in bottom water $\delta^{18}O$ signals can form due to differences in the location of deep-water formation and circulation patterns, and transient changes in deep water circulation have been proposed across abrupt environmental perturbations such as the Paleocene Eocene Thermal Maximum [e.g. *Nunes and Norris*, 2006; *Tripati and Elderfield*, 2005]. During the early Cenozoic the Southern Ocean was the dominant deep water source [*D Thomas et al.*, 2003], while evidence of smaller water mass ageing gradients during periods of warmth in the early to middle Eocene (54-38 Ma) suggest intervals of deep water formation at multiple locations [*Sexton et al.*, 2006a], and *Borrelli and Katz* [2015] suggest a more complicated circulation pattern in the North Pacific between 42 and 37 Ma that involves warm saline deep waters forming at low-latitudes in the Tethys. Evidence from Nd isotopes from the Southern Ocean suggest a circulation switch occurred during the MECO event, where deep water formation temporary occurred in the North Pacific [*Scher and Delaney*, 2010]. Comparison of benthic foraminifera records in this study supports a temporary change in circulation away from a single source of deep-water formation in the Southern Ocean, however, the circulation switch occurs after the MECO. Temperatures warmed dramatically in the Southern Ocean (~4 to 6 ˚C inferred warming during the MECO; **Figure 2-5**) and background $\delta^{13}C$ values increased to ~1.5 ‰ post-MECO at ~39.5 Ma while the Atlantic and Pacific Oceans remain closer to ~ 1.0 ‰. Taking into account the longer-term homogeneity in benthic $\delta^{13}C$ both pre- and post-event, the Southern Ocean $\delta^{13}C$ values could indicate a temporary change in circulation only if it occurs after the peak MECO. Further understanding of global circulation during the MECO requires empirical records from the North Pacific, and currently there are no

high-resolution benthic $\delta^{18}O$ records with robust age control with which to compare. Additionally, continental configuration during the Eocene could affect Atlantic and Pacific equatorial $\delta^{18}O$ records because the Panama Gateway formed a deep-water passage between the two basins [*Lyle et al.*, 2008 and references therein]. A coupled ocean-atmosphere climate modelling study by *Huber* [2002] simulating the eastern equatorial Pacific during the Paleogene shows water mass flow through the Panama Gateway from surface to deep as well as regions of vigorous upwelling in both the equatorial Pacific and Atlantic. Equatorial sites in both ocean basins may have been bathed by deep waters with similar properties that could result in a muted excursion in bottom water temperatures and similar water mass ages (via benthic $\delta^{13}C$), however a temperature offset between the Atlantic and Pacific would not be expected. Sedimentological records and modelling experiments are need to test whether increased zonal flow existed between the equatorial Atlantic and Pacific. Circulation patterns are not well understood in the Eocene, and existing records are of lower temporal resolution than those presented in this study and focus on longer time intervals.

Intriguingly, the interval of low $\delta^{18}O$ values (**Figure 2-8**) and dissolution observed (see **Chapter 3**) during the MECO at both equatorial Sites U1333 and 1260 is prolonged relative to other sites by >150 kyr. At Site U1333, carbonate decreases ~300 kyr before the onset of the MECO and the low carbonate interval begins extends into C18n.1n (low CAR, decreased foraminiferal accumulation **Figure 2-8**; [*Takata et al.*, 2013]; ~39.6 - 40.5 Ma). Sediments at Site 1260 exhibit a series of discrete clay layers throughout and after the peak of the event [This thesis, Chapter 3]. These differences could result from paleowater depth differences (Site U1333 ~3700 m paleodepth; Site 1260 ~2500 m paleodepth) or regional/interbasinal differences in CCD behaviour. However, a splice gap at Site U1333 and hiatus after the peak of the MECO at Site 1260 (**Supplemental Figure 2-8**) prevent a complete picture of the recovery at both sites and there is no deep end-member site in the Atlantic with a well-resolved age model to test this idea (but, see this thesis, Chapter 3). Furthermore, changes in CAR are a function of both productivity and preservation, and there is no accompanying evidence for prolonged heightened pCO_2 [*Bijl et al.*, 2010], and it is unclear how/if the MECO event interacts with CAE-3 and -4.

2.5 Summary and Conclusion

In this study, new benthic foraminiferal stable isotope records are presented from the late middle Eocene from ~38 to 46 Ma, which provide new insights into the long-term temperature history of the Pacific Ocean in the middle-late Eocene and allows us to test for environmental signals associated with the equatorial Pacific CAE events. These records demonstrate for the first time that there is no consistent relationship between CAEs and $\delta^{18}O$ as previously hypothesized and suggests the events are unlikely to be tied to repeated cooling and/or glaciation events. The equatorial Pacific records are most closely aligned with a mechanism that involves continental weathering-related changes in solute supply to the oceans, though we note the global nature of the CAEs has yet to be assessed in detail.

The available data across the MECO shows that the event is more complex than previously documented, including dampened warming in deep waters at equatorial latitudes in the Pacific and Atlantic, as well as a ~300 kyr global negative $\delta^{13}C$ excursion preceding warming. The MECO event has been difficult to reconstruct in carbon cycle modelling perhaps because critical features of the event have yet to be thoroughly identified in both sequence and geographic extent.

These findings also illustrate the instability of Eocene climate and the complex nature of the transition from the greenhouse to icehouse climate state, with the possible identification of a new cooling feature. If the isotopic shifts we observe are substantiated elsewhere, our results suggest cooling occurred much earlier than previously identified and that both short term warming and cooling events alternated throughout the middle Eocene.

2.6 Supplemental Figures

Supplemental Figure 2-1 Inter-laboratory offsets and correction in benthic foraminiferal stable isotopes.
Inter-laboratory offsets and correction in benthic foraminiferal stable isotopes. Cross-plots of the Gaussian interpolation of the means of (a1) $\delta^{18}O$ and (a2) $\delta^{13}C$ datasets (0.5 m step, 3m-filter window) generated at the National Oceanography Centre (NOCS) and the University of Bremen. Dotted lines mark 1:1 line. (b) Raw data (solid lines) generated at NOCS (blue) versus Bremen (red) and Gaussian interpolation values (circles). (b) NOCS values corrected to Bremen values using regressions in (a1, a2) ([$\delta^{18}O$ Bremen = [0.7643 * $\delta^{18}O$ NOCS]-0.09187] and $\delta^{13}C$ Bremen =[0.828 * $\delta^{13}C$ NOCS]-0.1517]. (c) Recompilation of NOCS data plotted with Bremen data and (d) combined NOCS and Bremen data. (e) Recompilation of complete dataset with spurious data points removed representing final dataset used in this study.

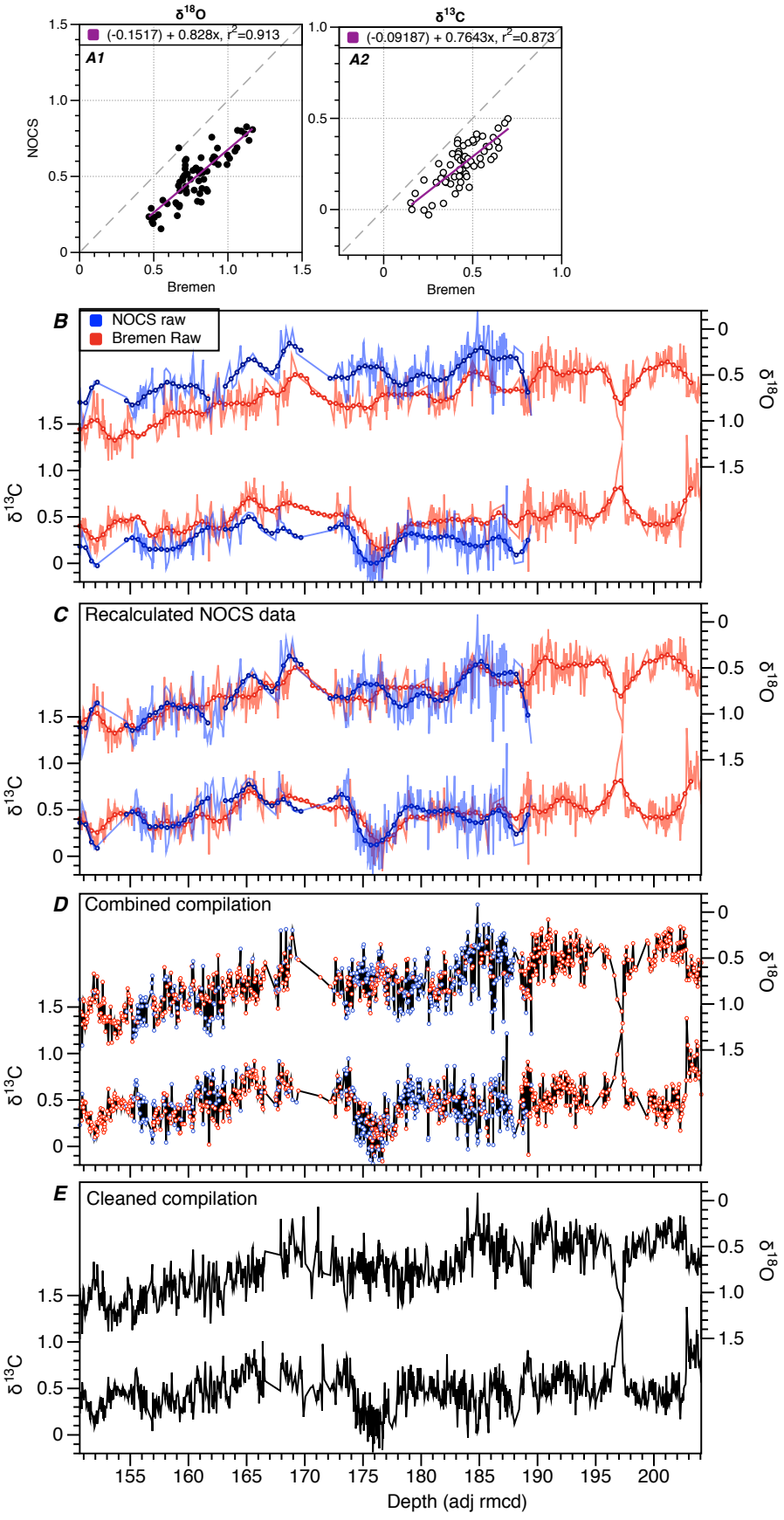
δ18O
(-0.1517) + 0.828x, r2=0.913
A1
NOCS
Bremen
δ13C
(-0.09187) + 0.7643x, r2=0.873
A2
Bremen
B
NOCS raw
Bremen Raw
C
Recalculated NOCS data
D
Combined compilation
E
Cleaned compilation
δ13C
δ18O
Depth (adj rmcd)

Supplemental Figure 2-2 Calculations used in determining estimated carbonate mass accumulation rates at Site U1333.
Calculations used in determining estimated carbonate mass accumulation rates at Site U1333. (a) Dry bulk density (DBD) (g/cm^3) calibrated from gamma ray attenuation and shipboard bulk density measurements [*Pälike et al.*, 2010] (b) linear sedimentation rates (LSR) from ages used in this study [*Pälike et al.*, 2010; *Westerhold et al.*, 2014], and (c) MAR ($g/cm^3/kyr$) calculated from DBD and LSR. (d) NMS Si counts expressed as SiO_2 (wt %) [*Westerhold et al.*, 2014] (grey line) and shipboard measurements (wt %; open circles) [*Pälike et al.*, 2012], (e) SiO_2 MAR ($g/cm^3/kyr$) calculated from MAR and SiO_2 (wt %). (f) NMS Ca counts expressed as $CaCO_3$ (wt %) [*Westerhold et al.*, 2014] (grey line), shipboard $CaCO_3$ (wt %; open circles) [*Pälike et al.*, 2010], and $CaCO_3$ (wt %; blue triangles; this study), (g) $CaCO_3$ MAR ($g/cm^3/kyr$) calculated from MAR and $CaCO_3$ (wt %). (h) Carbonate calibration between the Gaussian interpolation of the means of the XRF-generated NMS Ca counts and shipboard $CaCO_3$ (wt %) [*Westerhold et al.*, 2014], and (i) density calibration between the Gaussian interpolation of the means of the scanned GRA and shipboard density measurements NMS Ca [*Pälike et al.*, 2012].

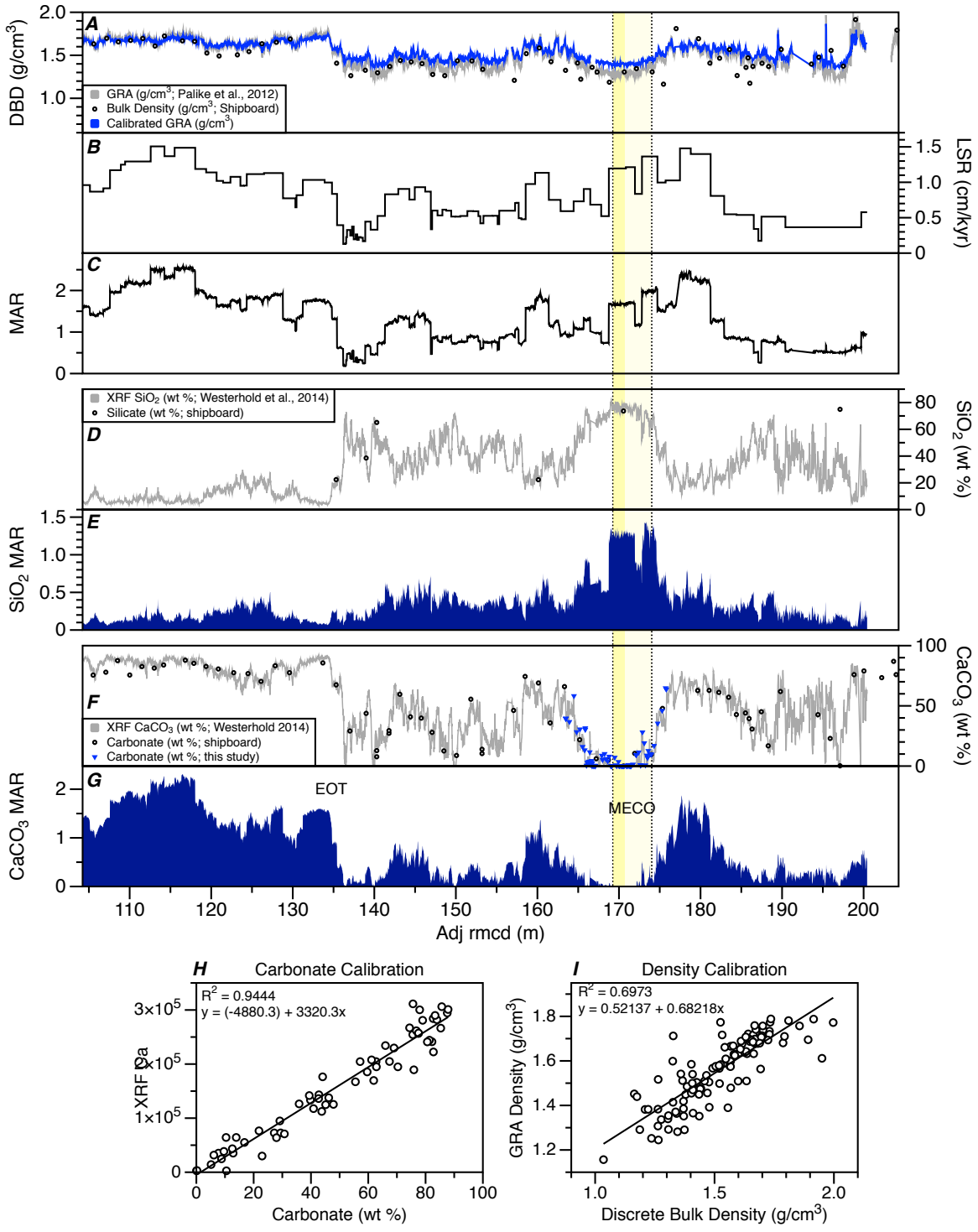
A
DBD (g/cm3)
GRA (g/cm3; Palike et al., 2012)
Bulk Density (g/cm3; Shipboard)
Calibrated GRA (g/cm3)
B
LSR (cm/kyr)
C
MAR
XRF SiO2 (wt %; Westerhold et al., 2014)
Silicate (wt %; shipboard)
D
SiO2 (wt %)
E
SiO2 MAR
F
XRF CaCO3 (wt %; Westerhold 2014)
Carbonate (wt %; shipboard)
Carbonate (wt %; this study)
CaCO3 (wt %)
G
CaCO3 MAR
EOT
MECO
Adj rmcd (m)
H
Carbonate Calibration
R2 = 0.9444
y = (-4880.3) + 3320.3x
XRF Ca
Carbonate (wt %)
I
Density Calibration
R2 = 0.6973
y = 0.52137 + 0.68218x
GRA Density (g/cm3)
Discrete Bulk Density (g/cm3)

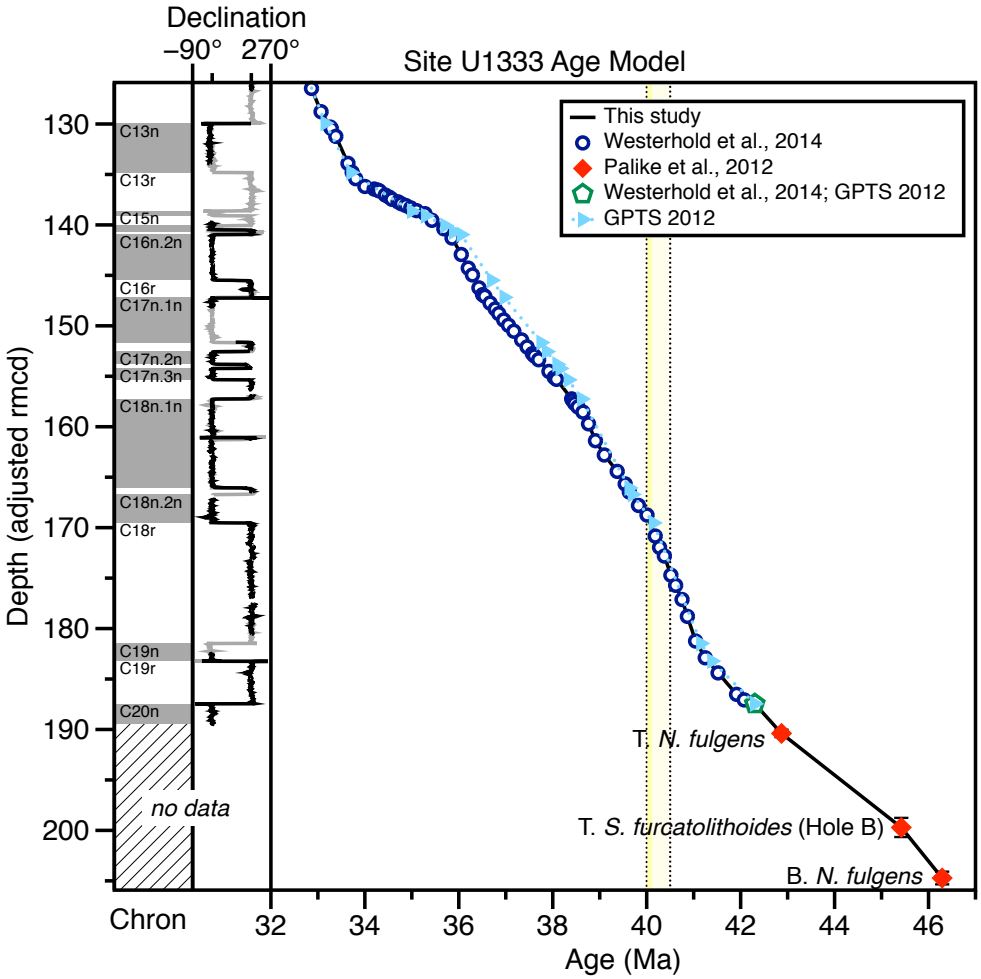

Supplemental Figure 2-3 Age versus depth plot for IODP Site U1333
Ages in this study are calculated from tuning tie-points in *Westerhold et al.* [2014] on the PEAT timescale with the exception of the oldest portion of the record (>187 adj rmcd; ~42 Ma) which utilizes linear interpolation between shipboard calcareous nannofossil datums [*Pälike et al.*, 2012]. For comparison ages are also reported on the Geomagnetic polarity time scale [*Gradstein et al.*, 2012]. Declination data and magnetochron boundaries from *Westerhold et al.* [2014]. Hexagonal green marker indicates magnetochron boundary from *Westerhold et al.* [2014] and assuming the age model of *Gradstein et al.* [2012].

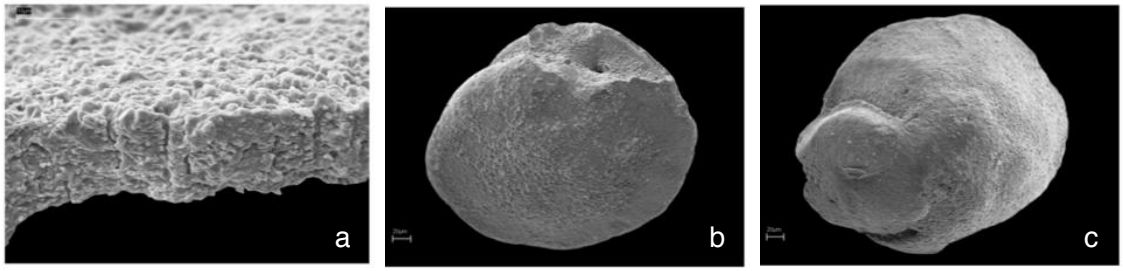

Supplemental Figure 2-4 Scanning electron microscope images from IODP Site U1333 that illustrate preservation state of N. truempyi.
(a) External and internal wall texture, (b) spiral, and (c) umbilical views. Scale bars are 100 μm.

Supplemental Figure 2-5 Stable isotope and corresponding paleomagnetic records across the middle Eocene with depth.
Bulk sediment (a) $\delta^{18}O$ and (b) $\delta^{13}C$ records from Site 702 [*Bohaty et al.*, 2009], bulk sediment and benthic foraminiferal records from Site 1051 [*Bohaty et al.*, 2009; *Edgar et al.*, 2010], benthic foraminiferal record from Site 1260 [*Edgar et al.*, 2007], benthic foraminiferal record from Site U1333 [this study], inclination data for Site 702 [*Clement and Hailwood*, 1991] and Site 1051 [*Edgar et al.*, 2010; *Ogg and Bardot*, 2001], declination data for Site 1260 [*Edgar et al.*, 2007; *Suganuma and Ogg*, 2006], and Site 1333 [*Westerhold et al.*, 2014].Vertical grey bar highlights magnetochron boundary of C18n.2n at Site U1333. Records are shown on a revised age scale calculated according to PEAT timescale magnetostratigraphy at Site U1333 [*Westerhold et al.*, 2014].

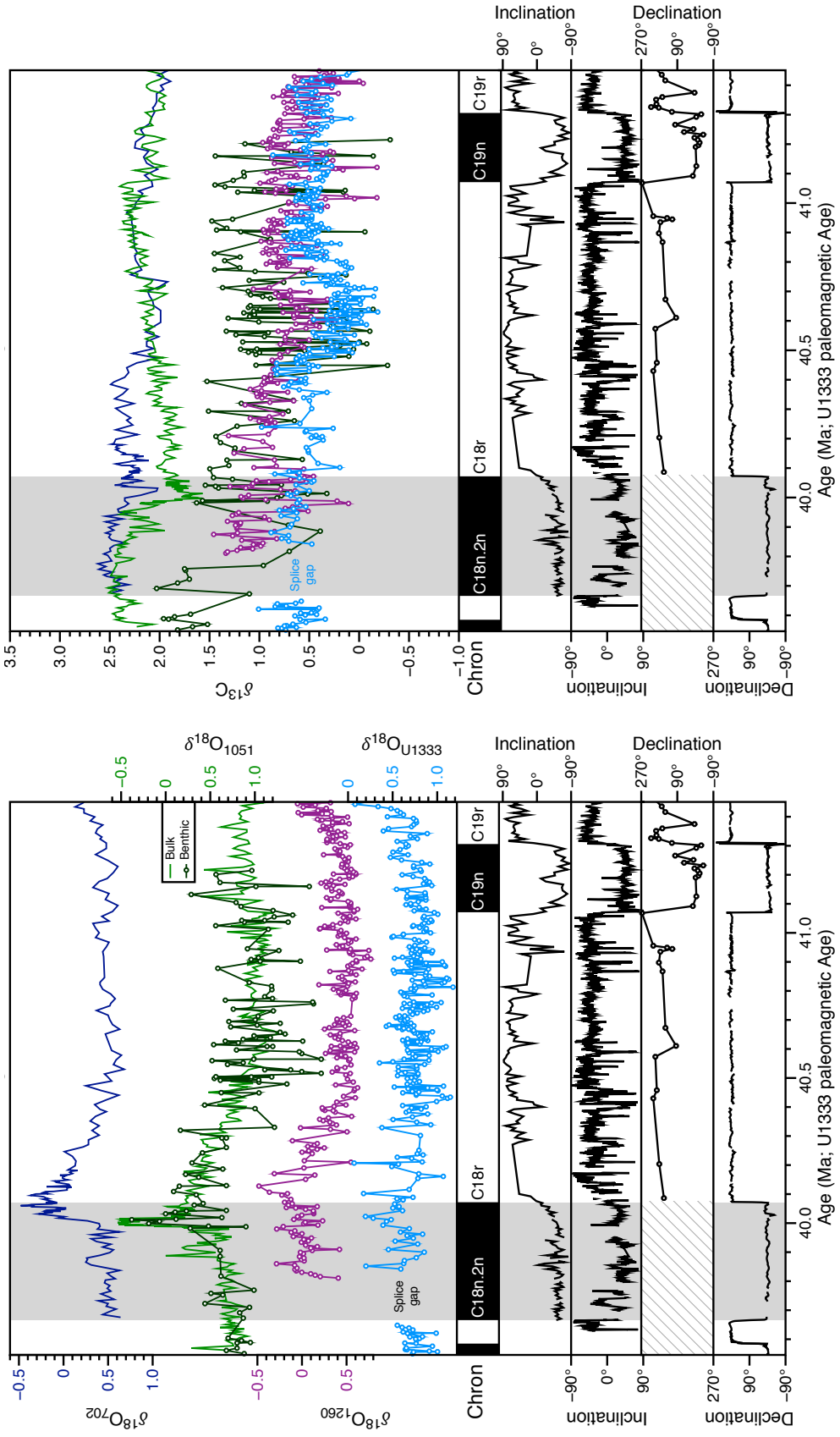
Inclination
Declination
δ13C
Chron
C19r
C19n
C18r
C18n.2n
Splice gap
Inclination
Declination
Age (Ma; U1333 paleomagnetic Age)
δ18O1051
δ18O1333
Bulk
Benthic
δ18O702
δ18O1260
Splice gap
Inclination
Declination
Age (Ma; U1333 paleomagnetic Age)

Supplemental Figure 2-6 Stable isotope and corresponding paleomagnetic records across the middle Eocene with depth.
(a) Site 702 bulk sediment $\delta^{18}O$ [*Bohaty et al.*, 2009] and inclination data [*Clement and Hailwood*, 1991], (b) Site 1051 bulk sediment and benthic foraminiferal $\delta^{18}O$ [*Bohaty et al.*, 2009; *Edgar et al.*, 2010] and inclination [*Edgar et al.*, 2010; *Ogg and Bardot*, 2001] (c) Site 1260 benthic foraminiferal $\delta^{18}O$ [*Edgar et al.*, 2007] and declination data [*Edgar et al.*, 2007; *Suganuma and Ogg*, 2006] (d) Site U1333 benthic foraminiferal $\delta^{18}O$ [this study] and declination data [*Westerhold et al.*, 2014]. Diagonal lines in (c) indicate interval without paleomagnetic data. Vertical grey bars highlight peak $\delta^{18}O$ low values during the MECO event at Sites 702 and 1051.

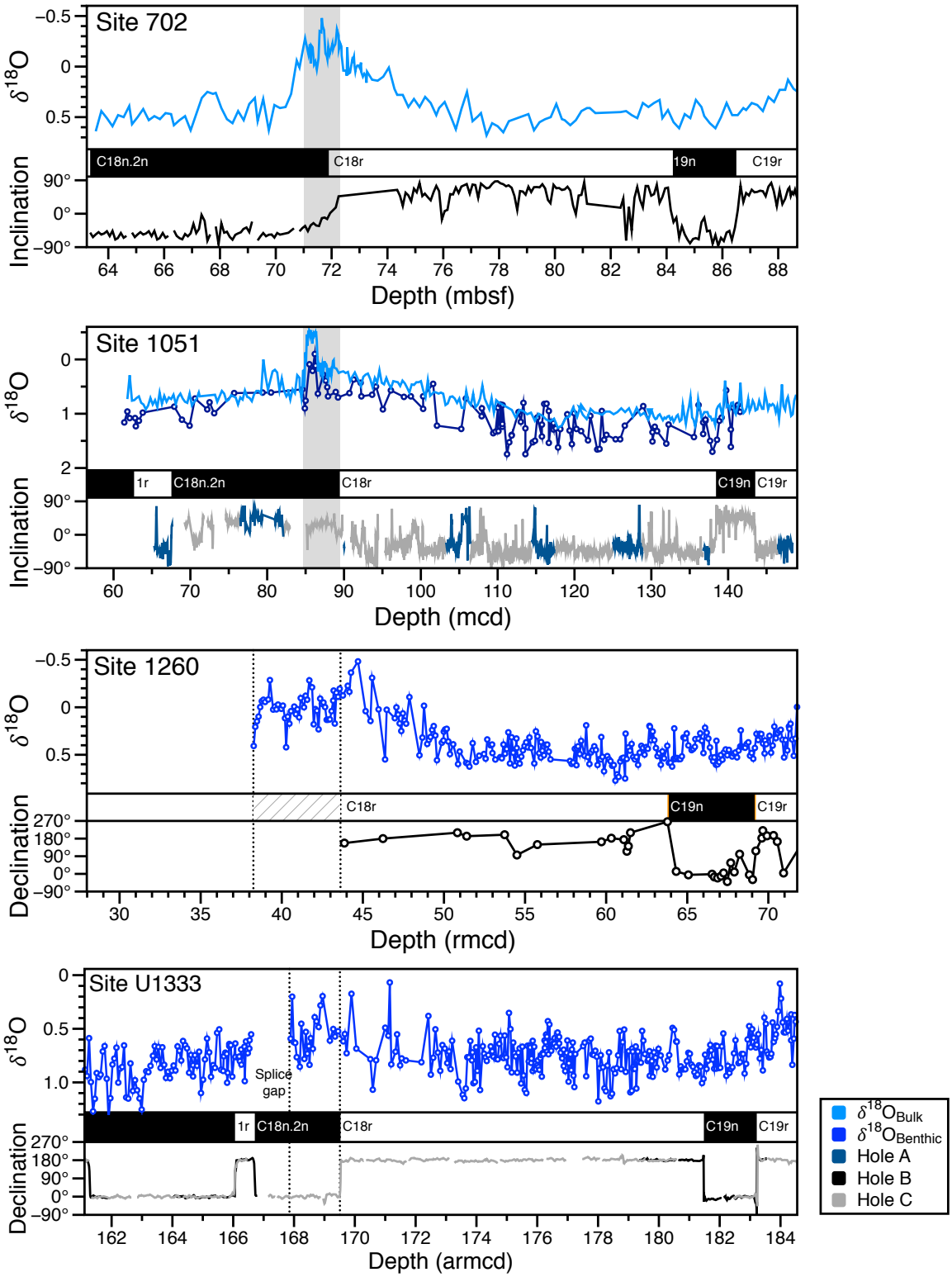
Site 702
δ18O
Inclination
C18n.2n
C18r
19n
C19r
Depth (mbsf)
Site 1051
1r
C18n.2n
C18r
C19n
C19r
Depth (mcd)
Site 1260
Declination
C18r
C19n
C19r
Depth (rmcd)
Site U1333
Splice gap
1r
C18n.2n
C18r
C19n
C19r
Depth (armcd)
δ18OBulk
δ18OBenthic
Hole A
Hole B
Hole C

Supplemental Figure 2-7 IODP Site U1333 benthic foraminiferal stable isotope and detailed sedimentological data versus depth.
Benthic foraminiferal (a) $\delta^{18}O$ and (b) $\delta^{13}C$ from *N. truempyi [this study]*, magnetic susceptibility records from (c) the combined spliced record (thick blue line) and (d) individual Hole U1333A (grey), Hole U1333B (blue), and Hole U1333C (red), with the same colour scheme continuing throughout the figure. (e) NMS Si counts expressed as SiO_2 (wt %). (f) NMS Ca counts expressed as $CaCO_3$ (wt %; circles) and discrete $CaCO_3$ (wt %) measurements (stars, [*Pälike et al.*, 2010]; diamonds, [this study]). (g) Individual samples used in this study used for isotopic analyses compared to (h) splice generated from Westerhold et al. [2014]. Markers in (a) indicate samples barren of benthic foraminifera (orange) and failed isotopic analyses (black). Dark blue circles in (a, b) indicate data removed from record due to down-hole contamination (U1333B 16H-1) and core overlapping (U1333B 18H-1). XRF $CaCO_3$ and SiO_2 records, splice, and magnetochron boundaries from Westerhold et al. [2014]. Core recovery, shipboard $CaCO_3$, and magnetic susceptibility from Pälike et al. [2012]. Nannofossil datums in from [Pälike et al., 2010; Toffanin et al., 2013].

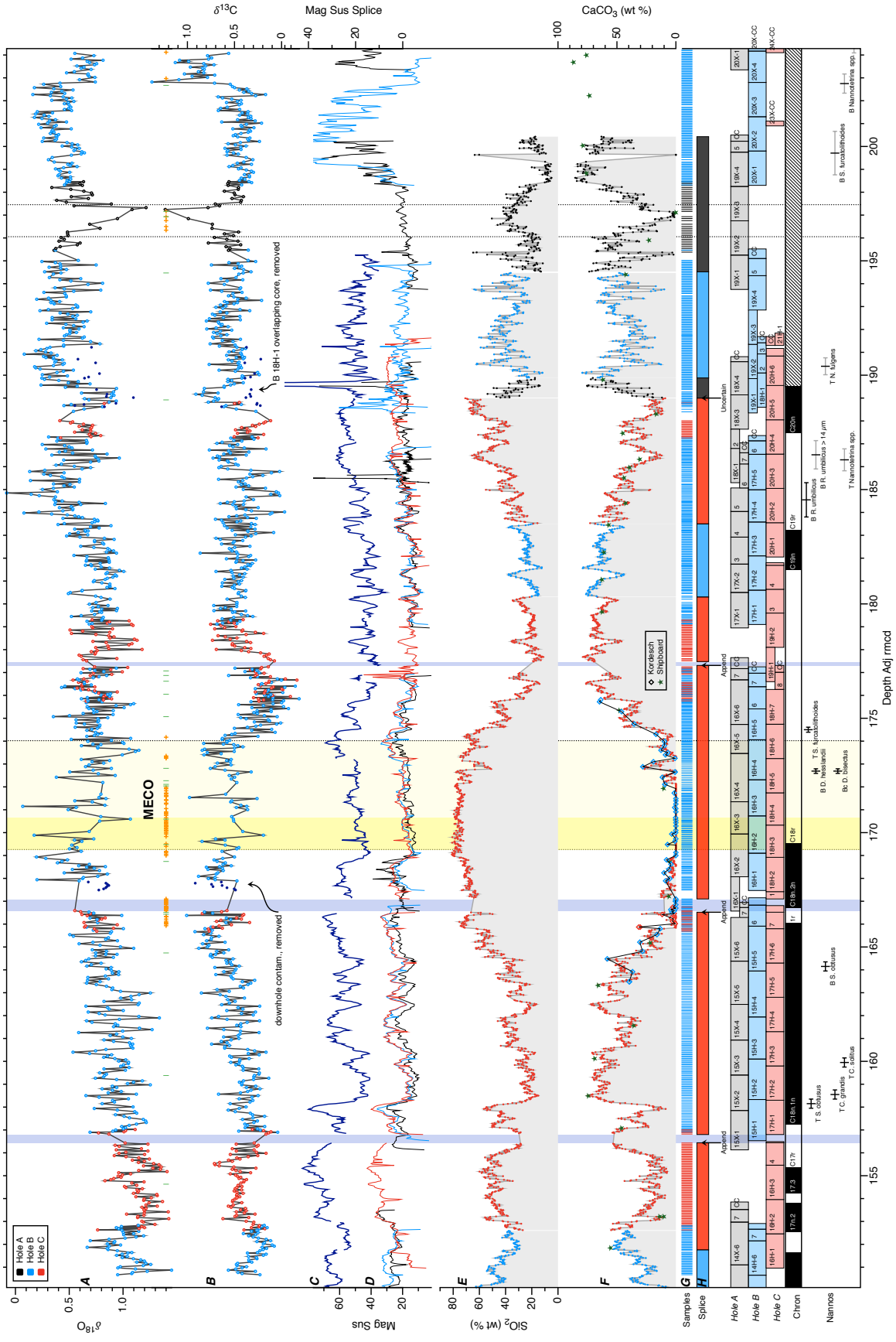
δ13C
Mag Sus Splice
CaCO3 (wt %)
MECO
B 18H-1 overlapping core, removed
downhole contam., removed
Hole A
Hole B
Hole C
δ18O
Mag Sus
SiO2 (wt %)
Kordesch
Shipboard
Samples
Splice
Chron
Nannos
Depth Adj rmcd

Supplemental Figure 2-8 Comparison of carbonate and silicate sediment components at equatorial Pacific Sites U1333, U1334, and 1218
Equatorial Pacific carbonate accumulation rate history versus paleowater depth [*Pälike et al., 2012*; *Westerhold et al.*, *unpublished*], and revised CCD [Chapter 3, this thesis]. Benthic foraminiferal $\delta^{18}O$ and $\delta^{13}C$ (‰) from Site U1333 (grey) [*this study*] and Site 1218 (blue) [*Lear et al., 2004*], $CaCO_3$ MAR ($g/cm^3/kyr$) calculated in this study (from MAR and $CaCO_3$), $CaCO_3$ (wt %) [*Westerhold et al.*, *unpublished*], SiO_2 MAR ($g/cm^3/kyr$) calculated in this study from MAR and SiO_2 (wt %), SiO_2 (wt %) [*Westerhold et al.*, *unpublished*], and Site 1218 C_{org} MAR (green circles) [*Lyle et al., 2004*].

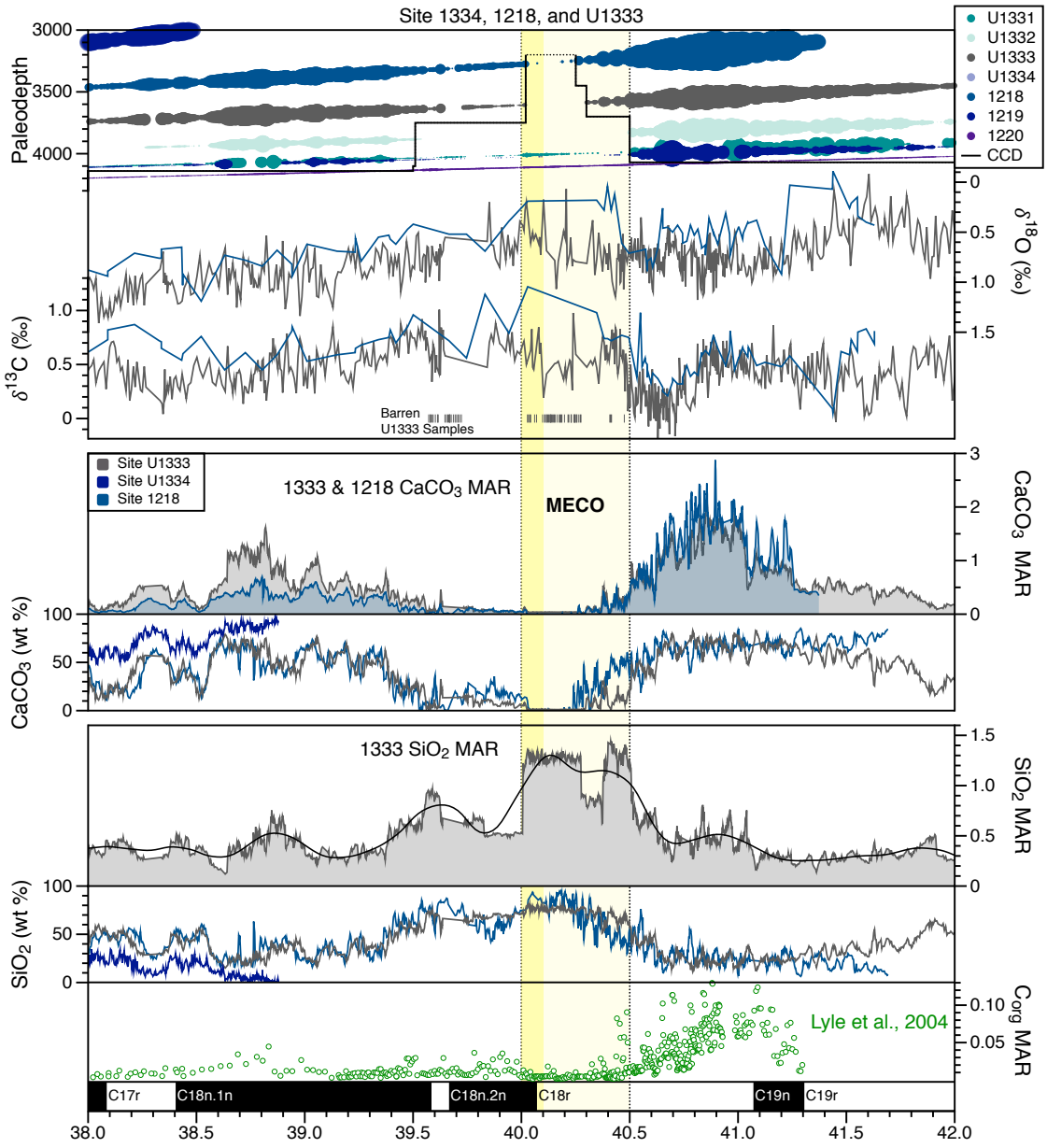
Site 1334, 1218, and U1333
Paleodepth
3000
3500
4000
U1331
U1332
U1333
U1334
1218
1219
1220
CCD
δ13C (‰)
1.0
0.5
0
δ18O (‰)
0
0.5
1.0
1.5
Barren
U1333 Samples
Site U1333
Site U1334
Site 1218
1333 & 1218 CaCO3 MAR
MECO
CaCO3 MAR
3
2
1
0
CaCO3 (wt %)
100
50
0
1333 SiO2 MAR
SiO2 MAR
1.5
1.0
0.5
0
SiO2 (wt %)
100
50
0
Lyle et al., 2004
Corg MAR
0.10
0.05
C17r
C18n.1n
C18n.2n
C18r
C19n
C19r
38.0
38.5
39.0
39.5
40.0
40.5
41.0
41.5
42.0

Chapter 3: Dynamic, large-magnitude Carbonate Compensation Depth changes during the Middle Eocene Climatic Optimum

Contents

**Chapter 3 is being prepared for submission for publication and will include the co-authors Steve Bohaty, Heiko Pälike, Paul Wilson, Kirsty Edgar, Claudia Agnini, Thomas Westerhold, and Ursula Röhl.*

3.1 Introduction

The Eocene (~56–34 Millions of years ago, Ma) is a critical period in the long-term global climate evolution of the Cenozoic, encompassing the transition from widespread greenhouse warmth pervasive during the early Eocene to an icehouse world with major Antarctic ice sheets and cooler temperatures [*Zachos et al.*, 2001a]. Superimposed on this long-term climate trend are several shorter-term events characterized by climatic instability, including numerous transient carbon cycle events during the early Eocene (~56 to 47.8 Ma) [*Kennett and Stott*, 1991; *Lourens et al.*, 2005; *Sexton et al.*, 2011; *E Thomas and Shackleton*, 1996; *Zachos et al.*, 2003] and middle Eocene (38 – 47.8 Ma) [*Bohaty and Zachos*, 2003; *Bohaty et al.*, 2009; *Edgar et al.*, 2007].

One particularly strong transient event is the Middle Eocene Climatic Optimum (MECO; ~ 40.1 Ma), which abruptly reversed long-term cooling during the middle Eocene for ~500 thousand years (kyr) [*Bohaty and Zachos*, 2003; *Bohaty et al.*, 2009]. The MECO event is recognized globally and is characterized by an increase in both surface and deep water temperatures (~3-5 °C), plankton and benthic assemblage shifts, and increased atmospheric carbon dioxide concentrations (pCO_2), [*Bijl et al.*, 2010; *Bohaty and Zachos*, 2003; *Bohaty et al.*, 2009; *Boscolo Galazzo et al.*, 2013; *Edgar et al.*, 2007; Edgar et al., 2010; *Jovane et al.*, 2007; *Moebius et al.*, 2014; *Moebius et al.*, 2015; *Pälike et al.*, 2012; *Savian et al.*, 2014; *Witkowski et al.*, 2014]. The MECO was also accompanied by a decrease in deep ocean carbonate accumulation in all major ocean basins, interpreted to indicate widespread deep-sea carbonate dissolution and global shoaling of the calcite compensation depth (CCD; a sediment property that occurs at the oceanic depth where the downward flux of carbonate rain delivered from calcifying organisms is balanced by dissolution) [*Bohaty et al.*, 2009; *Pälike et al.*, 2012].

The primary driving mechanism for the MECO is likely linked to an atmospheric CO_2 increase, the source of which has not yet been identified because prevailing hypotheses are incompatible with existing paleoclimate data. Given the long-to-intermediate timescale of the event (>500 kyr), CO_2 must have originated from a long-term flux imbalance where carbon input surpassed carbon output via burial [*Bijl et al.*, 2010; *Bohaty and Zachos*, 2003; *Bohaty et al.*, 2009]. However, on these timescales carbon input and warming should lead to increased silicate-weathering rates [*Berner et al.*, 1983; *Walker et al.*, 1981], in turn buffering the ocean and leading to increased carbonate accumulation and CCD deepening rather than the observed shoaling [*Sluijs et al.*, 2013].

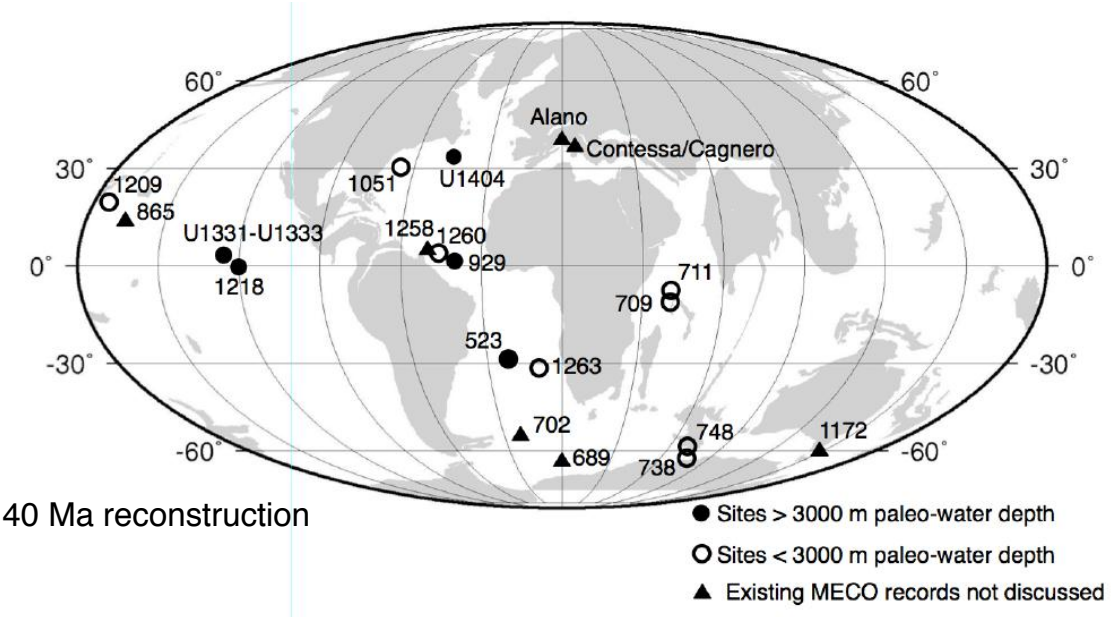

Figure 3-1 DSDP, ODP and IODP site location map of middle Eocene sections included in this study.
Approximate positions on ~40 Ma paleogeography from [*Hay et al.*, 1999; *ODSN*, 2011]. Solid circles are deep water sites (paleodepth >3000 m) and unfilled circles are shallow (paleodepth <3000 m).

This discrepancy between carbon cycle theory and observations in proxy records derived from sediment cores was deemed the MECO carbon cycle 'conundrum' and provided the impetus for a recent carbon cycle modelling study [*Sluijs et al.*, 2013]. The geochemical box model LOSCAR [*Zeebe*, 2012] was used to test the ability of a number of mechanisms involving increased pCO_2 and warming to simulate MECO signals of relatively stable carbonate $\delta^{13}C$

values and CCD shoaling. Of the seven scenarios tested, no single mechanism (temperature, inorganic versus organic carbon particulate rain ratios, the biological pump, volcanic degassing, and carbonate and silicate weathering) could reproduce both stable carbonate $\delta^{13}C$ values and critically, a long-term sustained CCD shoaling. The only plausible scenario that accurately approximated the MECO proxy records involved a combination of mechanisms: (i) carbon input from a flux imbalance (attributed to volcanic outgassing), (ii) small sea level-rise (from thermal expansion after 5 ˚C warming of the ocean and possible ice sheet melting) that ended shelf sediment weathering and or relocated carbonate burial from the deep sea to the shelf, and (iii) a short-lived pulse of $\delta^{13}C$-depleted carbon (to satisfy the $\delta^{18}O$ and $\delta^{13}C$ excursions at the peak of the event) [*Sluijs et al.*, 2013]. Though this result is compelling, the current lack of empirical measurements inhibits the ability of further test the scenario.

One means of understanding the global carbon system during the MECO is to better constrain changes in deep ocean chemistry, as recorded by the CCD. During Integrated Ocean Drilling Program (IODP) Exp. 320 and 321, eight new sites in the equatorial Pacific were drilled that targeted a flow line transect of sites to map high-resolution carbonate accumulation across an array of paleodepths (~ 3 to 5 km) through the Eocene [*Pälike et al.*, 2010] (**Figure 3-1**). These new carbonate data were combined with records from all available equatorial Pacific Deep-Sea Drilling Project (DSDP) and Ocean Drilling Program (ODP) sites to create the most highly constrained Cenozoic CCD curve to date [*Pälike et al.*, 2012] (**Supplemental Figure 3-1**). The Eocene portion of the CCD record suggests a generally shallow background depth (~4 km paleodepth) compared to today but with large fluctuations superimposed, including CCD shoaling related to 'hyperthermal' events [*Leon-Rodriguez and Dickens*, 2010; *Zachos et al.*, 2008] and CCD deepening related to Carbonate Accumulation Events (CAEs, numbered 1-7; between ~46–34 Ma) [*Lyle et al.*, 2005; *Olivarez Lyle and Lyle*, 2005; Olivarez Lyle and Lyle, 2006; *Pälike et al.*, 2012]. CAEs vary in magnitude (CCD shoaling from ~0.5 to 1.0 km) and duration (several hundred kyrs to ~1 Myr) and the largest (CAEs -3 and 4) bracket the MECO (**Supplemental Figure 3-1**). Evidence of global CCD shoaling during the MECO was first constrained by evidence of carbonate dissolution in the deep (~3500 m) Atlantic, Indian and Pacific Ocean basins and at shallower depths (~2000 m)

in the Pacific basin [*Bohaty et al.*, 2009]. Subsequent reconstructions from equatorial Pacific Exp. 320 and 321 showed evidence for at least ~900 m shoaling of the Pacific CCD [*Pälike et al.*, 2012]. However, a more detailed picture of the CCD across the MECO interval has been limited by the depth range of sites (restricted to ~ 3 to 4 km) and generally low sediment carbonate content [*Pälike et al.*, 2010]. As such, it is unclear how or if the CAEs interact with the MECO event, and the CAEs have yet to be observed outside the equatorial Pacific. Further, the only available Atlantic CCD record across this interval comes from two sites across the MECO event in the subtropical Atlantic with low-resolution carbonate records (ODP Site 523 and ODP Site 1263) [*Bohaty et al.*, 2009; *Sluijs et al.*, 2013].

Here, new reconstructions of changes in deep-sea carbonate burial at high resolution in Atlantic and Pacific drillcores across the MECO interval (~41.5 to 39.0 Ma) are presented (**Figure 3-1**). New benthic foraminiferal oxygen and bulk sediment carbon stable isotope records ($\delta^{18}O$ and $\delta^{13}C$), sediment carbonate content, and age constraints for two new sites (Equatorial Atlantic ODP Site 929, ~3935 m paleodepth; Pacific ODP Site 1209, ~1950 m paleodepth) are combined with new and published carbonate data sets from a depth transect of sites spanning a wide range of Eocene paleodepths (~2 to 4 km) in the Atlantic (DSDP Site 523, ODP Sites 1260 and 1263, and IODP Site U1404) and Pacific (IODP Sites U1331–U1333 and ODP Sites 1218–1220). Together, these records provide the first detailed record of global carbonate sedimentation spanning the MECO in order to investigate the current data-model inconsistencies.

Table 3-1 Summary of sites and data sets used in CCD and lysocline reconstruction across the MECO interval

Site	Paleo depth at 40 Ma	Modern water depth	Location Latitude, Longitude	Datasets used in this study; *(citation)*		Data generated for this study
Atlantic						
ODP 1263	2000	2717	subtropical mid Atlantic 28°31.98´S, 02°46.77´E	Magnetic susceptibility	*(Zachos et al., 2004)*	Magnetic susceptibility
				Age model	*(Westerhold and Röhl, 2013)*	$CaCO_3$, CAR
				$CaCO_3$, CAR, $\delta^{18}O$, $\delta^{13}C$	*(Bohaty et al., 2009)*	Benthic $\delta^{18}O$, $\delta^{13}C$
				$\delta^{18}O$, $\delta^{13}C$	*(Boscolo et al., 2014)*	Fragmentation (%)
ODP 1260	2550	2549	tropical western Atlantic 9°15.948´N, 54°32.633´W	$CaCO_3$, DBD, mag sus	*(Erbacher et al., 2004b)*	$CaCO_3$, CAR
				Age model	*(Westerhold and Röhl, 2013)*	
				Benthic $\delta^{18}O$, $\delta^{13}C$	*(Edgar et al. 2007; Edgar et al. 2010; Sexton et al., 2011)*	
DSDP 523	3350	4562	subtropical mid Atlantic 28°33.131'S, 2°15.078'W	Shipboard $CaCO_3$	*(Hsü and LaBrecque, 1986)*	
				Age model	*(Westerhold and Röhl 2013)*	
				$CaCO_3$, CAR, bulk sediment $\delta^{18}O$, $\delta^{13}C$	*(Bohaty et al., 2009)*	
IODP 1404	4000	4710	northwestern Atlantic 40°00.80'N, 51°48.60'W	Age model, $CaCO_3$, DBD	*(Norris et al., 2014)*	
ODP 929	3935	4356	equatorial Atlantic 5°58.568'N, 43°44.402'W	Shipboard $CaCO_3$	*(Shackleton et al., 1997)*	Age model, Biostratigraphy XRF, $CaCO_3$, CAR Bulk, benthic $\delta^{18}O$, $\delta^{13}C$
Pacific						
IODP 1209	1950	2387	tropical western Pacific 32°39.102'N, 158°30.359'E	Age model	*(Westerhold and Röhl, 2013)*	Biostratigraphy
				$\delta^{18}O$, $\delta^{13}C$	*(Dawber and Tripati, 2011a;b)*	$CaCO_3$, CAR
				Magnetic susceptibility	*(Bralower et al., 2002)*	
				$CaCO_3$, CAR	*(Bohaty et al., 2009)*	
IODP Exp. 320, Leg 199	~3400 to 4100	~4300 to 5130	equatorial Pacific 0 to 12°N, 120 to 140°W	$CaCO_3$	*(Lyle et al., 2005)*	Benthic $\delta^{18}O$, $\delta^{13}C$
				$CaCO_3$, CAR	*(Pälike et al., 2012)*	$CaCO_3$
				XRF based $CaCO_3$, CAR	*(Westerhold, pers comm)*	

DBD, dry bulk density (g cm^{-1})
CAR,carbonate accumulation rate (g cm^{-1} kyr^{-1})
LSR, linear sedimentation rate (cm kyr^{-1})
Mag sus, magnetic susceptibility

3.2 Materials and Methods

3.2.1 Geological setting and site selection

The five Atlantic and seven Pacific drill sites included in this study were chosen with the purpose of reconstructing basin-wide changes in carbonate accumulation across a range (~2–4 km) of paleo-water depths (**Figure 3-1**; **Table 3-1**). The middle Eocene sections recovered at ODP Sites 929 and 1209 were subject to the most intense sampling because they fill critical paleodepth gaps in published records and have multiple dissolution horizons evident within the upper middle Eocene sections in core photos indicating that they are situated close to the local CCD or lysocline.

ODP Site 929 (5˚58.568'N, 43˚44.402'W, 4356 m modern water depth (**Table 3-1**) is the deepest site drilled on Ceara Rise in the equatorial Atlantic on ODP Leg 154 and contains a sediment sequence spanning the lower Eocene through Oligocene [*Curry et al.*, 1995]. Ceara Rise sediments have been used extensively in Neogene and Paleogene research [e.g. *Pälike et al.*, 2006], but no studies have focused on the middle Eocene. Thus, the MECO has not yet been identified at this site. This study targets the upper middle Eocene interval of Hole 929E between Cores 929E-11R through -14R (568 to 606 mbsf; meters below sea floor), which contains a section composed predominantly of nannofossil chalk with moderately preserved benthic foraminifers [*Pearson and Chaisson*, 1997]. Sediment colour and composition exhibit decimetre to meter-scale cyclic variability, with alternations of darker and paler greenish grey chalks and clays grading into limestone [*Shackleton et al.*, 1997]. Only one hole was drilled at Site 929 through the upper middle Eocene study interval resulting in recovery gaps at each core break. Some intervals in Cores 929E-11R and 13R are also affected by sediment slumping and turbidity current deposition (**Appendix Table 5-4**) [*Curry et al.*, 1995].

The shallowest end member of the Atlantic compilation is Site 1263 (paleodepth ~2000 m; **Table 3-1**) comprised of calcareous nannofossil ooze

and chalk with calcium carbonate contents typically ~90–95 wt% [*Zachos et al.*, 2004] and an array of paleoclimate data are available for the MECO interval at this site [*Bohaty et al.*, 2009; *Boscolo Galazzo et al.*, 2015; *Boscolo Galazzo et al.*, 2014]. The expanded Eocene section at tropical western Atlantic Site 1260 provides a proximal mid-water (paleodepth: 2550 m; [*Erbacher et al.*, 2004]) complement to Site 929 and high-resolution (~5 kyr) stable isotope records ($\delta^{18}O$ and $\delta^{13}C$) [*Edgar et al.*, 2007; Edgar et al., 2010] as well as an orbitally tuned age model are available [*Westerhold and Röhl*, 2013]. Site 523 is a key Atlantic site because of its deeper mid-depth (paleodepth ~3350 m), and because carbonate content exhibit multiple minima during the MECO [*Bohaty et al.*, 2009; *Hsü and LaBrecque*, 1986]. Site 1404 is the deepest Atlantic site included in the compilation (paleodepth: 4000 m), and sediments predominantly comprised of claystone and radiolarian clay with very low carbonate content (0-30 wt %) and centimetre- to decimetre-scale greenish grey to dark greenish grey colour variations [*Norris et al.*, 2014b].

The Pacific CCD compilation of *Pälike et al.* [2012] across the MECO interval is primarily constrained by equatorial Pacific IODP Sites U1331-U1334 and ODP Sites 1218-1220 (**Table 3-1**). Newly available carbonate accumulation records for these sites [*Westerhold, pers comm 2015*] further increase data resolution to suborbital timescales. ODP Site 1209 in the northern subtropical Pacific (32˚39.108'N, 158˚30.356'E, 2387 m modern water depth; **Table 3-1**) is a key new addition to the Pacific compilation because the paleodepth is ~1950 m [*Bohaty et al.*, 2009], more than ~1000 m shallower than other equatorial sites. Although previous studies have targeted the middle Eocene interval of Site 1209 [*Bohaty et al.*, 2009; *Dawber and Tripati*, 2011b; 2012b; *Dutton et al.*, 2005; *Hancock and Dickens*, 2006] and benthic foraminiferal stable isotope ($\delta^{18}O$ and $\delta^{13}C$) records are available [*Dawber and Tripati*, 2011a; b], the position of the MECO has been debated and the event has not been documented in detail. Site 1209 contains an expanded Paleogene sediment sequence consisting largely of calcareous and nannofossil ooze and moderately preserved 'frosty' foraminifera [*Bralower et al.*, 2003]. Three holes were drilled (A, B, and C) and are spliced together to form a composite section [*Bralower et al.*, 2003; *Westerhold and Röhl*, 2006].

3.2.2 Samples and analytical procedures

3.2.2.1 Bulk carbonate and benthic foraminiferal stable isotopes: ODP Site 929 and 1263

In total 52 samples from ODP Site 929 and 40 samples from ODP Site 1263 were analysed for benthic foraminiferal $\delta^{18}O$ and $\delta^{13}C$. Samples from ODP Site 929 were also analysed for bulk sediment $\delta^{18}O$ and $\delta^{13}C$. Bulk sediment for all samples was dried in an oven at 50 ºC; subsequently disaggregated in a solution of deionized water and sodium hexametaphosphate overnight, washed over a 63-μm size mesh sieve, and then oven dried. All sample preparation was carried out at the University of Southampton National Oceanography Centre (NOCS), UK.

Between eight and twelve individuals of the epifaunal benthic foraminifer *Nuttallides truempyi* was picked from the 180-250 μm size fractions in each sample for isotopic ($\delta^{18}O$ and $\delta^{13}C$) analysis. Bulk sediment samples were homogenized by grinding using mortar and pestle prior to analysis. All stable isotope ratio measurements were measured on a Finnigan MAT 253 gas isotope ratio mass spectrometer connected to a Kiel IV automated carbonate preparation device at the Zentrum für Marine Tropenökologie ZMT at the University of Bremen and are calibrated against an in-house standard (Solnhofen limestone). Analytical precision based on replicates of Solnhofen limestone (1σ) was ±0.08 ‰ for $\delta^{18}O$ and ±0.02 ‰ for $\delta^{13}C$. All results are standardized relative to the Vienna Pee Dee Belemnite (VPDB) standard after calibration to the reference material NBS 19. Stable isotopes were corrected for isotopic disequilibrium with seawater as described in **Chapter 2**.

3.2.2.2 Calcium carbonate concentrations: ODP Sites 929, 1209, 1260 and 1263

Bulk sediment weight % $CaCO_3$ measurements for samples from Sites 929, 1209, 1260, and 1263 were generated by high-precision coulometry. Samples were oven dried and then homogenized by grinding using mortar and pestle prior to analysis and measured by high-precision coulometry on a UIC CM5015 CO_2 Coulometer at NOCS with an automated preparation device in which 1-8 mg; samples were reacted in acid using a carousel system. A calibration was generated from a powdered Carrera marble standard on samples between ~1 -

8 mg at the beginning and end of each sample run and a consistency standard of pure calcium carbonate was included between every 10 samples within a run. The limit of detection was 1.19 ± 0.21 wt % $CaCO_3$.

3.2.2.3 Magnetic susceptibility: ODP Sites 1263 and 1209

To ensure capture of the small-scale features in the clay component of sediments we augmented carbonate content records with discrete magnetic susceptibility measurements on 24 samples from ODP Site 1263 and 118 samples from ODP Site 1209 across the MECO interval. These measurements were made on a KLY-4S Kappabridge magnetic susceptibility meter (AGI CO, Inc.) at NOCS and corrected to the dry bulk weight of samples (defined as the >63 μm size fraction).

3.2.2.4 Fragmentation: ODP Site 1263

To assess carbonate dissolution of planktic foraminifera at Site 1263, fragmentation was quantified following the methods of *Leon-Rodriguez and Dickens* [2010] and *Colosimo et al.* [2006]. A microsplitter was used to separate at least ~300 foraminifers and fragments. The total number of whole planktic tests (Planktic) and foraminiferal test fragments (Frag; defined as roughly <75 % of a test) in the >125 μm size fraction were counted, and the degree of fragmentation (%) was calculated (**Equation 3-1**). The number eight is the average number of fragments a whole planktic test breaks into [*Le and Shackleton*, 1992].

Equation 3-1

$$\text{Fragmentation (\%)} = \left[\frac{\text{Frag}/8}{(\text{Frag}/8) + \text{Planktic}}\right] \times 100$$

3.2.2.5 Biostratigraphy: ODP Sites 929, 1209 and 1260

The occurrence of the planktic foraminifera *Orbulinoides beckmanni* within the MECO interval of sediments of ODP Sites 929 and 1209 was determined from the >300 μm washed fraction of the same samples used for calcium carbonate analyses following the methods of *Edgar et al.* [2010]. The ranges of calcareous nannofossil marker species *Sphenolithus furcatolithoides*, *Dictyococcites bisectus*, and *S. obtusus* were refined at ODP Sites 929, 1209, and 1260 from bulk sediment samples [*Agnini, pers comm 2015*].

3.2.2.6 X-ray fluorescence elemental intensities: ODP Site 929

XRF scanning produces a direct measure of elemental variations in sediments and can be used as an indicator of core lithology (Ca for carbonate content, Fe for terrigenous material [Lyle and Backman, 2013; *Röhl and Abrams*, 2000; *Sexton et al.*, 2011]). To ensure capture of the carbonate signal across the MECO in the condensed sediments of Site 929, bulk sediment weight % $CaCO_3$ measurements were augmented with high-resolution XRF-calibrated carbonate estimates. High-resolution $CaCO_3$ wt % data for Site 929 was then estimated from XRF Ca intensity (counts per second; cps) via linear regression with discrete $CaCO_3$ wt % measurements (**Supplemental Figure 3-2**) [e.g. *Jansen et al.*, 1998; *Tjallingii et al.*, 2007].

XRF core scanning data were acquired at the at the MARUM – Center for Marine and Environmental Sciences, University of Bremen, using the XRF Core Scanner 3, an Avaatech scanner (Serial No. 12) equipped with a Canberra X-PIPS SDD, Model SXD 15C-150-500 150eV resolution detector and an Oxford Instruments 100W Neptune Rh X-ray tube. XRF data were collected every 2 cm downcore over a 1 cm^2 area and with a slit size of 11 mm measured over three separate scans with voltage settings of 10 kV (0.12 mA; for elements Ca, Fe, Si, K, Ti, Al, and S), 30 kV (1.0 mA; for elements Sr, Rb, and Br), and 50 kV (1.0 mA; for the element Ba) with a 20 second sampling time. Raw data spectra were processed by the Analysis of X-ray spectra by Iterative Least square software (WIN AXIL) package from Canberra Eurisys. A 4-micron thin SPEXCerti Prep Ultralene foil was used to cover the split core surface and avoid contamination. Digital linescan and colorimetry data were made at intervals of 11 pixels/mm captured with the Section Half Imaging Logger (SHIL). Linescan images were compiled using IGOR-Pro software developed by R. Wilkens.

In preparation for the development of an astronomical age model for Site 929, multiple XRF-derived elemental records were initially analysed in the depth domain and barium (Ba) cycles were found to be the most pronounced. Spurious measurements from cracks or disturbed areas of the core were removed from data sets. The XRF elemental data were then resampled in the depth domain and linearly detrended using a Gaussian notch filter, and the dominant cyclicities in the depth domain were assessed using band pass

filtering in Analyseries 2.0 [*Paillard et al.*, 1996]. MTM power spectra was generated using the kSpectra Toolkit using three tapers and a resolution of 2, where confidence intervals of 90, 95, and 99% are based on a red noise estimation [*M E Mann and J M Lees*, 1996]. Prior to spectral analysis the MECO was removed to reduce the distorting effect from changes in sedimentation rate (**Supplemental Figure 3-3**).

Table 3-2 Biostratigraphic datum events identified in this study at ODP Sites 929 and 1209

Datum	Top depth	Top Sample	Bottom Depth	Base Sample	mid-point depth
ODP Site 929					
HO *O. beckmanni*	577.98	929E-12R-2, 10-12	579.36	929E-12R-2, 36-38	578.67
LO *O. beckmanni*	581.91	929E-12R-3, 139-141	582.00	929E-12R-4, 0-2	581.96
Base S. obtusus	578.65	929E 12R 1W 115,117	579.10	929E 12R 2W 10,12	578.88
Top S. spiniger	578.65	929E 12R 1W 115,117	579.10	929E 12R 2W 10,12	578.88
Base D. bisectus	579.36	929E 12R 2W 36,38	579.81	929E 12R 2W 81,83	579.59
Top S. furcatolithoides	582.72	929E 12R 4W 72,74	582.83	929E 12R 4W 83, 85	582.78
ODP Site 1209					
HO *O. beckmanni*	139.30	1209C-5H-3, 30-32	139.32	1209C-5H-3, 32-34	139.31
LO *O. beckmanni*	139.94	1209C-5H-3, 94-96	139.96	1209C-5H-3, 96-98	139.95
Base S. obtusus	152.30	1209C-5H-3,10	152.75	1209C-5H-3,55	152.53
Top S. furcatolithoides	153.25	1209C-5H-3,105	153.32	1209C-5H-3,112	153.29
Base D. bisectus	153.25	1209C-5H-3,105	153.32	1209C-5H-3,112	153.29

*Calcareous nannofossil datums from C. Agnini *[pers comm]*

3.2.2.7 Carbonate accumulation rate calculations

To account for dilution effects on $CaCO_3$ wt % records, linear sedimentation rates (LSR; cm kyr^{-1}) and dry bulk density (DBD; g cm^{-3}) estimates are used together with carbonate concentration data from XRF data (calibrated by coulometry on discrete samples) to calculate carbonate accumulation rates (CAR; g cm^{-2} kyr^{-1}) at all sites in this study where accumulation rates were not previously available (**Table 3-1**). Dry bulk density values (DBD; g cm^{-3}) were estimated using shipboard gamma ray attenuation (GRA) density (g cc^{-1}) measurements calibrated with discrete shipboard measurements of DBD. For Site 929, LSRs were calculated with varying rates (interpolated between the midpoints of each traditional LSR value) to smooth the dramatic changes in CAR that resulted from the LSR calculation method using only the tiepoints from the age model (**Supplemental Figure 3-4**). This method is used under the assumption that it is unlikely for accumulation to occur in a step-like manner. Formulas used in calculations are included in the **Supplemental Section 3.6.2**.

3.3 Results

3.3.1 Age model development

In order to compare carbonate accumulation records across the upper-middle Eocene interval between sites it was necessary to construct new and/or refine existing age models for the drill cores in this study from ODP Sites 929 and 1209. This necessitated compilation of available magnetostratigraphic, biostratigraphic, and isotopic records for all sites as well as the generation of new datasets. All ages in this study are presented on the astronomically calibrated 'PEAT' age model available for the middle Eocene through Oligocene (31–42.5 Ma, based on XRF core scanning, magnetostratigraphic and stable isotope data, and an average of the combined ages from Sites 1218, U1333, and U1334 [*Westerhold et al.*, 2014]). Data were converted to the PEAT age model using magnetostratigraphy where available and otherwise correlated with precise isotopic correlation between sites

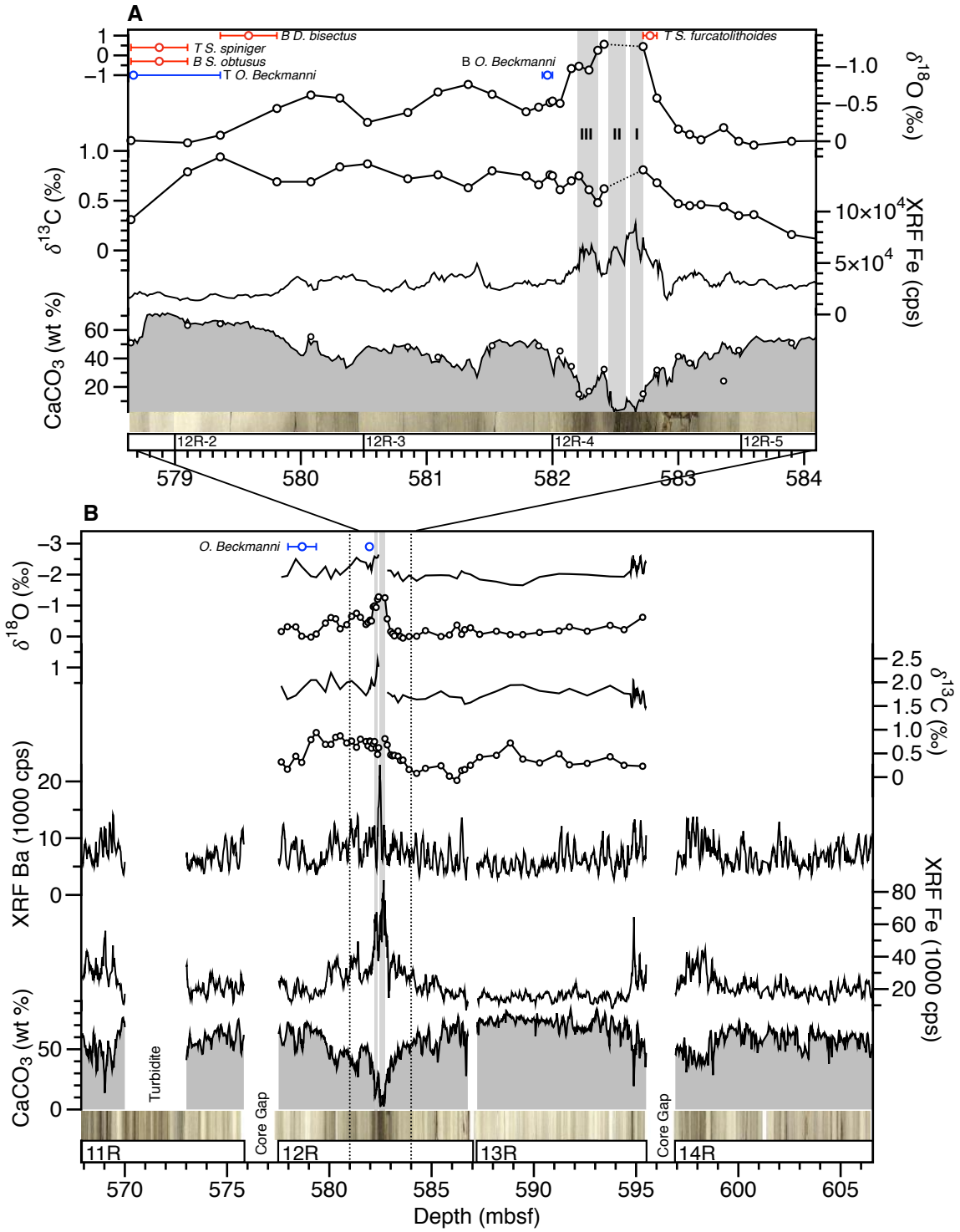

Figure 3-2 Paleoceanographic records from ODP Site 929 versus depth. Biostratigraphy, bulk sediment and benthic foraminiferal $\delta^{18}O$ and $\delta^{13}C$ (‰), calibrated $CaCO_3$ (grey; calibrated by coulometry on discrete samples) and discrete samples (circles), raw XRF Fe and Ba counts, linescan core photo composite, and core recovery from (a) the MECO and (b) study intervals. Revised placement of the LO and HO of *O. beckmanni* generated in this study and calcareous nannofossils [*Agnini, pers comm 2015*] are shown (red and blue circles). Grey bars mark dissolution horizons I-III (intervals of low carbonate content and high magnetic susceptibility).

3.3.1.1 A new age model for ODP Site 929

The middle Eocene interval at Site 929 has not been the focus of any study, however it was noted that available shipboard data (carbonate content, core magnetic susceptibility, and down-hole spectral reflectance records [*Curry et al.*, 1995]) tentatively suggest the presence of the MECO and CAEs [Supplementary information in *Pälike et al.*, 2012]. However, available biostratigraphic datasets are unable to provide high-resolution age control over the narrow study interval because planktic foraminiferal datums are both poorly constrained and widely spaced (~10 m spacing) [*Pearson and Chaisson*, 1997] (**Supplemental Figure 3-4**), and magnetostratigraphy is unreliable due to a weak paleomagnetic signal coupled with a strong magnetic overprint typical of Ceara Rise sediments [*Curry et al.*, 1995]. Thus, a new age model is developed in Hole 929E between 567.92 and 606.55 mbsf.

To confirm the presence of the MECO, reduce the depth uncertainty of the planktic foraminiferal zonal assignments, and test the synchroneity of datums, the occurrence of *O. beckmanni* and calcareous nannofossil marker species are re-evaluated with higher-resolution sampling (~10 cm; **Table 3-2**). *O. beckmanni* is a distinctive spherical species whose total range defines planktic foraminiferal Zone P13/E12 [*Berggren*, 1995; *Berggren and Pearson*, 2005] providing a key marker for the MECO. Here, the highest occurrence of *O. beckmanni* is determined at 578.67 mbsf and the lowest occurrence at 581.96 mbsf (**Figure 3-2**; **Table 3-2**). The LO occurs stratigraphically above the MECO, in contrast with previous findings that it occurs lower than or within the MECO [*Edgar et al.*, 2010; *Luciani et al.*, 2010]. This apparent 'young' age for the LO is attributed to the intense dissolution related to the MECO event. Consequently, the presence of *O. beckmanni* confidently ties the sediments in this interval at Site 929 to the MECO event but datums are not included in the age model.

An astronomical age model for Site 929 was developed primarily using Ba records derived from XRF core scanning. Spectral analysis in the depth domain reveals prominent ~20-25 cm cycles in Ba intensity over the majority of the study interval (**Figure 3-2**). Band pass filters and MTM power spectral analyses

of undisturbed intervals indicate that cycles in XRF Ba have orbital frequencies that can be constrained to eccentricity-modulated precession (**Supplemental Figure 3-3**). The dominance of eccentricity-modulated precession is consistent with findings from nearby Site 1260 *Westerhold and Röhl* [2013]. XRF Fe data has a lower signal-to-noise ratio and less clear spectral analyses than Ba, and is not used for correlation. However, Fe intensity exhibits two peaks within the MECO (**Figure 3-2**) coincident with discrete clay horizons as also observed at Site 1260 [*Westerhold and Röhl*, 2013]. The Ba record exhibits a single peak immediately between the two clay layers/Fe spikes and could relate to Ba from biogenic barite ($BaSO_4$), organic matter, carbonate, or detrital material. In marine sediments $BaSO_4$ production is strongly correlated to organic carbon export [*Dymond et al.*, 1992] and is thus, widely used as an export production proxy [e.g. *Paytan and Kastner*, 1996]. However, identification of $BaSO_4$ would require additional geochemical data. Furthermore, the large peak in Ba could represent barium remobilization during suboxic diagenesis rather than a productivity signal. Thus, for the narrow interval across the peak of the event Ba is not used for age model tuning.

The new age model is therefore based on the recognition of short eccentricity (100-kyr) and eccentricity modulated climatic precession (21-kyr) cycles observed in XRF-scanning Ba concentration data (**Supplemental Figure 3-4**) with revised planktic foraminiferal and calcareous nannofossil biostratigraphic events only used to inform tuning. A detailed explanation on the formulation of the age model is presented in **Supplemental Section 3.6.1**. Sample ages based on the new age model are in agreement with those defined by the biostratigraphic age model used in other studies [*Pagani et al.*, 2011; *Pearson and Chaisson*, 1997] (**Supplemental Figure 3-4**) except within the MECO interval itself due to dissolution driven decreased carbonate accumulation rates (<0.5 cm/kyr). Significant uncertainty remains regarding the interpretation of XRF data in sediments post-MECO and Core 929E 11R is essentially 'floating' with no distinct age constraints above the HO of *O. beckmanni* at 578.67 mbsf (**Table 3-2**) and a turbidite at 570 mbsf (**Appendix Table 5-4**). Continuing the study further into the early Eocene would reduce age uncertainties in post-MECO sediments, however, for this interval we assume sedimentation rates are similar to the average pre-MECO rates in our study interval (~11 m/Ma).

3.3.1.2 ODP Site 1209 age model

At Site 1209 three holes were drilled (A, B, and C) and are spliced together to form a composite section [*Bralower et al.*, 2003; *Westerhold and Röhl*, 2006]. However, the comparison of features between holes required in this study (i.e. published benthic foraminiferal stable isotopes from Holes 1209A and B vs. carbonate measurements in this thesis chapter from Hole 1209C) necessitated additional fine-scale (<10 cm) correlation of magnetic susceptibility records. Records from Holes 1209A and B are therefore converted by correlation to the depths of Hole 1209C rmcd and presented with depths labelled as 'Hole 1209C depth adjusted rmcd' (**Figure 3-3**).

The middle Eocene portion of the age model at Site 1209 has gone through several iterations regarding the presence of the MECO event in sediments at the site [*Bohaty et al.*, 2009; *Dawber and Tripati*, 2011b; 2012b; *Dutton et al.*, 2005; *Hancock and Dickens*, 2006]. The MECO was originally identified at Site 1209 by *Bohaty et al.* [2009] who observed a prominent carbonate dissolution horizon [*Hancock and Dickens*, 2006] and sharp increases in magnetic susceptibility [*Bralower et al.*, 2003; *Westerhold and Röhl*, 2006] at ~40 Ma based on the biostratigraphic age model that combined calcareous nannofossils and planktic foraminiferal datums [*Bralower et al.*, 2005; *Petrizzo et al.*, 2005]. Subsequent studies did not report the MECO across this same interval due to age model uncertainty [*Dawber and Tripati*, 2011b; 2012a]. Specifically, the planktic foraminiferal datum for *O. beckmanni* was removed from age calculations because it was defined by only three specimens [*Petrizzo et al.*, 2005] and its occurrence was inconsistent with the calcareous nannofossil datum for *D. scrippsae* [*Dawber and Tripati*, 2011b; 2012b; *Petrizzo et al.*, 2005]. However, *Dawber and Tripati* [2011b] note an ~0.8 ‰ negative benthic foraminifera $\delta^{18}O$ excursion at ~153.5 rmcd at precisely the depth of the dissolution horizon described in *Bohaty et al.* [2009].

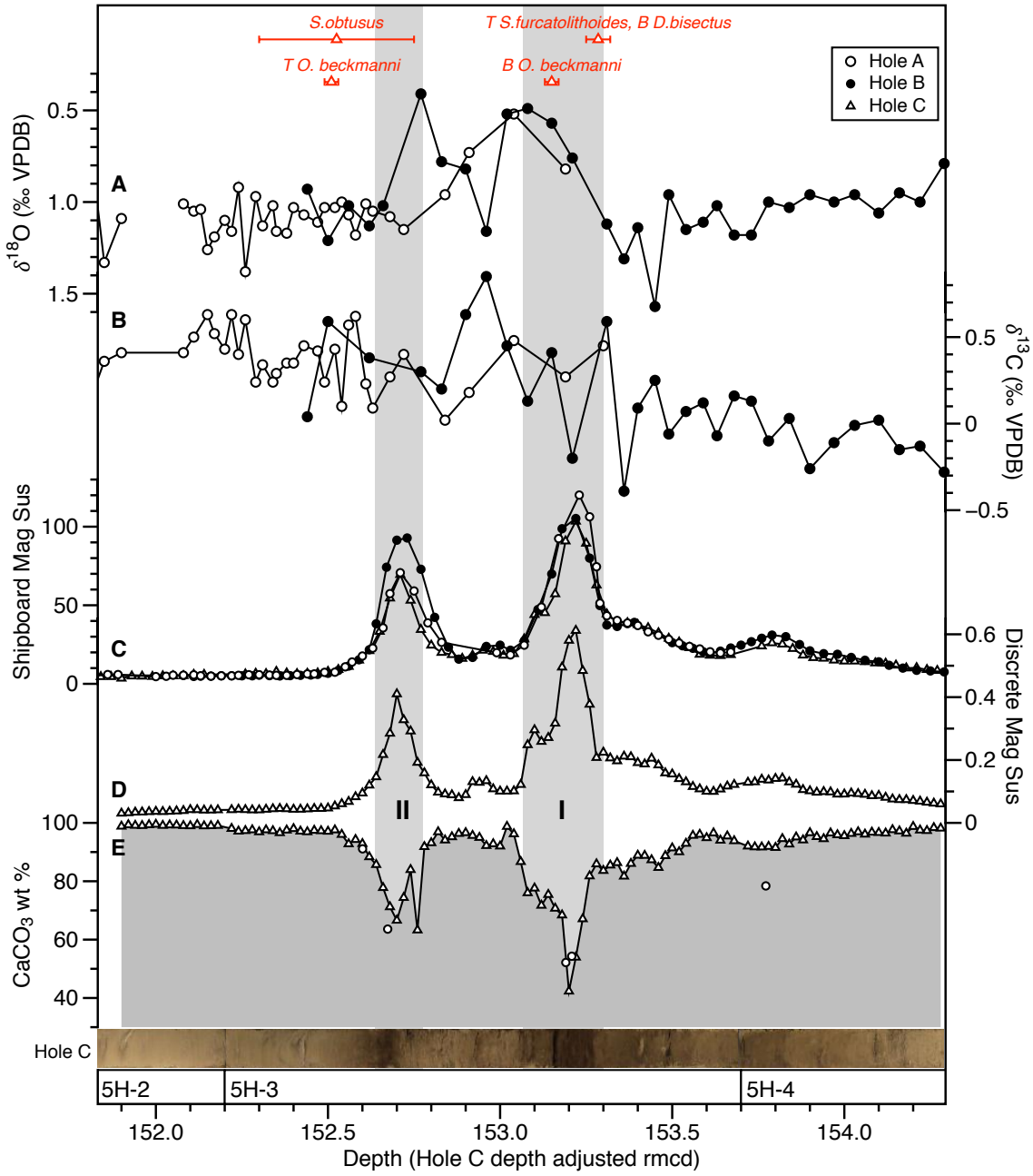

Figure 3-3 Paleoceanographic records from ODP Site 1209 versus depth. Benthic foraminiferal (a) $\delta^{18}O$ and (b) $\delta^{13}C$ (*Oridorsales umbonatus*, ‰) [*Dawber and Tripati, 2011a,b*], (c) magnetic susceptibility [*Bralower et al., 2002*], (d) discrete magnetic susceptibility from Hole 1209-C [*this study*], (e) carbonate content (wt %) from *Bralower et al.* [*2002*] (triangles) and this study (circles) plotted versus adjusted revised composite depth (Hole C depth adjusted revised meters composite depth]). Lower panel shows Hole 1209-C core photo composite and core recovery. Revised placement of the LO and HO of *O. beckmanni* generated in this study and calcareous nannofossils [*Agnini, pers comm 2015*] are shown (red circles). Grey bars mark dissolution horizons I-II (intervals of low carbonate content and high magnetic susceptibility).

Figure 3-4 Paleoceanographic records from IODP Site 1263 versus depth. Benthic foraminiferal and bulk sediment $\delta^{18}O$ and $\delta^{13}C$ ‰ (VPDB) [*Bohaty et al., 2009; Boscolo et al., 2014; this study*], planktic foraminifera (%) and (d) fragmentation (%) [*this study*], (e) shipboard magnetic susceptibility (green) [*Zachos et al., 2004*] and discrete magnetic susceptibility from Hole B [*this study*], and carbonate content (wt %) [*this study*] versus meters composite depth (mcd) from (a) the peak MECO and (b) MECO intervals. Lower panel shows Hole 1263-A and B core photo composite and Hole 1263-B core recovery. Grey bars mark dissolution horizons I, II (intervals of low carbonate content and high magnetic susceptibility).

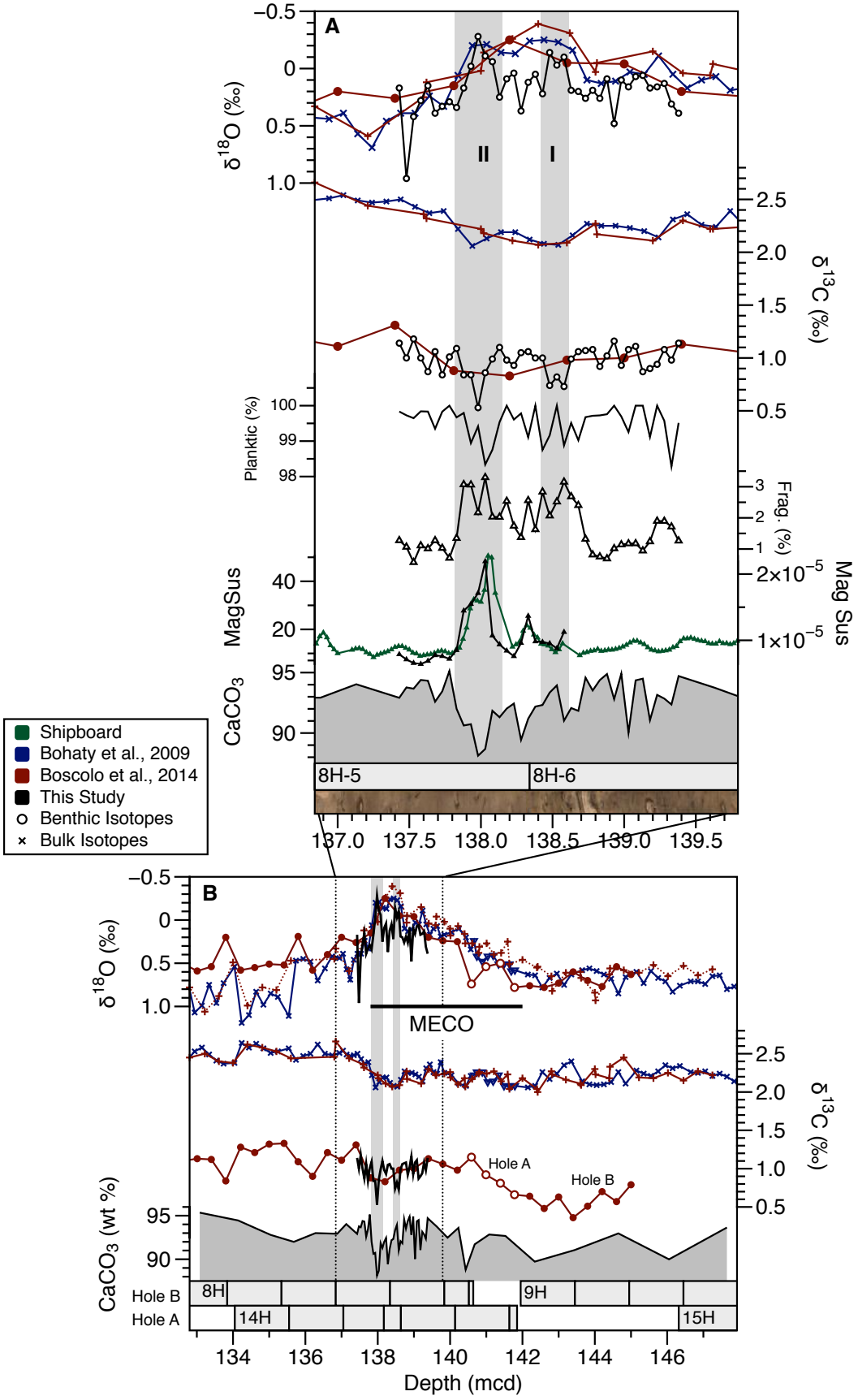
A
B
II
I
MECO
Hole A
Hole B
8H-5
8H-6
8H
9H
14H
15H
Shipboard
Bohaty et al., 2009
Boscolo et al., 2014
This Study
Benthic Isotopes
Bulk Isotopes
δ18O (‰)
δ13C (‰)
Planktic (%)
Frag. (%)
MagSus
Mag Sus
CaCO3
CaCO3 (wt %)
Depth (mcd)

To confirm the presence of the MECO and reduce the depth uncertainty of planktic foraminiferal zonal assignments, the occurrence of *O. beckmanni* and calcareous nannofossil marker species were re-evaluated with high-resolution sampling (2 cm; **Table 3-2**). Here, the HO of *O. beckmanni* is located at 139.31 rmcd and the LO at 139.95 rmcd (**Figure 3-3**). The LO is stratigraphically lower than the lowest observed $\delta^{18}O$ values defining the onset of the MECO consistent with an earlier LO at tropical sites [*Edgar et al.*, 2010]. This finding confirms the presence of the MECO at ~153.5 rmcd. Furthermore, the relatively narrow depth interval where *O. beckmanni* was found indicates that the interval is significantly condensed, with ~ 1–1.5 Myr represented by ~65 cm. Records from Site 1209 are presented on the biostratigraphic age model, with the exception of the narrow interval of the MECO which necessitated more precise isotopic correlation between sites. Thus, some ambiguity remains in the fine-scale timing of the Site 1209 records across the peak of the MECO, as the isotopic signal is not the same in all holes, in particular across the MECO cooling phase (**Figure 3-3**). Further refinement of the age model across this interval will require increased resolution of stable isotope records.

3.3.2 ODP Site 929: Stable isotope ($\delta^{18}O$ and $\delta^{13}C$) records

Foraminifera are present throughout the study interval where $CaCO_3$ is present above ~3 wt %. However, preservation is generally poor throughout, with moderate to severe dissolution evident from etching of the test and extensive fragmentation; specimens are sufficiently well preserved for taxonomic identification and biostratigraphy [*Curry et al.*, 1995; *Pearson and Chaisson*, 1997]. Further, all specimens appear "frosty" under the stereomicroscope [sensu *Sexton et al.*, 2006b], and scanning electron microscope images specimens reveal micron-scale cemented overgrowths on the broken specimen test walls (**Supplemental Figure 3-5**).

A continuous ~2.5 Myr long record of stable isotopes ($\delta^{18}O$ and $\delta^{13}C$) from epifaunal benthic foraminifer *N. truempyi* was generated at Site 929 (**Figure 3-2**). Despite the condensed nature of sediments at this site, key features - MECO warming and recovery are present in the stable isotope record and are consistent with previously published records of the event [*Bohaty et al.*, 2009; *Edgar et al.*, 2010]. The onset of MECO warming is identified at 583.90 mbsf

and is marked by a decrease in $\delta^{18}O$ values from ~0.0 ‰ to negative ~1.3 ‰ and an overall increase in $\delta^{13}C$ from ~0.0 to 0.8 ‰ between ~584 and 581 mbsf. Two samples were barren of benthic foraminifera due to low carbonate content (Samples 929E-12R-4, 52-54 cm and 62-64 cm; 582.52 to 582.62 mbsf) and there is no evidence for the short-lived negative carbon isotope excursion (CIE) at the peak of the MECO as documented in Southern Ocean records [*Bohaty et al.*, 2009] because the event is likely truncated by severe carbonate dissolution. Recovery from the MECO begins at 582.41 mbsf where $\delta^{18}O$ values begin to increase. Bulk sediment $\delta^{13}C$ and $\delta^{18}O$ values record the initial warming and recovery from the MECO and are offset from benthic foraminiferal records by ~ -1.50 ‰ in $\delta^{18}O$ and ~ 1.50 ‰ in $\delta^{13}C$ values but do not cover the peak of the event due to a lack of carbonate in three samples (Samples 929E-12R-4, 52-54 cm, 62-64 cm, and 72-74 cm; from 582.52 to 582.72 mbsf).

3.3.3 MECO dissolution events

At Site 929 sediment carbonate content ranges between ~1 and 65 wt % with a mean of 42 wt % (**Figure 3-2**). Three distinct dissolution horizons (labelled I, II, and III; **Table 3-3**) categorized by decreased carbonate content (to <15 wt %), increased XRF Fe/Ca, and dark horizons in core photos and linescan colour reflectance data are identified. Dissolution in the lower two horizons (I, II) is most severe (3–10 wt % carbonate) and increases up to 30 wt % (~582.40 mbsf) between horizons II and III. Although the $\delta^{18}O$ data gap at the peak of the event makes it difficult decipher when horizons II and III occurred with respect to the MECO, close inspection of carbonate and XRF Fe records indicate horizon II likely occurred during the warming phase of the MECO (**Figure 3-2**) while horizon III occurred during the cooling phase of the MECO (defined as the positive shift in $\delta^{18}O$ values after the peak excursion).

At Site 1209 new high-resolution (~2 cm sample spacing) carbonate content data range between ~40 and 98 wt % $CaCO_3$ (**Figure 3-3**). Increased resolution reveals that the single low-carbonate interval first reported in *Bralower et al.* [2002] is now comprised of two prominent dissolution horizons centred at ~153.2 and 152.7 rmcd (horizons I and II; **Table 3-3**) documented in all three holes. Both intervals are characterized by decreases in carbonate content, increases in magnetic susceptibility, and dark horizons in core photos.

Correlation of these horizons to events within the MECO is difficult because $\delta^{18}O$ and $\delta^{13}C$ values from Holes 1209A [*Dawber and Tripati*, 2011b] and Hole 1209B do not unambiguously define the position of the MECO with two $\delta^{18}O$ minima occurring in Hole 1209B and one at 1209A between these two.

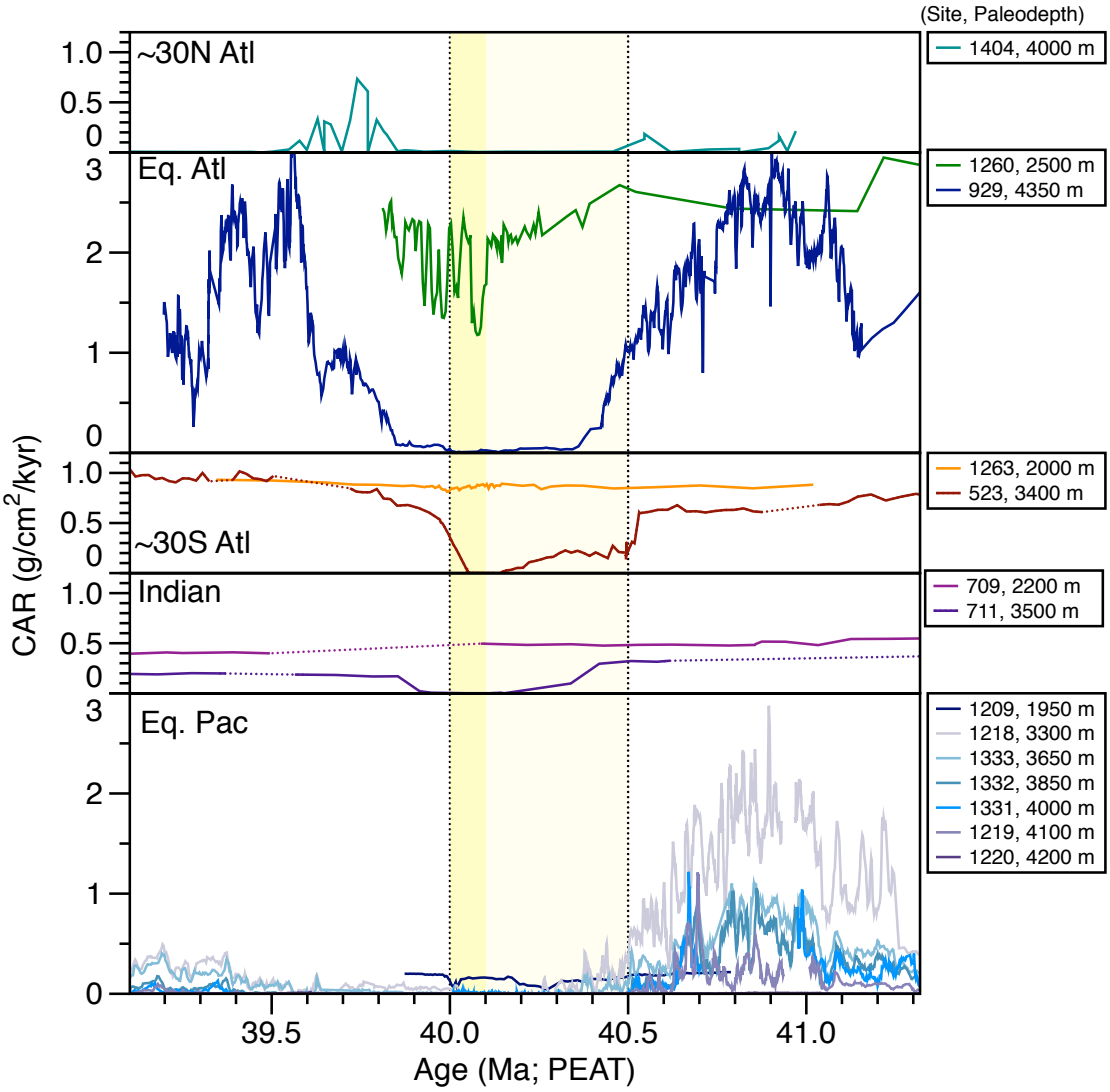

Figure 3-5 Interbasinal compilation of carbonate mass accumulation rate records for the late middle Eocene between 39.1 and 41.3 Ma encompassing CAE-3 and 4 and the MECO.
For these records, new carbonate mass accumulation rate (CAR; g/cm^2/kyr) datasets from Sites 1260, 929, 1263, and 1209 [*this study*] combined with CAR records from Sites U1331-U1334 and 1218-1220 [*Westerhold, unpublished*], Sites 523, 702, 709, and 711 [*Bohaty et al., 2009*], and Site U1408 [*Norris et al., 2014*] arranged by ocean basin. Paleowater depths of each site are indicated in legend. Dotted lines in records span unconformities or intervals with no core recovery. Shaded region marks MECO warming (light yellow) and peak-MECO CIE (darker yellow) as defined in *Bohaty et al.* [2009].

Table 3-3 Dissolution horizon definition and position relative to CCD and lysocline for sites used in compilation

Site (paleodepth)	Evidence of dissolution	Horizon #	Depth (m) Start	Depth (m) End	Thickness (m)	Age (Ma) Start	Age (Ma) End	Approximate Duration (kyr)	Location relative to MECO warming/cooling*	Location relative to CCD/Lysocline**
Atlantic										
IODP Site 1263	increase in fragmentation	I	138.42	138.62	0.20	40.03	40.06	31	warming phase	below lysocline
(2000 m)	Peak in magnetic susceptibility, 10 % decrease in wt % $CaCO_3$, increase in fragmentation	II	137.82	138.15	0.33	39.97	40.02	48	Peak MECO	below lysocline
IODP Site 1260	Peak in XRF Fe, 35 % decrease in wt % $CaCO_3$, increase in fragmentation	I	43.34	44.21	0.87	40.06	40.11	48	Peak MECO	below lysocline
(2550 m)	Peak in XRF Fe, ~20 % decrease in wt % $CaCO_3$	II to ~VI	40.532	42.804	~0.40 each	39.85	40.04	~30 each	Post Peak MECO	below lysocline
DSDP Site 523	<30 wt % $CaCO_3$	I	134.98	135.32	0.35	40.11	40.15	43	warming phase	below lysocline
(3350 m)	<10 wt % $CaCO_3$	II	134.23	134.27	0.04	39.99	40.07	81	Peak MECO	below CCD and lysocline
ODP Site 929	<10 wt % $CaCO_3$	I	582.61	582.72	0.11	40.16	40.44	287	warming phase	below CCD and lysocline
(3935 m)	<10 wt % $CaCO_3$	II	582.45	582.59	0.14	40.00	40.10	102	warming phase	below CCD and lysocline
	Peak in magnetic susceptibility, <15 wt % $CaCO_3$	III	582.21	582.34	0.13	39.85	39.92	63	cooling phase	below CCD and lysocline
IODP Site U1404	<10 wt % $CaCO_3$	I	244.590	255.560	10.97	39.92	40.47	553	not enough data	below CCD and lysocline
(4000 m)										
Pacific										
ODP Site 1209	Peak in magnetic susceptibility, 30 % decrease in wt % $CaCO_3$	I	139.88	140.15	0.27	40.19	40.30	112	warming phase	below lysocline
(1950 m)	Peak in magnetic susceptibility, 55 % decrease in wt % $CaCO_3$	II	139.41	139.61	0.20	40.00	40.03	39	possibly cooling phase	below lysocline
IODP Site 1218	<10 wt % $CaCO_3$	I	271.97	274.45	2.48	40.00	40.24	239	warming phase	below CCD and lysocline
(3250 m)										
IODP Site U1333	<10 wt % $CaCO_3$	I	165.80	172.76	6.96	39.99	40.28	295	warming and cooling phase	below CCD and lysocline
(3600 m)										
IODP Site U1332	<10 wt % $CaCO_3$	I	106.52	118.64	12.12	39.52	40.48	957	spans warming and cooling phase	below CCD and lysocline
(3850 m)										
IODP Site U1331	<10 wt % $CaCO_3$	I	63.77	88.45	24.68	39.50	40.48	979	spans warming and cooling phase	below CCD and lysocline
(4000 m)										
IODP Site 1219	<10 wt % $CaCO_3$	I	204.59	215.57	10.98	39.50	40.48	979	spans warming and cooling phase	below CCD and lysocline
(4000 m)										
IODP Site 1220	<5 wt % CaCO3									
(4100 m)									below CCD and lysocline for the duration of the study interval	

*MECO warming phase defined by decreasing $\delta^{18}O$ values; cooling phase defined by increasing $\delta^{18}O$ values, peak defined by lowest observed $\delta^{18}O$ values

**CCD defined as <15 wt % $CaCO_3$; Lysoline defined by evidence of dissolution and or significant decrease in $CaCO_3$

Similar to the new records for Sites 929 and 1209, two dissolution horizons are also evident in available records from subtropical Atlantic Site 523 [*Bohaty et al.*, 2009] (**Supplemental Figure 3-6**; **Table 3-3**). In Cores 523C-37H-3 and 38H-1, core photos reveal two dark horizons, one at the onset of MECO warming (across which carbonate content decreases from ~ 85 to ~38 wt %) and one at the peak of event (which reaches ~0 wt %). A thin condensed horizon containing Mn oxides occurs in the upper, more carbonate depleted interval [*Bohaty et al.*, 2009].

Previous work reported no change in carbonate content across the MECO at Site 1263 [*Bohaty et al.*, 2009; *Boscolo Galazzo et al.*, 2015], however, new higher resolution carbonate data reveals a drop in carbonate from ~95 to 86 wt % $CaCO_3$ at 138.04 m mcd (**Figure 3-4**; **Table 3-3**). This interval also corresponds to a narrow (~28 cm) peak in shipboard magnetic susceptibility [*Zachos et al.*, 2004] and new records of discrete magnetic susceptibility. Two intervals of increased fragmentation (horizons I and II; **Table 3-3**) correspond to excursions in new high-resolution benthic foraminiferal $\delta^{18}O$ and $\delta^{13}C$ values (~0.3 to 0.5 ‰ respectively) not observed in previous records [*Boscolo Galazzo et al.*, 2015]. Close inspection of bulk carbonate $\delta^{18}O$ values reveals two small negative ~0.2 ‰ excursions within the long-term negative ~1.0 ‰ MECO excursion [*Bohaty et al.*, 2009]. The single magnetic susceptibility peak correlates to the upper warm interval (horizon II).

At Site 1260 dissolution is marked by an ~87 cm-thick peak in XRF Fe values [*Westerhold and Röhl*, 2013] that corresponds to decreases from ~80 to 45 wt % in new high-resolution carbonate content data (**Supplemental Figure 3-7**). While Site 1260 has a significant siliciclastic (clay) sediment component [*Erbacher et al.*, 2004] that could decrease carbonate through dilution rather than dissolution, an increase in thermophyllic planktic foraminifera *Morozovelloides* [*Edgar et al.*, 2010] and visual inspection reveals poorly preserved and broken foraminiferal tests (K. Edgar pers. obs.) supporting both warming and dissolution in this interval. Furthermore, XRF Fe, carbonate content, and benthic foraminiferal $\delta^{18}O$ values [*Edgar et al.*, 2007; *Sexton et al.*, 2006a] show multiple similar fluctuations throughout the MECO interval. Age constraints across these horizons are difficult to define due to ambiguity regarding the location of the C18r/C18n magnetochron boundary, lack of

biostratigraphic constraints at the top of the section, and an unusual benthic $\delta^{18}O$ signal which initially led to the peak and recovery of the event considered absent [*Edgar et al.*, 2007; *Edgar et al.*, 2010; *Sexton et al.*, 2006a]. However, cyclostratigraphic analysis confirms the peak MECO is present at ODP Site 1260, though ambiguity still remains in the shallowest portion of the record (<44 rmcd) because it is not orbitally tuned [*Westerhold and Röhl*, 2013].

3.4 Interpretation and Discussion

3.4.1 Multi-site compilation of deep-sea carbonate accumulation

A new compilation of carbonate mass accumulation rate (MARs) estimates from this thesis chapter and published sources (**Figure 3-5**) confirm widespread carbonate dissolution during the MECO, supporting previous studies [*Bohaty et al.*, 2009; *Pälike et al.*, 2012]. New records from three sets of shallow-deep paired sites increase meridional coverage over the mid-latitude and equatorial Atlantic regions (Sites 1051 and U1404, 1260 and 929, 1263 and 523) and indicate similar trends in shallow and deep carbonate accumulation patterns globally across the MECO (**Figure 3-5**). All sites in at deeper paleodepths (>3000 m; subtropical Atlantic Site 523, northern Atlantic Site U1404, subtropical Indian Site 711, and equatorial Pacific Sites 1218–1220 and U1331–U1333; **Table 3-3**) exhibit the same broad (>500 kyr) patterns of accumulation: high carbonate MAR before the MECO followed by decrease and total loss of carbonate in the interval corresponding to the lowest observed benthic $\delta^{18}O$ values. However, there is significantly more variability in the shorter-term (<500 kyr). Accumulation at Site 523 increases during the MECO warming phase between 40.4 and 40.15 Ma and recovers to pre-event values at ~40.05 Ma while Site 929 remains low even after the event (until ~39.85 Ma). Shallower Site 1260 (~2500 m paleodepth) exhibits consistently high carbonate MARs during the MECO warming phase except for a sharp drop that corresponds to the lowest observed benthic foraminifera $\delta^{18}O$ values. Mid-latitude South Atlantic Site 1263 and subtropical Indian Site 709 are shallower still (at ~2000 m and 2200 m paleodepth, respectively) and only Site 1263 exhibits a small decrease in carbonate MARs at the peak of the MECO. Carbonate MARs at Site 1209 are the shallowest site in this compilation, and exhibit two distinct low carbonate MAR intervals at ~40.10 and 40.28 Ma.

3.4.2 Overall Magnitude of calcite compensation depth and lysocline shoaling in the Atlantic and Pacific

The CCD and lysocline are oceanic horizons that control the depth of calcite accumulation in the deep ocean. In sediment cores the CCD is identified as the near or complete absence of carbonate [*Delaney and Boyle*, 1988; *Lyle*, 2003; *Pälike et al.*, 2012; *Peterson and Backman*, 1990; *Van Andel*, 1975], and has previously been ascribed to a fixed carbonate content amount (e.g. 10 wt %) [*Van Andel*, 1975]. However, this method does not account for the range of processes that can lower sediment carbonate content (decreased carbonate flux or increased flux of other sediment components e.g. clay or biogenic opal). A more accurate definition of the CCD defines the depth where carbonate accumulation rates interpolated across the paleodepth transect reach zero [e.g. *Lyle*, 2003]. In this study, the CCD is defined by the ~10 wt % mark (the former method) due to the small near-zero carbonate MAR fluctuations at deeper sites in the study interval.

The lysocline is the oceanic depth horizon at which the rate of calcite dissolution is dramatically increased. This is difficult to define in sediments, but a sharp decrease in carbonate content (or carbonate MARs) or evidence for an increase in dissolution have been used to defined the lysocline depth in deep-sea sedimentary records [e.g. *Colosimo et al.*, 2006]. Here we interpret changes in the depth of the lysocline using a combination of evidence for carbonate dissolution including: increased planktic foraminiferal test fragmentation, presence of a clay-rich component (% $CaCO_3$ ≈ 0 % and a sharp increase in Fe values), and significantly decreased carbonate content. Planktic fragmentation has been shown to reliably predict intervals with impoverished preservation resulting from dissolution [*Colosimo et al.*, 2006; *Hancock and Dickens*, 2006; *Leon-Rodriguez and Dickens*, 2010]. Clay layers form when carbonate accumulation decreases to low rates, and even a small change in carbonate % in carbonate-rich sediments can signify significant dissolution because of the non-linearity of the system [*Ridgwell*, 2007; *Zeebe and Zachos*, 2007].

Reconstruction of the CCD and lysocline variability in this study is based on definitions above (**Figure 3-6**; $\delta^{18}O$ data and $CaCO_3$ data with 10 wt % mark

shown in **Supplemental Figure 3-8**). The presence of carbonate at all Atlantic sites in this study prior to ~40.5 Ma and after ~39.8 Ma indicates that the Atlantic CCD and lysocline were >4000 m both before and after the MECO event (**Figure 3-6**; **Table 3-3**). Maximum Atlantic CCD shoaling occurs during the peak of the MECO to ~3300 m (overall >1000 m Atlantic CCD shoaling at ~40 Ma) as evidenced by the total loss of carbonate at Site 523. At the same time, increased planktic foraminiferal fragmentation, clay layers, and significant carbonate loss at sites shallower than ~2500 m (Sites 1260 and 1263) suggest that the maximum Atlantic lysocline shoaling reached depths less than ~2000 m (overall >2000 m Atlantic lysocline shoaling at ~40 Ma).

In the Pacific basin, all sites shallower than ~4100 m contain carbonate prior to 40.5 Ma and after 39.5 Ma, suggesting that the Pacific CCD and lysocline were ~4100 m before and after the MECO event. During the peak of the MECO sites deeper than ~3000 m contain little or no carbonate, suggesting the maximum Pacific CCD shoaling reached water depths of ~3000 m (overall >1000 m Pacific CCD shoaling at ~40 Ma). A significant decrease in carbonate MARs at Site 1209 has been attributed to dissolution [*Bohaty et al.*, 2009], and closer inspection in this study shows evidence of increased clay content and a ~50 % drop in carbonate content, suggesting that the maximum Pacific lysocline shoaling occurs at depths shallower than ~2000 m (overall >2000 m Pacific lysocline shoaling at ~40 Ma).

Transient lysocline shoaling of more than ~2000 m in both the Atlantic and Pacific basins is well above the previously observed dissolution in the Atlantic (~500-1500 m reconstructed magnitude of CCD shoaling in the Atlantic; [*Bohaty et al.* [2009]) and Pacific (~900 m equatorial Pacific CCD shoaling [*Pälike et al.*, 2012]; **Supplemental Figure 3-1**). Though the total magnitude of CCD shoaling is not precisely constrained with these new data (carbonate MAR records from sites at shallower/deeper paleodepths is still necessary), the results show the magnitude of lysocline change during the MECO was closer to estimates for shoaling during the PETM hyperthermal (>2000 m; ~3600 m to 1500 m depth in the Atlantic basin; [*Zachos et al.*, 2005]). Although the PETM and MECO occur on different timescales, CCD fluctuations in the Paleogene have the capacity for larger changes because an overall shallow CCD causes higher sensitivity to forcing [*Pälike et al.*, 2012].

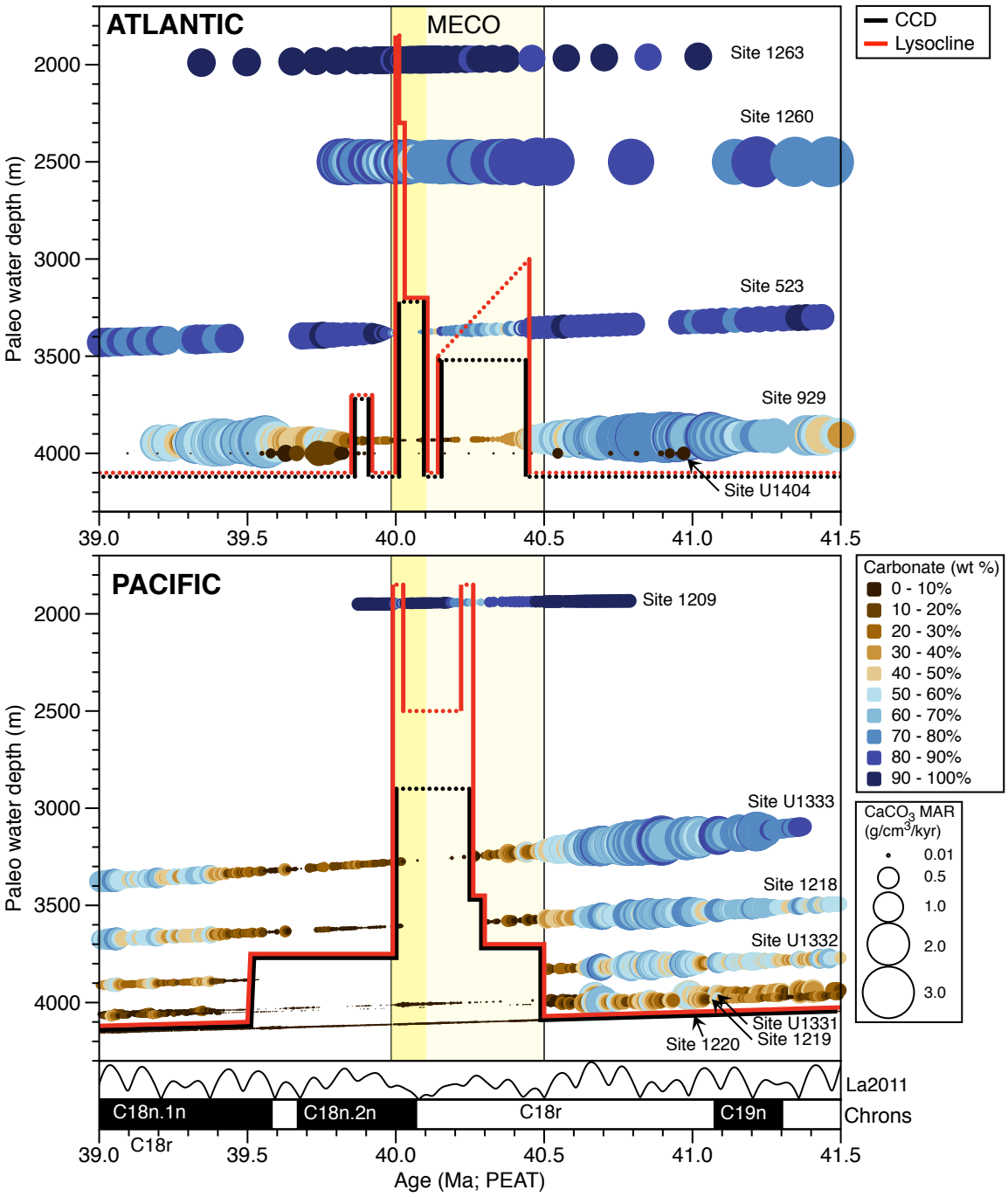

Figure 3-6 Carbonate compensation depth, lysocline depth, and carbonate accumulation rate reconstruction across the MECO in the Atlantic and Pacific. Carbonate accumulation rate (g/cm^2/kyr) history as a function of age and paleo water depth across a depth transect of sites (a) Atlantic and (b) Pacific. Lysocline (red line) and CCD (black line). Each circle represents one carbonate sample measurement and circle colour indicates $CaCO_3$ (wt %) as indicated in legend (brown—blue colour scale). Dotted lines in CCD and lysocline records span unconstrained depths due to limited data. Shaded region marks MECO warming (light yellow) and peak-MECO CIE (darker yellow) as defined in *Bohaty et al.* [*2009*]. Data sources are the same as in **Figure 3-5**.

One caveat is that the use of a broad geographical range of sites within each ocean basin may represent regional signals instead of basin-wide trends. However, the strategy of pairing nearby shallow/deep sites as in *Bohaty et al.* [2009] supports a similar magnitude of shoaling (e.g. neighbouring Sites 929 and 1260 alone suggest ~1500 m shoaling). Furthermore, coherency in records across hundreds of km is more likely a signal of a global phenomenon and not a regional productivity signal [*Lyle*, 2003; *Lyle et al.*, 2008].

3.4.3 New evidence for short-term CCD fluctuations during the MECO

While the overall trend of long-term (~500 kyr) increased and severe dissolution observed previously remains robust for the Atlantic and Pacific basins [*Bohaty et al.*, 2009; *Pälike et al.*, 2012], new records reveal superimposed shorter-term fluctuations in carbonate accumulation dissolution at multiple sites during the MECO. These variations indicate that the CCD crossed the paleodepth of the deeper sites (Sites 929, 523, and 1209) multiple times during the onset of warming and after the peak of the event (defined as the minimum $\delta^{18}O$ values). These short-lived (<100 kyrs) events indicate more dynamic CCD and lysocline behaviour than previously recognized (**Figure 3-6**; summarized in **Table 3-3**).

In the Atlantic Ocean basin there are two main phases of CCD and lysocline shoaling with transient deepening during the middle of the MECO event (**Figure 3-6**). Between ~40.5 and 40.15 Ma the lysocline shoaled up to ~3100 m while the CCD shoals to ~3500 (as evidenced by dissolution at Site 523 that is more intense and gradually declines with carbonate remaining relatively high, >50 wt %). Then, amid MECO warming between ~40.15 and ~40.10 Ma, an interval of transient CCD and lysocline deepening occurs. By the peak of the MECO event at 40.1 Ma, the largest magnitude and most severe shoaling begins as all sites below ~3000 m (Sites U1404, 929, 523) cease to accumulate carbonate and evidence of dissolution (clay, carbonate decreases, and fragmentation) is evident at shallower Sites 1263 and 1260. By ~40 Ma all sites abruptly begin accumulating carbonate again as the CCD and lysocline deepen >4000 m. Interestingly, between ~39.90 and 39.85 Ma the CCD and lysocline shoal for a third time during the recovery phase of the MECO (only crossing the depth of Site 929), before returning to pre-event depths.

There is similar evidence in the Pacific Ocean basin for two main phases of CCD and lysocline shoaling during the MECO event (**Figure 3-6**). The CCD and lysocline shoal gradually at the onset of the MECO to ~3200 m at ~40.3 Ma. At 40.28 Ma a ~40 % loss of carbonate at Site 1209 indicates the lysocline shoaled to ~2000 m during MECO warming. A significant paleodepth gap (between ~2000 to 3300 m) leaves the magnitude of CCD shoaling uncertain. The presence of carbonate up to 90 wt % at Site 1209 indicates the lysocline then deepened for several 100 kyr until the peak of the MECO when the lysocline again shoaled to <2000 m water depth. Finally, at ~40.0 Ma carbonate accumulation abruptly resumes at all sites shallower than ~3700 m, and at ~39.5 Ma the CCD and lysocline return to pre-event water depths.

The thickness of the clay layers should increase with increasing paleodepth because deeper sites experience dissolution first as the CCD begins to shoal [Zachos et al., 2005]. This is found to be true during the most severe MECO dissolution; the thickness of dissolution horizons increases in paleodepth succession, i.e., thicker in sediments from Site 929 than Site 1260 (**Table 3-3**). This pattern is therefore interpreted to represent a long-term dissolution event during the MECO superimposed with shorter-term fluctuations, instead of a single prolonged ~500 kyr dissolution.

The CCD and lysocline interpretations presented here rely on multiple assumptions for age model construction and site-to-site correlation. Importantly, fine-scale correlation between sites at the onset and peak of the MECO event is difficult due to a weak magnetic polarity signal in several sites included in this study [see discussion in *Edgar et al.*, 2010]. The peak of the MECO spans the top of magnetochron C18r and the lower ~13% of the duration of magnetochron C18n.2n at Site 702 while at Site 1051 the lowest benthic foraminiferal (and bulk) $\delta^{18}O$ values occur within the lower ~20 % of magnetochron C18n.2n (See discussion in this thesis, **Chapter 2**). At sites where magnetostratigraphy is not available, precise correlation relies on low-resolution stable isotope data. At Site 1209 the pattern of lower resolution stable isotopes across the MECO is unique and therefore difficult to correlate. The age of multiple clay horizons in the uppermost part of Site 1260 is not well constrained and only the main horizon at the peak of the MECO is included in the CCD and lysocline interpretations. Uncertainties in the

paleodepth calculations for each site also exist due to uncertainties in subsidence rate and initial ridge depth parameters. However, these issues represent relatively small-scale refinements to age models or paleodepth calculations that do not significantly alter the main conclusions in this study.

3.4.4 Fine-scale dissolution decoupled from MECO warming?

Compiling records of carbonate accumulation from multiple sites across the MECO interval in detail and subsequent age correlations has revealed new finer-scale patterns in stable isotopic composition and carbonate dissolution that have not been focused on. Close inspection of sites in both the Atlantic (Sites 929, 523) and Pacific (Site 1209) reveal fine-scale decoupling between dissolution, $\delta^{18}O$, and $\delta^{13}C$ during both the warming and cooling phases of the MECO event. However, other sites (Site 1209, 1263, 1260) document patterns of multiple $\delta^{18}O$, and $\delta^{13}C$ excursions in tandem with dissolution that occur during or near the peak of the MECO. The uppermost dissolution horizon at Site 929 occurs without corresponding isotopic signals and within the MECO cooling phase. Similarly, the lower dissolution horizon at Site 523 occurs without corresponding isotopic signals and within the MECO warming phase. Reinterpretation of the benthic isotope record at Site 1209 [*Dawber and Tripati*, 2011a; b] (**Figure 3-3**) could reveal a similar pattern; in sediments from Hole 1209A the upper dissolution horizon occurs during the cooling phase of the MECO. However, Hole 1209B $\delta^{18}O$ records exhibit two warming phases, with each warming phase corresponding to a dissolution horizon. Similarly, records from Site 1263 exhibit multiple phases of dissolution and also two small excursions benthic foraminiferal $\delta^{18}O$ and $\delta^{13}C$ (~0.5 ‰) that occur during what was previously described as the single peak of the MECO [*Boscolo Galazzo et al.*, 2015] and correspond to small (<0.3 ‰) excursions in bulk sediment $\delta^{18}O$ and $\delta^{13}C$ [*Bohaty et al.*, 2009] and intervals of increased fragmentation (**Figure 3-4**). However, only the upper horizon (II) corresponds to a peak in magnetic susceptibility and decreased carbonate content at the peak of the MECO while horizon I is not correlative with strong signals in either. Site 1260 also exhibits up to six intervals of dissolution that correspond to excursions in benthic $\delta^{18}O$ and $\delta^{13}C$, however there is significant age model uncertainty in the interval.

Together, these new data seem to contradict each other and the majority of existing MECO records where warming and dissolution appear to occur in tandem [*Bohaty and Zachos*, 2003; *Bohaty et al.*, 2009; *Edgar et al.*, 2010]. Further, this contrasts markedly with the Eocene hyperthermal events (PETM, H1, H2, and smaller hyperthermals), which are characterized by strongly concomitant trends in deep-sea carbonate dissolution, rapid global warming, and negative $\delta^{13}C$ excursions [*Cramer et al.*, 2003; *Edgar et al.*, 2007; *Galeotti et al.*, 2010; *Kirtland Turner et al.*, 2014; *Sexton et al.*, 2011; *Stap et al.*, 2010]. Further detailed work (e.g. at Site 1209) is necessary to determine if either of these patterns is pervasive. However, the apparent lack of adherence of the MECO to the characteristics of other earlier hyperthermal events further distinguishes it from these events (i.e., it is not a 'hyperthermal' event) and emphasizes its uniqueness.

3.4.5 Implications for MECO mechanisms and climate

These new records have important implications on factors that may have contributed to the large magnitude and dynamic dissolution patterns observed across the MECO event. The carbon cycle modelling scenario in *Sluijs et al.* [2013] that best reproduced basic features of the MECO (elevated pCO_2 over 500 kyr, minor changes in carbonate $\delta^{13}C$, and long-lived CCD shoaling) requires long-term carbon flux imbalances and multiple ad hoc mechanisms (small sea-level rise causing constant weathering and an increase in carbonate shelf burial). These forcings are therefore plausible but largely untested with data from the geological record. A comprehensive hypothesis explaining the CCD reconstruction presented in this study will require new detailed modelling of physical and biogeochemical changes across the MECO, beyond the scope of this paper. Nevertheless, new clues identified in this study that may help to disentangle the mechanisms responsible for the MECO are: (1) dissolution occurs at depths much shallower than previously accounted for (~2000 m paleodepth), (2) dissolution occurs in multiple pulses superimposed on a single prolonged event, (3) similar dissolution patterns occur in both the Atlantic and Pacific, and (4) fine-scale details of warming, dissolution, and deep sea $\delta^{13}C$ are not strongly concomitant at all locations during the onset and recovery of the MECO.

The magnitude and duration of carbon release during a transient warming event controls dissolution, yet until now significant uncertainty remained over the magnitude of CCD/lysocline shoaling in the Atlantic, and the Pacific was only spatially constrained in deep waters (~3500 – 4000 m paleodepth). A coeval CCD/lysocline shoaling in the Atlantic and Pacific Oceans implies a global signal, and not only significantly increases the estimated amount of seafloor area undersaturated with respect to calcite, it has implications for the total amount of carbon released during the MECO. However, large swings in the Eocene CCD are not unexpected; the CCD was highly sensitive to carbon cycle perturbations in the Eocene because it was much shallower than any other time in the Cenozoic, and thus has a smaller carbonate buffering capacity [*Pälike et al.*, 2012]. Therefore, due to a smaller amount of erodible calcite (due to less seafloor area with decreasing depth) [see supplemental discussion in *Pälike et al.*, 2012], CCD shoaling from ~4000 m to ~2000 m paleodepth would allow for roughly ~3000 petagrams equivalent of $CaCO_3$ available for compensation for dissolution.

New data in this study reveals dissolution occurred as a single prolonged event superimposed with multiple pulses, suggesting that there are likely multiple carbon injections into the ocean–atmosphere system during the MECO. This finding does not discount a ~500 kyr total duration of dissolution and long-term increase in pCO_2, but does require additional shorter-term variation. In fact, in light of this new finding a re-examination of the alkenone-based pCO_2 record reveals notable variation: there are two smaller peaks that flank a single large peak in pCO_2 concentrations during the MECO [*Bijl et al.*, 2010]. Furthermore, the highest pCO_2 concentrations occur ~100 kyr before the highest $\delta^{18}O$ values recorded in Southern Ocean Records and it is the latest peak in pCO_2 that corresponds to the 'peak' MECO [*Sluijs et al.*, 2013], though there are large uncertainties in the age model for the atmospheric CO_2 record [*Bijl et al.*, 2010]. While there is only a single pCO_2 record with which to compare, the similarities between variation in the pCO_2 and CCD are compelling.

The MECO carbon cycle 'conundrum' described by *Sluijs et al.* [2013] refers to a discrepancy between the observations in proxy records of CCD shoaling and carbon cycle theory, because silicate rock weathering should

buffer the ocean on ~500 kyr timescales and lead to CCD deepening [*Berner et al.*, 1983; *Walker et al.*, 1981]. Modelling scenarios in *Sluijs et al.* [2013] aimed to reproduce a single long-lived CCD shoaling, however the new records show the CCD and perhaps (pCO_2) exhibits more dynamic changes than previously observed. Specifically, the CCD recovered almost completely in the Atlantic (and at least partially recovered in the Pacific) in the middle of MECO warming. This suggests shorter-term carbon injection (~100 kyr), with the interval between injections too short (<100 kyr) to accommodate CCD buffering from continental weathering.

These findings also have implications for the source of carbon injected into the system. The longer-term background carbon release must still be sourced from geological reservoirs rather than the exogenic carbon cycle (i.e. the carbon contained within the oceans and atmosphere, which change on shorter timescales) [*Sluijs et al.*, 2013] and has consistently been attributed to increased outgassing during volcanism [*Bohaty et al.*, 2009; *Sluijs et al.*, 2013], though there is no direct evidence for increased middle Eocene volcanism at this time. In contrast, the shorter-term pulses (<100 kyr) require a source from the global exogenic carbon pool. The absence of corresponding shifts in temperature and deep-sea $\delta^{13}C$ suggests carbon release during the dissolution horizon at the onset of the MECO (observed at Sites 929, 523, and 1209) and during the dissolution horizon in the cooling phase (observed at Site 929) is not related to organic matter burial or release (e.g. methane hydrate release). If increased isotope resolution confirms the early dissolution horizon at Site 1209 does indeed occur during MECO cooling then this suggests similar lysocline behaviour in the much shallower Pacific.

These pulses require a mechanism of carbon release that can be repeated on short timescales. Multiple orbitally paced carbon release events have been proposed to occur within the PETM [*Bowen et al.*, 2015; *Zeebe*, 2013], and ETM2 [e.g. *D'Haenens et al.*, 2014]. However, the hyperthermals are fundamentally different in both the timescales of carbon release (tens of kyr) and mechanism (due to the association with coeval changes in warming and $\delta^{13}C$ excursions). If the pulses of carbon during the MECO were orbitally related they would likely have the same relationship between temperature and dissolution [e.g. *Stap et al.*, 2010]. The pacing of the pulses during the MECO

are longer than the hyperthermal events but do fall within orbital timescales, with approximate durations that vary somewhat but generally occur over ~100 kyr (**Table 3-3**).

Ultimately, disentangling the mechanism responsible for injecting multiple pulses of carbon into the ocean–atmosphere system during the MECO will first require coherence in the pattern of warming and dissolution that occurred. It is increasingly evident that the pattern of cooling during the MECO event and post-MECO cooling interpreted at Southern Ocean sites (~300 kyr abrupt temperature decrease; [*Bohaty et al.*, 2009]) might not be globally representative.

3.4.6 Evidence for the global nature of CAE-3 and CAE-4?

Prior to the MECO at ~42 Ma, the CCD deepened in the equatorial Pacific Ocean resulting in CAE-3, one of the most prominent of the series of seven CAEs during the Eocene [*Lyle et al.*, 2005; *Pälike et al.*, 2012]; **Supplemental Figure 3-1**. The event is at least partly associated with a local increase in carbonate sedimentation and organic carbon burial [*Lyle et al.*, 2005; *Olivarez Lyle and Lyle*, 2005; 2006]. The nature of CAE events is not well understood (See discussion in this thesis, **Chapter 2**) and these features have not been observed outside of the equatorial Pacific due to a lack of high-resolution records from sites deeper than ~3500 m in the Indian and Atlantic Ocean. However, new records from Site 929 and preliminary data from Site U1404 [*Norris et al.*, 2014c] exhibit carbonate MAR events similar in both magnitude and duration to CAEs-3 and -4 but in the equatorial and Northwest Atlantic, respectively (**Figure 3-5**). Therefore, these records are the first high-resolution evidence that the CAEs in the Pacific are present elsewhere and suggest a global coherence in CCD fluctuations across CAE-3 and 4.

This finding has significant implications on the paleoceanography of the middle Eocene. The ability of different mechanisms to reproduce the Eocene CCD fluctuations across the CAEs was tested using the 3-D model of intermediate complexity GENIE [*Panchuk et al.*, 2008; *Ridgwell and Schmidt*, 2010] and geochemical box model LOSCAR [*Zeebe*, 2012] (see This Thesis, Chapter 2). One scenario that was considered but could not be ruled out because of a lack of data was that CCD modulation occurred via a repeated

switch in the dominant deep-water source between the Southern Ocean and North Pacific. This hypothesis would then lead to opposite CCD behaviour being recorded in the Atlantic and Pacific Ocean basins and the CAEs would be out of phase. This study indicates that both the Pacific and Atlantic Ocean basins responded to broad patterns of global changes in weathering and dissolution concurrently (at least across CAE-3 and 4). The data therefore supports the postulation by *Pälike et al.* [2012] that it is unlikely that the CAEs are due to circulation-induced changes between Southern Ocean and North Pacific dominated sources. The age model within the CAE-3 interval of Site 929 is well-constrained by orbital tuning between the C19r event and the MECO [*Westerhold and Röhl*, 2013], and, given conservative maximum error of ± 0.25 Myr it is not possible to shift carbonate MARs at Site 929 completely out of phase with records in the equatorial Pacific. To conclusively exclude this scenario, detailed records of $CaCO_3$ MAR with paired well-dated benthic foraminiferal $\delta^{18}O$ and $\delta^{13}C$ records are needed from the Atlantic spanning all seven CAEs. Never the less, this finding helps to narrow the possible competing hypothesis for the CAEs discussed by *Pälike et al.* [2012], with only solute flux changes via increased continental weathering and increased organic carbon burial from marine plankton assemblage changes as mechanisms capable of explaining the observed changes in both carbonate accumulation and benthic $\delta^{18}O$ and $\delta^{13}C$.

3.5 Summary and Conclusions

To investigate CCD and lysocline variation during the MECO event, detailed records of Atlantic and Pacific carbonate accumulation are assembled between ~39 and 41.5 Ma at multiple deep-sea sites. New stratigraphy at ODP Sites 929 and 1209 identify the MECO and reveal overall shoaling reaches ~2000 m paleodepths in both the Atlantic and Pacific. Furthermore, these records reveal multiple pulses of carbonate dissolution during the onset and cooling phase of the event for the first time. Identification of multiple dissolution horizons at Atlantic Site 523 and other sites (Site 1260, and 1263) validates these findings and suggests that these features are global in nature. Compilation of carbonate accumulation records from the Atlantic and Pacific provides a compelling new picture of rapid (>100 kyr) fluctuations in the CCD

and lysocline during the MECO that occur before, during, and after the event. These results highlight the complex history of changes in ocean temperature and carbonate chemistry during the MECO and indicate that there were multiple carbon injections superimposed on the longer-term ~500 kyr warming event. These results provide a compelling new perspective on the magnitude and duration of dissolution during the MECO, and support possible mechanisms for carbon release to those that can act on timescales shorter than ~100 kyr.

Fully understanding the cause of large transient dissolution pulses during the MECO is key to understanding deep ocean chemistry and climate during the Eocene and requires further modelling of the physical and biogeochemical changes across the interval. To do so, a more globally diverse set of proxy records generated with high resolution and better age control is needed. In particular higher resolution records of carbonate accumulation are needed in the shallow Pacific (to test the magnitude of CCD shoaling and whether the CCD is as dynamic as it appears), and intermediate depths (to fill the data gap between 2500 – 3000 in both the Pacific and Atlantic). There is also a need for additional detailed *p*CO2 and continental weathering data to interpret the suggestions of weathering and for accurate estimates of the mass of carbon input.

3.6 Supplemental Information

3.6.1 Age Model Formulation

The age model in this study (**Supplemental Figure 3-4** Age-depth model for ODP Site 929.) was created in several steps and is based on a combination of the age models found in [*Westerhold and Röhl*, 2013] and *Ogg* [2012] (GPTS 2012). First, refined biostratigraphic age datums and benthic foraminiferal stable isotope stratigraphy were used to identify the location of the MECO at Hole 929E and the general phases of warming and cooling. These phases were also identified in Fe and Ba XRF data and the following three ages from [*Westerhold and Röhl*, 2013] were used to inform the tie points in our correlation: the commencement of long-term MECO warming (~40.45 Ma), the peak MECO (40.05 ±0.02 Ma) and C19r event (41.508 ±0.02 Ma).

Next, a detailed orbital tuning was developed in the depth domain, beginning with sections with the clearest Ba-cyclicity. Thus, the starting point was the strong precessional cyclicity in Ba XRF data in the lower portion of Core 929E 13R (Section 929E 13R; **Supplemental Figure 3-3**). Four distinct Ba eccentricity cycles (~587 – 594 mbsf) in Core 929E 13R were thus constrained between the MECO and C19r event and it was possible to correlate Ba cycles with precession and eccentricity in the La2004 orbital solution [*Laskar et al.*, 2004]. It was then possible to extend tuning to Core 929E, 14R. Ba peaks are correlated to precession maxima in La2004, although it should be noted that there is uncertainty in whether Ba peaks correspond to maxima or minima, and therefore the estimated error in our ages in Cores 13R and 14R are of ±20 kyr. Uncertainty in the age determination of Cores 929E, 11R and 12R is higher. The MECO interval is very condensed with sedimentation rates decreasing to less than 0.5 cm/kyr. Significant uncertainty remains regarding the interpretation of XRF data in sediments post-MECO and Core 929E 11R is essentially 'floating' with no distinct age constraints above the HO of *O. beckmanni* at 578.67 mbsf (**Table 3-2**) and a turbidite at 570 mbsf (**Appendix Table 5-4**). Continuing the study further into the early Eocene would reduce age uncertainties in post-MECO sediments, however, for this interval we assume sedimentation rates are similar to the average pre-MECO rates in our study interval (~11 m/Ma).

3.6.2 Formulas used in calculations

The equations used to calculate linear sedimentation rates (LSR; cm kyr^{-1}), mass accumulation rates (MAR; g cm^{-2} kyr^{-1}), and calculate carbonate accumulation rates (CAR; g cm^{-2} kyr^{-1}) are as follows:

$$\textit{CaCO}_3\textit{-calibrated XRF Ca} = (-0.20009) + (0.00013243)*(\text{XRF Ca})$$

$$\textit{DBD-calibrated GRA} = (-0.14408) + (1.0499)*(\text{GRA})$$

$$\textit{MAR} = (\text{LSR})*(\text{DBD})$$

$$\textit{CAR} = (\text{MAR})*(\text{CaCO}_3\ /100)$$

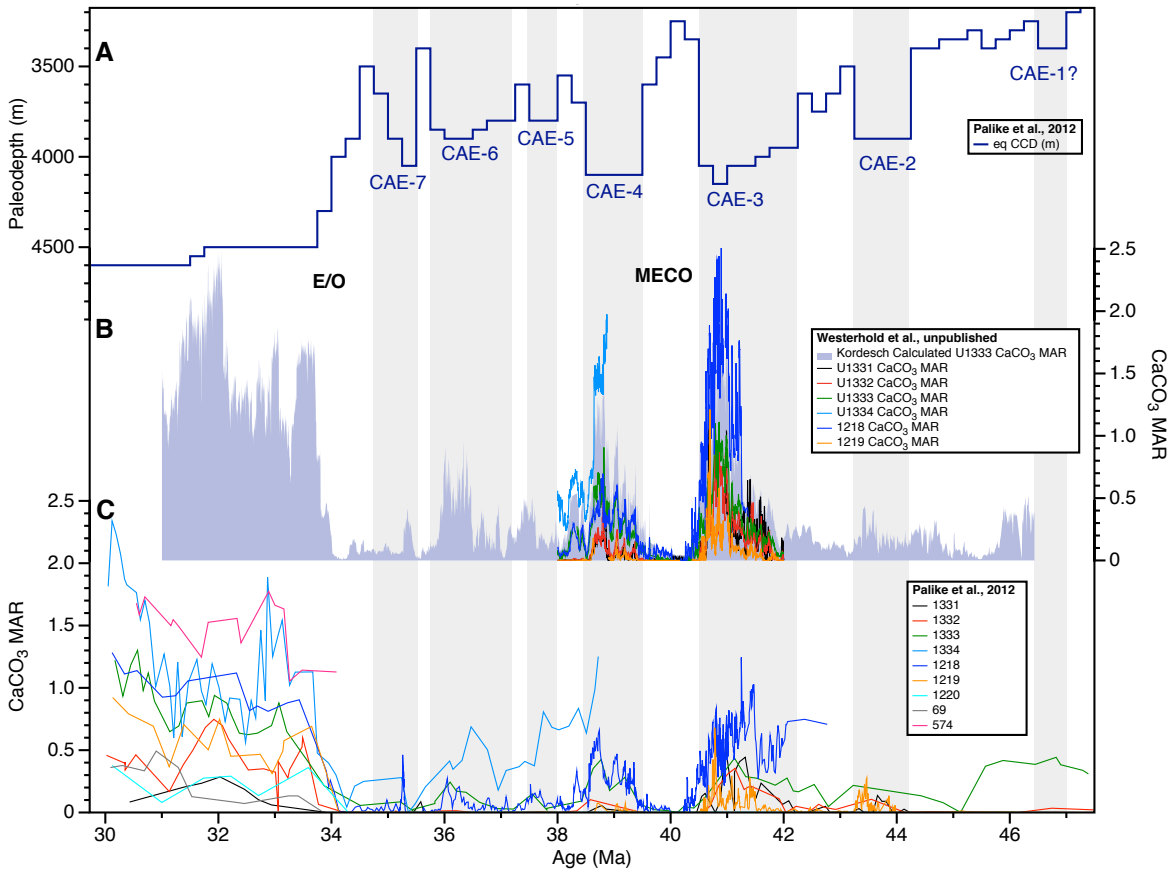

Supplemental Figure 3-1 CCD and carbonate accumulation rate history as a function of age from the Equatorial Pacific between ~30 and 46.5 Ma showing carbonate accumulation events (CAEs) 1-7.
(a) Equatorial Pacific CCD (blue line) calculated from a depth transect of sites from *Pälike et al.* [*2012*], (b) Carbonate accumulation rate (g/cm^2/kyr) calculated from calibrated $CaCO_3$ (lines; calibrated by coulometry on discrete samples) across CAE 3 and 4 [*Westerhold et al., unpublished; Westerhold et al., 2014*] and calibrated $CaCO_3$ from Site U1333 (shaded) across ~30 and 46.5 Ma calculated in this thesis from XRF Ca in *Westerhold et al.* [*2014*]. (c) Shipboard carbonate accumulation rate (g/cm^2/kyr) from *Pälike et al.* [*2010*]. Grey shaded bars show CAEs 1-7.

Supplemental Figure 3-2 Carbonate and density calibrations and results from carbonate accumulation rate calculation from ODP Site 929.
Calibration of (a) $CaCO_3$ (wt %) and XRF Ca (counts) for calibrated $CaCO_3$ and (b) calibration of dry bulk density (DD; g/cc) [*Curry et al., 1995*] and scanned gamma ray attenuation bulk density (GRA; g/cc) [*Curry et al., 1995*]. (c) Comparison of measured coulometry samples (red) and calibrated $CaCO_3$ (grey; calibrated by coulometry), and resulting carbonate accumulation record (CAR, $g/cm^2/kyr$; blue). Comparison of measured GRA (g/cc; red) calibrated dry bulk density (DBD; grey; calibrated by GRA), linear sedimentation rate (LSR; cm/kyr), and resulting mass accumulation rate record (MAR, $g/cm^2/kyr$; blue).

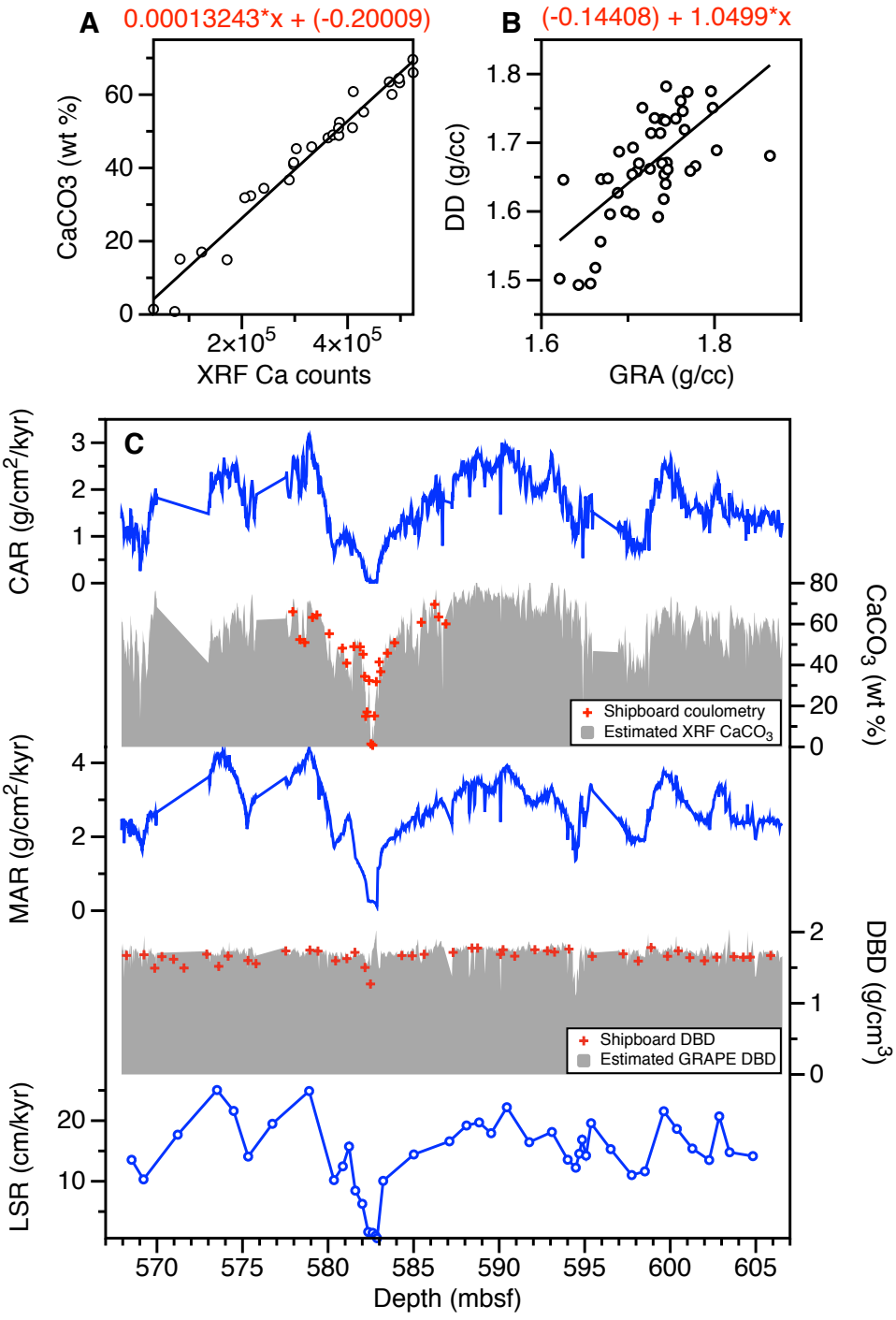
A
0.00013243*x + (-0.20009)
CaCO3 (wt %)
XRF Ca counts
B
(-0.14408) + 1.0499*x
DD (g/cc)
GRA (g/cc)
C
CAR (g/cm2/kyr)
Shipboard coulometry
Estimated XRF CaCO3
CaCO3 (wt %)
MAR (g/cm2/kyr)
Shipboard DBD
Estimated GRAPE DBD
DBD (g/cm3)
LSR (cm/kyr)
Depth (mbsf)

Supplemental Figure 3-3 Comparison of middle Eocene XRF datasets and filter outputs, and power spectra from ODP Site 929 used for orbital tuning.
XRF Ba (counts; purple lines) and filter outputs (grey lines) versus depth (metres below sea level; mbsf) and the results from MTM spectral analysis (power vs. frequency plots; panels below) with dominant cyclicity in depth [>99% confidence] labeled. Resulting age depth model tie points are shown (red). Data from turbidites (brown bars) and across the MECO excluded from spectral analyses. Filter frequencies are as labeled in bottom panels.

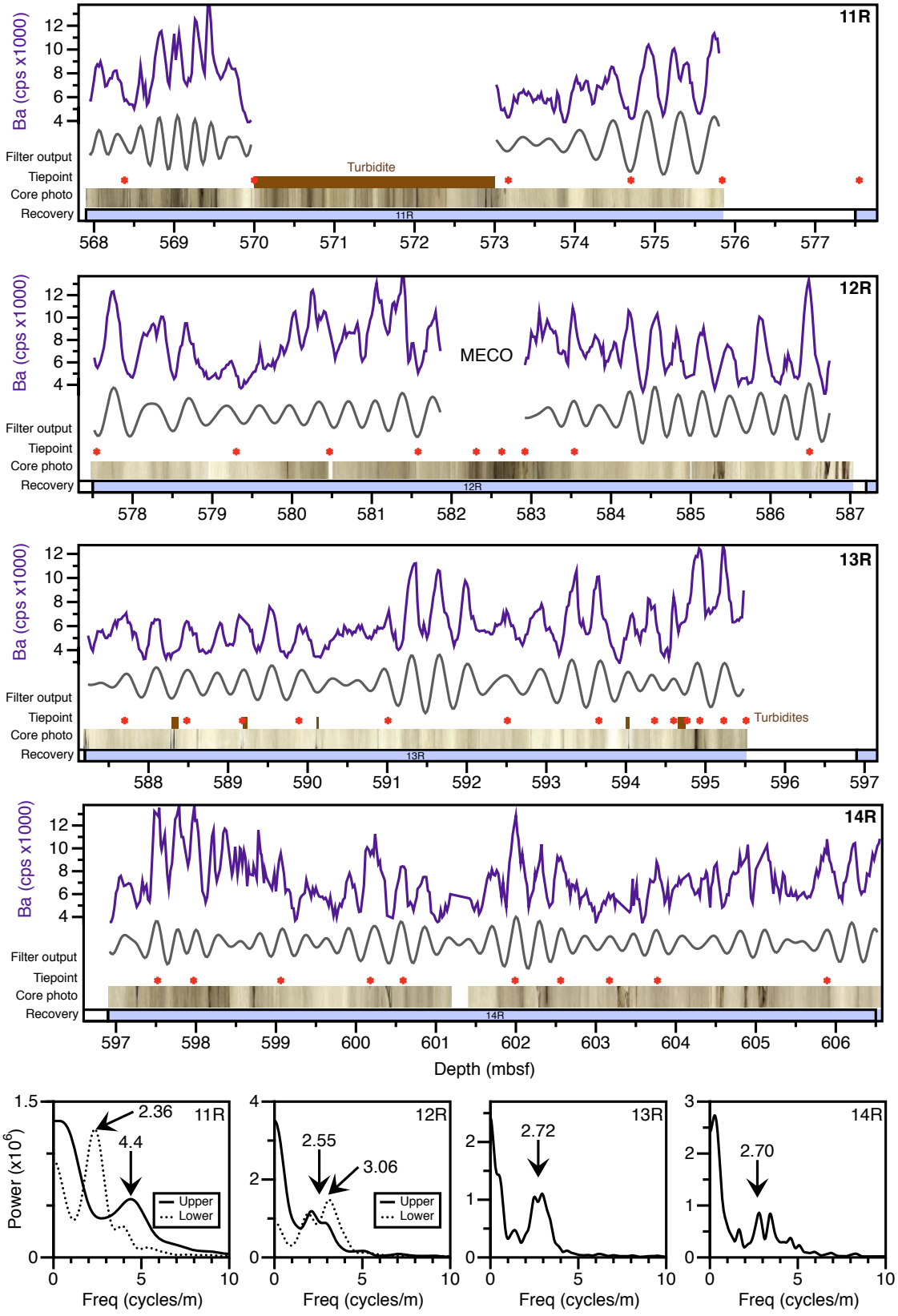
11R
12R
13R
14R
Ba (cps x1000)
Filter output
Tiepoint
Core photo
Recovery
Turbidite
MECO
Turbidites
Depth (mbsf)
Power (x10^6)
Freq (cycles/m)
Upper
Lower
2.36
4.4
2.55
3.06
2.72
2.70

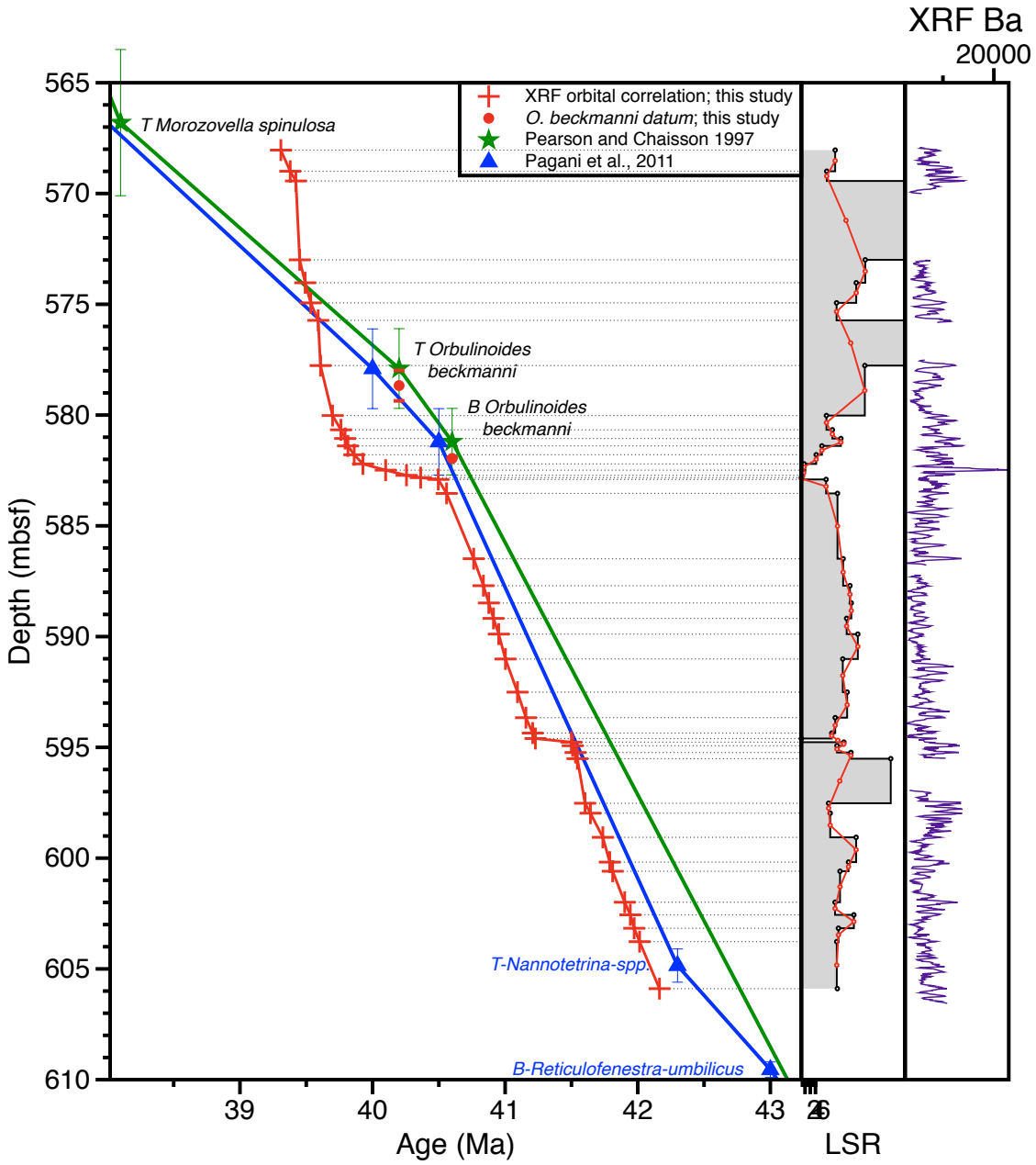

Supplemental Figure 3-4 Age-depth model for ODP Site 929.
Age-depth tie points generated in this study (red) from orbitally tuned precession-paced XRF Fe and Ba records show overall agreement with calcareous nannofossil and planktic biostratigraphic datums and age models from Pearson and Chaisson [*1997*] (green) and Pagani et al., [*2011*] (blue). Revised placement of the LO and HO of O. beckmanni generated in this study are shown (circles). Right panel shows resulting linear sedimentation rates (LSR) and raw XRF Ba data (purple). mbsf = metres below sea floor.

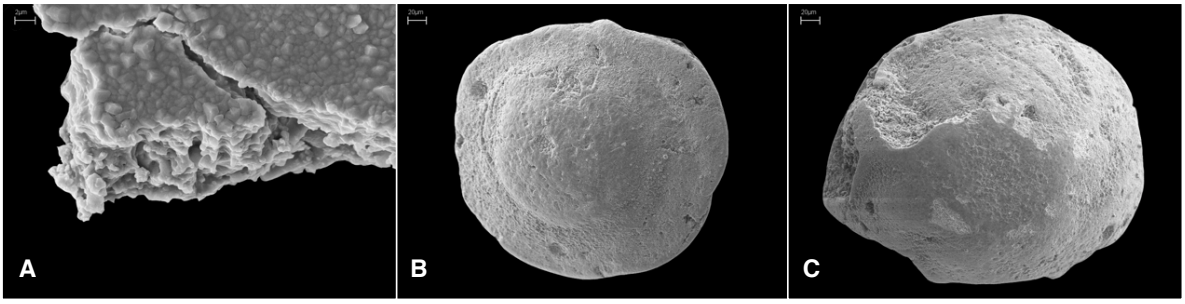

Supplemental Figure 3-5 Scanning electron micrograph images from ODP Site 929 of the recrystallized benthic foraminifera *Nuttallides truempyi.*
(a) Wall texture, (b) spiral, and (c) umbilical views. (Sample 929E-12R-4, 6-8cm)

Supplemental Figure 3-6 Paleoceanographic records versus depth across the late middle Eocene MECO interval for sites included in the CCD compilation. (a) ODP Site 523 bulk sediment $\delta^{18}O$ and carbonate content (wt %) from [*Bohaty et al., 2009*]. (b) IODP Site U1333 benthic foraminiferal $\delta^{18}O$ [*this thesis, Chapter 2*], calcareous nannofossil datums [*Toffanin et al., 2013*], XRF Fe [*Westerhold et al., 2014*], and $CaCO_3$ (wt %) from *Westerhold et al., 2014* (shaded) and this study (black line). (c) IODP Site U1408 $CaCO_3$ (wt %) [*Norris et al., 2014*].

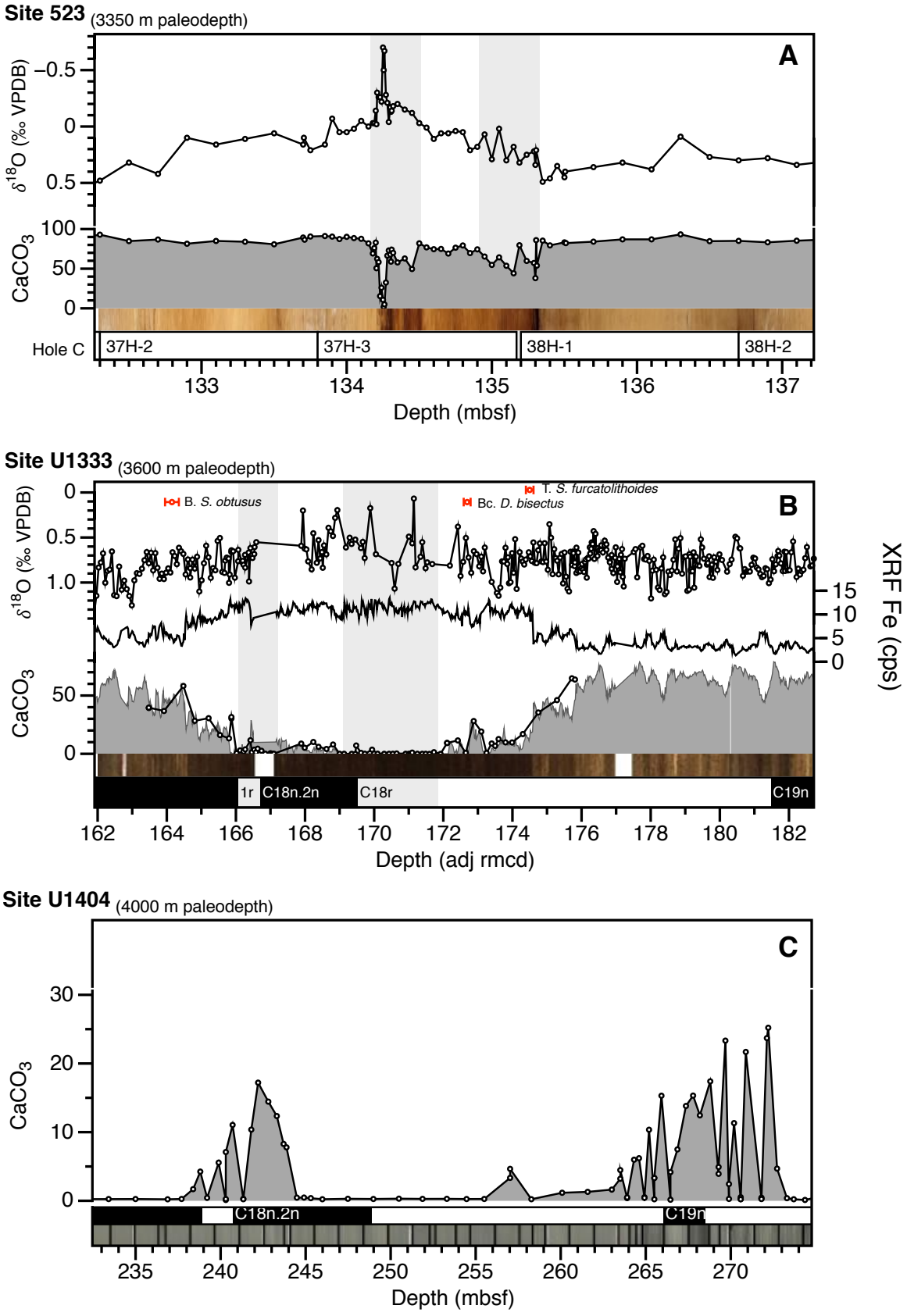
Site 523 (3350 m paleodepth)
A
δ18O (‰ VPDB)
−0.5
0
0.5
CaCO3
100
50
0
Hole C
37H-2
37H-3
38H-1
38H-2
133
134
135
136
137
Depth (mbsf)
Site U1333 (3600 m paleodepth)
B
B. S. obtusus
T. S. furcatolithoides
Bc. D. bisectus
δ18O (‰ VPDB)
0
0.5
1.0
CaCO3
50
0
XRF Fe (cps)
15
10
5
0
1r
C18n.2n
C18r
C19n
162
164
166
168
170
172
174
176
178
180
182
Depth (adj rmcd)
Site U1404 (4000 m paleodepth)
C
CaCO3
30
20
10
0
C18n.2n
C19n
235
240
245
250
255
260
265
270
Depth (mbsf)

Supplemental Figure 3-7 Carbonate and isotope stratigraphy across the MECO interval of ODP Site 1260.
Benthic foraminiferal and bulk sediment (a) $\delta^{18}O$ and $\delta^{13}C$ (‰) [*Edgar et al., 2007; 2010; Sexton et al., 2006*], (b) XRF Fe (cps) [*Westerhold et al., 2014*], and (c) carbonate content (wt %) [*this study*] plotted versus revised meters composite depth (rmcd). Lower panel shows core photo and magnetostratigraphy. Gray bars indicate dissolution horizons (intervals of low carbonate content and high magnetic susceptibility). The Top and Bottom of *O. beckmanni* [*Edgar et al., 2010*] are shown (red circles).

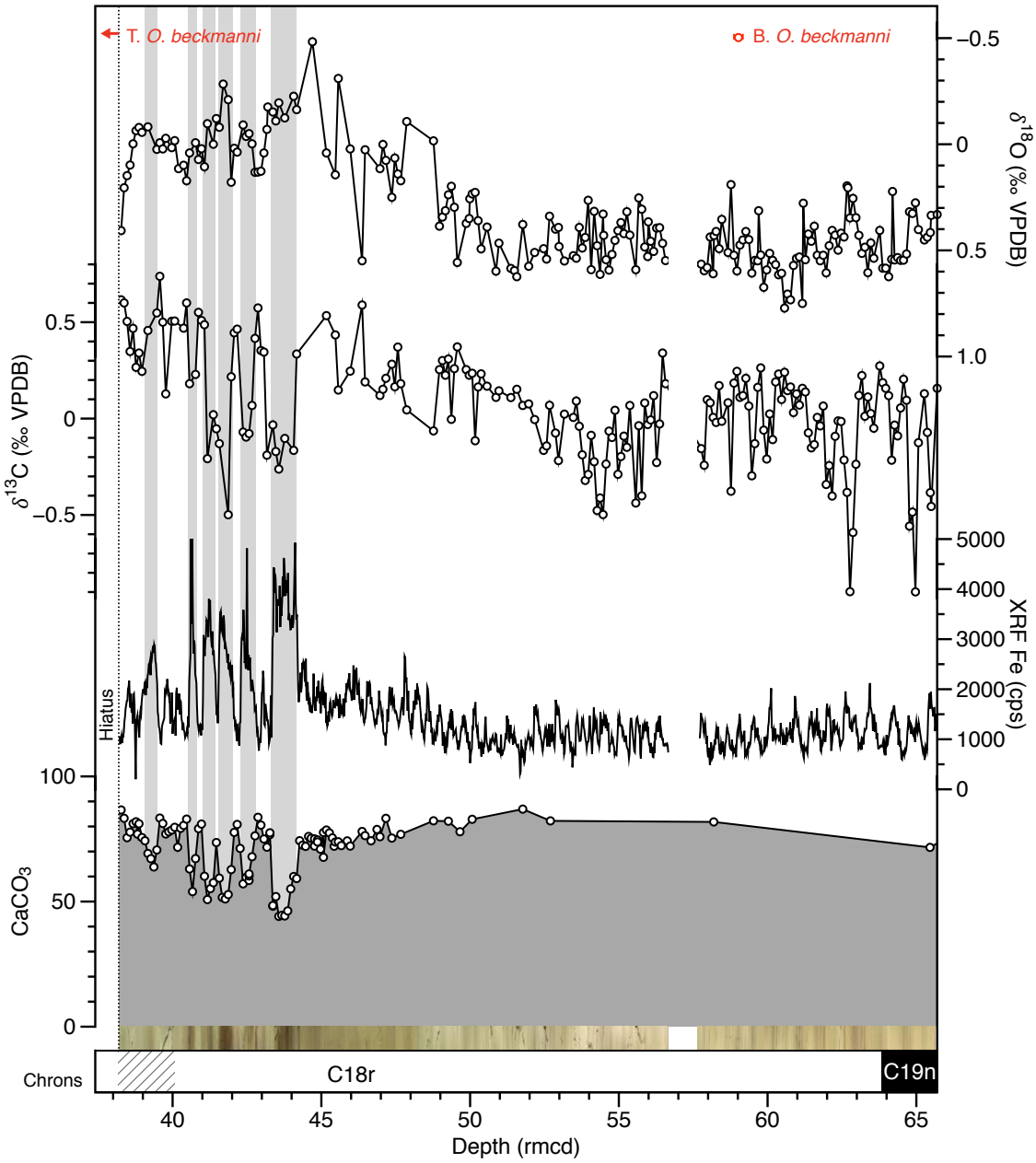
T. O. beckmanni
B. O. beckmanni
δ18O (‰ VPDB)
δ13C (‰ VPDB)
XRF Fe (cps)
CaCO3
Hiatus
Chrons
C18r
C19n
Depth (rmcd)

Supplemental Figure 3-8 Benthic foraminiferal stable isotopes, lysocline depth, and carbonate content reconstruction across the MECO

Benthic foraminiferal (a) $\delta^{18}O$ (‰) and (b) $\delta^{13}C$ (‰) from sites included in this study and Sites 738 and 748 in the Southern Ocean from *Bohaty et al.*, [2009], (c) lysocline as a function of paleo water depth from the Pacific (blue) and Atlantic (red) ocean basins, (d) Atlantic and (e) Pacific carbonate $CaCO_3$ (wt %) datasets across a depth transect of sites in the (c) Atlantic and (e) Pacific Basins. Dotted lines in lysocline records span unconstrained depths due to limited data. Shaded region marks MECO warming (light yellow) and peak-MECO CIE (darker yellow) as defined from sites Sites 738 and 748 in *Bohaty et al.* [*2009*]. Data sources are the same as in **Figure 3-5**.

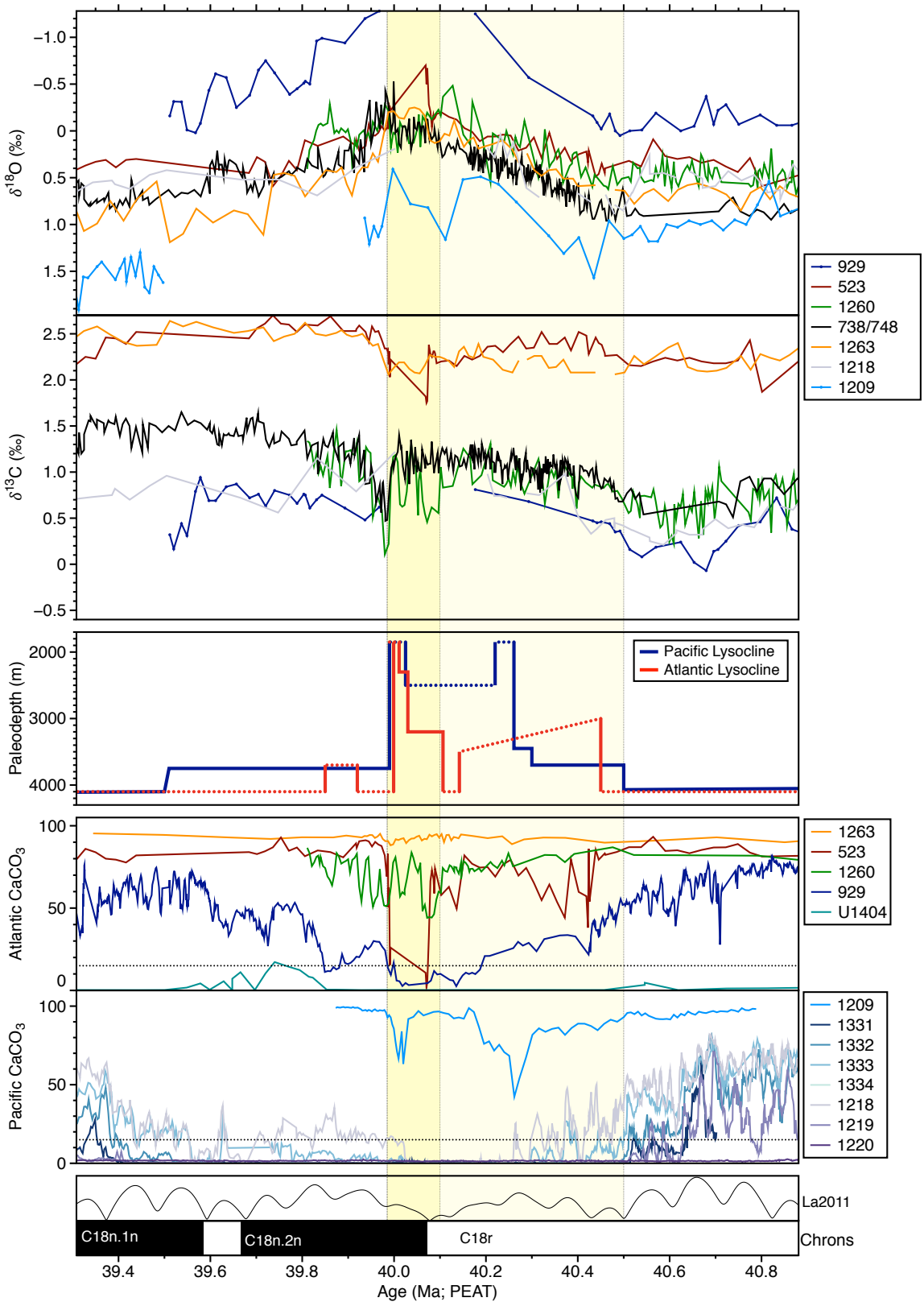
δ18O (‰)
−1.0
−0.5
0
0.5
1.0
1.5
929
523
1260
738/748
1263
1218
1209
δ13C (‰)
2.5
2.0
1.5
1.0
0.5
0
−0.5
Paleodepth (m)
2000
3000
4000
Pacific Lysocline
Atlantic Lysocline
Atlantic CaCO3
100
50
0
1263
523
1260
929
U1404
Pacific CaCO3
100
50
0
1209
1331
1332
1333
1334
1218
1219
1220
La2011
C18n.1n
C18n.2n
C18r
Chrons
39.4
39.6
39.8
40.0
40.2
40.4
40.6
40.8
Age (Ma; PEAT)

Chapter 4: Evidence for hyperthermals in the middle Eocene: the magnetochron C19r event

Contents

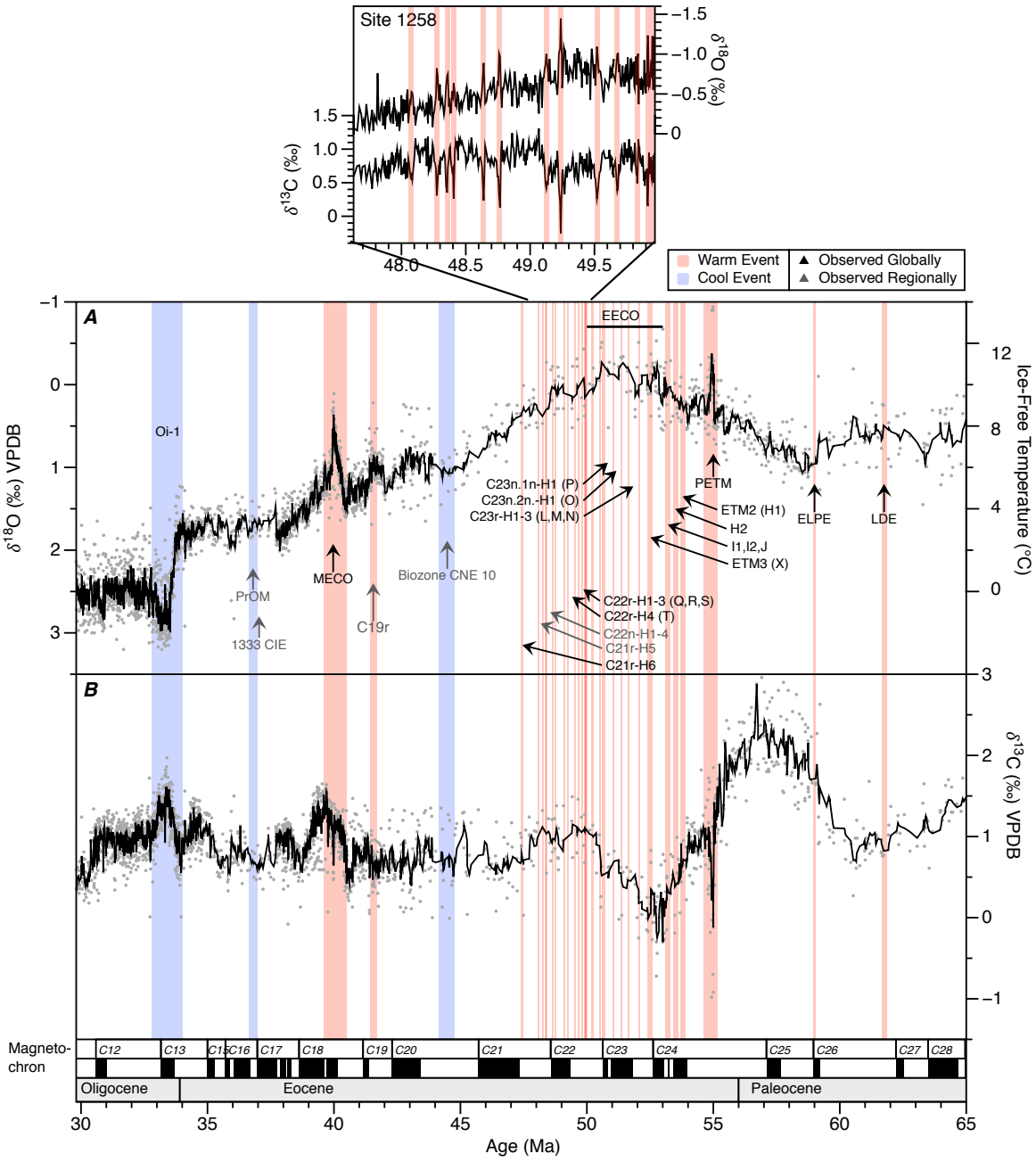

Figure 4-1 Long-term climatic context of transient events
Benthic oxygen stable isotope compilation data (A, $\delta^{18}O$ *and B,* $\delta^{13}C$*;* ‰) showing changes in global temperature and ice volume and carbon storage history in the Paleogene from Zachos et al., [2008]. Solid black line indicates a 5-point running mean. Coloured bars highlight intervals of warm or hyperthermal events (red) and cool (blue) climate events that have been observed globally (black arrows) and regionally (grey arrows). Events and acronyms described in detail in **Table 4-1**. Inset shows monospecific benthic stable isotope record from Site 1258 [*Sexton et al., 2011*].

4.1 Introduction

Ancient abrupt global warming events or 'hyperthermals' provide key opportunities to study the impact of the rapid release of carbon to the oceans and atmosphere on timescales of thousands to tens of thousands of years [e.g. *Dickens et al.*, 1995; *Zeebe and Zachos*, 2007]. As such, hyperthermals are the subject of much interest as partial analogues for anthropogenic climate change impacts and recoveries. The largest and most studied of the hyperthermals is the Paleocene Eocene Thermal Maximum (PETM; ~56 million years ago, Ma), which is associated with rapid global surface and deep ocean warming (5-7 ˚C), a negative Carbon Isotope Excursion (CIE; $\delta^{13}C$ ~ -3 ‰), and widespread deep-sea carbonate dissolution [*Kennett and Stott*, 1991; *Penman et al.*, 2014; *Sluijs et al.*, 2007; *E Thomas and Shackleton*, 1996; *Zachos et al.*, 2003; *Zachos et al.*, 2005]. Current best estimates suggest that carbon input during the onset of the event occurred within 5-20 thousands of years (kyrs) [*Cui et al.*, 2011; *McInerney and Wing*, 2011; *Zeebe et al.*, 2016; Kirtland-Turner and Ridgewell, 2016] with a slow recovery to background values resulting in a total PETM duration of <200 kyrs [*Röhl and Abrams*, 2000; *Röhl et al.*, 2007]. The event also profoundly impacted biotic assemblages on land and in the oceans [*McInerney and Wing*, 2011; *Speijer et al.*, 2012], and resulted in the largest Cenozoic extinction of deep-sea benthic foraminifera in the last ~90 Ma [*E Thomas*, 2006; 2007].

Recent work has revealed a large number of additional transient (<250 kyr duration) so-called 'hyperthermal' events in the Paleocene and early Eocene [*Bohaty and Zachos*, 2003; *Edgar et al.*, 2007; *Kirtland Turner et al.*, 2014; *Lourens et al.*, 2005; *Scher et al.*, 2014; *Sexton et al.*, 2011; *Zachos et al.*, 2001a] (**Figure 4-1**; **Table 4-1**). More than 10 events are now reported from the warmest interval of the Paleogene – the Early Eocene Climatic Optimum (EECO; ~53-51 Ma), predominantly from marine records. These events are smaller in magnitude than the PETM but with some similarities: negative shifts in $\delta^{18}O$ (<1 ‰), and dissolution of marine carbonates coupled with negative $\delta^{13}C$

excursions (<1 ‰) [*Cramer et al.*, 2003; *Kirtland Turner et al.*, 2014; *Leon-Rodriguez and Dickens*, 2010; *Littler et al.*, 2014; *Lourens et al.*, 2005; *Sexton et al.*, 2011; *E Thomas and Zachos*, 2000], that imply a common cause– release of isotopically light carbon to the ocean-atmosphere system, causing ocean acidification and warming [*Hönisch et al.*, 2012 and references therein].

The initial discovery of a sequence of events between ~56 and 52 Ma (i.e. PETM, ETM2 and ETM3) suggested that hyperthermals are semi-regularly paced, becoming smaller in size and more closely-spaced through time. These precise patterns of hyperthermal occurrence on orbital timescales eventually lead to the suggestion that these events were driven by a carbon cycle response to a thermal threshold. This conceptual model predicts that carbon release is first initiated through temperature maxima from orbitally paced high-amplitude variations in insolation (specifically through eccentricity forcing) [*Galeotti et al.*, 2010; *Lauretano et al.*, 2015; *Lourens et al.*, 2005; *Lunt et al.*, 2011; *Cramer et al.*, 2003; *Westerhold et al.*, 2009; *Westerhold et al.*, 2007; *Zachos et al.*, 2010; DeConto et al., 2012]. These forcings then drive the climate system past some critical threshold that triggers carbon release, such as seasonality changes that lead to changes in overturning circulation and intermediate water warming that result in methane hydrate release [*Lunt et al.*, 2011]. Critically, the thermodynamic threshold model can account for increasing hyperthermal frequency with progressive background warming and eventual cessation due to depletion of the carbon reservoir during peak EECO warmth (when the highest atmospheric carbon dioxide concentrations (pCO_2) and temperatures over the Cenozoic occurred **Figure 4-1**; [*Anagnostou et al.*, 2016; *Greenwood and Wing*, 1995; *Pearson and Palmer*, 2000; *Pearson et al.*, 2001; *Zachos et al.*, 2001a; *Zhang et al.*, 2013]). Proposed carbon sources for the 'early' hyperthermals include marine gas hydrates [*Dickens*, 2011; *Dickens et al.*, 1995], terrestrial peat deposits [*Kurtz et al.*, 2003], and Antarctic permafrost [*DeConto et al.*, 2012]. More recent work, however, points to the existence of many more small hyperthermals throughout the Early and early Middle Eocene suggestive of the operation of a different mechanism involving a more mobile ocean carbon source [*Kirtland Turner et al.*, 2014; *Sexton et al.*, 2011].

Table 4-1 Comparison of key features characterizing transient events in the Paleogene

Event type	*Δ $\delta^{18}O$*	*Δ $\delta^{13}C$*	*Age (Ma)*	*Event duration (kyr)*	*Δ CaCO3 (wt %)*	*Δ CCD*	*Citation*	*Location Observed*
Late Danian Event (LDE; C2)	-	-	61.75	~200	Dissolution	Shoaling	Bornemann et al., 2009; Sprong et al., 2011, 2012; Westerhold et al., 2011	Global
Early Late Paleocene Event (ELPE) Mid Paleocene Biotic Event (MPBE)	-	-	59	50			Petrizzo 2005; Bernaola et al., 2007; Dinares-Turell et al., 2007; Littler et al., 2014	Global
Paleocene-Eocene Thermal Maximum (PETM, or ETM1)	-	-	56	<100	Dissolution	Shoaling	Kennett and Stott, 1991; Thomas and Shackleton, 1996; Zachos et al., 3003, 2005	Global
Eocene Thermal Maximum-2 (ETM2, ELMO, H1, or C24r-H8)	-	-	53.7	<100	Dissolution	Shoaling	Laurens et al., 2005; Sluijs et al., 2009; Galeotti et al., 2010; Leon-Rodriguez and Dickens, 2010; Stap et al., 2009, 2010	Global
C24r-H8 (H2)	-	-	53.6	<100	Dissolution	Shoaling	Cramer et al., 2003; Stap et al., 2009, 2010	Global
C24n.3n-H1,2 (I1, I2)	-	-	53.2	<100	Dissolution	Shoaling	Cramer et al., 2003; Leon-Rodriguez and Dickens, 2010	Global
J	-	-	52.86	<100	Dissolution	Shoaling	Lauretano, et al., 2016	South Atlantic
Eocene Thermal Maximum-3 (ETM3, or X, K, or C24n.1n-H1)	-	-	52.5	<100	Dissolution	Shoaling	Cramer et al., 2003; Rohl et al., 2005; Agnini et al., 2009; Galeotti et al., 2010; Leon-Rodriguez and Dickens, 2010	Global
C23r-H1-3 (L, M, N) C23n.2n.-H1 (O) C23n.1n-H1 (P) C22r-H1-3 (Q, R, S) C22r-H4 (T)	-	-	51.8 to 50	40	Dissolution	Shoaling	Kirtland et al., 2014; Lauretano, et al., 2016; Sexton et al., 2011	Likely Global
U, V, W	-	-	50.3 to 49.9	<100	Dissolution	Shoaling	Lauretano, et al., 2016	South Atlantic
C22n-H1-4 C21r-H1-5	-	-	49.7 to 48.2	40	Dissolution	Shoaling	Sexton et al., 2011	Likely Global
C21R-H6	-	-	47.44	40	Dissolution	Shoaling	Sexton et al., 2011; Payros et al., 2012	Likely Global
Biozone CNE10 event	+	+	~44.7	<500	Dissolution	Shoaling	This Thesis, Chapter 2	Equatorial Pacific
Magnetochron C19r Event	-	-	41.5	~100	Dissolution	Shoaling	Edgar et al., 2007; Westerhold et al., 2014; This study	Global
Magnetochron C19r-H2 Event	-	-	~41.4	~100	Dissolution	Shoaling	This Study	Global
Middle Eocene Climatic Optimum (MECO)	-	small -	40.5 to 40	500	Dissolution	Shoaling	Bohaty and Zachos 2003; Bohaty et al., 2009; Edgar et al., 2010	Global
Site U1333 CIE	-	-	37	~200	Dissolution	Shoaling	This Thesis, Chapter 2	Equatorial Pacific
Priabonian Oxygen Isotope Maximum Event (PrOM)	+	?	~37	~140	Presumed accumulation	Presumed deepening	Scher et al., 2014	Southern Ocean
Eocene Oligocene Transition (Oi-1)	+	+	34	~400	Accumulation	Deepening	Coxall and Wilson, 2011; Coxall et al., 2005; Kennett and Stott, 1991; Shackleton and Kennett, 1975; Zachos et al., 1996, 2001	Global

Though hyperthermals have now been shown to occur from ~57 to 47 Ma [*Kirtland Turner et al.*, 2014; *Sexton et al.*, 2011] (**Figure 4-1**), and it has been shown that the general pattern of paired negative $\delta^{18}O$ and $\delta^{13}C$ excursions persists for much longer [*Kirtland Turner*, 2014], there have been few studies focused on potential hyperthermal occurrence during the middle Eocene (47.8 – 38 Ma). Notably, global warming occurred during the Middle Eocene Climatic Optimum (MECO) event at ~40 Ma [*Bohaty and Zachos*, 2003; *Bohaty et al.*, 2009] which is sometimes referred to as a hyperthermal event. However, the MECO is distinct from the earlier hyperthermals in that warming occurs gradually over ~500 kyrs and ends abruptly, it lacks pronounced coupled $\delta^{18}O$ and $\delta^{13}C$ excursions, and thus, was likely caused by a different mechanism [*Bohaty and Zachos*, 2003; *Bohaty et al.*, 2009] and will not be discussed here. As of now, the only contending event is the magnetochron C19r event occurring at 41.50 Ma [*Edgar et al.*, 2007], more than six million years after the last known hyperthermal event (**Figure 4-1**). This event is characterized by pronounced stable isotope excursions in both benthic and planktic foraminiferal records (> -0.4 ‰ in $\delta^{18}O$ and > -1.2 ‰ in $\delta^{13}C$) and a larger magnitude shift in bulk isotopes (~ -1.8 ‰ in $\delta^{18}O$ and ~ -1.1‰ in $\delta^{13}C$) for ~100 kyr [*Edgar et al.*, 2007; *Westerhold and Röhl*, 2013]. The peaks of the isotopic excursions also coincide with a highly dissolved foraminiferal assemblage, a ~40 wt % drop in carbonate content, and a well-developed red clay layer that is interpreted as a shoaling of the Carbonate Compensation Depth shallower than 2500 m (CCD; the oceanic depth where the downward flux of carbonate rain delivered from calcifying organisms is balanced by dissolution) [*Edgar et al.*, 2007]. While the loss of foraminiferal carbonate across the event prevents detection of the true magnitude of the isotopic excursion in benthic and planktic foraminiferal records, bulk isotopes suggest a considerable perturbation to the local carbon and climate cycle [*Edgar et al.*, 2007]. If accurate, the bulk record implies tropical surface water warming of up to ~8 ˚C (assuming no salinity influence on $\delta^{8}O$ values) within ~100 kyr. The C19r event has been correlated to an exceptionally strong insolation peak (~573 W/m^2 at 41.520 Ma in boreal summer at 65 ˚N, the highest insolation value of the last ~45 Ma [*Laskar et al.*, 2004]) [*Westerhold and Röhl*, 2013], however caution is warranted because considerable uncertainty remains in the short-term (obliquity/ precession) components of the orbital solutions this far

back in time, primarily due to the effects of tidal dissipation and dynamical ellipticity [*Laskar et al.*, 2011a; *Laskar et al.*, 2004]. Furthermore, the C19r event has so far only been described from Ocean Drilling Program (ODP) Site 1260 in the equatorial Atlantic (**Figure 4-2**) even though stable isotopes records spanning the latter part of magnetochron C19r exist from two sites in the Pacific (ODP Site 1218 [*Lear et al.*, 2004; *Tripati et al.*, 2005] and ODP Site 1209 on Shatsky Rise [Dawber and Tripati, 2011a; b]; **Figure 4-2**). Neither of these the records show evidence of the event, most likely due to low sedimentation rates and gaps in core recovery [*Bralower et al.*, 2003; *Edgar et al.*, 2007; *Lyle et al.*, 2002a]. The similarities in character and orbital timing of the C19r event to the late Paleogene and early Eocene hyperthermals is compelling, however the event occurs >6 Myr after the other reported hyperthermals, lacks complete foraminiferal records, and is only observed at a single locality. Thus, the status of the C19r event as a hyperthermal remains uncertain.

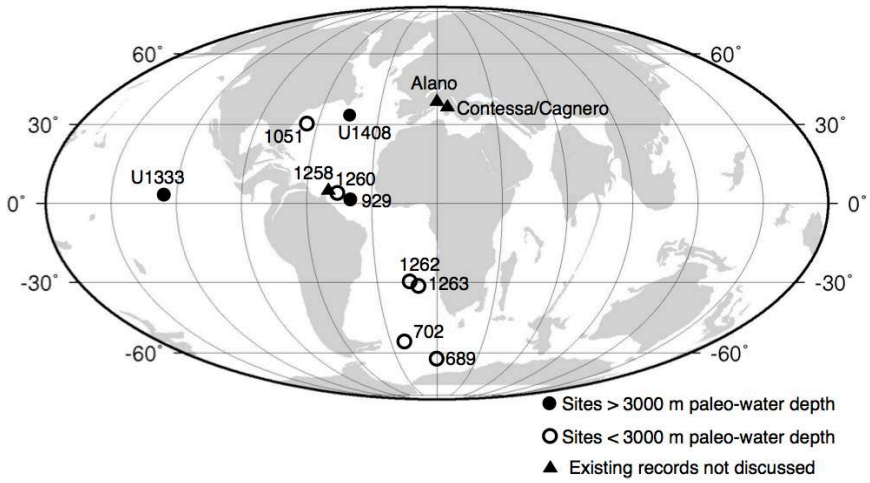

Figure 4-2 DSDP, ODP and IODP site location map of middle Eocene sections included in this study.
Approximate positions on ~40 Ma paleogeography from [*Hay et al.*, 1999; *ODSN*, 2011] showing drillsites with core records spanning the C19r Event as discussed in this study. Solid circles are deep water sites (paleodepth >3000 m) and unfilled circles are shallow (paleodepth <3000 m).

Here, new records of bulk sediment and benthic foraminiferal oxygen and carbon stable isotope records ($\delta^{18}O$ and $\delta^{13}C$) and X-ray fluorescence (XRF) core scans are presented spanning the later half of magnetochron C19r from multiple deep-sea sites in the Atlantic (ODP Sites 702 and 929) and Pacific

basins (ODP Site U1333) (**Figure 4-2**). These data are combined with published data sets to assess the reproducibility of the C19r event as described by *Edgar et al.* [2007]

4.2 Materials and Methods

4.2.1 Site Selection

ODP Site 702 is located on the central Islas Orcadas Rise in the South Atlantic (**Figure 1-2**; 50˚56.786'S, 26˚22.117'W; 3083 meters below sea level, mbsl). Drilling difficulties at this site resulted in only one hole (Hole 702B) through sediments of middle Eocene age [*Ciesielski and Kristoffersen*, 1988], however recovery was relatively stratigraphically complete. The site has a well-resolved magnetostratigraphy [*Ciesielski and Kristoffersen*, 1988; *Clement and Hailwood*, 1991] which indicates that magnetochron C19r is present. Published bulk sediment carbon isotopes indicate a small negative excursion towards the top of magnetochron C19r (**Figure 4-4**; [*Bohaty et al.*, 2009]). Here I present new data focused on the middle Eocene interval of Hole 702B from 88.36 to 94.26 metres below sea floor (mbsf) (Cores Hole 702B-10X through Hole 702B-11X) with an average sample spacing of ~10 cm (1 sample per ~10 kyr). The age model for this site follows *Bohaty et al.* [2009] and is based on magnetostratigraphy from [*Ciesielski and Kristoffersen*, 1988; *Clement and Hailwood*, 1991].

ODP Site 929 (5˚58.568'N, 43˚44.402'W, 4356 m modern water depth; [*Curry et al.*, 1995]) is the deepest end-member of a suite of sites drilled on Ceara Rise, in the equatorial Atlantic (**Figure 4-2**) and contains a sediment sequence spanning early Eocene through Oligocene age [*Curry et al.*, 1995]. Ceara Rise sediments have been used extensively for Neogene and Paleogene research [e.g. *Pagani et al.*, 2011; *Pälike et al.*, 2006] but no studies to date have focused on the middle Eocene, and neither the MECO or C19r event have been previously documented. Here I target a narrow upper middle Eocene interval of Hole 929E in the bottom of Core 929E-13R (594.72 – 595.48 mbsf, with an average sample spacing of ~2 cm), which is composed predominantly of nannofossil chalk with moderately preserved 'frosty' benthic foraminifers [*Pearson and Chaisson*, 1997; sensu *Sexton et al.*, 2006b]. A new age model

for this site was developed between 567.92 and 606.55 mbsf using biostratigraphy as the basis for an orbitally tuned age model [This thesis, Chapter 3].

4.2.2 Carbon and oxygen isotope analysis of bulk sediment and benthic foraminifera

Sediment samples were dried in an oven at 50 ºC and the dry bulk weight recorded. Samples were then disaggregated in a solution of deionized water and sodium hexametaphosphate overnight, and then washed over a 63-μm size mesh sieve and oven-dried. Coarse fraction (wt %) data are calculated for each sample by dividing the amount of bulk sediment sample (in grams) in the >63 μm size fraction after sediment washing by the total initial dry bulk sediment weight (in grams) and then multiplied by 100. Bulk sediment samples were homogenized by grinding using mortar and pestle. All sample preparation was carried out at the University of Southampton National Oceanography Centre, UK, except for samples from Site 929, which were prepared by Thomas Westerhold at the MARUM University of Bremen.

In total, 58 samples from Site 702 were taken at 10 cm spacing between 88.36 and 91.57 mbsf (~9 kyrs). Between eight to twelve specimens of the epifaunal benthic foraminifer *Nuttallides truempyi* were picked from the 180-250 μm sieve size fractions for isotopic ($\delta^{18}O$ and $\delta^{13}C$) analysis. From Site 929, 42 samples at 2 cm spacing (~ 20 kyrs) were analysed for stable isotopes from bulk sediment.

All stable isotope samples were measured on a Finnigan MAT 253 gas isotope ratio mass spectrometer connected to a Kiel IV automated carbonate preparation device at the Zentrum für Marine Tropenökologie ZMT at the University of Bremen and are calibrated to in-house standard (Solnhofen limestone). Analytical precision based on replicates of Solnhofen limestone (1σ) was ±0.08 ‰ for $\delta^{18}O$ and ±0.02 ‰ for $\delta^{13}C$. All results are standardized relative to the Vienna Pee Dee Belemnite (VPDB) standard after calibration to the reference material NBS 19. Benthic foraminiferal stable isotope values were corrected for isotopic disequilibrium with seawater as follows: benthic $\delta^{18}O$ of *N. truempyi* were adjusted to *Cibicidoides* values ($\delta^{18}O_{Cib} = (\delta^{18}O_{Nutt} + 0.10)/0.89$ [*Katz et al.*, 2003]) and converted to temperature using *Kim and O'Neil* [1997]

as modified by *Bemis et al.* [1998] and using an ice-free $\delta^{18}O_{sw}$ of -1.2 ‰ (VPDB). Benthic $\delta^{13}C$ values were adjusted to *Cibicidoides* values ($\delta^{13}C_{Cib} = \delta^{13}C_{Nutt} + 0.34$ [*Katz et al.*, 2003]).

4.3 Results

4.3.1 Stratigraphic markers for the Magnetochron C19r Event

In order to locate and compare the fine details of isotopic and physical property records between sites, it is necessary to first define the relative position of the magnetochron C19r event in terms of bio- and magnetostratigraphy. A well-resolved magnetostratigraphy (± 10 cm) in the middle Eocene interval of ODP Site 1260 clearly shows that the excursion occurs within magnetochron C19r [*Edgar et al.*, 2007; *Suganuma and Ogg*, 2006]. A recently developed cyclostratigraphy confirms that this interpretation is robust [*Westerhold and Röhl*, 2013], though the top of the section at this site has since undergone several age model iterations because of ambiguity over the location of the C18r/C18n magnetochron boundary and lack of biostratigraphic constraints [*Edgar et al.*, 2007; *Edgar et al.*, 2010; *Westerhold and Röhl*, 2013]. The C19r event occurs ~72 % through magnetochron C19r at Site 1260 (**Figure 4-3**). This provides a rough estimate for the location of the C19r event, though it does not account for variable sedimentation rates within the chron.

The C19r event falls in the middle of planktic foraminiferal and calcareous nannofossil biozones E11/P12 (E11 defined as the *Morozovella lehneri* partial range zone between the last appearance of *Guembilitrioides nuttalli* at ~42.3 Ma and the first appearance of *Orbulinoides beckmanni* at ~40.5 Ma) and calcareous nannofossil zones NP16/CNE14 (between the last appearances of *Cribrocentrum reticulatum* at ~42.37 Ma and *Dictyococcites bisectus* at ~40.34 Ma) [*Agnini et al.*, 2014; *Berggren*, 1995; *Berggren and Pearson*, 2005; *Martini*, 1971]). Unfortunately these biozones are particularly long (>2 Myr) and sparse in secondary biostratigraphic tie-points so while biozones are useful as confirmation of relative ages, magnetostratigraphy is used in this study to determine the age of the C19r event and as markers for

the event elsewhere [*Agnini et al.*, 2014; *Wade et al.*, 2011; *Westerhold and Röhl*, 2013].

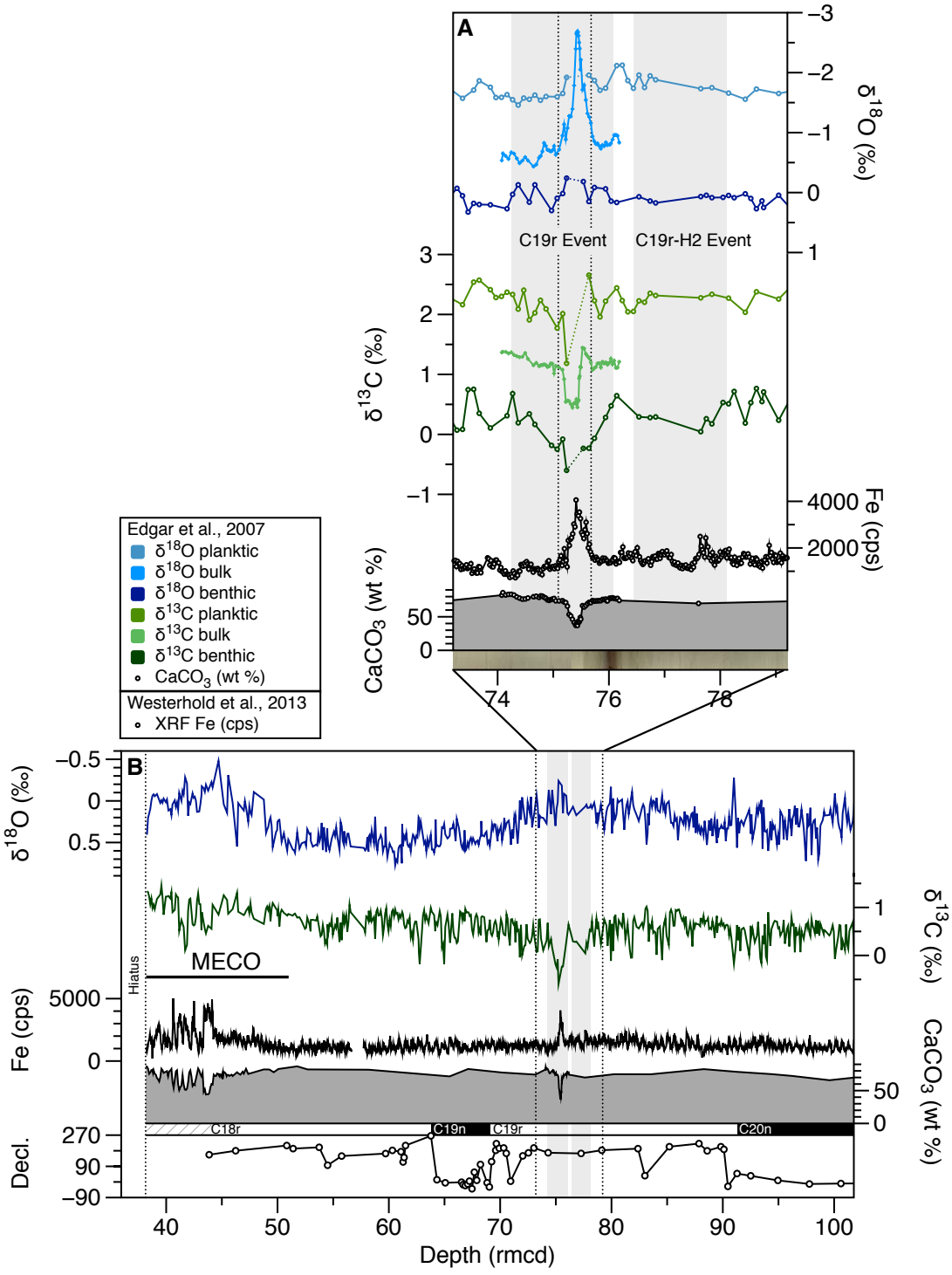

Figure 4-3 ODP Site 1260 carbonate and isotope stratigraphy across the study and MECO.
Benthic foraminiferal $\delta^{18}O$ and $\delta^{13}C$ (‰) from (A) the study interval and (B) the site with XRF FE [*Westerhold et al., 2013*], carbonate content (wt %) from *Erbacher et al.* [2007] and this study (MECO interval). Magnetostratigraphy

from *Suganuma and Ogg* [2006] and *Edgar et al.* [2007]. Grey shaded bars mark C19r and C19r-H2 events. Dotted lines in (A) marks the C19r excursion in bulk sediment $\delta^{18}O$ and $\delta^{13}C$.

4.3.2 Age Models

Age models across the magnetochron C19r interval were compiled and constructed for all drillcores in this study. As some of these sediment sections have not been heavily studied, we utilize all available magnetostratigraphic and biostratigraphic data. The large peak in XRF Fe at ~594.9 mbsf provided the first line of evidence for an excursion at Site 929 and prompted the rest of the investigations in this study. Through close inspection of cyclicity in XRF Ba records by orbital tuning, the C19r event was identified by cycle counting backwards from the MECO event and found to be in line with the pronounced eccentricity peak at 41.52 Ma, precisely when the C19r event occurs in sediments at Site 1260 [Westerhold and Röhl, 2013]; see detailed Site 929 age model formulation in Chapter]. Orbitally tuned XRF data from Site 929 [This thesis, Chapter 3], Site 1260 [Westerhold and Röhl, 2013], and Site U1333 [Westerhold et al., 2014] provide the most detailed age models in this study while reliable magnetostratigraphic records are available from Site 702 [Ciesielski and Kristoffersen, 1988; Clement and Hailwood, 1991]. The higher-resolution magnetostratigraphy at Site 702 [Clement and Hailwood, 1991] confirms the position of the C19r event, where the benthic $\delta^{13}C$ excursion occurs ~71 % through magnetochron C19r (**Figure 4-4**), in close agreement with the event at Site 1260 (72%; see **Section 4.3.1**). All ages in this study are presented on the cyclostratigraphic age model of *Westerhold and Röhl* [2013], which is based on precessional cycles in XRF Fe scanning data from ODP Site 1260.

4.3.3 Benthic foraminiferal stable isotopes

Foraminifera are present throughout the study interval at all three chosen sites. Preservation at Sites 702 and 929 are moderately preserved and consistently 'frosty' [*Sexton et al.*, 2006b]. Background sediment carbonate content is high (~70-90 wt %) throughout the study interval at Sites 702 [*Ciesielski and Kristoffersen*, 1988] and 1260 [*Edgar et al.*, 2007; *Erbacher et*

al., 2004], and lower (~50-60 wt %) at Sites 929 [*This thesis, Chapter 3*] and U1333 [*Pälike et al.*, 2010; *Westerhold et al.*, 2014].

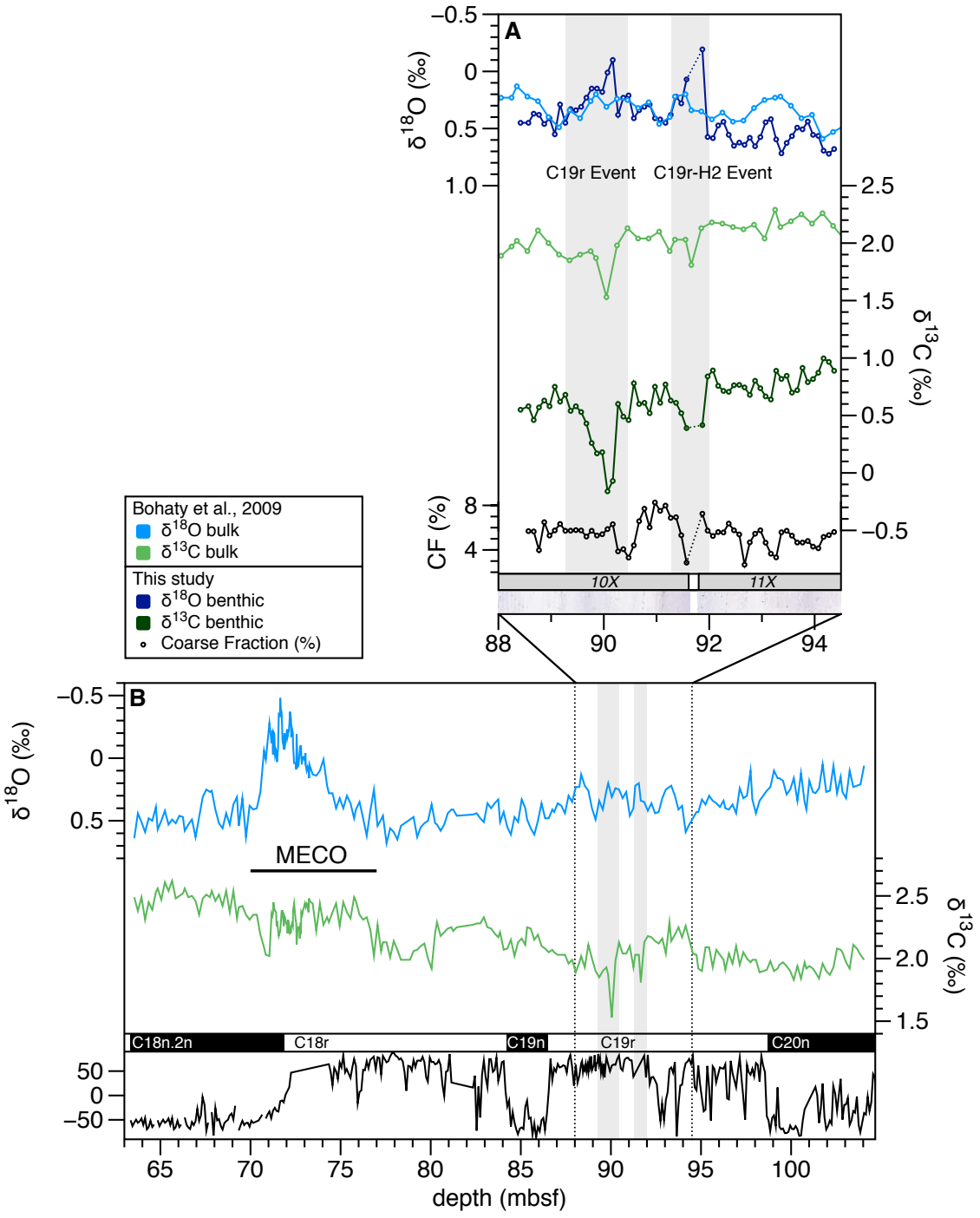

Figure 4-4 ODP Site 702 carbonate and isotope stratigraphy across the study and MECO.
Bulk sediment [*Bohaty et al., 2009*] and benthic foraminiferal [*this study*] $\delta^{18}O$ and $\delta^{13}C$ (‰) from (a) the study interval and (b) the site. Magnetostratigraphy

from Clement and Hailwood [1991]. Grey shaded bars mark C19r and C19r-H2 events.

Benthic foraminiferal records display consistent trends in $\delta^{18}O$ and $\delta^{13}C$ across all sites throughout the study interval (**Table 4-2**). Following an interval of longer-term $\delta^{18}O$ decrease and steady $\delta^{13}C$ values for much of magnetochron C19r (~42.2 and 41.5 Ma), benthic foraminiferal $\delta^{18}O$ and $\delta^{13}C$ values rapidly decrease by 0.5 – 1.0 ‰ across the C19r event (**Figure 4-3**, **Figure 4-6**). Bulk sediment $\delta^{18}O$ and $\delta^{13}C$ records show similar patterns of change, but with a larger variance in magnitude with $\delta^{18}O$ rapidly decreasing by 0.3 to 2.0 ‰ and $\delta^{13}C$ by 0.5 to 0.7 ‰ across the C19r event (**Table 4-2**). The exception to these trends is the bulk sediment $\delta^{13}C$ record from Site 929, which shows an *increase* by 0.6 ‰ across the C19r event. Unfortunately, low middle Eocene sedimentation rates at this site [~11 m/Ma; This thesis, Chapter 3] hinder development of a high-resolution benthic stable isotope stratigraphy.

Table 4-2 Summary of the key features characterizing the C19r and C19r-H2 Events in this study

	Site		ODP Site 1260	ODP Site 702	ODP Site 929	U1333	U1408
Location, Latitude, Longitude			western Atlantic 9°15.948´N, 54°32.633´W	South Atlantic 50°56.786'S, 26°22.117'W	equatorial Atlantic 5°58.568'N, 43°44.402'W	equatorial Pacific 0°30.996′N, 138°25.159′W	north Atlantic 41°26.3′N, 49°47.1′W
Modern water depth (m)			2549	3083	4356	4853	3022
C19r Event	*Δ δ18O (‰)*	*benthic*	-0.5*	-0.5	-	-0.5	-0.6
		bulk sediment	-2.0	-0.3	-0.6	uncertain	-0.5
		planktic	*	-	-	-	-0.6
	Δ δ13C (‰)	*benthic*	-1.0*	-0.9	-	-0.7	-0.3
		bulk sediment	-0.7	-0.5	+0.6	uncertain	-0.4
		planktic	*	-	-	-	uncertain
	Δ CaCO3 (wt %)		-40	-	-50	-25	-10
	Addional evidence		Fe excursion; core photo	core photo	Fe excursion; core photo	Fe excursion	Fe excursion, coarse fraction
	Excursion centered at		75.41 rmcd	90.05 mbsf	594.90 mbsf	184.85 a rmcd	82.25 m CSF-A
	Certainty of hyperthern		**high**	**high**	**high**	**medium**	**low**
C19r-H2 Event	*Δ δ18O (‰)*	*benthic*	~0	-0.7*	-	-0.3	-0.4
		bulk sediment	-	-0.3	-0.6	uncertain	uncertain
		planktic	~0	-	-	-	-0.4
	Δ δ13C (‰)	*benthic*	-0.5	-0.5*	-	-0.6	-0.2
		bulk sediment	-	-0.3	-0.5	uncertain	-0.6
		planktic	~0	-	-	-	uncertain
	Δ CaCO3 (wt %)		-	-	-20	-10	-10
	Addional evidence		Fe excursion		Fe excursion; core photo	Fe excursion	Fe excursion, coarse fraction
	Excursion centered at		77.66 rmcd	91.66 mbsf	590.20 mbsf	185.78 a rmcd	83.00 m CSF-A
	Certainty of hyperthern		**low**	**high**	**high**	**medium**	**low**

**value uncertain due to hiatius*

At Site 702, bulk [*Bohaty et al.*, 2009] and new benthic foraminiferal $\delta^{18}O$ records are remarkably similar in terms of absolute values (between ~0.7 and -0.1 ‰;**Figure 4-4**). In contrast, benthic foraminiferal $\delta^{13}C$ values vary between ~1.0 and -0.1 ‰ throughout the record, offset by approximately -1.2 ‰ from bulk sediment values, consistent with the existence of a water column DIC gradient. Taken at face value, the $\delta^{18}O$ data could imply the lack of a surface-deep temperature gradient in the water column above Site 702 and thus, the presence of a well-mixed water column. However, given the fact that all other sites show isotopic offsets between bulk and benthic foraminifera (**Figure 4-3**, **Figure 4-5**, **Figure 4-6**), the frosty style of carbonate preservation [*Ciesielski and Kristoffersen*, 1988], the lack of a surface-deep $\delta^{18}O$ signal at Site 702 more likely reflects diagenetic overprinting and not a water column DIC gradient. While previous Paleogene studies indicate that diagenesis typically has only a negligible effect on benthic foraminiferal isotope ($\delta^{18}O$ and $\delta^{13}C$) records [*Edgar et al.*, 2013; *Voigt et al.*], bulk sediment records are strongly susceptible to diagenetic overprinting at the seafloor [*Schrag et al.*, 1995; *Stoll and Schrag*, 2000].

New stable isotope records from equatorial Pacific Site U1333 [This thesis, Chapter 2] also exhibit three prominent $\delta^{18}O$ and $\delta^{13}C$ excursions in the upper portion of magnetochron C19r that approach the magnitude seen at Site 1260 (~0.6‰ in $\delta^{18}O$ and ~0.4 ‰ in $\delta^{13}C$ occurring between 41.41 and 41.80 Ma; ~184 to 186 m rmcd; **Figure 4-6**). The centre isotopic excursion at ~41.6 Ma is most similar to the C19r hyperthermal as it is ~170 kyr in duration (<200 kyr at Site 1260), corresponds to a prominent peak in XRF Fe, and decreases in sediment carbonate content. The excursion also occurs at the warmest portion of the long-term warming pattern in benthic isotopes clearly visible at Site 1260 and U1333 during most of magnetochron C19r (**Figure 4-7**). However, some uncertainty remains in correlating these isotopic excursions as the orbital tuning resolution at Site U1333 is based on eccentricity (400 kyrs) [*Westerhold et al.*, 2014].

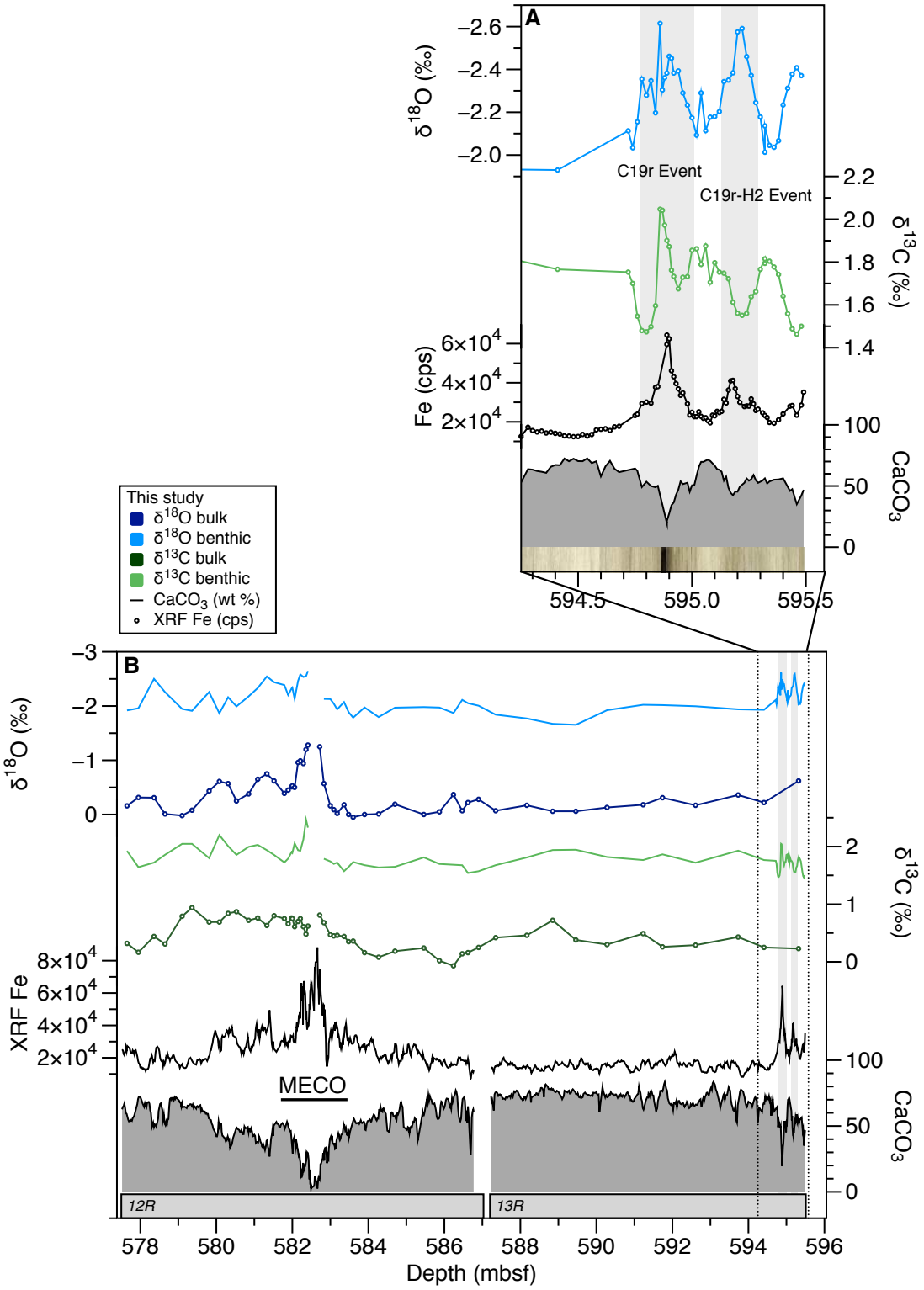

Figure 4-5 ODP Site 929 carbonate and isotope stratigraphy across the study Interval and MECO.
Bulk sediment and benthic foraminiferal $\delta^{18}O$ and $\delta^{13}C$ (‰) [*this study*] from (a) the study interval and (b) the site with XRF Fe and $CaCO_3$ (wt %) [*this study*]. Grey shaded bars mark C19r and C19r-H2 events.

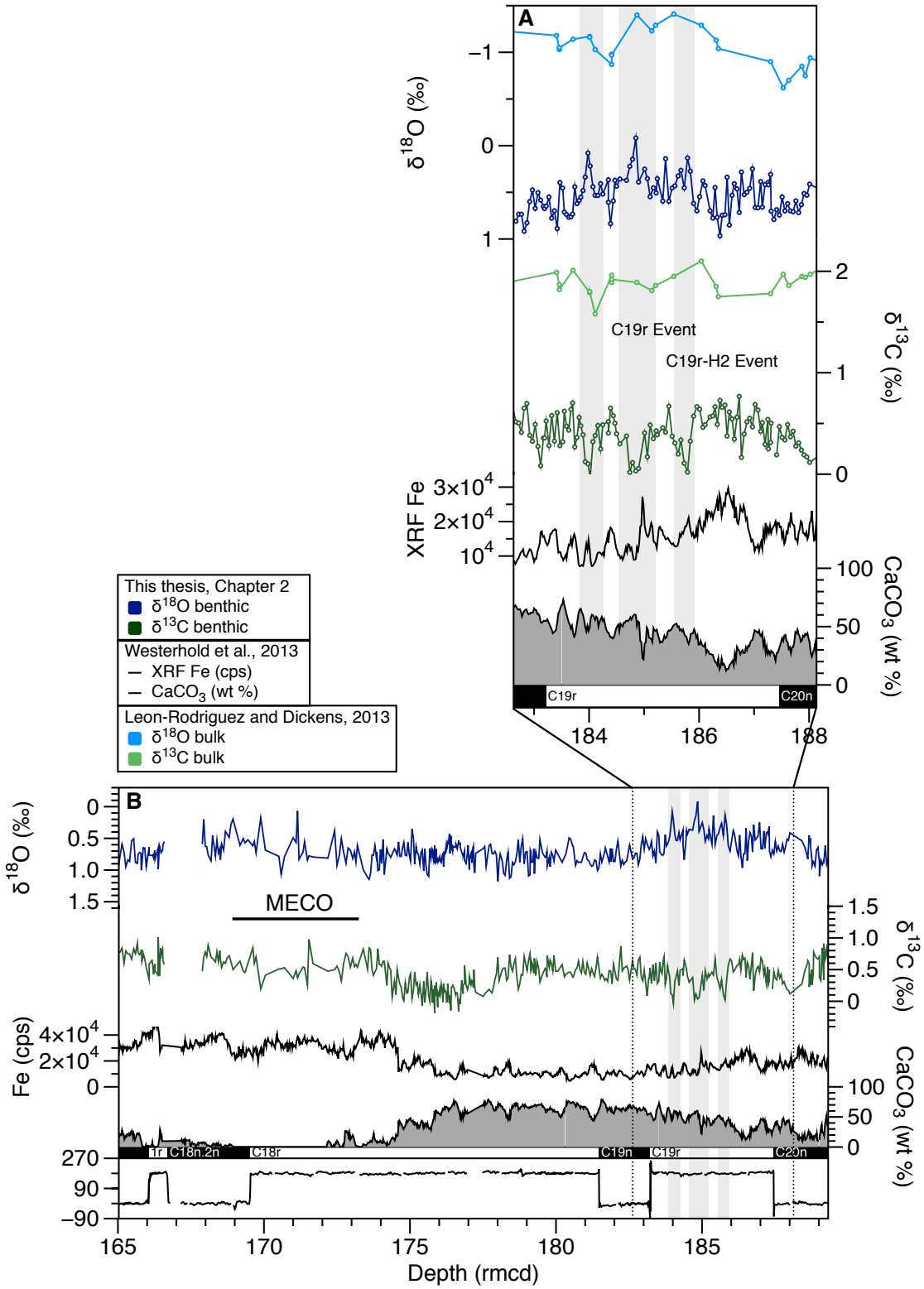

Figure 4-6 IODP Site U1333 carbonate and isotope stratigraphy across the study and MECO Interval.
Bulk sediment [*Leon-Rodriguez and Dickens, 2013*] and benthic foraminiferal [*This thesis, Chapter 2*] $\delta^{18}O$ and $\delta^{13}C$ (‰) from (a) the study interval and (b) the site with XRF Fe, $CaCO_3$ (wt %) [*Westerhold et al., 2014*; *Pälike et al., 2010*] and magnetostratigraphy [*Westerhold et al., 2014*]. Grey shaded bars mark C19r, C19r-H2 events, and third isotopic excursion.

One new feature in the stable isotope records at Sites 702, 929, and U1333 is a second $\delta^{18}O$ and $\delta^{13}C$ excursion that precedes the C19r event (~41.6 at Site 1260; **Figure 4-7**; **Table 4-2**). This excursion, hereafter referred to as 'C19r-H2' [according to the scheme in *Sexton et al.*, 2011], is most evident in benthic foraminiferal records as a -0.5 ‰ $\delta^{13}C$ excursion. Close inspection of benthic $\delta^{13}C$ values at Site 1260 [*Edgar et al.*, 2007; *Edgar et al.*, 2010] also reveal a -0.5 ‰ $\delta^{13}C$ excursion prior to the C19r event (**Figure 4-3**). At Sites 702 and 929, the carbon isotope excursion is coeval with an $\delta^{18}O$ excursion (-0.3 ‰ in bulk sediment at both sites and -0.7 ‰ in benthic foraminiferal calcite at Site 702); however, the true magnitude of C19r-H2 excursions at Site 702 is hindered by a core gap between 702B-10X and 11X (**Figure 4-4**). The isotopic excursion is accompanied signs of carbonate dissolution, in the form of a clay horizon (carbonate content decrease and XRF Fe increase) at Sites 929 and U1333, and decease in coarse fraction wt % at Site 702.

The duration of the C19r-H2 event is difficult to constrain because it was not the focus of previous studies so sampling resolution is low across the interval, at Site 702 the event is truncated, and estimates of its duration differ between Sites 1260 and U1333 (~100 kyrs; **Figure 4-7**) and Site 929 (<20 kyr; **Figure 4-8**). Both Sites 929 and 1260 exhibit precessional scale cyclicity in XRF records, and at Site 929 the duration of the C19r-H2 isotopic excursion corresponds to one precessional cycle (~20 kyr) while the isotopic excursion spans approximately 4 (~120 kyr) at Site 1260 (**Figure 4-8**). Further high-resolution records across this interval are needed to determine the true duration of the C19r-H2 event.

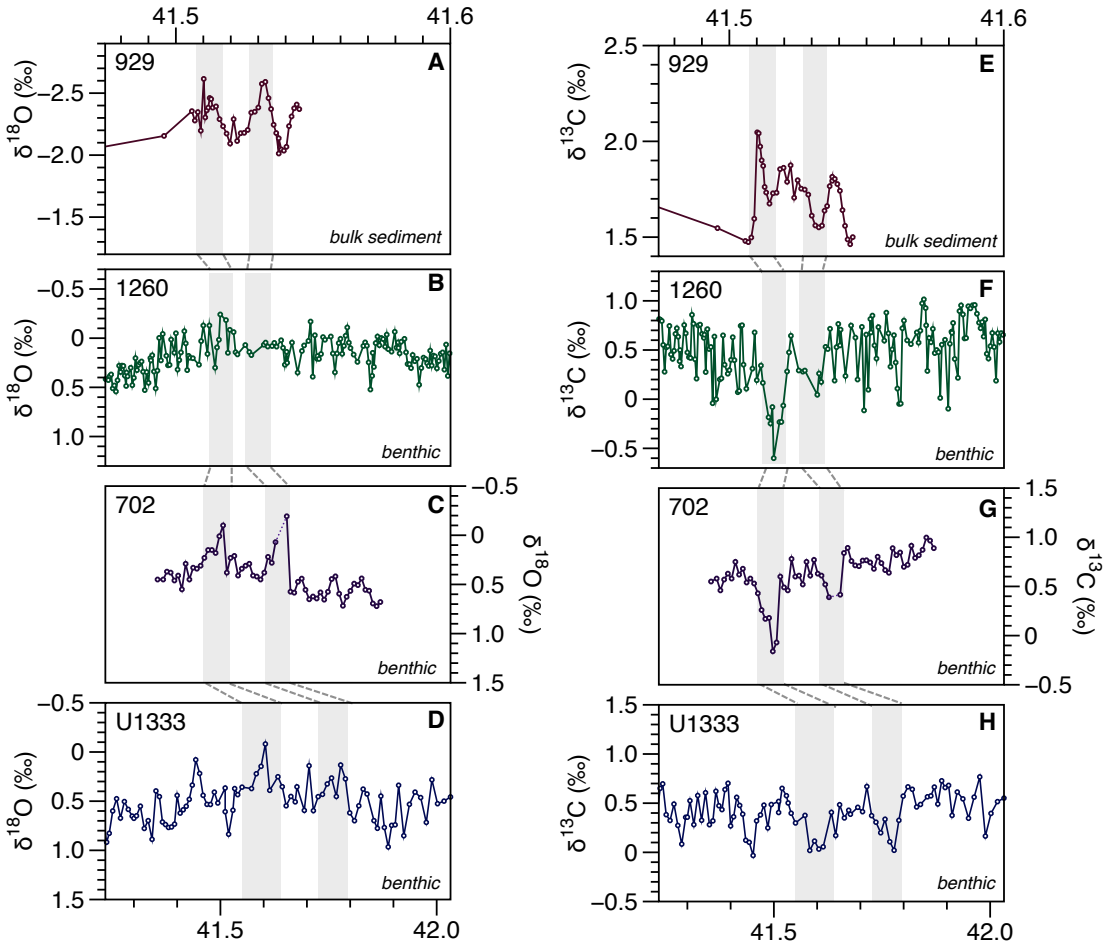

Figure 4-7 Stable isotopes across the C19r and C19r-H2 Events versus age at sites included in this study.
(a-d) $\delta^{18}O$ (‰) and (e-h) $\delta^{13}C$ (‰) from bulk sediment (a, e) and benthic foraminifera at Sites included in this study. Grey shaded bars mark intervals of the C19r and C19r-H2 events. Note the scale difference in panels A and E. Sites 929 and 702 from this study, Site 1260 from *Edgar et al.*, [*2007, 2010*], and Site U1333 from *This thesis*, [*Chapter 2*].

4.4 Discussion

4.4.1 How is the C19r event defined?

The C19r event at equatorial Atlantic Site 1260 is characterized by prominent negative stable isotopic shifts in $\delta^{18}O$ and $\delta^{13}C$ recorded in both benthic foraminifera and bulk sediment in conjunction with carbonate dissolution at 41.50 Ma [*Edgar et al.*, 2007; *Edgar et al.*, 2010; *Westerhold and Röhl*, 2013]. However, the precise timing of the onset and recovery of the event is difficult to define because the isotopic excursions in bulk sediment are expressed over a much thinner stratigraphic interval (~ 0.59 m from 75.09 to 75.68 m rmcd) than the benthic foraminiferal signal (~1.86 m from 74.26 to 76.12 m rmcd; **Figure 4-3**). Similarly, the planktic foraminiferal isotope record and sediment physical properties (XRF Fe, carbonate content) more closely match the bulk sediment excursion. It is the narrower discrete peak in the XRF Fe record that is used for orbital tuning and development of the orbital age model at Site 1260, giving estimates of the event duration on the order of ~40-50 kyr [*Westerhold and Röhl*, 2013]. Other studies define hyperthermal excursions using $\delta^{13}C$, based on the onset (point at which $\delta^{13}C$ begins to decrease and including 'trough to peak') and recovery (termination when $\delta^{13}C$ returns to a value approximately as heavy as the onset and including 'peak to trough') [*Kirtland Turner and Ridgwell*, 2013; *Sexton et al.*, 2011; *Zachos et al.*, 2005]. Arguably, *Westerhold and Röhl* [2013] applies this method for the C19r event using the bulk sediment isotope excursion. However, other hyperthermals show concurrent shifts in bulk sediment and planktic and benthic isotopic excursions [e.g. PETM, ETM2, and smaller hyperthermals; *Kirtland Turner et al.*, 2014; *Littler et al.*, 2014; *Sexton et al.*, 2011; *Stap et al.*, 2009]. A further complication is that if the C19r event were truly global in nature, foraminiferal, bulk sediment, and physical properties should react in unison. Thus, in this study the hyperthermal at Site 1260 is conservatively estimated to be ~100 kyr in duration on the basis of the benthic record *Westerhold and Röhl* [2013]) (**Figure 4-8**). This is not the case at other sites in this study across the C19r event, where benthic and bulk sediment signals are coeval (**Figure 4-4**, **Figure 4-5**, **Figure 4-6**).

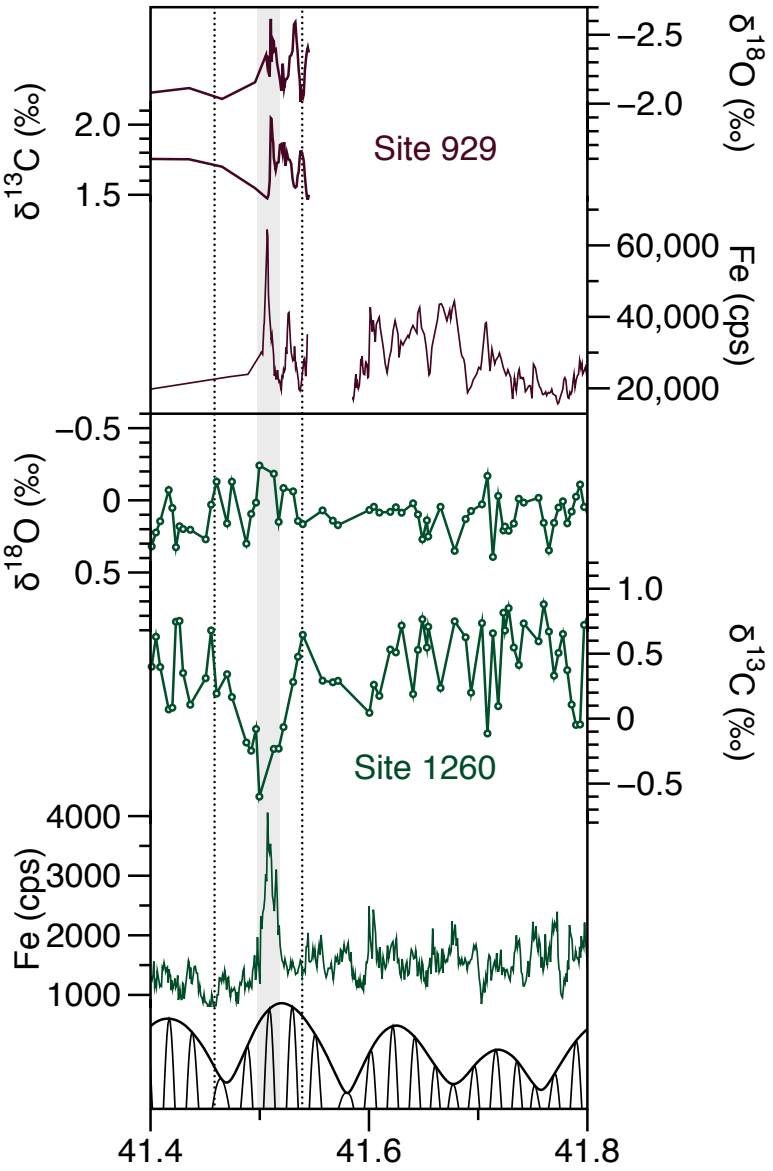

Figure 4-8 ODP Site 929 and Site 1260 stable isotopes across the C19r and C19r-H2 excursions with age.
$\delta^{18}O$ and $\delta^{13}C$ (‰) from (a) bulk sediment at Site 929 [*this study*] and (b) benthic foraminiferal from Site 1260 [*Edgar et al., 2007*]. Dotted lines mark the C19r event as expressed in benthic foraminiferal $\delta^{13}C$ from Site 1260. Grey shaded bar marks the C19r event as expressed in bulk sediment $\delta^{13}C$ and sediment properties at Site 1260.

4.4.2 Is the magnetochron C19r event a hyperthermal?

The short-lived negative $\delta^{18}O$ and $\delta^{13}C$ excursions in bulk and benthic stable isotope records at Sites 702 and 929 suggest for the first time that the magnetochron C19r event is clearly a reproducible feature of late middle Eocene records in the Atlantic Ocean, and the signals are consistent with previous observations from stable isotope records at equatorial Atlantic Site 1260 [Edgar et al., 2007]. At all sites the event is associated with characteristically low sedimentation rates, intense dissolution of carbonate, and increased Fe, implying significant CCD shoaling across the event. Furthermore, new stable isotope records from equatorial Pacific Site U1333 [This thesis, Chapter 2] also exhibit prominent $\delta^{18}O$ and $\delta^{13}C$ excursions (~0.6 ‰ in $\delta^{18}O$ and ~0.4 ‰ in $\delta^{13}C$) corresponding to the C19r event that approach the magnitudes seen at Site 1260 (**Figure 4-6**), as well as increased dissolution of carbonate. While other stable isotope records across this time interval exist elsewhere in the Pacific [Sites 1218 and 1209; *Dawber and Tripati*, 2011a; b; *Lear et al.*, 2004], the C19r event cannot be identified within these records due to their low temporal resolution, poor core recovery, and age model uncertainties. However, the data presented in this chapter that shows the presence of these isotopic perturbations in both the Atlantic and Pacific Oceans implies that the C19r is indeed a global phenomenon, and that the variations observed in the $\delta^{18}O$ and $\delta^{13}C$ reservoir are global and not local effects.

The magnitude of the $\delta^{13}C$ excursion (~0.7 to 1.0 ‰ in benthic foraminifera) suggests a mechanism of carbon release similar to the early Eocene hyperthermals, and a carbon source from a mobile surficial reservoir [*Kirtland Turner et al.*, 2014; *Sexton et al.*, 2011]. The ~ -0.5 ‰ decrease in benthic foraminiferal $\delta^{18}O$ implies a rapid ~2 ˚C warming in the deep ocean with similar warming in the surface ocean (~ -0.3 to 0.6 ‰ decrease in bulk sediment $\delta^{18}O$) above background temperatures. This result is in contrast to the larger surface warming predicted by bulk sediment records (~ -2.0 ‰) at Site 1260 [*Edgar et al.*, 2007], which is not reproduced elsewhere. These findings, paired with dissolution in both the Atlantic and Pacific Ocean across the event, suggests a

global increase in ocean acidity and CCD shoaling as the result of carbon release to depths as shallow as ~2500 m paleodepth in the equatorial Atlantic, ~2250 m paleodepth in the south Atlantic, and ~3000 m paleodepth in the Pacific.

For an event to be considered a hyperthermal, it must meet common criteria: coincident negative isotope excursions in $\delta^{18}O$ and $\delta^{13}C$ (inferred as rapid warming and isotopically light carbon release, respectively) paired with a distinct decrease in wt % carbonate content (inferred as CCD shoaling in response to carbon input) and occur globally on short timescales (~<100 kyr) [*Kirtland Turner and Ridgwell*, 2013; *Lourens et al.*, 2005; *Stap et al.*, 2009; *Zachos et al.*, 2005]. Based on these criteria, the C19r event is clearly a hyperthermal, because rapid global warming, carbon release, and dissolution approach hyperthermal-scale values in magnitude, duration, and timing. Furthermore, the identification of a global event within magnetochron C19r means that the isotopic excursion and dissolution can be used as a stratigraphic marker for future workers in this time interval, which has previously remained sparse in stratigraphic tiepoints.

4.4.3 Is the magnetochron C19r event exceptional?

The C19r event was originally defined primarily by distinct but isolated $\delta^{13}C$ and $\delta^{18}O$ excursions in bulk and foraminiferal calcite at Site 1260. The new records presented here, however, indicate for the first time that the event may instead be one (albeit the largest) of a sequence of short-lived excursions that occur during magnetochron C19r. The second isotopic excursion, or 'C19r-H2 event' (**See 4.3.3**; **Table 4-2**) is defined by a negative $\delta^{13}C$ excursion in benthic foraminiferal records (~0.5 ‰) from the Atlantic and Pacific Oceans as well as bulk sediment records in the Atlantic (~0.3 to 0.5 ‰) over ~100 kyr, indicating a significant short-term global carbon cycle perturbation preceding the C19r event (**Figure 4-7**). The CIE is accompanied by warming of surface and deep waters (negative ~0.3 to 0.6 ‰ in bulk sediment and negative ~0.0 to 0.7 ‰ in benthic $\delta^{18}O$) as well as evidence of sediment carbonate dissolution indicating CCD shoaling in both Atlantic and Pacific Oceans. These features are similar in magnitude, duration, and character to the event originally documented at Site

1260, and given the geographic distribution of records, suggest that both events are global phenomena.

At Site U1333 three large negative benthic $\delta^{18}O$ excursions occur in close succession (~100 kyr apart and lasting for ~100 kyr). This is an indication that there may be a larger number of events within C19r that could be either below detection elsewhere (e.g. in the Atlantic Ocean), or perhaps not captured by the records available at Sites 929 and 702. This series of hyperthermal events is similar to sequences of hyperthermals identified throughout the Early and early middle Eocene (~48-50 Ma) [*Kirtland Turner et al.*, 2014; *Sexton et al.*, 2011] and the hyperthermals bracketing the PETM (~56-52 Ma) [*Cramer et al.*, 2009; *Galeotti et al.*, 2010; *Lourens et al.*, 2005; *Zachos et al.*, 2010]. A number of those hyperthermals were found to be paired (I1 and I2 in magnetochron C24n.3n; H1 and H2 near the C24n/C24r boundary; E1 and E2 in C24r; C1 and C2 in C24r; B1 and B2 in C25n; **Table 4-1**) and appear to be bundled into short-eccentricity cycles (~100 kyr) and separated from another pair by the long eccentricity cycle (~400 kyr) [*Cramer et al.*, 2003; *Zachos et al.*, 2010].

To quantitatively assess the significance of the C19r and C19r-H2 events in the context of background climate trends as well as to investigate the occurrence of other possible events, the two longest middle Eocene records included in this study (Sites 1260 and U1333) were tested for excursions that exceed the 'typical' 1σ background variability in both benthic foraminiferal $\delta^{13}C$ and $\delta^{18}O$ (following the methods defined in *Kirtland Turner et al.* [2014]; **Figure 4-9**). Between ~42.6 and 39.8 Ma at Site 1260, 26 negative $\delta^{18}O$ excursions and 23 negative $\delta^{13}C$ excursions extend $>1\sigma$ beyond the mean detrended background values, 16 of which correspond to negative excursions in both $\delta^{13}C$ and $\delta^{18}O$ (a necessary criteria for categorization as a hyperthermal event). Notably, there are nine negative $\delta^{13}C$ excursions that extend $>2\sigma$ beyond the mean detrended background variance, including the C19r event, two excursions during the MECO, and two prominent negative (~0.5 ‰) excursions at ~41.1 and 41.2 Ma [noted in *Edgar et al.*, 2010]. However, of these nine, only the C19r event and an isotopic excursion at ~42.18 Ma extend beyond $>2\sigma$ in both $\delta^{13}C$ and $\delta^{18}O$. At Site U1333 between ~46.1 and 37.2 Ma, there are 49 negative excursions in $\delta^{18}O$ and 28 in $\delta^{13}C$ exceeding 1σ, with 21

occurring in both $\delta^{13}C$ and $\delta^{18}O$. Of those, there are ten negative $\delta^{13}C$ excursions and eight negative $\delta^{18}O$ excursions that exceed 2σ, with only the MECO and the three excursions in magnetochron C19r that exceed 2σ in both $\delta^{13}C$ and $\delta^{18}O$ (**Figure 4-7**). Based on this analysis, there is strong evidence that the C19r event exceeds background variability at both sites and therefore might be classified as a hyperthermal. The C19r-H2 excursion exceeds 2σ background variability at Site U1333 and exceeds 1σ at Site 1260. Given this (albeit smaller) significance, and the fact that the C19r-H2 excursion corresponds to warming, carbon release, and dissolution in multiple ocean basins, it is also given the hyperthermal classification. Beyond this, there are not many significant $>2\sigma$ excursions that align between the two sites; for example, there is little evidence for the prominent Site 1260 excursion at ~42.18 Ma in records from Site U1333. While the amplitude and variance of $\delta^{13}C$ excursions in these records appear similar to excursions reported in the Paleogene through Miocene [*Kirtland Turner*, 2014; *Kirtland Turner et al.*, 2014; *Sexton et al.*, 2011], excursions that exceed 2σ such as the C19r event are more likely to be discrete global events.

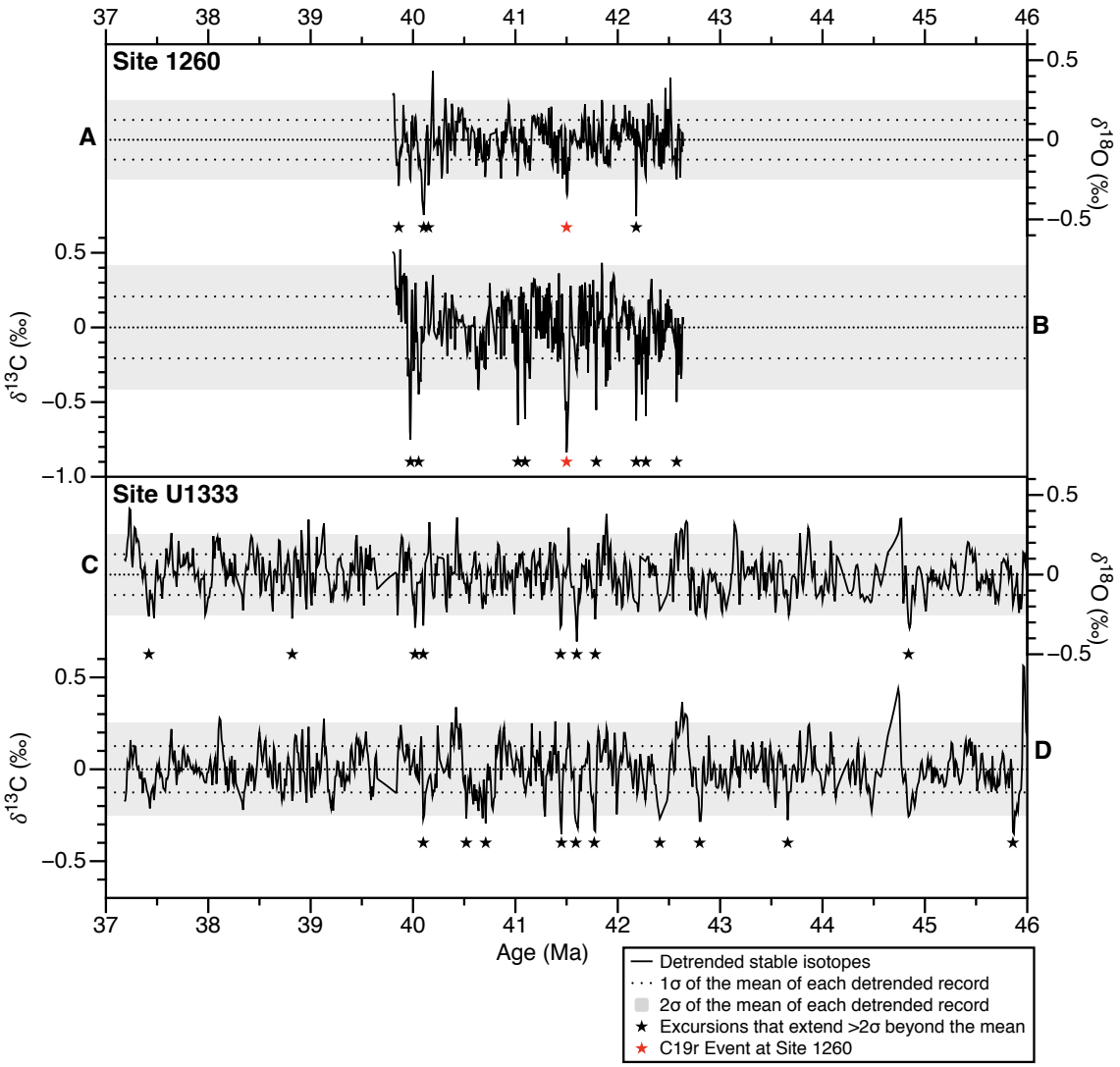

Figure 4-9 Stable isotope excursions throughout the middle Eocene. Benthic foraminiferal $\delta^{18}O$ and $\delta^{13}C$ (‰) from (a, b) Site 1260 [*Edgar et al., 2007, 2010*], and (c, d) Site U1333 [This thesis, Chapter 2]. Dashed lines indicate ±1σ around the mean of detrended $\delta^{18}O$ and $\delta^{13}C$ values and grey shaded bars indicate ±2σ. Stars mark quantitative identification of negative $\delta^{18}O$ and $\delta^{13}C$ excursions that extend greater than 2σ beyond the mean of each detrended record, following the methods in *Kirtland et al. [2014]*.

4.4.4 Implications for hyperthermal mechanisms

It is an important finding that the magnetochron C19r and C19r-H2 events are true hyperthermals because it significantly extends evidence of hyperthermal occurrence through the middle Eocene, a time interval with a colder background state than the early Paleogene (**Figure 1-1**). The similar sedimentological character and apparent orbital control on hyperthermals suggests the operation of a common forcing mechanism throughout the smaller hyperthermals of the Paleocene and early Eocene [*Stap et al.*, 2010], and perhaps longer [*Kirtland Turner*, 2014; *Kirtland Turner et al.*, 2014]. Hypotheses for the mechanism responsible for triggering hyperthermal events in the late Paleocene and early Eocene remain controversial but include the repeated orbitally paced releases of isotopically light carbon from an 'external' reservoir, including methane hydrates ($\delta^{13}C$ = -60 ‰), terrestrial carbon stored in permafrost, or peat (organic sources = -25 ‰) [*DeConto et al.*, 2012; *Lunt et al.*, 2011; *Zachos et al.*, 2010]. These carbon sources are widely acknowledged as likely responsible for the PETM, where the large CIE (~ -3 ‰) necessitates an extremely isotopically light carbon source and the interval between perturbations is sufficiently long (>100 kyr) to allow for the build-up of methane hydrate or permafrost carbon reservoirs [*DeConto et al.*, 2012; *Dickens*, 2003; *Lunt et al.*, 2011]. A recent modelling study by *Kirtland Turner et al.* [2014] extended the threshold model of Lunt et al., [2011] past the EECO and the results suggested that eccentricity forcings (causing seasonality variations) superimposed on a long term change in climate could plausibly lead to slowed overturning circulation and warming at intermediate water depths capable of triggering methane hydrate releases. However, in order for the model scenario to reproduce the observed pattern of hyperthermal frequency during long-term Eocene background cooling (specifically, the decrease in frequency), the rate of cooling had to be increased past the rate that existing empirical data compilations potentially not support (data supports symmetrical warming/cooling before/after the EECO) [*Cramer et al.*, 2009; *Zachos et al.*, 2001a]. Furthermore, while this scenario requires only small amounts (a few hundred petagrams C) of carbon release from methane, it is unlikely that methane hydrate reservoirs would continue because carbon reservoirs would

be depleted by the EECO [*Komar et al.*, 2013], suggesting the source of carbon might not be from a sedimentary reservoir.

Ultimately, *Kirtland Turner et al.* [2014] found no support for the previously widely held concept of a thermally controlled threshold for carbon release events spanning ~57-47 Ma (excluding the PETM) which implies a decrease in hyperthermal magnitude and increase in hyperthermal frequency with increasing background temperature. It is hypothesized that the more modest (<1 ‰ CIEs) hyperthermals in the early Eocene to middle Eocene transition are likely to be orbitally triggered by carbon release from a more readily exchangeable surficial reservoir than a sediment source, involving the redistribution of carbon from either the ocean, atmosphere, or biosphere, with the oceans being the largest and therefore most likely of these reservoirs [*Kirtland Turner et al.*, 2014; *Sexton et al.*, 2011]. According to mass balance calculations, smaller hyperthermals (~0.5 ‰ CIEs) are more likely to be attributed to the repeated release of dissolved organic carbon from a deep ocean reservoir by ventilation and carbon sequestration in the ocean [*Sexton et al.*, 2011] or from the terrestrial biosphere involving a transfer of carbon from the continents to the deep ocean [*Kirtland Turner*, 2014]. The new records presented in this study support these findings and significantly extend the hyperthermal presence into the middle Eocene. From ~46 to ~37 Ma, with particular focus on the magnetochron C19r interval, there is evidence of at least two additional hyperthermals that exhibit carbon cycle perturbations significantly above background variability on par with earlier Eocene hyperthermals in magnitude and duration. These findings support orbital forcing of hyperthermals, as the C19r event was likely triggered by an exceptionally strong eccentricity peak, and the ~100 kyr between the C19r and C19r-H2 events is sufficient time to build up a surficial carbon reservoir (and not an exogenic one). Furthermore, this finding also confirms that hyperthermals are persistent regardless of markedly different background climate regimes, suggesting a strong carbon cycle-climate response in cooler greenhouse climates without the presence of large-scale ice sheets.

4.5 Summary and Conclusion

The interval of dissolution and isotopic shifts during the C19r event first documented in the Atlantic at Site 1260 is now substantiated elsewhere in the Atlantic and Pacific, along with at least one other hyperthermal excursion, providing evidence that hyperthermals were not restricted to the late Paleocene through early middle Eocene (~48-50 Ma) [*Kirtland Turner et al.*, 2014; *Sexton et al.*, 2011] but also occurred much later in the middle Eocene when long-term temperature trends had a significantly cooler background state.

While the records presented in this study show the occurrence of transient climate events continues during the middle Eocene, a data gap still exists from ~46 to 47.5 Ma where there are no high resolution benthic foraminiferal stable isotopes. Furthermore, recently discovered transient events during the Eocene remain observed at only one site location. To obtain a better estimate of their true magnitude and number of hyperthermals across the middle Eocene more records is needed, particularly because this critical gap in our knowledge can help explain the fundamental dynamics of climate perturbations on short timescales and in warm climates.

Chapter 5: Concluding Remarks

Contents

5.1 Summary

The projects incorporated in this thesis are focused on developing new paleoceanographic and sedimentological records across the middle to late Eocene (~46 and 35 Ma). The Eocene encompasses a critical transitional period of Earth's history: the shift from a warmer 'greenhouse' climate with high atmospheric pCO_2, with little or no ice and high global temperatures to a cooler 'icehouse' world with permanent ice sheets in the Southern Hemisphere at ~34 Ma. However, while the multi-million year climate patterns of the Eocene are generally well known, the details of shorter-term fluctuations (< 500 kyr) over this time interval are poorly constrained. In part this is because most high-resolution Eocene studies have typically focused on the early Eocene rapid warming events (e.g., the PETM; [*Kennett and Stott*, 1991; *E Thomas and Shackleton*, 1996; *Zachos et al.*, 2003; *Zachos et al.*, 2005].) or the Eocene-Oligocene transition [*Coxall et al.*, 2005; *Diester-Haass and Zahn*, 1996; *Shackleton and Kennett*, 1975; *Zachos et al.*, 2001a] but also classically because of a dearth of middle Eocene deep-sea material on which to work. In the past fifteen years new drilling on Walvis Ridge (Leg 208) [*Zachos et al.*, 2004], Demerara Rise (Leg 207) [*Erbacher et al.*, 2004], Blake Nose (Leg 171B) [*Norris et al.*, 1998], and in the equatorial Pacific (Leg 199) [*Lyle et al.*, 2002a] have yielded shallowly buried Eocene sediments with carbonate microfossils that were remarkably successful in yielding new insights into dynamism of greenhouse worlds. However, the recent recovery of very expanded Eocene sediment sequences in the equatorial Pacific from IODP Exp. 320/321 [*Pälike et al.*, 2010] and the Northwest Atlantic from IODP Exp. 342 [*Norris et al.*, 2014c] have enabled investigation into middle Eocene climate at unprecedented detail. This is due to of a number of factors; high sedimentation rates (up to ~10 cm/kyr), continuous sediments with astronomically tuned chronology, and the ability to fill critical gaps in previous research (i.e. exceptionally well preserved carbonate microfossils compared to typical pelagic sites from Exp. 342; carbonate across Eocene from very deep Pacific Ocean from Exp. 320). These sediments are utilized in this thesis in conjunction with a combination of new records from older drillcores and a

compilation of published records to provide new insights into the middle and late Eocene. Specifically this thesis aims to characterize the nature and timing of background environmental change and identify and constrain short-term perturbations in the climate and carbon cycle during the middle Eocene in order to better understand how Earth systems function in greenhouse climates. This is increasingly important as projections of anthropogenic climate change indicate pCO_2 concentrations in the coming century not previously seen on Earth for tens of millions of years.

In this final chapter the scientific objectives posed in **Chapter 1** that motivated this work are addressed and the main outcomes of this thesis are summarized. Lastly, future directions for paleoceanographic studies that could further this work are discussed.

5.2 Conclusions

5.2.1 Chapter 2: Middle Eocene greenhouse climate instability in the equatorial Pacific (IODP Site U1333)

New monospecific benthic foraminifera stable isotope ($\delta^{18}O$ and $\delta^{13}C$) records generated across the middle to late Eocene at IODP Site U1333 represent the longest high-resolution record from any ocean basin in this interval to date. These new records provide the first test of the hypothesis that the seven CAEs recorded in equatorial Pacific sediments are associated with transient global cooling and/or glaciation and may have been caused by a similar mechanism to the EOT [*Burgess et al.*, 2008; *Dawber and Tripati*, 2011b; *Lyle et al.*, 2002a; *Lyle et al.*, 2005; *Olivarez Lyle and Lyle*, 2005; 2006; *Tripati et al.*, 2005]. Critically these records show that the amplitude and timing of $\delta^{18}O$ and $\delta^{13}C$ shifts in benthic foraminiferal calcite does not consistently correspond to fluctuations in equatorial Pacific deep-sea carbonate accumulation. Implying that CAEs are not associated with global cooling/glaciation events.

The new stable isotope records here also represent an opportunity to revisit the feasibility of several of the hypothesized driving mechanisms for CAEs as highlighted by the modelling experiments of *Pälike et al.* [2012]. In the

absence of a correlation between $\delta^{18}O$ trends and CAEs, both transient changes in shelf-basin fractionation (i.e., a shift from shallow to deep carbonate accumulation associated with sea level fall) and increased organic carbon burial from changes in organism basal metabolic rate should be excluded from further consideration because they are both temperature dependent processes. The most plausible mechanisms invoke increased solute flux from continental weathering, or increased organic carbon burial from changes in marine plankton assemblages (and is backed up by findings from Chapter 3).

Together, the records in this chapter illustrate the complex nature of the transition from the greenhouse to icehouse climate state. Site U1333 benthic foraminifera stable isotopes are the first high-resolution records to span the interval between ~42.6 and 46.2 Ma and have led to the discovery a transient positive $\delta^{13}C$ and $\delta^{18}O$ excursion and carbonate dissolution at ~44.7 Ma that has not been previously documented. The pronounced positive excursions share few similarities with other observed transient events in the Eocene. However, at ~37.25 Ma, a prominent excursion (~ -0.7 ‰ $\delta^{13}C$) may correspond to the PrOM cooling event recorded in the Southern Ocean [*Scher et al.*, 2014].

Additionally, these new stable isotope records fully span the CAE-3 and MECO event, not recovered in full during ODP Leg 199 [*Lear et al.*, 2004], providing the first detailed record from the Pacific Ocean. Based on the magnitude of $\delta^{18}O$ excursion from benthic foraminifera at ~41.5 Ma showing general agreement with Atlantic records [*Edgar et al.*, 2007], there is no support for bipolar glaciation. New data across the MECO shows that the event is more complex than previously documented, including a seemingly dampened warming trend in deep waters at equatorial latitudes (~0.5 ‰ $\delta^{18}O$ vs. ~1.0 $\delta^{18}O$ in the Southern Ocean [*Bohaty et al.*, 2009]), a slow recovery to background values (by >150 kyr), as well as a ~300 kyr global negative $\delta^{13}C$ excursion preceding warming. Meaning that perhaps the MECO event has been difficult to reconstruct in carbon cycle modelling because critical features of the event have yet to be thoroughly identified in both sequence and geographic extent.

5.2.2 Chapter 3: Dynamic, large-magnitude Carbonate Compensation Depth changes during the MECO

In this chapter new stable isotope ($\delta^{18}O$ and $\delta^{13}C$) data, bulk sediment carbonate content, and age constraints for ODP Sites 929 and 1209 are combined with new and published carbonate content records to form a depth transect of sites with Eocene paleodepths between ~2 - 4 km in both the Atlantic and Pacific Oceans, and provided the first look at deep-sea carbonate burial at high temporal resolution across the MECO interval. The MECO is identified for the first time at ODP Site 929 in the equatorial Atlantic (~3935 m paleodepth) and ODP Site 1209 in the Pacific (~1950 m paleodepth) which form critical end-members for constraining the full magnitude of the CCD change across the MECO in both ocean basins.

This resulting new CCD compilation provided the opportunity to investigate an apparent inconsistency in the proposed MECO driving mechanism, namely that widespread carbonate dissolution could be sustained for >100 kyr without counterbalanced effects from weathering [*Sluijs et al.*, 2013]. The new CCD record confirms the relatively long-lived (~300-600 kyr) and global nature of CCD shoaling that occurred with the onset of MECO warming. However, overall rapid and extreme lysocline shoaling to water depths as shallow as ~2 km (>1 km shallower than previous CCD estimates [*Bohaty et al.*, 2009; *Pälike et al.*, 2012]) with superimposed variation over much shorter timescales (<100 kyrs) that occurs both during and after the MECO. These transient CCD/lysocline variations occur in mid-level deep waters (2 – 4 km) and are likely a direct response to multiple pulses of carbon input to the ocean–atmosphere system during the MECO which resulted in repeated episodes of deep-sea acidification and subsequent carbonate compensation, and thus, prolonged dissolution. This result represents a critical piece of information that can provides further insight into the timing and duration of potential causal mechanisms behind the MECO event.

Patterns of carbonate accumulation in the Atlantic Ocean reported here are similar in magnitude and timing to CAEs-3 and 4 recorded in the Pacific Ocean and represent the first evidence for synchronous events in both basins. This finding also helps to further narrow down the hypothesized driving mechanism

for CAEs [*Pälike et al.*, 2012] by conclusively ruling out switches in the dominant deep-water source between the Southern and North Pacific Oceans (i.e. impacting water mass aging gradients) which would necessitate asynchronous Atlantic and Pacific CCD responses (much like across glacial-interglacial cycles of the past 800 kyrs [*Broecker*, 1971; *Sexton and Barker*, 2012].

5.2.3 Chapter 4: An investigation into the spatial extent of the magnetochron C19r hyperthermal event

New lithological and geochemical data including stable isotopes ($\delta^{18}O$ and $\delta^{13}C$) from benthic foraminifera and bulk sediment at Sites 929, 702, and U1408 through a late middle Eocene time slice (~41.5 – 42.0 Ma) within magnetochron C19r were combined with existing datasets to determine the nature and extent of the little known C19r event. These new records clearly show evidence for $\delta^{18}O$ and $\delta^{13}C$ excursions (>0.5 to 1.0 ‰) in surface and deep waters associated with CCD shoaling of at least ~2500 m at ~41.8 Ma, ~70 % of the way through magnetochron C19r at all investigated sites. Thus, the C19r event fulfils the criteria (based on analogy to the PETM) to be defined as a 'hyperthermal' including rapid warming, carbon release, CCD shoaling, and that the event is globally extensive above background levels.

These records also show evidence for a second hyperthermal, 'C19r-H2', which occurs ~100 kyr prior to the C19r event. Further, analysis of the long-term benthic foraminifera stable isotope records from Sites 1260 (~40 – 42.5 Ma [*Edgar et al.*, 2007; *Sexton et al.*, 2006a]) and U1333 (~37 - 46 Ma; this thesis, Chapter 2) reveal that the C19r event is not exceptional and that there are multiple transient events throughout the middle Eocene. This finding builds on an increasing body of data implying that these smaller hyperthermals are not isolated occurrences in the late Paleocene to early Eocene [*Kirtland Turner*, 2014; *Kirtland Turner et al.*, 2014; *Sexton et al.*, 2011]. These records significantly extend the occurrence of hyperthermals ~6 million years into the middle Eocene when long-term temperature trends had a significantly cooler background state.

5.3 Future work

The long-term high-resolution benthic foraminifera stable isotope record from the equatorial Pacific presented in Chapter 2 represents an important step forward in unravelling the so-called Eocene "doubthouse" interval by significantly increasing the resolution of data across the Eocene climate gap between ~40 and 46 Ma [*Pälike and Hilgen*, 2008] and providing an additional means for establishing robust age control across the middle Eocene interval. However, fully closing the Eocene gap with high-resolution, astronomically calibrated sediments requires records that extend further back in time than the records presented here. Fortunately, the recent drilling during IODP Expedition 342 in the Northwest Atlantic [*Norris et al.*, 2014c] recovered expanded deep-sea sediments spanning the Eocene that in time will yield stable isotope records at an unprecedented resolution (~3cm/kyr) as well as providing a high-latitude signal from a climatically sensitive region of the world's oceans poorly recovered in Paleogene studies, and complement the records from the equatorial Pacific in this study.

While the new records presented in this thesis help to narrow the list of plausible forcing mechanisms for the CAEs the exact mechanism remains unknown. Tackling this question requires globally extensive carbonate and benthic foraminifera stable isotope records across all seven CAEs to obtain a basic understanding of their geographical extent and whether they are all present in the Atlantic and Indian Ocean basins. Critically, there are currently no existing records from shallow waters (e.g. planktic foraminiferal $\delta^{18}O$ and $\delta^{13}C$), detailed changes in marine ecology, or global weathering rates (e.g., Sr isotope records) to further test this hypothesis.

Furthermore, across the MECO interval, fully understanding the cause of large transient dissolution pulses is key to understanding deep ocean chemistry and climate during the event and requires further modelling of the physical and biogeochemical changes. To do so, a more globally diverse set of proxy records is needed. In particular higher resolution records of carbonate accumulation are needed in the shallow Pacific and intermediate depths to fill data gaps between ~2500 – 3000 m paleodepth. Critically, there is also a need

for estimates of continental weathering rates to assess and constrain the model predictions of *Sluijs et al.* [2013].

Constraining the rate and precise timing of environmental changes is critical to understanding the possible driving mechanisms of an event, yet an on-going challenge with MECO is fine-scale correlation between sites. This is often exacerbated by reduced sedimentation rates across the peak of the event (even in expanded sediments) due to strong carbonate dissolution during the event and has posed a considerable challenge in correlating the records of carbonate accumulation (e.g. Chapter 3). An orbitally tuned timescale based on XRF data and bulk sediment isotopes exists at a single site (Site 1260) and indicates no missing cycles [*Westerhold and Röhl*, 2013]. However there are uncertainties in the magnetostratigraphy at the peak of the event and benthic foraminifera $\delta^{18}O$ isotopes do not match the 'classic' Southern Ocean records [*Bohaty and Zachos*, 2003; *Bohaty et al.*, 2009] resulting in challenging site-to-site correlations. Site U1333 has the first orbitally tuned age model to span both the onset and recovery of the MECO [*Westerhold et al.*, 2014], however the isotopic signals more closely resemble Site 1260 and do not provide strong tiepoints for site-to-site correlations with records based on lower-resolution age models. Therefore, further development of orbitally tuned age models will be critical to deconvolving the precise timing and rates of change across the MECO. Furthermore, future work should aim to maximise the sampling resolution to ~1-2 cm spacing across the peak MECO interval (including XRF-scanning but also bulk sediment and benthic foraminifera stable isotopes where possible) as this has provided significant crucial details as to the nature of the event (i.e. short term fluctuations in $\delta^{18}O$ and $\delta^{13}C$ and carbonate content at the peak of the event in records from Sites 929, 1209 and 1263) and target expanded sites to help to build more robust age models.

Appendices

Appendix A Data Tables for Chapter 2: Middle Eocene greenhouse climate instability in the equatorial Pacific: Site U1333

Appendix Table 5-1 IODP Exp. 320 Site U1333 benthic foraminifera isotopic composition and coarse fraction data

Hole	Core	Type	Section	Type	Top (cm)	Bottom (cm)	Top (m CSF-A)	Bottom (m CSF-A)	Depth (rmcd; m revised CCSF-A)	Depth (m adj rmcd; m adj rev CCSF-A)	Coarse Fraction (wt %)	Barren Sample	$\delta^{13}C$ measured at Bremen (‰, VPDB)	$\delta^{18}O$ measured at Bremen (‰, VPDB)	$\delta^{13}C$ measured at NOCS (‰, VPDB)	$\delta^{18}O$ measured at NOCS (‰, VPDB)	$\delta^{13}C$ compiled (‰, VPDB)	$\delta^{18}O$ compiled (‰, VPDB)	$\delta^{13}C$ adjusted to Cibs (true+0.34)	$\delta^{18}O$ adjusted to Cibs (true+0.1/0.89)	Age (Ma) [WK Age]
B	14	H	6	W	1	3	129.21	129.23	150.67	150.67	12.0				0.230	0.950	0.230	0.950	0.570	1.180	37.198
B	14	H	6	W	6	8	129.26	129.28	150.72	150.72	13.0		0.420	1.080			0.420	1.080	0.760	1.326	37.207
B	14	H	6	W	11	13	129.31	129.33	150.77	150.77	12.3		0.463	1.089			0.463	1.089	0.803	1.336	37.217
B	14	H	6	W	16	18	129.36	129.38	150.82	150.82	12.4		0.278	1.224			0.278	1.224	0.618	1.488	37.227
B	14	H	6	W	21	23	129.41	129.43	150.87	150.87	12.5				0.565	1.451	0.565	1.451	0.905	1.743	37.236
B	14	H	6	W	26	28	129.46	129.48	150.92	150.92	12.0		0.487	1.115			0.487	1.115	0.827	1.365	37.246
B	14	H	6	W	31	33	129.51	129.53	150.97	150.97	11.9		0.419	0.952			0.419	0.952	0.759	1.182	37.255
B	14	H	6	W	36	38	129.56	129.58	151.02	151.02	11.0		0.373	0.974			0.373	0.974	0.713	1.207	37.265
B	14	H	6	W	41	43	129.61	129.63	151.07	151.07	11.5		0.473	1.187			0.473	1.187	0.813	1.447	37.274
B	14	H	6	W	46	48	129.66	129.68	151.12	151.12	11.5		0.480	1.257			0.480	1.257	0.820	1.525	37.284
B	14	H	6	W	51	53	129.71	129.73	151.17	151.17	10.5		0.466	1.212			0.466	1.212	0.806	1.474	37.293
B	14	H	6	W	56	58	129.76	129.78	151.22	151.22	10.3		0.317	1.128			0.317	1.128	0.657	1.380	37.303
B	14	H	6	W	61	63	129.81	129.83	151.27	151.27	10.1		0.347	1.197			0.347	1.197	0.687	1.458	37.312
B	14	H	6	W	66	68	129.86	129.88	151.32	151.32	9.8		0.348	1.165			0.348	1.165	0.688	1.421	37.322
B	14	H	6	W	71	73	129.91	129.93	151.37	151.37	9.0		0.261	1.095			0.261	1.095	0.601	1.343	37.331
B	14	H	6	W	76	78	129.96	129.98	151.42	151.42	10.3		0.266	0.994			0.266	0.994	0.606	1.229	37.341
B	14	H	6	W	81	83	130.01	130.03	151.47	151.47	9.9		0.352	1.038			0.352	1.038	0.692	1.279	37.349
B	14	H	6	W	86	88	130.06	130.08	151.52	151.52	7.9		0.193	0.941			0.193	0.941	0.533	1.170	37.357
B	14	H	6	W	91	93	130.11	130.13	151.57	151.57	8.3		0.165	0.991			0.165	0.991	0.505	1.226	37.366
B	14	H	6	W	96	98	130.16	130.18	151.62	151.62	8.7		0.363	1.045			0.363	1.045	0.703	1.287	37.374
B	14	H	6	W	98	100	130.18	130.20	151.64	151.64	9.0		0.256	1.081			0.256	1.081	0.596	1.327	37.378
B	14	H	6	W	106	108	130.26	130.28	151.72	151.72	9.9		0.230	0.947			0.230	0.947	0.570	1.176	37.391
B	14	H	6	W	111	113	130.31	130.33	151.77	151.77	8.5		0.196	0.861			0.196	0.861	0.536	1.080	37.399
B	14	H	6	W	116	118	130.36	130.38	151.82	151.82	7.4		0.160	0.852			0.160	0.852	0.500	1.070	37.408
B	14	H	6	W	121	123	130.41	130.43	151.87	151.87	8.3		0.206	0.667			0.206	0.667	0.546	0.861	37.416
B	14	H	6	W	126	128	130.46	130.48	151.92	151.92	8.3				0.078	0.872	0.078	0.872	0.418	1.092	37.425
B	14	H	6	W	131	133	130.51	130.53	151.97	151.97	8.4		0.100	0.977			0.100	0.977	0.440	1.210	37.433
B	14	H	6	W	136	138	130.56	130.58	152.02	152.02	9.1		0.194	0.854			0.194	0.854	0.534	1.072	37.442
B	14	H	6	W	141	143	130.61	130.63	152.07	152.07	9.3		0.181	0.916			0.181	0.916	0.521	1.141	37.450
B	14	H	6	W	146	148	130.66	130.68	152.12	152.12	9.5		0.261	0.923			0.261	0.923	0.601	1.150	37.458
B	14	H	7	W	0	2	130.70	130.72	152.16	152.16	9.1		0.117	0.695			0.117	0.695	0.457	0.894	37.465
B	14	H	7	W	6	8	130.76	130.78	152.22	152.22	9.7		0.164	0.870			0.164	0.870	0.504	1.090	37.475
B	14	H	7	W	11	13	130.81	130.83	152.27	152.27	10.0		0.246	1.019			0.246	1.019	0.586	1.257	37.484
B	14	H	7	W	16	18	130.86	130.88	152.32	152.32	10.7		0.302	1.121			0.302	1.121	0.642	1.372	37.492
B	14	H	7	W	21	23	130.91	130.93	152.37	152.37	10.8		0.349	1.191			0.349	1.191	0.689	1.451	37.501
B	14	H	7	W	26	28	130.96	130.98	152.42	152.42	10.5		0.276	1.006			0.276	1.006	0.616	1.242	37.509
B	14	H	7	W	31	33	131.01	131.03	152.47	152.47	10.1		0.406	1.098			0.406	1.098	0.746	1.347	37.518
B	14	H	7	W	36	38	131.06	131.08	152.52	152.52	10.1		0.249	1.002			0.249	1.002	0.589	1.238	37.526
B	14	H	7	W	41	43	131.11	131.13	152.57	152.57	9.6		0.319	1.146			0.319	1.146	0.659	1.401	37.535
B	14	H	7	W	46	48	131.16	131.18	152.62	152.62	8.0		0.262	0.989			0.262	0.989	0.602	1.224	37.543
C	16	H	2	W	16	18	128.26	128.28	152.63	152.63	6.8		0.399	0.764			0.399	0.764	0.739	0.971	37.545
C	16	H	2	W	21	23	128.31	128.33	152.68	152.68	7.8		0.177	1.149			0.177	1.149	0.517	1.403	37.553
B	14	H	CC	W	1	3	131.22	131.24	152.68	152.68	7.3		0.238	0.960			0.238	0.960	0.578	1.191	37.553
C	16	H	2	W	26	28	128.36	128.38	152.73	152.73	8.2		0.320	1.199			0.320	1.199	0.660	1.460	37.562
B	14	H	CC	W	6	8	131.27	131.29	152.73	152.73	8.6		0.153	0.939			0.153	0.939	0.493	1.167	37.562
C	16	H	2	W	30	32	128.40	128.42	152.77	152.77	9.1		0.240	1.175			0.240	1.175	0.580	1.433	37.569
B	14	H	CC	W	11	13	131.32	131.34	152.78	152.78	8.9		0.210	0.985			0.210	0.985	0.550	1.219	37.571
C	16	H	2	W	35	37	128.45	128.47	152.82	152.82	8.5		0.235	1.136			0.235	1.136	0.575	1.389	37.578
B	14	H	CC	W	16	18	131.37	131.39	152.83	152.83	9.3		0.184	1.141			0.184	1.141	0.524	1.394	37.580
C	16	H	2	W	40	42	128.50	128.52	152.87	152.87	8.6		0.302	1.296			0.302	1.296	0.642	1.569	37.588
C	16	H	2	W	45	47	128.55	128.57	152.92	152.92	7.8										37.597
C	16	H	2	W	50	52	128.60	128.62	152.97	152.97	10.0		0.295	1.189			0.295	1.189	0.635	1.448	37.607
C	16	H	2	W	54	56	128.64	128.66	153.01	153.01	11.1		0.376	1.175			0.376	1.175	0.716	1.433	37.616
C	16	H	2	W	60	62	128.70	128.72	153.07	153.07	12.1										37.630
C	16	H	2	W	65	67	128.75	128.77	153.12	153.12	12.3		0.623	1.425			0.623	1.425	0.963	1.713	37.642
C	16	H	2	W	70	72	128.80	128.82	153.17	153.17	11.0		0.349	1.135			0.349	1.135	0.689	1.388	37.654
C	16	H	2	W	75	77	128.85	128.87	153.22	153.22	11.8		0.495	1.138			0.495	1.138	0.835	1.391	37.666
C	16	H	2	W	80	82	128.90	128.92	153.27	153.27	10.7		0.478	1.194			0.478	1.194	0.818	1.454	37.678

(**Appendix Table 5-1** continued)

Hole	Core	Type	Section	Type	Top (cm)	Bottom (cm)	Top (m CSF-A)	Bottom (m CSF-A)	Depth (rmcd; m revised CCSF-A)	Depth (m adj rmcd; m adj rev CCSF-A)	Coarse Fraction (wt %)	Barren Sample	$\delta^{13}C$ measured at Bremen (‰, VPDB)	$\delta^{18}O$ measured at Bremen (‰, VPDB)	$\delta^{13}C$ measured at NOCS (‰, VPDB)	$\delta^{18}O$ measured at NOCS (‰, VPDB)	$\delta^{13}C$ compiled (‰, VPDB)	$\delta^{18}O$ compiled (‰, VPDB)	$\delta^{13}C$ adjusted to Cibs (true+0.34)	$\delta^{18}O$ adjusted to Cibs (true+0.1/0.89)	Age (Ma) [WK Age]
C	16	H	2	W	85	87	128.95	128.97	153.32	153.32	12.3		0.282	1.033			0.282	1.033	0.622	1.273	37.690
C	16	H	2	W	90	92	129.00	129.02	153.37	153.37	10.7		0.396	1.197			0.396	1.197	0.736	1.457	37.701
C	16	H	2	W	95	97	129.05	129.07	153.42	153.42	11.4		0.480	1.420			0.480	1.420	0.820	1.708	37.711
C	16	H	2	W	100	102	129.10	129.12	153.47	153.47	10.8		0.377	1.200			0.377	1.200	0.717	1.461	37.720
C	16	H	2	W	104	106	129.14	129.16	153.51	153.51	11.8		0.435	1.194			0.435	1.194	0.775	1.454	37.728
C	16	H	2	W	110	112	129.20	129.22	153.57	153.57	11.5		0.385	1.214			0.385	1.214	0.725	1.476	37.739
C	16	H	2	W	115	117	129.25	129.27	153.62	153.62	11.8		0.536	1.176			0.536	1.176	0.876	1.434	37.749
C	16	H	2	W	120	122	129.30	129.32	153.67	153.67	13.3		0.565	1.318			0.565	1.318	0.905	1.593	37.758
C	16	H	2	W	125	127	129.35	129.37	153.72	153.72	12.3		0.513	1.213			0.513	1.213	0.853	1.475	37.768
C	16	H	2	W	130	132	129.40	129.42	153.77	153.77	14.7										37.777
C	16	H	2	W	135	137	129.45	129.47	153.82	153.82	14.0		0.423	1.242			0.423	1.242	0.763	1.508	37.787
C	16	H	2	W	140	142	129.50	129.52	153.87	153.87	16.0		0.521	1.367			0.521	1.367	0.861	1.648	37.796
C	16	H	2	W	145	147	129.55	129.57	153.92	153.92	15.1		0.519	1.192			0.519	1.192	0.859	1.452	37.806
C	16	H	3	W	1	3	129.61	129.63	153.98	153.98	16.1		0.495	1.196			0.495	1.196	0.835	1.456	37.817
C	16	H	3	W	6	8	129.66	129.68	154.03	154.03	14.3		0.474	1.262			0.474	1.262	0.814	1.530	37.826
C	16	H	3	W	11	13	129.71	129.73	154.08	154.08	14.1		0.444	1.120			0.444	1.120	0.784	1.370	37.836
C	16	H	3	W	16	18	129.76	129.78	154.13	154.13	12.5		0.478	1.318			0.478	1.318	0.818	1.593	37.845
C	16	H	3	W	21	23	129.81	129.83	154.18	154.18	11.0		0.474	1.314			0.474	1.314	0.814	1.589	37.855
C	16	H	3	W	26	28	129.86	129.88	154.23	154.23	12.7		0.409	1.098			0.409	1.098	0.749	1.346	37.864
C	16	H	3	W	31	33	129.91	129.93	154.28	154.28	11.2		0.474	1.136			0.474	1.136	0.814	1.389	37.874
C	16	H	3	W	36	38	129.96	129.98	154.33	154.33	10.5		0.503	1.145			0.503	1.145	0.843	1.399	37.883
C	16	H	3	W	41	43	130.01	130.03	154.38	154.38	13.5		0.425	1.130			0.425	1.130	0.765	1.382	37.893
C	16	H	3	W	46	48	130.06	130.08	154.43	154.43	9.4		0.493	1.179			0.493	1.179	0.833	1.437	37.902
C	16	H	3	W	51	53	130.11	130.13	154.48	154.48	10.0		0.476	1.026			0.476	1.026	0.816	1.266	37.912
C	16	H	3	W	56	58	130.16	130.18	154.53	154.53	9.7		0.421	1.013			0.421	1.013	0.761	1.251	37.921
C	16	H	3	W	61	63	130.21	130.23	154.58	154.58	8.6		0.462	1.127			0.462	1.127	0.802	1.379	37.931
C	16	H	3	W	66	68	130.26	130.28	154.63	154.63	8.5										37.940
C	16	H	3	W	71	73	130.31	130.33	154.68	154.68	12.0				0.432	1.082	0.432	1.082	0.772	1.328	37.950
C	16	H	3	W	71	73	130.31	130.33	154.68	154.68											37.950
C	16	H	3	W	76	78	130.36	130.38	154.73	154.73	9.5		0.401	1.195			0.401	1.195	0.741	1.455	37.959
C	16	H	3	W	81	83	130.41	130.43	154.78	154.78	8.0		0.398	0.832			0.398	0.832	0.738	1.047	37.969
C	16	H	3	W	86	88	130.46	130.48	154.83	154.83	9.1		0.372	0.887			0.372	0.887	0.712	1.109	37.978
C	16	H	3	W	91	93	130.51	130.53	154.88	154.88	10.5		0.452	0.914			0.452	0.914	0.792	1.140	37.988
C	16	H	3	W	96	98	130.56	130.58	154.93	154.93	10.2		0.433	0.981			0.433	0.981	0.773	1.215	37.997
C	16	H	3	W	101	103	130.61	130.63	154.98	154.98	9.8		0.470	0.954			0.470	0.954	0.810	1.184	38.007
C	16	H	3	W	106	108	130.66	130.68	155.03	155.03	9.8		0.489	0.994			0.489	0.994	0.829	1.229	38.016
C	16	H	3	W	111	113	130.71	130.73	155.08	155.08	9.5		0.545	1.070			0.545	1.070	0.885	1.315	38.026
C	16	H	3	W	116	118	130.76	130.78	155.13	155.13	10.2		0.329	0.960			0.329	0.960	0.669	1.191	38.036
C	16	H	3	W	121	123	130.81	130.83	155.18	155.18	10.8		0.440	1.409			0.440	1.409	0.780	1.696	38.049
C	16	H	3	W	126	128	130.86	130.88	155.23	155.23			0.485	1.146			0.485	1.146	0.825	1.400	38.061
C	16	H	3	W	131	133	130.91	130.93	155.28	155.28	12.5				0.523	1.347	0.523	1.347	0.863	1.625	38.073
C	16	H	3	W	136	138	130.96	130.98	155.33	155.33	10.5				0.273	1.278	0.273	1.278	0.613	1.548	38.083
C	16	H	3	W	141	143	131.01	131.03	155.38	155.38	12.4				0.506	1.354	0.506	1.354	0.846	1.634	38.092
C	16	H	3	W	146	148	131.06	131.08	155.43	155.43	12.8				0.663	1.190	0.663	1.190	1.003	1.450	38.100
C	16	H	4	W	1	3	131.11	131.13	155.48	155.48	11.0				0.706	1.334	0.706	1.334	1.046	1.611	38.108
C	16	H	4	W	6	8	131.16	131.18	155.53	155.53	10.6				0.713	1.284	0.713	1.284	1.053	1.555	38.117
C	16	H	4	W	11	13	131.21	131.23	155.58	155.58					0.658	1.144	0.658	1.144	0.998	1.398	38.125
C	16	H	4	W	16	18	131.26	131.28	155.63	155.63			0.524	1.197			0.524	1.197	0.864	1.457	38.133
C	16	H	4	W	21	23	131.31	131.33	155.68	155.68	13.7				0.562	1.087	0.562	1.087	0.902	1.333	38.142
C	16	H	4	W	26	28	131.36	131.38	155.73	155.73	12.0				0.442	1.245	0.442	1.245	0.782	1.511	38.150
C	16	H	4	W	31	33	131.41	131.43	155.78	155.78	15.8				0.475	1.147	0.475	1.147	0.815	1.401	38.158
C	16	H	4	W	36	38	131.46	131.48	155.83	155.83	13.8				0.355	1.027	0.355	1.027	0.695	1.267	38.167
C	16	H	4	W	41	43	131.51	131.53	155.88	155.88	11.7				0.253	0.919	0.253	0.919	0.593	1.145	38.175
C	16	H	4	W	46	48	131.56	131.58	155.93	155.93	10.5				0.544	1.201	0.544	1.201	0.884	1.461	38.184
C	16	H	4	W	51	53	131.61	131.63	155.98	155.98	8.8				0.165	0.963	0.165	0.963	0.505	1.194	38.192
C	16	H	4	W	56	58	131.66	131.68	156.03	156.03	8.6				0.268	1.026	0.268	1.026	0.608	1.265	38.200
C	16	H	4	W	61	63	131.71	131.73	156.08	156.08	9.9				0.481	1.231	0.481	1.231	0.821	1.496	38.209
C	16	H	4	W	66	68	131.76	131.78	156.13	156.13					0.292	0.937	0.292	0.937	0.632	1.165	38.217
C	16	H	4	W	71	73	131.81	131.83	156.18	156.18	7.0				0.524	1.171	0.524	1.171	0.864	1.428	38.225
C	16	H	4	W	76	78	131.86	131.88	156.23	156.23											38.234

(**Appendix Table 5-1** continued)

Hole	Core	Type	Section	Type	Top (cm)	Bottom (cm)	Top (m CSF-A)	Bottom (m CSF-A)	Depth (rmcd; m revised CCSF-A)	Depth (m adj rmcd; m adj rev CCSF-A)	Coarse Fraction (wt %)	Barren Sample	$\delta^{13}C$ measured at Bremen (‰, VPDB)	$\delta^{18}O$ measured at Bremen (‰, VPDB)	$\delta^{13}C$ measured at NOCS (‰, VPDB)	$\delta^{18}O$ measured at NOCS (‰, VPDB)	$\delta^{13}C$ compiled (‰, VPDB)	$\delta^{18}O$ compiled (‰, VPDB)	$\delta^{13}C$ adjusted to Cibs (true+0.34)	$\delta^{18}O$ adjusted to Cibs (true+0.1/0.89)	Age (Ma) [WK Age]
C	16	H	4	W	81	83	131.91	131.93	156.28	156.28	6.9				0.262	0.964	0.262	0.964	0.602	1.196	38.242
C	16	H	4	W	86	88	131.96	131.98	156.33	156.33	6.5				0.248	0.927	0.248	0.927	0.588	1.154	38.250
C	16	H	4	W	91	93	132.01	132.03	156.38	156.38	6.8				0.482	1.231	0.482	1.231	0.822	1.496	38.259
C	16	H	4	W	96	98	132.06	132.08	156.43	156.43	7.0				0.291	1.020	0.291	1.020	0.631	1.258	38.267
C	17	H	1	W	1	3	131.11	131.13	156.82	156.82	14.1				0.166	0.869	0.166	0.869	0.506	1.089	38.332
C	17	H	1	W	6	8	131.16	131.18	156.87	156.87	18.0				0.138	0.772	0.138	0.772	0.478	0.980	38.341
B	15	H	1	W	36	38	131.56	131.58	157.57	156.90	9.1				0.041	0.693	0.041	0.693	0.381	0.891	38.346
C	17	H	1	W	11	13	131.21	131.23	156.92	156.92	9.6				0.113	1.008	0.113	1.008	0.453	1.245	38.349
B	15	H	1	W	41	43	131.61	131.63	157.62	156.95	9.1				0.455	0.905	0.455	0.905	0.795	1.130	38.354
C	17	H	1	W	16	18	131.26	131.28	156.97	156.97	9.5		0.260	1.043	0.124	1.004	0.192	1.024	0.532	1.263	38.357
B	15	H	1	W	46	48	131.66	131.68	157.67	157.00	13.7		0.227	0.932			0.227	0.932	0.567	1.160	38.362
C	17	H	1	W	21	23	131.31	131.33	157.02	157.02	9.5				0.310	1.112	0.310	1.112	0.650	1.362	38.366
B	15	H	1	W	51	53	131.71	131.73	157.72	157.05	10.2		0.256	1.003			0.256	1.003	0.596	1.239	38.371
B	15	H	1	W	56	58	131.76	131.78	157.77	157.10	11.2		0.333	0.942	0.442	1.105	0.388	1.023	0.728	1.262	38.379
B	15	H	1	W	61	63	131.81	131.83	157.82	157.15	13.8		0.179	0.988			0.179	0.988	0.519	1.222	38.387
B	15	H	1	W	66	68	131.86	131.88	157.87	157.20	14.9		0.362	1.057			0.362	1.057	0.702	1.300	38.396
B	15	H	1	W	71	73	131.91	131.93	157.92	157.26	14.4		0.390	1.125			0.390	1.125	0.730	1.376	38.405
B	15	H	1	W	76	78	131.96	131.98	157.97	157.33	14.5		0.294	1.216			0.294	1.216	0.634	1.479	38.414
B	15	H	1	W	81	83	132.01	132.03	158.02	157.39	12.1		0.257	1.210			0.257	1.210	0.597	1.472	38.424
B	15	H	1	W	86	88	132.06	132.08	158.07	157.46	13.9		0.414	1.188			0.414	1.188	0.754	1.447	38.434
B	15	H	1	W	91	93	132.11	132.13	158.12	157.53	12.2		0.304	1.060			0.304	1.060	0.644	1.303	38.443
B	15	H	1	W	96	98	132.16	132.18	158.17	157.60	12.9		0.181	1.010			0.181	1.010	0.521	1.247	38.453
B	15	H	1	W	101	103	132.21	132.23	158.22	157.67	13.6				0.309	0.930	0.309	0.930	0.649	1.158	38.462
B	15	H	1	W	106	108	132.26	132.28	158.27	157.73	13.0		0.332	1.127			0.332	1.127	0.672	1.379	38.474
B	15	H	1	W	111	113	132.31	132.33	158.32	157.80	13.8		0.492	1.109			0.492	1.109	0.832	1.358	38.488
B	15	H	1	W	116	118	132.36	132.38	158.37	157.87	15.9		0.566	0.947			0.566	0.947	0.906	1.176	38.502
B	15	H	1	W	121	123	132.41	132.43	158.42	157.94	13.5				0.450	0.733	0.450	0.733	0.790	0.936	38.516
B	15	H	1	W	126	128	132.46	132.48	158.47	158.01	10.5		0.378	1.093			0.378	1.093	0.718	1.340	38.530
B	15	H	1	W	131	133	132.51	132.53	158.52	158.08	10.6										38.545
B	15	H	1	W	136	138	132.56	132.58	158.57	158.15	8.1		0.546	0.806			0.546	0.806	0.886	1.018	38.559
B	15	H	1	W	141	143	132.61	132.63	158.62	158.22	7.6		0.336	0.921			0.336	0.921	0.676	1.147	38.574
B	15	H	1	W	146	148	132.66	132.68	158.67	158.29			0.305	0.903			0.305	0.903	0.645	1.127	38.589
B	15	H	2	W	1	3	132.71	132.73	158.72	158.36	6.9		0.450	1.050			0.450	1.050	0.790	1.292	38.604
B	15	H	2	W	6	8	132.76	132.78	158.77	158.43	6.0		0.298	0.781	0.331	0.774	0.314	0.777	0.654	0.986	38.618
B	15	H	2	W	11	13	132.81	132.83	158.82	158.50	6.0		0.250	0.655			0.250	0.655	0.590	0.848	38.633
B	15	H	2	W	16	18	132.86	132.88	158.87	158.56	5.9				0.670	1.124	0.670	1.124	1.010	1.375	38.644
B	15	H	2	W	21	23	132.91	132.93	158.92	158.62	6.7				0.437	0.862	0.437	0.862	0.777	1.081	38.650
B	15	H	2	W	26	28	132.96	132.98	158.97	158.68	6.4		0.360	0.983			0.360	0.983	0.700	1.217	38.656
B	15	H	2	W	31	33	133.01	133.03	159.02	158.74	7.0		0.325	0.902			0.325	0.902	0.665	1.126	38.662
B	15	H	2	W	36	38	133.06	133.08	159.07	158.80	9.7				0.230	0.806	0.230	0.806	0.570	1.017	38.668
B	15	H	2	W	41	43	133.11	133.13	159.12	158.86	7.5		0.373	0.940			0.373	0.940	0.713	1.169	38.674
B	15	H	2	W	46	48	133.16	133.18	159.17	158.91	5.9		0.275	0.901			0.275	0.901	0.615	1.125	38.680
B	15	H	2	W	51	53	133.21	133.23	159.22	158.97	5.9				0.424	1.253	0.424	1.253	0.764	1.521	38.686
B	15	H	2	W	56	58	133.26	133.28	159.27	159.03	7.3				0.421	1.042	0.421	1.042	0.761	1.283	38.692
B	15	H	2	W	61	63	133.31	133.33	159.32	159.09			0.448	1.097			0.448	1.097	0.788	1.345	38.698
B	15	H	2	W	66	68	133.36	133.38	159.37	159.15	7.6		0.405	1.179			0.405	1.179	0.745	1.437	38.704
B	15	H	2	W	71	73	133.41	133.43	159.42	159.21	6.2		0.298	0.940			0.298	0.940	0.638	1.169	38.710
B	15	H	2	W	76	78	133.46	133.48	159.47	159.26	5.5		0.136	0.743			0.136	0.743	0.476	0.947	38.716
B	15	H	2	W	81	83	133.51	133.53	159.52	159.32	6.0		0.145	0.721	0.446	0.918	0.295	0.819	0.635	1.033	38.722
B	15	H	2	W	86	88	133.56	133.58	159.57	159.38	8.6				0.289	0.829	0.289	0.829	0.629	1.044	38.728
B	15	H	2	W	91	93	133.61	133.63	159.62	159.44	5.1		0.240	0.846			0.240	0.846	0.580	1.063	38.734
B	15	H	2	W	96	98	133.66	133.68	159.67	159.50	5.9		0.236	0.783			0.236	0.783	0.576	0.992	38.740
B	15	H	2	W	101	103	133.71	133.73	159.72	159.55	6.2										38.746
B	15	H	2	W	106	108	133.76	133.78	159.77	159.61	7.0		0.408	1.022			0.408	1.022	0.748	1.261	38.752
B	15	H	2	W	111	113	133.81	133.83	159.82	159.67	5.8		0.242	0.823			0.242	0.823	0.582	1.037	38.758
B	15	H	2	W	116	118	133.86	133.88	159.87	159.73	7.4				0.408	1.056	0.408	1.056	0.748	1.299	38.764
B	15	H	2	W	121	123	133.91	133.93	159.92	159.79	7.8		0.412	0.984	0.422	0.973	0.417	0.979	0.757	1.212	38.769
B	15	H	2	W	126	128	133.96	133.98	159.97	159.85	7.6		0.485	1.004			0.485	1.004	0.825	1.240	38.774
B	15	H	2	W	131	133	134.01	134.03	160.02	159.90	7.8		0.453	1.049			0.453	1.049	0.793	1.291	38.779
B	15	H	2	W	136	138	134.06	134.08	160.07	159.96	6.4		0.540	1.052			0.540	1.052	0.880	1.294	38.784

(**Appendix Table 5-1** continued)

Hole	Core	Type	Section	Type	Top (cm)	Bottom (cm)	Top (m CSF-A)	Bottom (m CSF-A)	Depth (rmcd; m revised CCSF-A)	Depth (m adj rmcd; m adj rev CCSF-A)	Coarse Fraction (wt %)	Barren Sample	$\delta^{13}C$ measured at Bremen (‰, VPDB)	$\delta^{18}O$ measured at Bremen (‰, VPDB)	$\delta^{13}C$ measured at NOCS (‰, VPDB)	$\delta^{18}O$ measured at NOCS (‰, VPDB)	$\delta^{13}C$ compiled (‰, VPDB)	$\delta^{18}O$ compiled (‰, VPDB)	$\delta^{13}C$ adjusted to Cibs (true+0.34)	$\delta^{18}O$ adjusted to Cibs (true+0.1/0.89)	Age (Ma) [WK Age]
B	15	H	2	W	141	143	134.11	134.13	160.12	160.01	7.0		0.444	0.960			0.444	0.960	0.784	1.191	38.789
B	15	H	2	W	146	148	134.16	134.18	160.17	160.07	7.4		0.414	1.010	0.476	1.039	0.445	1.025	0.785	1.264	38.793
B	15	H	3	W	1	3	134.21	134.23	160.22	160.12	5.2		0.323	0.890	0.366	0.959	0.345	0.924	0.685	1.151	38.798
B	15	H	3	W	6	8	134.26	134.28	160.27	160.18	4.9				0.533	0.821	0.533	0.821	0.873	1.035	38.803
B	15	H	3	W	11	13	134.31	134.33	160.32	160.23	6.1				0.551	0.856	0.551	0.856	0.891	1.074	38.808
B	15	H	3	W	16	18	134.36	134.38	160.37	160.29	4.5				0.238	0.893	0.238	0.893	0.578	1.116	38.813
B	15	H	3	W	21	23	134.41	134.43	160.42	160.34	3.8		0.282	0.787	0.425	0.591	0.354	0.689	0.694	0.887	38.818
B	15	H	3	W	26	28	134.46	134.48	160.47	160.40	8.7				0.165	0.535	0.165	0.535	0.505	0.713	38.823
B	15	H	3	W	31	33	134.51	134.53	160.52	160.46	6.7		0.286	0.745			0.286	0.745	0.626	0.949	38.828
B	15	H	3	W	36	38	134.56	134.58	160.57	160.52	6.3		0.360	0.841			0.360	0.841	0.700	1.057	38.833
B	15	H	3	W	41	43	134.61	134.63	160.62	160.58	7.4				0.604	1.091	0.604	1.091	0.944	1.339	38.838
B	15	H	3	W	46	48	134.66	134.68	160.67	160.64	9.4				0.603	1.078	0.603	1.078	0.943	1.324	38.844
B	15	H	3	W	51	53	134.71	134.73	160.72	160.70	9.5		0.554	1.069			0.554	1.069	0.894	1.313	38.849
B	15	H	3	W	56	58	134.76	134.78	160.77	160.75	10.3		0.743	1.090			0.743	1.090	1.083	1.337	38.854
B	15	H	3	W	61	63	134.81	134.83	160.82	160.81	11.3		0.580	1.060			0.580	1.060	0.920	1.303	38.859
B	15	H	3	W	66	68	134.86	134.88	160.87	160.87	7.0				0.640	0.912	0.640	0.912	0.980	1.138	38.864
B	15	H	3	W	71	73	134.91	134.93	160.92	160.94	7.0		0.536	0.823			0.536	0.823	0.876	1.037	38.870
B	15	H	3	W	76	78	134.96	134.98	160.97	161.00	8.5		0.453	1.077			0.453	1.077	0.793	1.322	38.876
B	15	H	3	W	81	83	135.01	135.03	161.02	161.07	9.2		0.553	0.897	0.678	1.099	0.615	0.998	0.955	1.234	38.881
B	15	H	3	W	86	88	135.06	135.08	161.07	161.13	8.3		0.391	0.930	0.531	0.832	0.461	0.881	0.801	1.102	38.887
B	15	H	3	W	91	93	135.11	135.13	161.12	161.19	8.3		0.442	0.940			0.442	0.940	0.782	1.169	38.893
B	15	H	3	W	96	98	135.16	135.18	161.17	161.26	9.5				0.239	0.588	0.239	0.588	0.579	0.772	38.898
B	15	H	3	W	101	103	135.21	135.23	161.22	161.32	7.4		0.437	0.997			0.437	0.997	0.777	1.233	38.904
B	15	H	3	W	106	108	135.26	135.28	161.27	161.39	7.3				0.613	1.270	0.613	1.270	0.953	1.539	38.910
B	15	H	3	W	111	113	135.31	135.33	161.32	161.45	7.4				0.788	1.153	0.788	1.153	1.128	1.408	38.918
B	15	H	3	W	116	118	135.36	135.38	161.37	161.51	7.7		0.433	0.913			0.433	0.913	0.773	1.138	38.927
B	15	H	3	W	121	123	135.41	135.43	161.42	161.58	10.0		0.475	0.951			0.475	0.951	0.815	1.181	38.935
B	15	H	3	W	126	128	135.46	135.48	161.47	161.64	9.3		0.433	0.928			0.433	0.928	0.773	1.155	38.944
B	15	H	3	W	131	133	135.51	135.53	161.52	161.71	10.3		0.366	0.711			0.366	0.711	0.706	0.911	38.952
B	15	H	3	W	136	138	135.56	135.58	161.57	161.77	11.3				0.234	0.661	0.234	0.661	0.574	0.856	38.961
B	15	H	3	W	141	143	135.61	135.63	161.62	161.84	10.5		0.579	0.966			0.579	0.966	0.919	1.198	38.969
B	15	H	3	W	146	148	135.66	135.68	161.67	161.90	9.0				0.741	1.337	0.741	1.337	1.081	1.615	38.978
B	15	H	4	W	1	3	135.71	135.73	161.72	161.96	8.8		0.669	1.147			0.669	1.147	1.009	1.401	38.987
B	15	H	4	W	6	8	135.76	135.78	161.77	162.03	6.9		0.301	0.833			0.301	0.833	0.641	1.048	38.995
B	15	H	4	W	11	13	135.81	135.83	161.82	162.09	6.0		0.425	0.778			0.425	0.778	0.765	0.987	39.004
B	15	H	4	W	16	18	135.86	135.88	161.87	162.16	5.5		0.277	0.676			0.277	0.676	0.617	0.872	39.012
B	15	H	4	W	21	23	135.91	135.93	161.92	162.22	6.0				0.582	1.002	0.582	1.002	0.922	1.238	39.021
B	15	H	4	W	26	28	135.96	135.98	161.97	162.28	5.3		0.412	0.871			0.412	0.871	0.752	1.091	39.029
B	15	H	4	W	31	33	136.01	136.03	162.02	162.35	6.5				0.461	0.856	0.461	0.856	0.801	1.074	39.038
B	15	H	4	W	36	38	136.06	136.08	162.07	162.41	5.1		0.232	0.655			0.232	0.655	0.572	0.848	39.046
B	15	H	4	W	41	43	136.11	136.13	162.12	162.48	4.0				0.636	1.140	0.636	1.140	0.976	1.393	39.055
B	15	H	4	W	46	48	136.16	136.18	162.17	162.55	5.4				0.555	1.151	0.555	1.151	0.895	1.405	39.064
B	15	H	4	W	51	53	136.21	136.23	162.22	162.62	7.6				0.494	0.823	0.494	0.823	0.834	1.037	39.074
B	15	H	4	W	56	58	136.26	136.28	162.27	162.70	7.6				0.572	1.080	0.572	1.080	0.912	1.325	39.084
B	15	H	4	W	61	63	136.31	136.33	162.32	162.77	8.1		0.394	0.979			0.394	0.979	0.734	1.212	39.094
B	15	H	4	W	66	68	136.36	136.38	162.37	162.84	8.5		0.591	1.073			0.591	1.073	0.931	1.318	39.105
B	15	H	4	W	71	73	136.41	136.43	162.42	162.92	6.3				0.653	1.149	0.653	1.149	0.993	1.404	39.117
B	15	H	4	W	76	78	136.46	136.48	162.47	162.99	7.1				0.852	1.253	0.852	1.253	1.192	1.521	39.130
B	15	H	4	W	81	83	136.51	136.53	162.52	163.06	8.3		0.556	0.976			0.556	0.976	0.896	1.209	39.142
B	15	H	4	W	86	88	136.56	136.58	162.57	163.14	8.2				0.685	0.896	0.685	0.896	1.025	1.119	39.154
B	15	H	4	W	91	93	136.61	136.63	162.62	163.21	7.9		0.405	0.904			0.405	0.904	0.745	1.128	39.167
B	15	H	4	W	96	98	136.66	136.68	162.67	163.28	6.6		0.439	0.846			0.439	0.846	0.779	1.063	39.179
B	15	H	4	W	101	103	136.71	136.73	162.72	163.36	6.2		0.357	0.752			0.357	0.752	0.697	0.957	39.192
B	15	H	4	W	106	108	136.76	136.78	162.77	163.42	4.9		0.327	0.662			0.327	0.662	0.667	0.856	39.202
B	15	H	4	W	111	113	136.81	136.83	162.82	163.48	8.1		0.416	0.786			0.416	0.786	0.756	0.996	39.213
B	15	H	4	W	116	118	136.86	136.88	162.87	163.54	14.5		0.272	0.701	0.298	0.639	0.285	0.670	0.625	0.865	39.223
B	15	H	4	W	121	123	136.91	136.93	162.92	163.61	9.5		0.514	0.865			0.514	0.865	0.854	1.084	39.234
B	15	H	4	W	126	128	136.96	136.98	162.97	163.67	9.3		0.531	0.673			0.531	0.673	0.871	0.869	39.244
B	15	H	4	W	131	133	137.01	137.03	163.02	163.73	7.8		0.538	0.836			0.538	0.836	0.878	1.052	39.255
B	15	H	4	W	136	138	137.06	137.08	163.07	163.79	11.9				0.698	0.958	0.698	0.958	1.038	1.189	39.265

(**Appendix Table 5-1** continued)

Hole	Core	Type	Section	Type	Top (cm)	Bottom (cm)	Top (m CSF-A)	Bottom (m CSF-A)	Depth (rmcd; m revised CCSF-A)	Depth (m adj rmcd; m adj rev CCSF-A)	Coarse Fraction (wt %)	Barren Sample	$\delta^{13}C$ measured at Bremen (‰, VPDB)	$\delta^{18}O$ measured at Bremen (‰, VPDB)	$\delta^{13}C$ measured at NOCS (‰, VPDB)	$\delta^{18}O$ measured at NOCS (‰, VPDB)	$\delta^{13}C$ compiled (‰, VPDB)	$\delta^{18}O$ compiled (‰, VPDB)	$\delta^{13}C$ adjusted to Cibs (true+0.34)	$\delta^{18}O$ adjusted to Cibs (true+0.1/0.89)	Age (Ma) [WK Age]
B	15	H	4	W	141	143	137.11	137.13	163.12	163.86	10.5		0.512	0.901			0.512	0.901	0.852	1.125	39.276
B	15	H	4	W	146	148	137.16	137.18	163.17	163.92	7.2		0.612	0.961			0.612	0.961	0.952	1.192	39.286
B	15	H	5	W	1	3	137.21	137.23	163.22	163.98	8.8		0.493	0.891			0.493	0.891	0.833	1.113	39.297
B	15	H	5	W	6	8	137.26	137.28	163.27	164.04	8.9		0.484	0.843			0.484	0.843	0.824	1.060	39.307
B	15	H	5	W	11	13	137.31	137.33	163.32	164.10	10.3		0.599	0.877	0.819	0.901	0.709	0.889	1.049	1.111	39.318
B	15	H	5	W	16	18	137.36	137.38	163.37	164.17	8.9		0.450	0.664			0.450	0.664	0.790	0.858	39.328
B	15	H	5	W	21	23	137.41	137.43	163.42	164.23	9.5		0.530	0.705			0.530	0.705	0.870	0.904	39.339
B	15	H	5	W	26	28	137.46	137.48	163.47	164.29	11.4		0.581	0.796			0.581	0.796	0.921	1.007	39.349
B	15	H	5	W	31	33	137.51	137.53	163.52	164.35	8.9		0.544	0.614			0.544	0.614	0.884	0.802	39.360
B	15	H	5	W	36	38	137.56	137.58	163.57	164.42	7.4		0.590	0.653			0.590	0.653	0.930	0.846	39.370
B	15	H	5	W	41	43	137.61	137.63	163.62	164.48	19.8		0.516	0.682			0.516	0.682	0.856	0.879	39.380
B	15	H	5	W	46	48	137.66	137.68	163.67	164.55	13.2		0.735	0.910			0.735	0.910	1.075	1.135	39.389
B	15	H	5	W	51	53	137.71	137.73	163.72	164.61	12.5				0.758	0.744	0.758	0.744	1.098	0.948	39.398
B	15	H	5	W	56	58	137.76	137.78	163.77	164.68			0.752	0.944			0.752	0.944	1.092	1.173	39.407
B	15	H	5	W	56	58	137.76	137.78	163.77	164.68	12.2		0.700	0.840			0.700	0.840	1.040	1.056	39.407
B	15	H	5	W	61	63	137.81	137.83	163.82	164.74	13.6		0.614	0.746			0.614	0.746	0.954	0.951	39.416
B	15	H	5	W	66	68	137.86	137.88	163.87	164.81	14.2		0.688	0.845			0.688	0.845	1.028	1.062	39.425
B	15	H	5	W	71	73	137.91	137.93	163.92	164.88	14.1		0.562	0.714			0.562	0.714	0.902	0.915	39.434
B	15	H	5	W	76	78	137.96	137.98	163.97	164.94	16.2		0.879	1.099			0.879	1.099	1.219	1.347	39.443
B	15	H	5	W	81	83	138.01	138.03	164.02	165.01	13.7		0.786	0.975			0.786	0.975	1.126	1.208	39.452
B	15	H	5	W	86	88	138.06	138.08	164.07	165.07	13.5		0.771	0.786			0.771	0.786	1.111	0.996	39.461
B	15	H	5	W	91	93	138.11	138.13	164.12	165.14	12.0				0.838	0.591	0.838	0.591	1.178	0.777	39.470
B	15	H	5	W	96	98	138.16	138.18	164.17	165.21	13.5		0.600	0.720			0.600	0.720	0.940	0.921	39.479
B	15	H	5	W	101	103	138.21	138.23	164.22	165.27	13.7		0.795	0.948			0.795	0.948	1.135	1.178	39.488
B	15	H	5	W	106	108	138.26	138.28	164.27	165.34	15.0		0.747	0.839			0.747	0.839	1.087	1.055	39.497
B	15	H	5	W	111	113	138.31	138.33	164.32	165.40	12.9		0.745	0.864			0.745	0.864	1.085	1.083	39.506
B	15	H	5	W	116	118	138.36	138.38	164.37	165.47	13.5		0.665	0.538			0.665	0.538	1.005	0.717	39.515
B	15	H	5	W	121	123	138.41	138.43	164.42	165.54					0.827	0.506	0.827	0.506	1.167	0.681	39.524
B	15	H	5	W	126	128	138.46	138.48	164.47	165.60	14.0		0.751	0.882			0.751	0.882	1.091	1.103	39.533
B	15	H	5	W	131	133	138.51	138.53	164.52	165.67	14.2		0.920	0.893			0.920	0.893	1.260	1.116	39.542
C	17	H	6	W	138	140	139.98	140.00	165.69	165.69	13.0		0.767	0.756			0.767	0.756	1.107	0.962	39.545
B	15	H	5	W	136	138	138.56	138.58	164.57	165.74	13.3		0.736	0.723			0.736	0.723	1.076	0.925	39.550
C	17	H	6	W	144	146	140.04	140.06	165.75	165.75	14.1										39.551
C	17	H	6	W	148	150	140.08	140.10	165.79	165.79	14.4		0.776	0.734			0.776	0.734	1.116	0.937	39.556
B	15	H	5	W	141	143	138.61	138.63	164.62	165.80	15.3		0.814	1.003			0.814	1.003	1.154	1.239	39.557
C	17	H	7	W	1	3	140.11	140.13	165.82	165.82	13.3		0.629	0.911			0.629	0.911	0.969	1.136	39.559
B	15	H	5	W	146	148	138.66	138.68	164.67	165.87	18.6		0.749	0.661			0.749	0.661	1.089	0.855	39.564
C	17	H	7	W	6	8	140.16	140.18	165.87	165.87	11.4		0.728	0.642			0.728	0.642	1.068	0.834	39.565
C	17	H	7	W	11	13	140.21	140.23	165.92	165.92	11.8		0.664	0.653			0.664	0.653	1.004	0.846	39.570
B	15	H	6	W	1	3	138.71	138.73	164.72	165.93	18.7	X									39.572
C	17	H	7	W	16	18	140.26	140.28	165.97	165.97	13.2		0.534	0.946			0.534	0.946	0.874	1.175	39.576
B	15	H	6	W	6	8	138.76	138.78	164.77	166.00	19.2	X									39.579
C	17	H	7	W	21	23	140.31	140.33	166.02	166.02	13.6	X									39.581
B	15	H	6	W	11	13	138.81	138.83	164.82	166.07	16.8		0.591	0.763			0.591	0.763	0.931	0.970	39.586
C	17	H	7	W	26	28	140.36	140.38	166.07	166.07	14.7		0.340	0.637			0.340	0.637	0.680	0.828	39.587
C	17	H	7	W	31	33	140.41	140.43	166.12	166.12	13.7				0.690		0.690		1.030		39.592
B	15	H	6	W	16	18	138.86	138.88	164.87	166.13	16.0	X									39.593
C	17	H	7	W	36	38	140.46	140.48	166.17	166.17	14.3		0.644	0.771			0.644	0.771	0.984	0.979	39.598
B	15	H	6	W	21	23	138.91	138.93	164.92	166.20	15.0		0.540	0.759			0.540	0.759	0.880	0.965	39.601
C	17	H	7	W	41	43	140.51	140.53	166.22	166.22	15.2		0.426	0.802			0.426	0.802	0.766	1.014	39.603
B	15	H	6	W	26	28	138.96	138.98	164.97	166.26					0.587	0.693	0.587	0.693	0.927	0.891	39.608
C	17	H	7	W	46	48	140.56	140.58	166.27	166.27	15.4		0.479	0.834			0.479	0.834	0.819	1.049	39.609
C	17	H	7	W	51	53	140.61	140.63	166.32	166.32	15.7	X									39.614
B	15	H	6	W	31	33	139.01	139.03	165.02	166.33	14.9	X									39.615
C	17	H	7	W	56	58	140.66	140.68	166.37	166.37	14.9		0.415	0.667			0.415	0.667	0.755	0.862	39.620
B	15	H	6	W	36	38	139.06	139.08	165.07	166.38	14.6		1.008	0.988			1.008	0.988	1.348	1.223	39.621
C	17	H	7	W	61	63	140.71	140.73	166.42	166.42	15.3		0.402	0.618			0.402	0.618	0.742	0.807	39.625
B	15	H	6	W	41	43	139.11	139.13	165.12	166.43	12.9										39.626
C	17	H	7	W	65	67	140.75	140.77	166.46	166.46	15.6		0.842	0.697			0.842	0.697	1.182	0.896	39.630
B	15	H	6	W	46	48	139.16	139.18	165.17	166.48	16.2		0.732	0.727			0.732	0.727	1.072	0.929	39.632

(**Appendix Table 5-1** continued)

Hole	Core	Type	Section	Type	Top (cm)	Bottom (cm)	Top (m CSF-A)	Bottom (m CSF-A)	Depth (rmcd; m revised CCSF-A)	Depth (m adj rmcd; m adj rev CCSF-A)	Coarse Fraction (wt %)	Barren Sample	$\delta^{13}C$ measured at Bremen (‰, VPDB)	$\delta^{18}O$ measured at Bremen (‰, VPDB)	$\delta^{13}C$ measured at NOCS (‰, VPDB)	$\delta^{18}O$ measured at NOCS (‰, VPDB)	$\delta^{13}C$ compiled (‰, VPDB)	$\delta^{18}O$ compiled (‰, VPDB)	$\delta^{13}C$ adjusted to Cibs (true+0.34)	$\delta^{18}O$ adjusted to Cibs (true+0.1/0.89)	Age (Ma) [WK Age]
C	17	H	7	W	70	72	140.80	140.82	166.51	166.51	15.1										39.637
B	15	H	6	W	51	53	139.21	139.23	165.22	166.53	17.5		0.820	0.684			0.820	0.684	1.160	0.881	39.639
C	17	H	CC	W	1	3	140.83	140.85	166.54	166.54	14.2		0.637	0.606			0.637	0.606	0.977	0.793	39.641
B	15	H	6	W	56	58	139.26	139.28	165.27	166.58	16.4	X									39.647
C	17	H	CC	W	6	8	140.88	140.90	166.59	166.59	15.9		0.580	0.552			0.580	0.552	0.920	0.733	39.648
B	15	H	6	W	61	63	139.31	139.33	165.32	166.63	17.9	X									39.654
B	15	H	6	W	66	68	139.36	139.38	165.37	166.68	17.0										39.661
C	17	H	CC	W	17	19	140.99	141.01	166.70	166.70	15.5	X									39.664
B	15	H	6	W	68	70	139.38	139.40	165.39	166.70	18.5										39.664
B	15	H	6	W	71	73	139.41	139.43	165.42	166.73	17.2										39.669
C	17	H	CC	W	21	23	141.03	141.05	166.74	166.74	16.7	X									39.670
B	15	H	6	W	76	78	139.46	139.48	165.47	166.78	18.9	X									39.676
B	15	H	CC	W	1	3	139.53	139.55	165.54	166.85	15.6	X									39.686
B	15	H	CC	W	6	8	139.58	139.60	165.59	166.90	14.7	X									39.694
B	15	H	CC	W	11	13	139.63	139.65	165.64	166.95	15.1	X									39.701
B	15	H	CC	W	16	18	139.68	139.70	165.69	167.00	15.9	X									39.708
B	15	H	CC	W	21	23	139.73	139.75	165.74	167.05	15.4	X									39.715
B	15	H	CC	W	26	28	139.78	139.80	165.79	167.10	18.1	X									39.723
B	16	H	1	W	1	3	140.71	140.73	166.72	167.49	11.1	removed									39.780
B	16	H	1	W	6	8	140.76	140.78	166.77	167.54	12.2	removed									39.787
B	16	H	1	W	11	13	140.81	140.83	166.82	167.59	9.4	removed									39.794
B	16	H	1	W	16	18	140.86	140.88	166.87	167.64	7.4	removed									39.802
B	16	H	1	W	21	23	140.91	140.93	166.92	167.69	17.5	removed									39.809
B	16	H	1	W	26	28	140.96	140.98	166.97	167.74	13.9	removed									39.816
B	16	H	1	W	31	33	141.01	141.03	167.02	167.79	15.9	removed									39.824
B	16	H	1	W	36	38	141.06	141.08	167.07	167.84		removed									39.833
B	16	H	1	W	41	43	141.11	141.13	167.12	167.89			0.474	0.592			0.474	0.592	0.814	0.778	39.842
B	16	H	1	W	46	48	141.16	141.18	167.17	167.94	23.5				0.705	0.200	0.705	0.200	1.045	0.338	39.852
B	16	H	1	W	51	53	141.21	141.23	167.22	167.99			0.777	0.624			0.777	0.624	1.117	0.813	39.861
B	16	H	1	W	56	58	141.26	141.28	167.27	168.04			0.707	0.632			0.707	0.632	1.047	0.822	39.871
B	16	H	1	W	61	63	141.31	141.33	167.32	168.09			0.882	0.765			0.882	0.765	1.222	0.972	39.881
B	16	H	1	W	71	73	141.41	141.43	167.42	168.19	25.3		0.694	0.854			0.694	0.854	1.034	1.072	39.900
B	16	H	1	W	76	78	141.46	141.48	167.47	168.24			0.677	0.453			0.677	0.453	1.017	0.621	39.909
B	16	H	1	W	81	83	141.51	141.53	167.52	168.29											39.919
B	16	H	1	W	86	88	141.56	141.58	167.57	168.34			0.620	0.781			0.620	0.781	0.960	0.990	39.928
B	16	H	1	W	91	93	141.61	141.63	167.62	168.39	23.3		0.782	0.529			0.782	0.529	1.122	0.707	39.938
B	16	H	1	W	96	98	141.66	141.68	167.67	168.44			0.627	0.732			0.627	0.732	0.967	0.935	39.948
B	16	H	1	W	101	103	141.71	141.73	167.72	168.49			0.799	0.662			0.799	0.662	1.139	0.856	39.957
B	16	H	1	W	103	105	141.73	141.75	167.74	168.51			0.658	0.836			0.658	0.836	0.998	1.052	39.962
B	16	H	1	W	106	108	141.76	141.78	167.77	168.55			0.535	0.588			0.535	0.588	0.875	0.773	39.969
B	16	H	1	W	111	113	141.81	141.83	167.82	168.62			0.622	0.687			0.622	0.687	0.962	0.884	39.981
B	16	H	1	W	116	118	141.86	141.88	167.87	168.68	15.0				0.597	0.392	0.597	0.392	0.937	0.553	39.993
B	16	H	1	W	121	123	141.91	141.93	167.92	168.74			0.685	0.432			0.685	0.432	1.025	0.597	40.006
B	16	H	1	W	121	123	141.91	141.93	167.92	168.74											40.006
B	16	H	1	W	126	128	141.96	141.98	167.97	168.81			0.717	0.483			0.717	0.483	1.057	0.655	40.012
B	16	H	1	W	131	133	142.01	142.03	168.02	168.87			0.625	0.282			0.625	0.282	0.965	0.429	40.017
B	16	H	1	W	136	138	142.06	142.08	168.07	168.94	18.1				0.500	0.196	0.500	0.196	0.840	0.332	40.023
B	16	H	1	W	141	143	142.11	142.13	168.12	169.00		X									40.028
B	16	H	1	W	146	148	142.16	142.18	168.17	169.06		X									40.033
B	16	H	2	W	1	3	142.21	142.23	168.22	169.13	17.8	X									40.039
B	16	H	2	W	6	8	142.26	142.28	168.27	169.18	18.0	X	0.633	0.610			0.633	0.610	0.973	0.798	40.043
B	16	H	2	W	11	13	142.31	142.33	168.32	169.24	18.1										40.048
B	16	H	2	W	16	18	142.36	142.38	168.37	169.29	19.2				0.475	0.503	0.475	0.503	0.815	0.677	40.052
B	16	H	2	W	21	23	142.41	142.43	168.42	169.35	18.4		0.454	0.572			0.454	0.572	0.794	0.755	40.057
B	16	H	2	W	26	28	142.46	142.48	168.47	169.40	16.6	X									40.061
B	16	H	2	W	31	33	142.51	142.53	168.52	169.45	15.8		0.598	0.523			0.598	0.523	0.938	0.700	40.066
B	16	H	2	W	33	35	142.53	142.55	168.54	169.48	16.5										40.068
B	16	H	2	W	36	38	142.56	142.58	168.57	169.51	17.7	X									40.070
B	16	H	2	W	41	43	142.61	142.63	168.62	169.56	15.1										40.075
B	16	H	2	W	46	48	142.66	142.68	168.67	169.62	16.8		0.845	0.617			0.845	0.617	1.185	0.806	40.080

(**Appendix Table 5-1** continued)

Hole	Core	Type	Section	Type	Top (cm)	Bottom (cm)	Top (m CSF-A)	Bottom (m CSF-A)	Depth (rmcd; m revised CCSF-A)	Depth (m adj rmcd; m adj rev CCSF-A)	Coarse Fraction (wt %)	Barren Sample	$\delta^{13}C$ measured at Bremen (‰, VPDB)	$\delta^{18}O$ measured at Bremen (‰, VPDB)	$\delta^{13}C$ measured at NOCS (‰, VPDB)	$\delta^{18}O$ measured at NOCS (‰, VPDB)	$\delta^{13}C$ compiled (‰, VPDB)	$\delta^{18}O$ compiled (‰, VPDB)	$\delta^{13}C$ adjusted to Cibs (true+0.34)	$\delta^{18}O$ adjusted to Cibs (true+0.1/0.89)	Age (Ma) [WK Age]
B	16	H	2	W	51	53	142.71	142.73	168.72	169.67	18.3		0.601	0.549			0.601	0.549	0.941	0.729	40.084
B	16	H	2	W	56	58	142.76	142.78	168.77	169.73	16.5		0.701	0.728			0.701	0.728	1.041	0.930	40.089
B	16	H	2	W	61	63	142.81	142.83	168.82	169.78	14.8										40.093
B	16	H	2	W	66	68	142.86	142.88	168.87	169.83	15.1	X									40.098
B	16	H	2	W	71	73	142.91	142.93	168.92	169.89	10.7				0.193	0.174	0.193	0.174	0.533	0.308	40.102
B	16	H	2	W	76	78	142.96	142.98	168.97	169.94	16.7	X									40.107
B	16	H	2	W	81	83	143.01	143.03	169.02	170.00	17.3	X									40.111
B	16	H	2	W	86	88	143.06	143.08	169.07	170.05	17.6		0.412	0.685			0.412	0.685	0.752	0.882	40.116
B	16	H	2	W	88	90	143.08	143.10	169.09	170.07	18.5	X									40.118
B	16	H	2	W	91	93	143.11	143.13	169.12	170.10		X									40.120
B	16	H	2	W	96	98	143.16	143.18	169.17	170.16	17.0	X									40.125
B	16	H	2	W	101	103	143.21	143.23	169.22	170.21	16.0	X									40.129
B	16	H	2	W	106	108	143.26	143.28	169.27	170.27	16.4	X									40.134
B	16	H	2	W	108	110	143.28	143.30	169.29	170.29	16.2	X									40.136
B	16	H	2	W	111	113	143.31	143.33	169.32	170.32	16.1	X									40.138
B	16	H	2	W	116	118	143.36	143.38	169.37	170.38	16.3	X									40.143
B	16	H	2	W	121	123	143.41	143.43	169.42	170.43	14.9	X									40.148
B	16	H	2	W	126	128	143.46	143.48	169.47	170.48	18.1	X									40.152
B	16	H	2	W	128	130	143.48	143.50	169.49	170.51	17.0		0.509	0.783			0.509	0.783	0.849	0.992	40.154
B	16	H	2	W	131	133	143.51	143.53	169.52	170.54	16.2	X									40.157
B	16	H	2	W	136	138	143.56	143.58	169.57	170.59	16.8		0.512	1.068			0.512	1.068	0.852	1.312	40.161
B	16	H	2	W	141	143	143.61	143.63	169.62	170.65	18.2	X									40.166
B	16	H	2	W	146	148	143.66	143.68	169.67	170.70	18.1		0.530	0.793			0.530	0.793	0.870	1.003	40.170
B	16	H	3	W	1	3	143.71	143.73	169.72	170.75	17.5	X									40.175
B	16	H	3	W	6	8	143.76	143.78	169.77	170.81	19.1	X									40.179
B	16	H	3	W	11	13	143.81	143.83	169.82	170.86	21.1	X									40.183
B	16	H	3	W	16	18	143.86	143.88	169.87	170.91		X									40.187
B	16	H	3	W	21	23	143.91	143.93	169.92	170.96	15.6										40.191
B	16	H	3	W	26	28	143.96	143.98	169.97	171.00	15.7		0.360	0.490			0.360	0.490	0.700	0.663	40.195
B	16	H	3	W	31	33	144.01	144.03	170.02	171.05		X									40.199
B	16	H	3	W	36	38	144.06	144.08	170.07	171.10	20.6		0.480	0.564			0.480	0.564	0.820	0.746	40.203
B	16	H	3	W	41	43	144.11	144.13	170.12	171.15	14.8		0.370	0.068			0.370	0.068	0.710	0.189	40.207
B	16	H	3	W	46	48	144.16	144.18	170.17	171.20	21.2		0.432	0.832			0.432	0.832	0.772	1.047	40.211
B	16	H	3	W	51	53	144.21	144.23	170.22	171.25		X									40.215
B	16	H	3	W	56	58	144.26	144.28	170.27	171.29	20.8	X									40.219
B	16	H	3	W	61	63	144.31	144.33	170.32	171.34	16.4		0.541	0.714			0.541	0.714	0.881	0.915	40.223
B	16	H	3	W	66	68	144.36	144.38	170.37	171.39	17.4		0.529	0.552			0.529	0.552	0.869	0.732	40.227
B	16	H	3	W	68	70	144.38	144.40	170.39	171.41	17.5	X									40.229
B	16	H	3	W	71	73	144.41	144.43	170.42	171.44	15.5	X									40.231
B	16	H	3	W	76	78	144.46	144.48	170.47	171.49	16.9		0.261	0.841			0.261	0.841	0.601	1.057	40.235
B	16	H	3	W	81	83	144.51	144.53	170.52	171.54	17.5				0.977	0.776	0.977	0.776	1.317	0.985	40.239
B	16	H	3	W	86	88	144.56	144.58	170.57	171.58	16.8	X									40.243
B	16	H	3	W	88	90	144.58	144.60	170.59	171.60	17.5	X									40.245
B	16	H	3	W	91	93	144.61	144.63	170.62	171.63	16.6	X									40.247
B	16	H	3	W	96	98	144.66	144.68	170.67	171.68	16.6		0.593	0.795			0.593	0.795	0.933	1.005	40.251
B	16	H	3	W	98	100	144.68	144.70	170.69	171.70	15.9	X									40.253
B	16	H	3	W	101	103	144.71	144.73	170.72	171.73		X									40.255
B	16	H	3	W	111	113	144.81	144.83	170.82	171.83	16.4	X									40.263
B	16	H	3	W	116	118	144.86	144.88	170.87	171.87	15.4										40.267
B	16	H	3	W	121	123	144.91	144.93	170.92	171.92	15.9	X									40.271
B	16	H	3	W	126	128	144.96	144.98	170.97	171.97	17.1	X									40.275
B	16	H	3	W	131	133	145.01	145.03	171.02	172.04	21.2										40.283
B	16	H	3	W	136	138	145.06	145.08	171.07	172.11	15.6										40.293
B	16	H	3	W	141	143	145.11	145.13	171.12	172.19	14.9		0.475	0.812			0.475	0.812	0.815	1.025	40.302
B	16	H	3	W	146	148	145.16	145.18	171.17	172.27	16.1										40.311
B	16	H	4	W	1	3	145.21	145.23	171.22	172.34	15.9				0.535		0.535		0.875		40.320
B	16	H	4	W	6	8	145.26	145.28	171.27	172.42					0.498	0.380	0.498	0.380	0.838	0.540	40.329
B	16	H	4	W	11	13	145.31	145.33	171.32	172.50	15.3		0.519	0.999	0.593	0.856	0.556	0.927	0.896	1.154	40.339
B	16	H	4	W	16	18	145.36	145.38	171.37	172.58	15.1		0.466	0.770			0.466	0.770	0.806	0.978	40.348
B	16	H	4	W	21	23	145.41	145.43	171.42	172.65	16.1		0.323	0.505			0.323	0.505	0.663	0.680	40.357

(**Appendix Table 5-1** continued)

Hole	Core	Type	Section	Type	Top (cm)	Bottom (cm)	Top (m CSF-A)	Bottom (m CSF-A)	Depth (rmcd; m revised CCSF-A)	Depth (m adj rmcd; m adj rev CCSF-A)	Coarse Fraction (wt %)	Barren Sample	$\delta^{13}C$ measured at Bremen (‰, VPDB)	$\delta^{18}O$ measured at Bremen (‰, VPDB)	$\delta^{13}C$ measured at NOCS (‰, VPDB)	$\delta^{18}O$ measured at NOCS (‰, VPDB)	$\delta^{13}C$ compiled (‰, VPDB)	$\delta^{18}O$ compiled (‰, VPDB)	$\delta^{13}C$ adjusted to Cibs (true+0.34)	$\delta^{18}O$ adjusted to Cibs (true+0.1/0.89)	Age (Ma) [WK Age]
B	16	H	4	W	26	28	145.46	145.48	171.47	172.73	15.0		0.600	0.722			0.600	0.722	0.940	0.924	40.366
B	16	H	4	W	31	33	145.51	145.53	171.52	172.81	15.2		0.756	0.892			0.756	0.892	1.096	1.115	40.376
B	16	H	4	W	36	38	145.56	145.58	171.57	172.88	15.7				0.706	0.652	0.706	0.652	1.046	0.845	40.382
B	16	H	4	W	41	43	145.61	145.63	171.62	172.96	15.9		0.537	0.684			0.537	0.684	0.877	0.881	40.387
B	16	H	4	W	46	48	145.66	145.68	171.67	173.04	15.4		0.638	0.919	0.725	0.721	0.681	0.820	1.021	1.034	40.393
B	16	H	4	W	51	53	145.71	145.73	171.72	173.10	15.2		0.546	0.712			0.546	0.712	0.886	0.912	40.397
B	16	H	4	W	56	58	145.76	145.78	171.77	173.15	16.5				0.583	0.876	0.583	0.876	0.923	1.096	40.401
B	16	H	4	W	61	63	145.81	145.83	171.82	173.20	21.4				0.536	0.612	0.536	0.612	0.876	0.800	40.405
B	16	H	4	W	66	68	145.86	145.88	171.87	173.25	17.3	X									40.408
B	16	H	4	W	71	73	145.91	145.93	171.92	173.30	17.7	X									40.412
B	16	H	4	W	76	78	145.96	145.98	171.97	173.35	17.9	X									40.416
B	16	H	4	W	81	83	146.01	146.03	172.02	173.40	15.8				0.824	0.993	0.824	0.993	1.164	1.228	40.419
B	16	H	4	W	86	88	146.06	146.08	172.07	173.45	17.3				0.642		0.642		0.982		40.423
B	16	H	4	W	91	93	146.11	146.13	172.12	173.50	24.3				0.790		0.790		1.130		40.427
B	16	H	4	W	96	98	146.16	146.18	172.17	173.55	9.7		0.404	1.078	0.602	1.153	0.503	1.116	0.843	1.366	40.430
B	16	H	4	W	101	103	146.21	146.23	172.22	173.60	16.9				0.842	1.147	0.842	1.147	1.182	1.401	40.434
B	16	H	4	W	106	108	146.26	146.28	172.27	173.65	16.7				0.818	1.056	0.818	1.056	1.158	1.299	40.438
B	16	H	4	W	111	113	146.31	146.33	172.32	173.70	14.4		0.499	0.765			0.499	0.765	0.839	0.972	40.441
B	16	H	4	W	116	118	146.36	146.38	172.37	173.75	14.2		0.411	0.766			0.411	0.766	0.751	0.973	40.445
B	16	H	4	W	121	123	146.41	146.43	172.42	173.80	15.8				0.465	0.614	0.465	0.614	0.805	0.802	40.449
B	16	H	4	W	126	128	146.46	146.48	172.47	173.85	15.4		0.508	0.794			0.508	0.794	0.848	1.004	40.452
B	16	H	4	W	128	130	146.48	146.50	172.49	173.87	15.7		0.618	0.720			0.618	0.720	0.958	0.921	40.454
B	16	H	4	W	131	133	146.51	146.53	172.52	173.90	14.9		0.827	1.008			0.827	1.008	1.167	1.245	40.456
B	16	H	4	W	136	138	146.56	146.58	172.57	173.95	15.4		0.580	0.996			0.580	0.996	0.920	1.231	40.459
B	16	H	4	W	141	143	146.61	146.63	172.62	173.99					0.581	0.673	0.581	0.673	0.921	0.869	40.463
B	16	H	4	W	146	148	146.66	146.68	172.67	174.03	14.9		0.551	0.892			0.551	0.892	0.891	1.115	40.466
B	16	H	5	W	1	3	146.71	146.73	172.72	174.08	27.9				0.631	0.518	0.631	0.518	0.971	0.695	40.469
B	16	H	5	W	6	8	146.76	146.78	172.77	174.12	26.8				0.629	1.071	0.629	1.071	0.969	1.316	40.472
B	16	H	5	W	11	13	146.81	146.83	172.82	174.17	22.2	X									40.475
B	16	H	5	W	16	18	146.86	146.88	172.87	174.21	22.3				0.251	0.663	0.251	0.663	0.591	0.857	40.479
B	16	H	5	W	21	23	146.91	146.93	172.92	174.25	20.1				0.600	0.733	0.600	0.733	0.940	0.936	40.482
B	16	H	5	W	26	28	146.96	146.98	172.97	174.30	14.2				0.529	0.767	0.529	0.767	0.869	0.974	40.485
B	16	H	5	W	31	33	147.01	147.03	173.02	174.34	12.7		0.494	0.800			0.494	0.800	0.834	1.011	40.488
B	16	H	5	W	36	38	147.06	147.08	173.07	174.39	20.7				0.068	0.745	0.068	0.745	0.408	0.950	40.492
B	16	H	5	W	41	43	147.11	147.13	173.12	174.43	18.3										40.495
B	16	H	5	W	46	48	147.16	147.18	173.17	174.47	15.4				0.317	0.664	0.317	0.664	0.657	0.859	40.498
B	16	H	5	W	51	53	147.21	147.23	173.22	174.52	16.4				0.105	0.710	0.105	0.710	0.445	0.910	40.501
B	16	H	5	W	56	58	147.26	147.28	173.27	174.56	10.5				0.501	0.761	0.501	0.761	0.841	0.967	40.504
B	16	H	5	W	61	63	147.31	147.33	173.32	174.61	16.2		0.363	0.555			0.363	0.555	0.703	0.736	40.508
B	16	H	5	W	66	68	147.36	147.38	173.37	174.65	16.0				0.273	0.781	0.273	0.781	0.613	0.990	40.511
B	16	H	5	W	71	73	147.41	147.43	173.42	174.70	17.5				0.223	0.785	0.223	0.785	0.563	0.994	40.515
B	16	H	5	W	76	78	147.46	147.48	173.47	174.75	15.7				0.052	0.641	0.052	0.641	0.392	0.833	40.519
B	16	H	5	W	81	83	147.51	147.53	173.52	174.79	17.1				0.010	0.565	0.010	0.565	0.350	0.747	40.524
B	16	H	5	W	86	88	147.56	147.58	173.57	174.84	15.2				0.289	0.765	0.289	0.765	0.629	0.972	40.528
B	16	H	5	W	91	93	147.61	147.63	173.62	174.89	11.9				0.128	0.773	0.128	0.773	0.468	0.981	40.533
B	16	H	5	W	96	98	147.66	147.68	173.67	174.93	13.3				0.143	0.563	0.143	0.563	0.483	0.745	40.538
B	16	H	5	W	101	103	147.71	147.73	173.72	174.98	12.2		0.376	0.767			0.376	0.767	0.716	0.974	40.542
B	16	H	5	W	106	108	147.76	147.78	173.77	175.02	15.2		0.434	0.858			0.434	0.858	0.774	1.076	40.547
B	16	H	5	W	111	113	147.81	147.83	173.82	175.07	14.8				0.047	0.352	0.047	0.352	0.387	0.508	40.552
B	16	H	5	W	116	118	147.86	147.88	173.87	175.12	15.6				0.183	0.503	0.183	0.503	0.523	0.677	40.556
B	16	H	5	W	121	123	147.91	147.93	173.92	175.16	10.6		0.461	0.907			0.461	0.907	0.801	1.131	40.561
B	16	H	5	W	126	128	147.96	147.98	173.97	175.21	25.2				0.259	0.629	0.259	0.629	0.599	0.819	40.565
B	16	H	5	W	131	133	148.01	148.03	174.02	175.25	18.6				0.293	0.728	0.293	0.728	0.633	0.930	40.570
B	16	H	5	W	136	138	148.06	148.08	174.07	175.29	14.9				0.110	0.757	0.110	0.757	0.450	0.963	40.574
B	16	H	5	W	141	143	148.11	148.13	174.12	175.34	14.8		0.260	0.909			0.260	0.909	0.600	1.134	40.578
B	16	H	5	W	146	148	148.16	148.18	174.17	175.38	16.7				0.111	0.723	0.111	0.723	0.451	0.925	40.583
B	16	H	6	W	1	3	148.21	148.23	174.22	175.42	18.6				-0.073	0.683	-0.073	0.683	0.267	0.879	40.587
B	16	H	6	W	6	8	148.26	148.28	174.27	175.47	17.1		0.315	1.010			0.315	1.010	0.655	1.247	40.591
B	16	H	6	W	11	13	148.31	148.33	174.32	175.51	17.5				-0.020	0.667	-0.020	0.667	0.320	0.862	40.596
B	16	H	6	W	16	18	148.36	148.38	174.37	175.55	20.3		0.244	0.983	0.142	0.887	0.193	0.935	0.533	1.163	40.600

(**Appendix Table 5-1** continued)

Hole	Core	Type	Section	Type	Top (cm)	Bottom (cm)	Top (m CSF-A)	Bottom (m CSF-A)	Depth (rmcd; m revised CCSF-A)	Depth (m adj rmcd; m adj rev CCSF-A)	Coarse Fraction (wt %)	Barren Sample	$\delta^{13}C$ measured at Bremen (‰, VPDB)	$\delta^{18}O$ measured at Bremen (‰, VPDB)	$\delta^{13}C$ measured at NOCS (‰, VPDB)	$\delta^{18}O$ measured at NOCS (‰, VPDB)	$\delta^{13}C$ compiled (‰, VPDB)	$\delta^{18}O$ compiled (‰, VPDB)	$\delta^{13}C$ adjusted to Cibs (true+0.34)	$\delta^{18}O$ adjusted to Cibs (true+0.1/0.89)	Age (Ma) [WK Age]
B	16	H	6	W	21	23	148.41	148.43	174.42	175.59	11.2				0.456	1.069	0.456	1.069	0.796	1.314	40.604
B	16	H	6	W	26	28	148.46	148.48	174.47	175.64	15.8		0.091	1.099			0.091	1.099	0.431	1.347	40.608
B	16	H	6	W	31	33	148.51	148.53	174.52	175.68	12.1				-0.001	0.658	-0.001	0.658	0.339	0.852	40.613
B	16	H	6	W	36	38	148.56	148.58	174.57	175.72	6.7		0.325	0.805			0.325	0.805	0.665	1.017	40.617
C	18	H	7	W	100	102	149.24	149.26	175.75	175.75	10.6				0.241	0.658	0.241	0.658	0.581	0.852	40.620
B	16	H	6	W	41	43	148.61	148.63	174.62	175.77	12.5		-0.005	0.728	-0.038	0.620	-0.022	0.674	0.318	0.870	40.621
C	18	H	7	W	105	107	149.29	149.31	175.80	175.80	8.1		0.190	0.818			0.190	0.818	0.530	1.031	40.625
B	16	H	6	W	46	48	148.66	148.68	174.67	175.81	11.8		0.059	0.779	0.129	0.775	0.094	0.777	0.434	0.985	40.625
C	18	H	7	W	110	112	149.34	149.36	175.85	175.85	6.6		0.246	0.894			0.246	0.894	0.586	1.117	40.629
B	16	H	6	W	51	53	148.71	148.73	174.72	175.85	12.4				-0.186	0.613	-0.186	0.613	0.154	0.801	40.630
C	18	H	7	W	115	117	149.39	149.41	175.90	175.90	6.5				0.298	0.872	0.298	0.872	0.638	1.093	40.634
B	16	H	6	W	56	58	148.76	148.78	174.77	175.90	12.5				0.091	0.668	0.091	0.668	0.431	0.863	40.635
C	18	H	7	W	120	122	149.44	149.46	175.95	175.95	6.5		-0.093	0.820			-0.093	0.820	0.247	1.034	40.639
B	16	H	6	W	61	63	148.81	148.83	174.82	175.96	5.8		0.140	0.876			0.140	0.876	0.480	1.097	40.640
C	18	H	7	W	125	127	149.49	149.51	176.00	176.00	6.9		0.096	0.840			0.096	0.840	0.436	1.056	40.644
B	16	H	6	W	66	68	148.86	148.88	174.87	176.02	6.6				0.181	0.795	0.181	0.795	0.521	1.005	40.646
B	16	H	6	W	68	70	148.88	148.90	174.89	176.04	10.3		0.115	0.857			0.115	0.857	0.455	1.075	40.648
C	18	H	7	W	130	132	149.54	149.56	176.05	176.05	6.9										40.649
B	16	H	6	W	71	73	148.91	148.93	174.92	176.07	4.6		0.188	0.798	0.350	0.967	0.269	0.883	0.609	1.104	40.651
C	18	H	7	W	135	137	149.59	149.61	176.10	176.10	5.9		0.184	0.774			0.184	0.774	0.524	0.982	40.654
B	16	H	6	W	76	78	148.96	148.98	174.97	176.13	8.7				-0.013	0.744	-0.013	0.744	0.327	0.948	40.656
C	18	H	7	W	140	142	149.64	149.66	176.15	176.15	6.0		0.279	0.946			0.279	0.946	0.619	1.175	40.659
B	16	H	6	W	81	83	149.01	149.03	175.02	176.18	8.4		0.173	0.786	0.133	0.668	0.153	0.727	0.493	0.929	40.662
C	18	H	7	W	145	147	149.69	149.71	176.20	176.20	5.6		0.173	0.736			0.173	0.736	0.513	0.939	40.664
B	16	H	6	W	86	88	149.06	149.08	175.07	176.24	9.8		0.138	0.609			0.138	0.609	0.478	0.797	40.667
C	18	H	7	W	150	152	149.74	149.76	176.25	176.25	5.0		-0.013	0.679			-0.013	0.679	0.327	0.875	40.668
C	18	H	8	W	1	3	149.77	149.79	176.28	176.28	5.3		-0.003	0.625			-0.003	0.625	0.337	0.815	40.671
B	16	H	6	W	91	93	149.11	149.13	175.12	176.29					0.279	0.555	0.279	0.555	0.619	0.735	40.673
C	18	H	8	W	5	7	149.81	149.83	176.32	176.32	5.2		0.108	0.573			0.108	0.573	0.448	0.756	40.675
B	16	H	6	W	96	98	149.16	149.18	175.17	176.35	9.4				-0.035	0.429	-0.035	0.429	0.305	0.595	40.678
C	18	H	8	W	10	12	149.86	149.88	176.37	176.37	6.2		0.089	0.738			0.089	0.738	0.429	0.942	40.680
B	16	H	7	W	1	3	149.21	149.23	175.22	176.40	7.0				-0.146	0.460	-0.146	0.460	0.194	0.629	40.683
C	18	H	8	W	15	17	149.91	149.93	176.42	176.42	5.5		0.223	0.616			0.223	0.616	0.563	0.804	40.685
B	16	H	7	W	6	8	149.26	149.28	175.27	176.46					0.234	0.705	0.234	0.705	0.574	0.904	40.689
C	18	H	8	W	20	22	149.96	149.98	176.47	176.47	4.8		0.247	0.620			0.247	0.620	0.587	0.809	40.690
B	16	H	7	W	11	13	149.31	149.33	175.32	176.51	8.5				0.210	0.640	0.210	0.640	0.550	0.832	40.694
C	18	H	8	W	25	27	150.01	150.03	176.52	176.52	4.2				0.166		0.166		0.506		40.695
B	16	H	7	W	16	18	149.36	149.38	175.37	176.56	9.1		0.136	0.709	0.081	0.571	0.108	0.640	0.448	0.831	40.699
C	18	H	8	W	30	32	150.06	150.08	176.57	176.57	4.0				0.135	0.587	0.135	0.587	0.475	0.772	40.700
B	16	H	7	W	21	23	149.41	149.43	175.42	176.62											40.704
C	18	H	8	W	35	37	150.11	150.13	176.62	176.62	4.8		0.132	0.666			0.132	0.666	0.472	0.861	40.704
B	16	H	7	W	26	28	149.46	149.48	175.47	176.67	12.6				0.002	0.590	0.002	0.590	0.342	0.775	40.709
C	18	H	8	W	40	42	150.16	150.18	176.67	176.67	5.9		-0.163	0.535			-0.163	0.535	0.177	0.713	40.709
B	16	H	7	W	31	33	149.51	149.53	175.52	176.72	13.7				0.045	0.576	0.045	0.576	0.385	0.760	40.714
C	18	H	8	W	45	47	150.21	150.23	176.72	176.72	7.8		-0.040	0.636			-0.040	0.636	0.300	0.827	40.714
B	16	H	7	W	36	38	149.56	149.58	175.57	176.77	7.2				0.330	0.723	0.330	0.723	0.670	0.924	40.719
C	18	H	8	W	50	52	150.26	150.28	176.77	176.77	8.5										40.719
B	16	H	7	W	41	43	149.61	149.63	175.62	176.82	6.4				0.255	0.776	0.255	0.776	0.595	0.984	40.724
C	18	H	8	W	55	57	150.31	150.33	176.82	176.82	7.6		0.119	0.768			0.119	0.768	0.459	0.975	40.724
B	16	H	7	W	46	48	149.66	149.68	175.67	176.87	6.3				0.563	0.848	0.563	0.848	0.903	1.065	40.729
C	18	H	8	W	60	62	150.36	150.38	176.87	176.87	7.6		0.279	0.695			0.279	0.695	0.619	0.893	40.729
C	18	H	8	W	65	67	150.41	150.43	176.92	176.92	7.3		0.260	0.895			0.260	0.895	0.600	1.118	40.734
C	18	H	8	W	70	72	150.46	150.48	176.97	176.97	7.9		0.186	0.725			0.186	0.725	0.526	0.927	40.739
B	16	H	CC	W	1	3	149.78	149.80	175.79	176.99	10.5		0.238	0.609			0.238	0.609	0.578	0.797	40.740
C	18	H	CC	W	1	3	150.52	150.54	177.03	177.03	9.2		0.276	0.993			0.276	0.993	0.616	1.228	40.744
B	16	H	CC	W	6	8	149.83	149.85	175.84	177.04	9.0		0.389	0.821			0.389	0.821	0.729	1.035	40.745
C	18	H	CC	W	5	7	150.56	150.58	177.07	177.07	8.9										40.748
B	16	H	CC	W	11	13	149.88	149.90	175.89	177.09	7.7				0.262	0.738	0.262	0.738	0.602	0.942	40.750
C	18	H	CC	W	10	12	150.61	150.63	177.12	177.12	7.0		0.328	0.886			0.328	0.886	0.668	1.108	40.753
B	16	H	CC	W	16	18	149.93	149.95	175.94	177.14	7.1				0.313	0.692	0.313	0.692	0.653	0.890	40.755

(**Appendix Table 5-1** continued)

Hole	Core	Type	Section	Type	Top (cm)	Bottom (cm)	Top (m CSF-A)	Bottom (m CSF-A)	Depth (rmcd; m revised CCSF-A)	Depth (m adj rmcd; m adj rev CCSF-A)	Coarse Fraction (wt %)	Barren Sample	$\delta^{13}C$ measured at Bremen (‰, VPDB)	$\delta^{18}O$ measured at Bremen (‰, VPDB)	$\delta^{13}C$ measured at NOCS (‰, VPDB)	$\delta^{18}O$ measured at NOCS (‰, VPDB)	$\delta^{13}C$ compiled (‰, VPDB)	$\delta^{18}O$ compiled (‰, VPDB)	$\delta^{13}C$ adjusted to Cibs (true+0.34)	$\delta^{18}O$ adjusted to Cibs (true+0.1/0.89)	Age (Ma) [WK Age]
C	18	H	CC	W	15	17	150.66	150.68	177.17	177.17	7.7		0.221	0.629			0.221	0.629	0.561	0.819	40.757
B	16	H	CC	W	21	23	149.98	150.00	175.99	177.19	7.9				0.495	0.937	0.495	0.937	0.835	1.165	40.758
C	18	H	CC	W	20	22	150.71	150.73	177.22	177.22	7.6				0.212	1.043	0.212	1.043	0.552	1.285	40.760
C	18	H	CC	W	23	25	150.74	150.76	177.25	177.25	6.4		0.141	0.736			0.141	0.736	0.481	0.939	40.762
C	19	H	1	W	90	92	151.00	151.02	177.51	177.51	8.9		0.076	0.661			0.076	0.661	0.416	0.855	40.780
C	19	H	1	W	90	92	151.00	151.02	177.51	177.51											40.780
C	19	H	1	W	95	97	151.05	151.07	177.56	177.56	7.6		0.118	0.629			0.118	0.629	0.458	0.819	40.783
C	19	H	1	W	100	102	151.10	151.12	177.61	177.61	7.4				0.142	0.942	0.142	0.942	0.482	1.171	40.786
C	19	H	1	W	110	112	151.20	151.22	177.71	177.71	6.3		0.186	0.611			0.186	0.611	0.526	0.799	40.793
C	19	H	1	W	115	117	151.25	151.27	177.76	177.76	6.9		0.190	0.580	0.127	0.604	0.158	0.592	0.498	0.777	40.796
C	19	H	1	W	120	122	151.30	151.32	177.81	177.81	7.7		0.132	0.739			0.132	0.739	0.472	0.943	40.800
C	19	H	1	W	125	127	151.35	151.37	177.86	177.86	8.7		0.223	0.745			0.223	0.745	0.563	0.949	40.803
C	19	H	1	W	130	132	151.40	151.42	177.91	177.91	12.5				0.350	0.705	0.350	0.705	0.690	0.905	40.807
C	19	H	1	W	135	137	151.45	151.47	177.96	177.96	9.5		0.427	0.760			0.427	0.760	0.767	0.966	40.810
C	19	H	1	W	140	142	151.50	151.52	178.01	178.01	7.5				0.693	1.177	0.693	1.177	1.033	1.435	40.813
C	19	H	1	W	144	146	151.54	151.56	178.05	178.05	7.4		0.326	0.868			0.326	0.868	0.666	1.088	40.816
C	19	H	1	W	148	150	151.58	151.60	178.09	178.09	11.5		0.391	0.746			0.391	0.746	0.731	0.951	40.819
C	19	H	2	W	5	7	151.65	151.67	178.16	178.16	8.2				0.498	0.859	0.498	0.859	0.838	1.078	40.823
C	19	H	2	W	10	12	151.70	151.72	178.21	178.21	9.2				0.524	1.055	0.524	1.055	0.864	1.298	40.827
C	19	H	2	W	15	17	151.75	151.77	178.26	178.26	8.4				0.522	1.082	0.522	1.082	0.862	1.329	40.830
C	19	H	2	W	20	22	151.80	151.82	178.31	178.31	8.0		0.330	0.843			0.330	0.843	0.670	1.060	40.834
C	19	H	2	W	25	27	151.85	151.87	178.36	178.36	10.2		0.371	0.720			0.371	0.720	0.711	0.921	40.837
C	19	H	2	W	30	32	151.90	151.92	178.41	178.41	9.9				0.734	1.129	0.734	1.129	1.074	1.381	40.840
C	19	H	2	W	35	37	151.95	151.97	178.46	178.46	7.7				0.546	1.106	0.546	1.106	0.886	1.355	40.844
C	19	H	2	W	40	42	152.00	152.02	178.51	178.51	6.7				0.475	0.878	0.475	0.878	0.815	1.099	40.847
C	19	H	2	W	45	47	152.05	152.07	178.56	178.56	7.7				0.599	0.915	0.599	0.915	0.939	1.141	40.851
C	19	H	2	W	50	52	152.10	152.12	178.61	178.61	6.5				0.675	0.867	0.675	0.867	1.015	1.087	40.854
C	19	H	2	W	55	57	152.15	152.17	178.66	178.66	4.3				0.377	0.748	0.377	0.748	0.717	0.952	40.857
C	19	H	2	W	60	62	152.20	152.22	178.71	178.71	4.5		0.191	0.521			0.191	0.521	0.531	0.698	40.861
C	19	H	2	W	65	67	152.25	152.27	178.76	178.76	6.6				0.278	0.877	0.278	0.877	0.618	1.097	40.864
C	19	H	2	W	70	72	152.30	152.32	178.81	178.81	7.2		0.421	0.625			0.421	0.625	0.761	0.815	40.867
C	19	H	2	W	75	77	152.35	152.37	178.86	178.86	6.1		0.412	0.507			0.412	0.507	0.752	0.682	40.871
C	19	H	2	W	80	82	152.40	152.42	178.91	178.91	7.1		0.710	0.902			0.710	0.902	1.050	1.126	40.875
C	19	H	2	W	85	87	152.45	152.47	178.96	178.96	7.8				0.605	0.718	0.605	0.718	0.945	0.919	40.878
C	19	H	2	W	90	92	152.50	152.52	179.01	179.01	9.1				0.486	0.710	0.486	0.710	0.826	0.910	40.882
C	19	H	2	W	95	97	152.55	152.57	179.06	179.06	8.2				0.643	1.093	0.643	1.093	0.983	1.340	40.885
C	19	H	2	W	100	102	152.60	152.62	179.11	179.11	8.5				0.753	1.078	0.753	1.078	1.093	1.324	40.889
B	17	H	1	W	1	3	150.21	150.23	179.12	179.12	7.0				0.687	0.685	0.687	0.685	1.027	0.882	40.890
B	17	H	1	W	3	5	150.23	150.25	179.14	179.14	9.3				0.474	0.713	0.474	0.713	0.814	0.914	40.891
B	17	H	1	W	5	7	150.25	150.27	179.16	179.16	6.0				0.627	0.876	0.627	0.876	0.967	1.096	40.892
C	19	H	2	W	105	107	152.65	152.67	179.16	179.16	7.9				0.503	0.854	0.503	0.854	0.843	1.072	40.892
C	19	H	2	W	110	112	152.70	152.72	179.21	179.21	8.1				0.559	0.874	0.559	0.874	0.899	1.095	40.896
B	17	H	1	W	13	15	150.33	150.35	179.24	179.24	7.7				0.443	0.665	0.443	0.665	0.783	0.860	40.898
C	19	H	2	W	115	117	152.75	152.77	179.26	179.26	6.3				0.678	1.057	0.678	1.057	1.018	1.300	40.900
B	17	H	1	W	18	20	150.38	150.40	179.29	179.29	8.2				0.541	0.801	0.541	0.801	0.881	1.013	40.902
C	19	H	2	W	120	122	152.80	152.82	179.31	179.31	7.0		0.408	0.713			0.408	0.713	0.748	0.913	40.903
B	17	H	1	W	24	26	150.44	150.46	179.35	179.35	6.9				0.631	0.809	0.631	0.809	0.971	1.021	40.906
B	17	H	1	W	30	32	150.50	150.52	179.41	179.41	7.0				0.508	0.816	0.508	0.816	0.848	1.029	40.910
B	17	H	1	W	34	36	150.54	150.56	179.45	179.45	9.5				0.306	0.520	0.306	0.520	0.646	0.697	40.913
B	17	H	1	W	38	40	150.58	150.60	179.49	179.49	7.4				0.361	0.611	0.361	0.611	0.701	0.799	40.916
B	17	H	1	W	43	45	150.63	150.65	179.54	179.54	7.7				0.427	0.735	0.427	0.735	0.767	0.938	40.920
B	17	H	1	W	53	55	150.73	150.75	179.64	179.63	6.4				0.519	0.800	0.519	0.800	0.859	1.012	40.926
B	17	H	1	W	57	59	150.77	150.79	179.68	179.66	7.8				0.497	0.784	0.497	0.784	0.837	0.993	40.928
B	17	H	1	W	62	64	150.82	150.84	179.73	179.69	10.2				0.381	0.709	0.381	0.709	0.721	0.909	40.930
B	17	H	1	W	64	66	150.84	150.86	179.75	179.70	6.3				0.719	0.939	0.719	0.939	1.059	1.168	40.931
B	17	H	1	W	73	75	150.93	150.95	179.84	179.77	9.1				0.535	0.802	0.535	0.802	0.875	1.014	40.936
B	17	H	1	W	78	80	150.98	151.00	179.89	179.80	8.5				0.648	0.948	0.648	0.948	0.988	1.177	40.938
B	17	H	1	W	83	85	151.03	151.05	179.94	179.84	9.6				0.598	0.719	0.598	0.719	0.938	0.921	40.941
B	17	H	1	W	90	92	151.10	151.12	180.01	179.89	7.6				0.477	0.769	0.477	0.769	0.817	0.977	40.944
B	17	H	1	W	94	96	151.14	151.16	180.05	179.93	8.5				0.720	0.860	0.720	0.860	1.060	1.079	40.948

(**Appendix Table 5-1** continued)

Hole	Core	Type	Section	Type	Top (cm)	Bottom (cm)	Top (m CSF-A)	Bottom (m CSF-A)	Depth (rmcd; m revised CCSF-A)	Depth (m adj rmcd; m adj rev CCSF-A)	Coarse Fraction (wt %)	Barren Sample	$\delta^{13}C$ measured at Bremen (‰, VPDB)	$\delta^{18}O$ measured at Bremen (‰, VPDB)	$\delta^{13}C$ measured at NOCS (‰, VPDB)	$\delta^{18}O$ measured at NOCS (‰, VPDB)	$\delta^{13}C$ compiled (‰, VPDB)	$\delta^{18}O$ compiled (‰, VPDB)	$\delta^{13}C$ adjusted to Cibs (true+0.34)	$\delta^{18}O$ adjusted to Cibs (true+0.1/0.89)	Age (Ma) [Wk Age]
B	17	H	1	W	98	100	151.18	151.20	180.09	179.99	9.3				0.475	0.687	0.475	0.687	0.815	0.884	40.952
B	17	H	1	W	103	105	151.23	151.25	180.14	180.06	9.5				0.474	0.749	0.474	0.749	0.814	0.954	40.957
B	17	H	1	W	113	115	151.33	151.35	180.24	180.21	11.1				0.578	0.879	0.578	0.879	0.918	1.100	40.968
B	17	H	1	W	118	120	151.38	151.40	180.29	180.29	10.2				0.385	0.795	0.385	0.795	0.725	1.006	40.973
B	17	H	1	W	123	125	151.43	151.45	180.34	180.34	10.8				0.428	0.745	0.428	0.745	0.768	0.950	40.977
B	17	H	1	W	134	136	151.54	151.56	180.45	180.45	5.8				0.461	0.492	0.461	0.492	0.801	0.665	40.985
B	17	H	1	W	139	141	151.59	151.61	180.50	180.50	6.8				0.455	0.510	0.455	0.510	0.795	0.685	40.988
B	17	H	1	W	146	148	151.66	151.68	180.57	180.57	7.8				0.382	0.618	0.382	0.618	0.722	0.807	40.993
B	17	H	1	W	148	150	151.68	151.70	180.59	180.59	8.2		0.379	0.621			0.379	0.621	0.719	0.810	40.995
B	17	H	2	W	1	3	151.71	151.73	180.62	180.62	6.3										40.997
B	17	H	2	W	6	8	151.76	151.78	180.67	180.67	5.5		0.500	0.925			0.500	0.925	0.840	1.152	41.000
B	17	H	2	W	11	13	151.81	151.83	180.72	180.72	8.3		0.523	0.851			0.523	0.851	0.863	1.069	41.004
B	17	H	2	W	16	18	151.86	151.88	180.77	180.77	6.4		0.560	0.840	0.709	0.919	0.634	0.879	0.974	1.100	41.008
B	17	H	2	W	21	23	151.91	151.93	180.82	180.82			0.459	0.804	0.544	0.948	0.502	0.876	0.842	1.096	41.011
B	17	H	2	W	26	28	151.96	151.98	180.87	180.87	8.8		0.397	0.775	0.498	0.980	0.448	0.878	0.788	1.098	41.015
B	17	H	2	W	31	33	152.01	152.03	180.92	180.92	5.8		0.629	0.803			0.629	0.803	0.969	1.015	41.018
B	17	H	2	W	36	38	152.06	152.08	180.97	180.97	8.7		0.477	0.742	0.441	0.706	0.459	0.724	0.799	0.926	41.022
B	17	H	2	W	41	43	152.11	152.13	181.02	181.02			0.416	0.796	0.436	0.670	0.426	0.733	0.766	0.936	41.025
B	17	H	2	W	46	48	152.16	152.18	181.07	181.07	9.5		0.603	0.834			0.603	0.834	0.943	1.049	41.029
B	17	H	2	W	51	53	152.21	152.23	181.12	181.12	10.0		0.509	0.831	0.504	0.876	0.506	0.854	0.846	1.072	41.033
B	17	H	2	W	56	58	152.26	152.28	181.17	181.17	12.7		0.408	0.905			0.408	0.905	0.748	1.129	41.036
B	17	H	2	W	61	63	152.31	152.33	181.22	181.22	7.5		0.539	0.876	0.488	1.004	0.513	0.940	0.853	1.169	41.040
B	17	H	2	W	66	68	152.36	152.38	181.27	181.27	13.1		0.446	0.927			0.446	0.927	0.786	1.154	41.045
B	17	H	2	W	71	73	152.41	152.43	181.32	181.32	8.8				0.391	0.841	0.391	0.841	0.731	1.057	41.051
B	17	H	2	W	76	78	152.46	152.48	181.37	181.37	7.3		0.526	0.853			0.526	0.853	0.866	1.071	41.057
B	17	H	2	W	81	83	152.51	152.53	181.42	181.42					0.697	1.007	0.697	1.007	1.037	1.243	41.064
B	17	H	2	W	86	88	152.56	152.58	181.47	181.47	9.2		0.458	0.872	0.617	1.061	0.538	0.967	0.878	1.198	41.070
B	17	H	2	W	91	93	152.61	152.63	181.52	181.52	10.5		0.249	0.687	0.484	0.797	0.366	0.742	0.706	0.946	41.076
B	17	H	2	W	96	98	152.66	152.68	181.57	181.57	5.8				0.425	0.874	0.425	0.874	0.765	1.094	41.082
B	17	H	2	W	101	103	152.71	152.73	181.62	181.62	6.1		0.390	0.797			0.390	0.797	0.730	1.008	41.088
B	17	H	2	W	103	105	152.73	152.75	181.64	181.64											41.091
B	17	H	2	W	106	108	152.76	152.78	181.67	181.67	6.6		0.331	0.706			0.331	0.706	0.671	0.906	41.095
B	17	H	2	W	108	110	152.78	152.80	181.69	181.69	7.3				0.348	0.650	0.348	0.650	0.688	0.843	41.097
B	17	H	2	W	111	113	152.81	152.83	181.72	181.72	8.3		0.357	0.701			0.357	0.701	0.697	0.900	41.101
B	17	H	2	W	116	118	152.86	152.88	181.77	181.77					0.312	0.787	0.312	0.787	0.652	0.997	41.107
B	17	H	2	W	121	123	152.91	152.93	181.82	181.82	9.2		0.485	0.872			0.485	0.872	0.825	1.092	41.113
B	17	H	2	W	126	128	152.96	152.98	181.87	181.87	11.0				0.478	0.658	0.478	0.658	0.818	0.851	41.119
B	17	H	2	W	128	130	152.98	153.00	181.89	181.89	9.3		0.409	0.871			0.409	0.871	0.749	1.091	41.122
B	17	H	2	W	131	133	153.01	153.03	181.92	181.92	8.9		0.275	0.662			0.275	0.662	0.615	0.856	41.126
B	17	H	2	W	136	138	153.06	153.08	181.97	181.97	10.1				0.586	0.866	0.586	0.866	0.926	1.085	41.132
B	17	H	2	W	141	143	153.11	153.13	182.02	182.02	8.6		0.469	0.863			0.469	0.863	0.809	1.082	41.138
B	17	H	2	W	146	148	153.16	153.18	182.07	182.07	6.8		0.348	0.664			0.348	0.664	0.688	0.858	41.144
B	17	H	3	W	1	3	153.21	153.23	182.12	182.12	7.8		0.329	0.544			0.329	0.544	0.669	0.724	41.150
B	17	H	3	W	6	8	153.26	153.28	182.17	182.17	8.1				0.465		0.465		0.805		41.156
B	17	H	3	W	11	13	153.31	153.33	182.22	182.22	8.2				0.865	0.939	0.865	0.939	1.205	1.167	41.163
B	17	H	3	W	16	18	153.36	153.38	182.27	182.27	8.4		0.480	0.846			0.480	0.846	0.820	1.063	41.169
B	17	H	3	W	21	23	153.41	153.43	182.32	182.32	7.7				0.524	0.912	0.524	0.912	0.864	1.137	41.175
B	17	H	3	W	26	28	153.46	153.48	182.37	182.37	9.3		0.539	0.874			0.539	0.874	0.879	1.094	41.181
B	17	H	3	W	31	33	153.51	153.53	182.42	182.42	9.8		0.555	0.858			0.555	0.858	0.895	1.076	41.187
B	17	H	3	W	36	38	153.56	153.58	182.47	182.47	7.6		0.498	0.729			0.498	0.729	0.838	0.931	41.194
B	17	H	3	W	41	43	153.61	153.63	182.52	182.52	13.8				0.336	0.607	0.336	0.607	0.676	0.794	41.200
B	17	H	3	W	46	48	153.66	153.68	182.57	182.57	7.9										41.206
B	17	H	3	W	51	53	153.71	153.73	182.62	182.62	7.5				0.637	0.821	0.637	0.821	0.977	1.035	41.212
B	17	H	3	W	56	58	153.76	153.78	182.67	182.67	9.6				0.515	0.810	0.515	0.810	0.855	1.023	41.218
B	17	H	3	W	61	63	153.81	153.83	182.72	182.72					0.504	0.735	0.504	0.735	0.844	0.938	41.225
B	17	H	3	W	66	68	153.86	153.88	182.77	182.77	9.6		0.390	0.735	0.434		0.412	0.735	0.752	0.938	41.231
B	17	H	3	W	71	73	153.91	153.93	182.82	182.82	9.4		0.651	0.917			0.651	0.917	0.991	1.143	41.237
B	17	H	3	W	76	78	153.96	153.98	182.87	182.87	9.6		0.528	0.894	0.865	0.759	0.696	0.827	1.036	1.041	41.243
B	17	H	3	W	81	83	154.01	154.03	182.92	182.92	10.4				0.383	0.600	0.383	0.600	0.723	0.786	41.251
B	17	H	3	W	86	88	154.06	154.08	182.97	182.97					0.324	0.475	0.324	0.475	0.664	0.646	41.260

(**Appendix Table 5-1** continued)

Hole	Core	Type	Section	Type	Top (cm)	Bottom (cm)	Top (m CSF-A)	Bottom (m CSF-A)	Depth (rmcd; m revised CCSF-A)	Depth (m adj rmcd; m adj rev CCSF-A)	Coarse Fraction (wt %)	Barren Sample	δ ^{13}C measured at Bremen (‰, VPDB)	δ ^{18}O measured at Bremen (‰, VPDB)	δ ^{13}C measured at NOCS (‰, VPDB)	δ ^{18}O measured at NOCS (‰, VPDB)	δ ^{13}C compiled (‰, VPDB)	δ ^{18}O compiled (‰, VPDB)	δ ^{13}C adjusted to Cibs (true+0.34)	δ ^{18}O adjusted to Cibs (true+0.1/0.89)	Age (Ma) [WK Age]
B	17	H	3	W	91	93	154.11	154.13	183.02	183.02	9.0				0.491	0.672	0.491	0.672	0.831	0.867	41.269
B	17	H	3	W	96	98	154.16	154.18	183.07	183.07	9.8				0.274	0.504	0.274	0.504	0.614	0.679	41.278
B	17	H	3	W	101	103	154.21	154.23	183.12	183.12	10.8				0.084	0.583	0.084	0.583	0.424	0.768	41.287
B	17	H	3	W	106	108	154.26	154.28	183.17	183.17	12.7				0.357	0.652	0.357	0.652	0.697	0.845	41.296
B	17	H	3	W	108	110	154.28	154.30	183.19	183.19	11.6				0.358	0.674	0.358	0.674	0.698	0.870	41.300
B	17	H	3	W	111	113	154.31	154.33	183.22	183.22	11.8		0.525	0.649			0.525	0.649	0.865	0.842	41.306
B	17	H	3	W	116	118	154.36	154.38	183.27	183.27					0.282	0.551	0.282	0.551	0.622	0.732	41.315
B	17	H	3	W	121	123	154.41	154.43	183.32	183.32	12.7				0.578	0.777	0.578	0.777	0.918	0.986	41.324
B	17	H	3	W	126	128	154.46	154.48	183.37	183.37	10.4				0.326	0.698	0.326	0.698	0.666	0.896	41.333
B	17	H	3	W	131	133	154.51	154.53	183.42	183.42	11.6				0.606	0.888	0.606	0.888	0.946	1.110	41.342
B	17	H	3	W	136	138	154.56	154.58	183.47	183.47	9.7				0.281	0.396	0.281	0.396	0.621	0.557	41.351
B	17	H	3	W	141	143	154.61	154.63	183.52	183.52	7.8				0.320	0.454	0.320	0.454	0.660	0.623	41.359
B	17	H	3	W	146	148	154.66	154.68	183.57	183.55	9.1				0.621	0.712	0.621	0.712	0.961	0.912	41.366
B	17	H	4	W	1	3	154.71	154.73	183.62	183.59	11.4				0.474	0.738	0.474	0.738	0.814	0.941	41.373
B	17	H	4	W	6	8	154.76	154.78	183.67	183.63	12.6				0.435	0.767	0.435	0.767	0.775	0.975	41.380
B	17	H	4	W	11	13	154.81	154.83	183.72	183.67	11.1				0.639	0.762	0.639	0.762	0.979	0.969	41.387
B	17	H	4	W	16	18	154.86	154.88	183.77	183.70	10.2				0.702	0.733	0.702	0.733	1.042	0.936	41.394
B	17	H	4	W	21	23	154.91	154.93	183.82	183.74			0.281	0.491	0.256	0.392	0.269	0.442	0.609	0.609	41.400
B	17	H	4	W	26	28	154.96	154.98	183.87	183.78	10.1				0.362	0.622	0.362	0.622	0.702	0.811	41.407
B	17	H	4	W	31	33	155.01	155.03	183.92	183.82	10.0				0.559	0.588	0.559	0.588	0.899	0.773	41.414
B	17	H	4	W	36	38	155.06	155.08	183.97	183.85	9.0		0.477	0.552			0.477	0.552	0.817	0.733	41.421
B	17	H	4	W	41	43	155.11	155.13	184.02	183.89	7.5				0.388	0.481	0.388	0.481	0.728	0.653	41.428
B	17	H	4	W	46	48	155.16	155.18	184.07	183.93	8.2				0.123	0.337	0.123	0.337	0.463	0.491	41.435
B	17	H	4	W	51	53	155.21	155.23	184.12	183.98	10.7				0.102	0.079	0.102	0.079	0.442	0.201	41.443
B	17	H	4	W	56	58	155.26	155.28	184.17	184.02	10.7				-0.032	0.218	-0.032	0.218	0.308	0.357	41.452
B	17	H	4	W	61	63	155.31	155.33	184.22	184.07	8.9				0.320	0.441	0.320	0.441	0.660	0.608	41.460
B	17	H	4	W	66	68	155.36	155.38	184.27	184.11	5.9				0.380	0.532	0.380	0.532	0.720	0.711	41.469
B	17	H	4	W	71	73	155.41	155.43	184.32	184.16	11.2				0.480	0.534	0.480	0.534	0.820	0.712	41.477
B	17	H	4	W	76	78	155.46	155.48	184.37	184.21	9.9				0.249	0.408	0.249	0.408	0.589	0.571	41.486
B	17	H	4	W	81	83	155.51	155.53	184.42	184.25	11.9				0.486	0.519	0.486	0.519	0.826	0.695	41.494
B	17	H	4	W	86	88	155.56	155.58	184.47	184.30	9.0										41.502
B	17	H	4	W	91	93	155.61	155.63	184.52	184.35			0.405	0.607			0.405	0.607	0.745	0.794	41.511
B	17	H	4	W	91	93	155.61	155.63	184.52	184.35	9.7		0.518	0.366			0.518	0.366	0.858	0.524	41.511
B	17	H	4	W	96	98	155.66	155.68	184.57	184.39	11.1		0.641	0.844	0.661	0.828	0.651	0.836	0.991	1.052	41.519
B	17	H	4	W	101	103	155.71	155.73	184.62	184.44	9.7		0.576	0.592			0.576	0.592	0.916	0.778	41.529
B	17	H	4	W	103	105	155.73	155.75	184.64	184.47	9.9		0.502	0.372			0.502	0.372	0.842	0.530	41.533
B	17	H	4	W	106	108	155.76	155.78	184.67	184.50					0.397	0.434	0.397	0.434	0.737	0.600	41.540
B	17	H	4	W	111	113	155.81	155.83	184.72	184.56	8.4				0.299	0.357	0.299	0.357	0.639	0.514	41.550
B	17	H	4	W	116	118	155.86	155.88	184.77	184.62	8.1										41.561
B	17	H	4	W	121	123	155.91	155.93	184.82	184.68	13.9				0.376	0.372	0.376	0.372	0.716	0.530	41.572
B	17	H	4	W	126	128	155.96	155.98	184.87	184.74	9.1				0.019	0.221	0.019	0.221	0.359	0.361	41.583
B	17	H	4	W	131	133	156.01	156.03	184.92	184.79	6.1				0.114	0.146	0.114	0.146	0.454	0.276	41.594
B	17	H	4	W	136	138	156.06	156.08	184.97	184.85	8.5				0.033	-0.081	0.033	-0.081	0.373	0.021	41.604
B	17	H	4	W	141	143	156.11	156.13	185.02	184.90	10.0				0.056	0.390	0.056	0.390	0.396	0.550	41.614
B	17	H	4	W	146	148	156.16	156.18	185.07	184.95	13.2										41.624
B	17	H	5	W	1	3	156.21	156.23	185.12	185.01	10.4				0.407	0.252	0.407	0.252	0.747	0.395	41.633
B	17	H	5	W	6	8	156.26	156.28	185.17	185.06	10.0				0.171	0.353	0.171	0.353	0.511	0.509	41.643
B	17	H	5	W	11	13	156.31	156.33	185.22	185.11	11.8		0.484	0.547			0.484	0.547	0.824	0.727	41.652
B	17	H	5	W	16	18	156.36	156.38	185.27	185.17	9.7		0.350	0.452			0.350	0.452	0.690	0.620	41.663
B	17	H	5	W	21	23	156.41	156.43	185.32	185.22	11.5		0.428	0.507			0.428	0.507	0.768	0.682	41.673
B	17	H	5	W	23	25	156.43	156.45	185.34	185.24	12.8				0.387	0.354	0.387	0.354	0.727	0.510	41.677
B	17	H	5	W	31	33	156.51	156.53	185.42	185.34	12.2				0.458	0.594	0.458	0.594	0.798	0.780	41.694
B	17	H	5	W	36	38	156.56	156.58	185.47	185.39					0.413	0.140	0.413	0.140	0.753	0.269	41.705
B	17	H	5	W	41	43	156.61	156.63	185.52	185.45	10.2				0.669	0.596	0.669	0.596	1.009	0.782	41.715
B	17	H	5	W	46	48	156.66	156.68	185.57	185.51	9.3		0.373	0.454			0.373	0.454	0.713	0.622	41.726
B	17	H	5	W	51	53	156.71	156.73	185.62	185.56	8.7				0.307	0.431	0.307	0.431	0.647	0.596	41.736
B	17	H	5	W	56	58	156.76	156.78	185.67	185.62	10.0		0.199	0.325			0.199	0.325	0.539	0.478	41.747
B	17	H	5	W	61	63	156.81	156.83	185.72	185.67	13.0				0.337	0.264	0.337	0.264	0.677	0.410	41.757
B	17	H	5	W	66	68	156.86	156.88	185.77	185.73	10.6		0.108	0.452			0.108	0.452	0.448	0.620	41.768
B	17	H	5	W	71	73	156.91	156.93	185.82	185.79	13.9				0.021	0.132	0.021	0.132	0.361	0.261	41.778

(**Appendix Table 5-1** continued)

Hole	Core	Type	Section	Type	Top (cm)	Bottom (cm)	Top (m CSF-A)	Bottom (m CSF-A)	Depth (rmcd; m revised CCSF-A)	Depth (m adj rmcd; m adj rev CCSF-A)	Coarse Fraction (wt %)	Barren Sample	$\delta^{13}C$ measured at Bremen (‰, VPDB)	$\delta^{18}O$ measured at Bremen (‰, VPDB)	$\delta^{13}C$ measured at NOCS (‰, VPDB)	$\delta^{18}O$ measured at NOCS (‰, VPDB)	$\delta^{13}C$ compiled (‰, VPDB)	$\delta^{18}O$ compiled (‰, VPDB)	$\delta^{13}C$ adjusted to Cibs (true+0.34)	$\delta^{18}O$ adjusted to Cibs (true+0.1/0.89)	Age (Ma) [WK Age]
B	17	H	5	W	76	78	156.96	156.98	185.87	185.84	11.4				0.326	0.273	0.326	0.273	0.666	0.419	41.789
B	17	H	5	W	81	83	157.01	157.03	185.92	185.90	13.1		0.533	0.578	0.611	0.660	0.572	0.619	0.912	0.808	41.799
B	17	H	5	W	86	88	157.06	157.08	185.97	185.96	13.7		0.666	0.699			0.666	0.699	1.006	0.898	41.810
B	17	H	5	W	91	93	157.11	157.13	186.02	186.01	13.3		0.558	0.496	0.725	0.599	0.641	0.547	0.981	0.727	41.820
B	17	H	5	W	96	98	157.16	157.18	186.07	186.07	13.4		0.461	0.377			0.461	0.377	0.801	0.536	41.830
B	17	H	5	W	101	103	157.21	157.23	186.12	186.11			0.487	0.427			0.487	0.427	0.827	0.592	41.839
B	17	H	5	W	106	108	157.26	157.28	186.17	186.16	15.5										41.847
B	17	H	5	W	111	113	157.31	157.33	186.22	186.20	14.8		0.565	0.698			0.565	0.698	0.905	0.897	41.855
B	17	H	5	W	116	118	157.36	157.38	186.27	186.25	13.7				0.574	0.776	0.574	0.776	0.914	0.984	41.863
B	17	H	5	W	121	123	157.41	157.43	186.32	186.29	13.0				0.664	0.449	0.664	0.449	1.004	0.616	41.871
B	17	H	5	W	126	128	157.46	157.48	186.37	186.33	17.1		0.414	0.477	0.569	1.059	0.492	0.768	0.832	0.975	41.879
B	17	H	5	W	131	133	157.51	157.53	186.42	186.38	18.8				0.728	0.965	0.728	0.965	1.068	1.197	41.888
B	17	H	5	W	136	138	157.56	157.58	186.47	186.42	17.4				0.659	0.746	0.659	0.746	0.999	0.950	41.896
B	17	H	5	W	141	143	157.61	157.63	186.52	186.47	16.4				0.681	0.741	0.681	0.741	1.021	0.944	41.904
B	17	H	5	W	146	148	157.66	157.68	186.57	186.51					0.376	0.338	0.376	0.338	0.716	0.492	41.912
B	17	H	6	W	1	3	157.71	157.73	186.62	186.55	16.8		0.613	0.851			0.613	0.851	0.953	1.069	41.924
B	17	H	6	W	6	8	157.76	157.78	186.67	186.60	17.1				0.544	0.532	0.544	0.532	0.884	0.710	41.937
B	17	H	6	W	11	13	157.81	157.83	186.72	186.64	14.5				0.347	0.408	0.347	0.408	0.687	0.571	41.950
B	17	H	6	W	16	18	157.86	157.88	186.77	186.69	14.7				0.562	0.463	0.562	0.463	0.902	0.633	41.963
B	17	H	6	W	21	23	157.91	157.93	186.82	186.73	13.2				0.767	0.716	0.767	0.716	1.107	0.917	41.976
B	17	H	6	W	26	28	157.96	157.98	186.87	186.77					0.165	0.282	0.165	0.282	0.505	0.430	41.989
B	17	H	6	W	31	33	158.01	158.03	186.92	186.82	12.8				0.396	0.526	0.396	0.526	0.736	0.703	42.002
B	17	H	6	W	36	38	158.06	158.08	186.97	186.87	13.7				0.516	0.499	0.516	0.499	0.856	0.673	42.017
B	17	H	6	W	41	43	158.11	158.13	187.02	186.92	14.1				0.551	0.457	0.551	0.457	0.891	0.626	42.032
B	17	H	6	W	46	48	158.16	158.18	187.07	186.97	16.9				0.466	0.249	0.466	0.249	0.806	0.392	42.046
B	17	H	6	W	51	53	158.21	158.23	187.12	187.02	13.5				0.686	0.663	0.686	0.663	1.026	0.857	42.061
B	17	H	6	W	56	58	158.26	158.28	187.17	187.07	12.7		0.632	0.666			0.632	0.666	0.972	0.861	42.076
B	17	H	6	W	61	63	158.31	158.33	187.22	187.12	11.6				0.422	0.385	0.422	0.385	0.762	0.545	42.104
B	17	H	CC	W	1	3	158.34	158.36	187.25	187.15	11.1		0.508	0.660			0.508	0.660	0.848	0.854	42.122
B	17	H	CC	W	6	8	158.39	158.41	187.30	187.20	9.9				0.294	0.416	0.294	0.416	0.634	0.580	42.151
B	17	H	CC	W	11	13	158.44	158.46	187.35	187.25					0.540	0.396	0.540	0.396	0.880	0.557	42.179
C	20	H	4	W	70	72	159.30	159.32	187.26	187.26	14.7				0.250	0.420	0.250	0.420	0.590	0.584	42.185
B	17	H	CC	W	16	18	158.49	158.51	187.40	187.30	11.5				0.313	0.308	0.313	0.308	0.653	0.459	42.208
C	20	H	4	W	75	77	159.35	159.37	187.31	187.31	14.7				0.503	0.702	0.503	0.702	0.843	0.901	42.214
C	20	H	4	W	80	82	159.40	159.42	187.36	187.36	12.6					0.792		0.792	0.340	1.002	42.243
C	20	H	4	W	85	87	159.45	159.47	187.41	187.41	16.0				0.190	0.686	0.190	0.686	0.530	0.883	42.272
C	20	H	4	W	90	92	159.50	159.52	187.46	187.46	15.3				0.468	0.744	0.468	0.744	0.808	0.949	42.301
C	20	H	4	W	95	97	159.55	159.57	187.51	187.51	13.0				0.362	0.550	0.362	0.550	0.702	0.731	42.311
C	20	H	4	W	100	102	159.60	159.62	187.56	187.56	12.2				0.336	0.699	0.336	0.699	0.676	0.898	42.320
C	20	H	4	W	105	107	159.65	159.67	187.61	187.61	13.1				0.489	0.621	0.489	0.621	0.829	0.810	42.330
C	20	H	4	W	110	112	159.70	159.72	187.66	187.66	14.1		0.368	0.699			0.368	0.699	0.708	0.898	42.340
C	20	H	4	W	115	117	159.75	159.77	187.71	187.71	14.6				0.424	0.707	0.424	0.707	0.764	0.907	42.350
C	20	H	4	W	120	122	159.80	159.82	187.76	187.76	12.3				0.276	0.592	0.276	0.592	0.616	0.777	42.359
C	20	H	4	W	125	127	159.85	159.87	187.81	187.81	11.0				0.309	0.717	0.309	0.717	0.649	0.918	42.369
C	20	H	4	W	130	132	159.90	159.92	187.86	187.86	13.0				0.237	0.632	0.237	0.632	0.577	0.822	42.379
C	20	H	4	W	135	137	159.95	159.97	187.91	187.91	11.7				0.190	0.513	0.190	0.513	0.530	0.689	42.388
C	20	H	4	W	140	142	160.00	160.02	187.96	187.96	11.6				0.170	0.531	0.170	0.531	0.510	0.709	42.398
C	20	H	4	W	145	147	160.05	160.07	188.01	188.01	13.3				0.116	0.412	0.116	0.412	0.456	0.576	42.408
B	19	X	1	W	6	8	162.76	162.78	188.42	188.42			0.273	0.539			0.273	0.539	0.613	0.718	42.487
B	19	X	1	W	16	18	162.86	162.88	188.52	188.52			0.481	0.638			0.481	0.638	0.821	0.829	42.507
B	19	X	1	W	26	28	162.96	162.98	188.62	188.62	17.0		0.613	0.809			0.613	0.809	0.953	1.021	42.526
B	18	H	1	W	1	3	159.71	159.73	188.62	188.62	11.2	removed									42.526
B	19	X	1	W	31	33	163.01	163.03	188.67	188.67	8.5		0.591	0.451			0.591	0.451	0.931	0.619	42.536
B	18	H	1	W	6	8	159.76	159.78	188.67	188.67	9.3	removed									42.536
B	19	X	1	W	36	38	163.06	163.08	188.72	188.72	9.7		0.428	0.518			0.428	0.518	0.768	0.695	42.546
B	18	H	1	W	11	13	159.81	159.83	188.72	188.72	9.9	removed									42.546
C	20	H	5	W	70	72	160.80	160.82	188.76	188.76	16.3		0.498	0.825			0.498	0.825	0.838	1.039	42.553
B	18	H	1	W	16	18	159.86	159.88	188.77	188.77	7.4	removed									42.555
C	20	H	5	W	75	77	160.85	160.87	188.81	188.81					0.448	0.863	0.448	0.863	0.788	1.082	42.563
B	19	X	1	W	46	48	163.16	163.18	188.82	188.82			0.778	0.869			0.778	0.869	1.118	1.089	42.565

(**Appendix Table 5-1** continued)

Hole	Core	Type	Section	Type	Top (cm)	Bottom (cm)	Top (m CSF-A)	Bottom (m CSF-A)	Depth (rmcd; m revised CCSF-A)	Depth (m adj rmcd; m adj rev CCSF-A)	Coarse Fraction (wt %)	Barren Sample	$\delta^{13}C$ measured at Bremen (‰, VPDB)	$\delta^{18}O$ measured at Bremen (‰, VPDB)	$\delta^{13}C$ measured at NOCS (‰, VPDB)	$\delta^{18}O$ measured at NOCS (‰, VPDB)	$\delta^{13}C$ compiled (‰, VPDB)	$\delta^{18}O$ compiled (‰, VPDB)	$\delta^{13}C$ adjusted to Cibs (true+0.34)	$\delta^{18}O$ adjusted to Cibs (true+0.1/0.89)	Age (Ma) [WK Age]
B	19	X	1	W	51	53	163.21	163.23	188.87	188.87	9.1		0.721	0.937			0.721	0.937	1.061	1.165	42.575
B	18	H	1	W	26	28	159.96	159.98	188.87	188.87	9.9	removed									42.575
B	19	X	1	W	56	58	163.26	163.28	188.92	188.92			0.681	0.683			0.681	0.683	1.021	0.880	42.585
B	18	H	1	W	31	33	160.01	160.03	188.92	188.92	11.4	removed									42.585
B	19	X	1	W	61	63	163.31	163.33	188.97	188.97	5.8		0.668	0.643			0.668	0.643	1.008	0.835	42.594
B	19	X	1	W	66	68	163.36	163.38	189.02	189.02			0.706	0.887			0.706	0.887	1.046	1.109	42.604
B	18	H	1	W	41	43	160.11	160.13	189.02	189.02	13.3	removed									42.604
B	18	H	1	W	46	48	160.16	160.18	189.07	189.07	11.5	removed									42.614
B	19	X	1	W	76	78	163.46	163.48	189.12	189.12	9.0		0.843	0.915			0.843	0.915	1.183	1.141	42.623
B	18	H	1	W	51	53	160.21	160.23	189.12	189.12	11.8	removed									42.623
B	19	X	1	W	81	83	163.51	163.53	189.17	189.17			0.910	0.894			0.910	0.894	1.250	1.117	42.633
B	18	H	1	W	56	58	160.26	160.28	189.17	189.17	13.3	removed									42.633
B	19	X	1	W	86	88	163.56	163.58	189.22	189.22	4.3		0.675	0.614			0.675	0.614	1.015	0.803	42.643
B	18	H	1	W	61	63	160.31	160.33	189.22	189.22	12.9	removed									42.643
B	19	X	1	W	91	93	163.61	163.63	189.27	189.27	8.9		0.830	0.912			0.830	0.912	1.170	1.137	42.653
B	18	H	1	W	66	68	160.36	160.38	189.27	189.27	12.1	removed									42.653
B	18	H	1	W	76	78	160.46	160.48	189.37	189.37	15.4	removed									42.672
B	18	H	1	W	76	78	160.46	160.48	189.37	189.37		removed									42.672
B	19	X	1	W	106	108	163.76	163.78	189.42	189.42			0.820	0.939			0.820	0.939	1.160	1.167	42.682
B	19	X	1	W	111	113	163.81	163.83	189.47	189.47	4.3		0.609	0.464			0.609	0.464	0.949	0.633	42.691
B	18	H	1	W	86	88	160.56	160.58	189.47	189.47	15.6	removed									42.691
B	19	X	1	W	116	118	163.86	163.88	189.52	189.52	5.2		0.611	0.573			0.611	0.573	0.951	0.757	42.701
B	19	X	1	W	121	123	163.91	163.93	189.57	189.57	7.9		0.542	0.238			0.542	0.238	0.882	0.379	42.711
B	19	X	1	W	126	128	163.96	163.98	189.62	189.62	6.3		0.504	0.693			0.504	0.693	0.844	0.891	42.720
B	19	X	1	W	131	133	164.01	164.03	189.67	189.67	6.8		0.407	0.491			0.407	0.491	0.747	0.664	42.730
B	19	X	1	W	136	138	164.06	164.08	189.72	189.72	8.5		0.570	0.584			0.570	0.584	0.910	0.768	42.740
B	19	X	1	W	141	143	164.11	164.13	189.77	189.77	13.1		0.530	0.403			0.530	0.403	0.870	0.565	42.750
B	19	X	1	W	146	148	164.16	164.18	189.82	189.82	13.6		0.569	0.270			0.569	0.270	0.909	0.415	42.759
B	19	X	2	W	1	3	164.21	164.23	189.87	189.87	8.0		0.422	0.245			0.422	0.245	0.762	0.388	42.769
B	18	H	1	W	126	128	160.96	160.98	189.87	189.87	8.1										42.769
B	19	X	2	W	6	8	164.26	164.28	189.92	189.92	6.9		0.404	0.318			0.404	0.318	0.744	0.469	42.779
B	18	H	1	W	131	133	161.01	161.03	189.92	189.92	12.8	removed									42.779
B	19	X	2	W	11	13	164.31	164.33	189.97	189.97	6.9		0.418	0.483			0.418	0.483	0.758	0.655	42.788
B	19	X	2	W	16	18	164.36	164.38	190.02	190.02	5.4		0.237	0.250			0.237	0.250	0.577	0.393	42.798
B	18	H	1	W	141	143	161.11	161.13	190.02	190.02	15.4	removed									42.798
B	19	X	2	W	21	23	164.41	164.43	190.07	190.07	3.7										42.808
B	18	H	1	W	146	148	161.16	161.18	190.07	190.07	15.5	removed									42.808
B	19	X	2	W	26	28	164.46	164.48	190.12	190.12	3.9		0.254	0.386			0.254	0.386	0.594	0.546	42.818
B	19	X	2	W	31	33	164.51	164.53	190.17	190.17	6.2		0.491	0.446			0.491	0.446	0.831	0.613	42.827
B	19	X	2	W	36	38	164.56	164.58	190.22	190.22	7.1		0.664	0.539			0.664	0.539	1.004	0.717	42.837
B	19	X	2	W	41	43	164.61	164.63	190.27	190.27	7.6		0.463	0.229			0.463	0.229	0.803	0.370	42.847
B	19	X	2	W	46	48	164.66	164.68	190.32	190.32	7.7		0.426	0.189			0.426	0.189	0.766	0.325	42.856
B	19	X	2	W	51	53	164.71	164.73	190.37	190.37	7.2		0.453	0.178			0.453	0.178	0.793	0.313	42.866
B	19	X	2	W	56	58	164.76	164.78	190.42	190.42	9.4		0.438	0.353			0.438	0.353	0.778	0.510	42.878
B	19	X	2	W	61	63	164.81	164.83	190.47	190.47	13.7		0.769	0.441			0.769	0.441	1.109	0.608	42.892
B	19	X	2	W	66	68	164.86	164.88	190.52	190.52	11.8		0.462	0.454			0.462	0.454	0.802	0.623	42.906
B	18	H	2	W	51	53	161.71	161.73	190.62	190.54	16.5										42.911
B	19	X	2	W	71	73	164.91	164.93	190.57	190.57	10.4		0.451	0.366			0.451	0.366	0.791	0.524	42.919
B	19	X	2	W	76	78	164.96	164.98	190.62	190.62	10.4		0.527	0.376			0.527	0.376	0.867	0.535	42.933
B	19	X	2	W	81	83	165.01	165.03	190.67	190.67	10.9		0.565	0.436			0.565	0.436	0.905	0.602	42.947
B	18	H	2	W	71	73	161.91	161.93	190.82	190.70	13.5										42.955
B	19	X	2	W	86	88	165.06	165.08	190.72	190.72	10.7		0.407	0.352			0.407	0.352	0.747	0.508	42.960
B	19	X	2	W	91	93	165.11	165.13	190.77	190.77			0.481	0.354			0.481	0.354	0.821	0.510	42.974
B	19	X	2	W	91	93	165.11	165.13	190.77	190.77	8.3		0.394	0.283			0.394	0.283	0.734	0.430	42.974
B	19	X	2	W	91	93	165.11	165.13	190.77	190.77			0.394	0.283			0.394	0.283	0.734	0.430	42.974
B	19	X	2	W	96	98	165.16	165.18	190.82	190.82	7.9		0.415	0.262			0.415	0.262	0.755	0.406	42.988
B	19	X	2	W	101	103	165.21	165.23	190.87	190.87	8.8		0.584	0.387			0.584	0.387	0.924	0.548	43.001
B	19	X	2	W	106	108	165.26	165.28	190.92	190.92	10.0		0.426	0.082			0.426	0.082	0.766	0.204	43.015
B	19	X	2	W	111	113	165.31	165.33	190.97	190.97	10.5		0.434	0.331			0.434	0.331	0.774	0.484	43.029
B	19	X	2	W	116	118	165.36	165.38	191.02	191.02	8.8		0.558	0.280			0.558	0.280	0.898	0.427	43.043

(**Appendix Table 5-1** continued)

Hole	Core	Type	Section	Type	Top (cm)	Bottom (cm)	Top (m CSF-A)	Bottom (m CSF-A)	Depth (rmcd; m revised CCSF-A)	Depth (m adj rmcd; m adj rev CCSF-A)	Coarse Fraction (wt %)	Barren Sample	$\delta^{13}C$ measured at Bremen (‰, VPDB)	$\delta^{18}O$ measured at Bremen (‰, VPDB)	$\delta^{13}C$ measured at NOCS (‰, VPDB)	$\delta^{18}O$ measured at NOCS (‰, VPDB)	$\delta^{13}C$ compiled (‰, VPDB)	$\delta^{18}O$ compiled (‰, VPDB)	$\delta^{13}C$ adjusted to Cibs (true+0.34)	$\delta^{18}O$ adjusted to Cibs (true+0.1/0.89)	Age (Ma) [WK Age]
B	19	X	2	W	121	123	165.41	165.43	191.07	191.07	7.5		0.508	0.190			0.508	0.190	0.848	0.326	43.056
B	19	X	2	W	126	128	165.46	165.48	191.12	191.12	9.8		0.419	0.236			0.419	0.236	0.759	0.378	43.070
B	19	X	2	W	131	133	165.51	165.53	191.17	191.17	9.4		0.382	0.292			0.382	0.292	0.722	0.441	43.084
B	19	X	2	W	136	138	165.56	165.58	191.22	191.22	9.9		0.475	0.321			0.475	0.321	0.815	0.474	43.097
B	18	H	3	W	31	33	162.51	162.53	191.42	191.22	6.1										43.097
B	19	X	2	W	141	143	165.61	165.63	191.27	191.27	8.7		0.661	0.449			0.661	0.449	1.001	0.616	43.111
B	19	X	2	W	146	148	165.66	165.68	191.32	191.32	7.2		0.494	0.449			0.494	0.449	0.834	0.616	43.125
B	19	X	3	W	1	3	165.71	165.73	191.37	191.37	9.3		0.759	0.785			0.759	0.785	1.099	0.994	43.138
B	19	X	3	W	6	8	165.76	165.78	191.42	191.42	9.4										43.152
B	19	X	3	W	11	13	165.81	165.83	191.47	191.47	7.9		0.516	0.698			0.516	0.698	0.856	0.897	43.166
B	19	X	3	W	16	18	165.86	165.88	191.52	191.52	7.6		0.629	0.446			0.629	0.446	0.969	0.613	43.179
B	18	H	CC	W	11	13	162.83	162.85	191.74	191.54	10.4										43.185
B	19	X	3	W	21	23	165.91	165.93	191.57	191.57	9.3		0.437	0.219			0.437	0.219	0.777	0.358	43.193
B	19	X	3	W	26	28	165.96	165.98	191.62	191.62	8.5		0.724	0.622			0.724	0.622	1.064	0.812	43.207
B	19	X	3	W	31	33	166.01	166.03	191.67	191.67	9.0		0.733	0.640			0.733	0.640	1.073	0.831	43.221
B	19	X	3	W	36	38	166.06	166.08	191.72	191.72	7.3		0.645	0.456			0.645	0.456	0.985	0.624	43.234
B	19	X	3	W	41	43	166.11	166.13	191.77	191.77	6.7		0.581	0.474			0.581	0.474	0.921	0.645	43.248
B	19	X	3	W	46	48	166.16	166.18	191.82	191.82	7.8		0.685	0.505			0.685	0.505	1.025	0.680	43.262
B	19	X	3	W	51	53	166.21	166.23	191.87	191.87	8.2		0.722	0.566			0.722	0.566	1.062	0.749	43.275
B	19	X	3	W	56	58	166.26	166.28	191.92	191.92	8.2		0.651	0.507			0.651	0.507	0.991	0.682	43.289
B	19	X	3	W	61	63	166.31	166.33	191.97	191.97	8.0		0.529	0.505			0.529	0.505	0.869	0.680	43.303
B	19	X	3	W	66	68	166.36	166.38	192.02	192.02	8.3		0.794	0.590			0.794	0.590	1.134	0.775	43.316
B	19	X	3	W	71	73	166.41	166.43	192.07	192.07	9.5		0.696	0.445			0.696	0.445	1.036	0.612	43.330
B	19	X	3	W	76	78	166.46	166.48	192.12	192.12	9.0		0.568	0.638			0.568	0.638	0.908	0.829	43.344
B	19	X	3	W	81	83	166.51	166.53	192.17	192.17	8.5		0.642	0.542			0.642	0.542	0.982	0.721	43.357
B	19	X	3	W	86	88	166.56	166.58	192.22	192.22	8.0		0.632	0.469			0.632	0.469	0.972	0.639	43.371
B	19	X	3	W	91	93	166.61	166.63	192.27	192.27	6.7		0.665	0.290			0.665	0.290	1.005	0.438	43.385
B	19	X	3	W	96	98	166.66	166.68	192.32	192.32	8.1		0.672	0.629			0.672	0.629	1.012	0.819	43.399
B	19	X	3	W	101	103	166.71	166.73	192.37	192.37	9.1		0.799	0.666			0.799	0.666	1.139	0.861	43.412
B	19	X	3	W	106	108	166.76	166.78	192.42	192.42	9.1		0.438	0.341			0.438	0.341	0.778	0.495	43.426
B	19	X	3	W	111	113	166.81	166.83	192.47	192.47	8.5		0.767	0.561			0.767	0.561	1.107	0.743	43.440
B	19	X	3	W	116	118	166.86	166.88	192.52	192.52	8.2		0.618	0.341			0.618	0.341	0.958	0.496	43.453
B	19	X	3	W	121	123	166.91	166.93	192.57	192.57	8.2		0.443	0.533			0.443	0.533	0.783	0.711	43.467
B	19	X	3	W	126	128	166.96	166.98	192.62	192.62	8.1		0.708	0.574			0.708	0.574	1.048	0.757	43.481
B	19	X	3	W	131	133	167.01	167.03	192.67	192.67	6.6		0.734	0.487			0.734	0.487	1.074	0.660	43.494
B	19	X	3	W	136	138	167.06	167.08	192.72	192.72	7.3		0.582	0.415			0.582	0.415	0.922	0.579	43.508
B	19	X	3	W	141	143	167.11	167.13	192.77	192.77	8.1		0.652	0.700			0.652	0.700	0.992	0.899	43.522
B	19	X	3	W	146	148	167.16	167.18	192.82	192.82	7.5		0.338	0.228			0.338	0.228	0.678	0.369	43.535
B	19	X	4	W	1	3	167.21	167.23	192.87	192.87	7.2		0.442	0.306			0.442	0.306	0.782	0.456	43.549
B	19	X	4	W	6	8	167.26	167.28	192.92	192.92	7.3		0.624	0.531			0.624	0.531	0.964	0.709	43.563
B	19	X	4	W	11	13	167.31	167.33	192.97	192.97	7.9		0.697	0.578			0.697	0.578	1.037	0.762	43.577
B	19	X	4	W	16	18	167.36	167.38	193.02	193.02	7.6		0.593	0.577			0.593	0.577	0.933	0.761	43.590
B	19	X	4	W	21	23	167.41	167.43	193.07	193.07	5.7		0.648	0.561			0.648	0.561	0.988	0.743	43.604
B	19	X	4	W	26	28	167.46	167.48	193.12	193.12	7.4		0.505	0.360			0.505	0.360	0.845	0.517	43.618
B	19	X	4	W	31	33	167.51	167.53	193.17	193.17	4.5		0.578	0.350			0.578	0.350	0.918	0.506	43.631
B	19	X	4	W	31	33	167.51	167.53	193.17	193.17			0.470	0.330			0.470	0.330	0.810	0.483	43.631
B	19	X	4	W	36	38	167.56	167.58	193.22	193.22	7.3		0.606	0.411			0.606	0.411	0.946	0.574	43.645
B	19	X	4	W	36	38	167.56	167.58	193.22	193.22											43.645
B	19	X	4	W	41	43	167.61	167.63	193.27	193.27	6.3		0.212	0.330			0.212	0.330	0.552	0.483	43.659
B	19	X	4	W	46	48	167.66	167.68	193.32	193.32	8.2		0.465	0.198			0.465	0.198	0.805	0.335	43.672
B	19	X	4	W	51	53	167.71	167.73	193.37	193.37	9.1		0.377	0.308			0.377	0.308	0.717	0.458	43.686
B	19	X	4	W	56	58	167.76	167.78	193.42	193.42	8.0		0.506	0.473			0.506	0.473	0.846	0.644	43.700
B	19	X	4	W	61	63	167.81	167.83	193.47	193.47	7.4		0.564	0.472			0.564	0.472	0.904	0.643	43.713
B	19	X	4	W	71	73	167.91	167.93	193.57	193.57	8.3		0.516	0.459			0.516	0.459	0.856	0.628	43.741
B	19	X	4	W	76	78	167.96	167.98	193.62	193.62	8.2		0.420	0.265			0.420	0.265	0.760	0.410	43.755
B	19	X	4	W	81	83	168.01	168.03	193.67	193.67	9.7		0.636	0.542			0.636	0.542	0.976	0.721	43.768
B	19	X	4	W	86	88	168.06	168.08	193.72	193.72	10.2		0.755	0.793			0.755	0.793	1.095	1.003	43.782
B	19	X	4	W	91	93	168.11	168.13	193.77	193.77	8.5		0.444	0.454			0.444	0.454	0.784	0.622	43.796
B	19	X	4	W	96	98	168.16	168.18	193.82	193.82	12.2		0.434	0.368			0.434	0.368	0.774	0.526	43.809
B	19	X	4	W	101	103	168.21	168.23	193.87	193.87	7.4										43.823

(**Appendix Table 5-1** continued)

Hole	Core	Type	Section	Type	Top (cm)	Bottom (cm)	Top (m CSF-A)	Bottom (m CSF-A)	Depth (rmcd; m revised CCSF-A)	Depth (m adj rmcd; m adj rev CCSF-A)	Coarse Fraction (wt %)	Barren Sample	$\delta^{13}C$ measured at Bremen (‰, VPDB)	$\delta^{18}O$ measured at Bremen (‰, VPDB)	$\delta^{13}C$ measured at NOCS (‰, VPDB)	$\delta^{18}O$ measured at NOCS (‰, VPDB)	$\delta^{13}C$ compiled (‰, VPDB)	$\delta^{18}O$ compiled (‰, VPDB)	$\delta^{13}C$ adjusted to Cibs (true+0.34)	$\delta^{18}O$ adjusted to Cibs (true+0.1/0.89)	Age (Ma) [WK Age]
B	19	X	4	W	106	108	168.26	168.28	193.92	193.92	6.9										43.837
B	19	X	4	W	111	113	168.31	168.33	193.97	193.97	7.5		0.608	0.674			0.608	0.674	0.948	0.870	43.850
B	19	X	4	W	116	118	168.36	168.38	194.02	194.02	10.4		0.779	0.810			0.779	0.810	1.119	1.022	43.864
B	19	X	4	W	121	123	168.41	168.43	194.07	194.07	8.2										43.878
B	19	X	4	W	126	128	168.46	168.48	194.12	194.12	7.3		0.579	0.515			0.579	0.515	0.919	0.691	43.891
B	19	X	4	W	131	133	168.51	168.53	194.17	194.17	5.8		0.412	0.413			0.412	0.413	0.752	0.576	43.905
B	19	X	4	W	136	138	168.56	168.58	194.22	194.22	5.3		0.644	0.607			0.644	0.607	0.984	0.794	43.919
B	19	X	4	W	141	143	168.61	168.63	194.27	194.27	5.6		0.484	0.315			0.484	0.315	0.824	0.466	43.933
B	19	X	4	W	146	148	168.66	168.68	194.32	194.32	6.2										43.946
B	19	X	5	W	1	3	168.71	168.73	194.37	194.37	7.8										43.960
B	19	X	5	W	6	8	168.76	168.78	194.42	194.42	9.7		0.454	0.352			0.454	0.352	0.794	0.508	43.974
B	19	X	5	W	11	13	168.81	168.83	194.47	194.47	7.9		0.408	0.423			0.408	0.423	0.748	0.588	43.987
B	19	X	5	W	16	18	168.86	168.88	194.52	194.52	7.1		0.325	0.271			0.325	0.271	0.665	0.417	44.001
B	19	X	5	W	21	23	168.91	168.93	194.57	194.57	5.2										44.015
B	19	X	5	W	26	28	168.96	168.98	194.62	194.62	4.3		0.405	0.474			0.405	0.474	0.745	0.645	44.028
B	19	X	5	W	31	33	169.01	169.03	194.67	194.67	4.1		0.499	0.420			0.499	0.420	0.839	0.585	44.042
B	19	X	5	W	36	38	169.06	169.08	194.72	194.72	7.9		0.445	0.313			0.445	0.313	0.785	0.464	44.056
B	19	X	5	W	41	43	169.11	169.13	194.77	194.77	9.2		0.424	0.421			0.424	0.421	0.764	0.585	44.069
B	19	X	5	W	46	48	169.16	169.18	194.82	194.82	7.9		0.745	0.750			0.745	0.750	1.085	0.955	44.083
B	19	X	5	W	51	53	169.21	169.23	194.87	194.87	7.7		0.461	0.415			0.461	0.415	0.801	0.578	44.097
B	19	X	5	W	56	58	169.26	169.28	194.92	194.92	8.6		0.559	0.371			0.559	0.371	0.899	0.529	44.111
B	19	X	5	W	61	63	169.31	169.33	194.97	194.97	8.8		0.275	0.246			0.275	0.246	0.615	0.388	44.124
B	19	X	5	W	66	68	169.36	169.38	195.02	195.02	10.1		0.355	0.584			0.355	0.584	0.695	0.768	44.138
A	19	X	2	W	12	14	169.62	169.64	195.38	195.38		X									44.237
A	19	X	2	W	20	22	169.7	169.72	195.46	195.46	11.3		0.564	0.359			0.564	0.359	0.904	0.516	44.258
B	19	X	CC	W	36	38	169.81	169.83	195.47	195.47	3.7		0.354	0.372			0.354	0.372	0.694	0.530	44.261
A	19	X	2	W	28	30	169.78	169.8	195.54	195.54	11.7		0.547	0.375			0.547	0.375	0.887	0.534	44.280
A	19	X	2	W	36	38	169.86	169.88	195.62	195.62	11.4		0.590	0.416			0.590	0.416	0.930	0.580	44.302
A	19	X	2	W	44	46	169.94	169.96	195.70	195.70	10.2		0.434	0.575			0.434	0.575	0.774	0.758	44.324
A	19	X	2	W	52	54	170.02	170.04	195.78	195.78	11.3		0.778	0.601			0.778	0.601	1.118	0.788	44.346
A	19	X	2	W	60	62	170.1	170.12	195.86	195.86	13.0		0.463	0.405			0.463	0.405	0.803	0.567	44.368
A	19	X	2	W	68	70	170.18	170.2	195.94	195.94	12.8		0.581	0.454			0.581	0.454	0.921	0.622	44.390
A	19	X	2	W	76	78	170.26	170.28	196.02	196.02	9.2		0.712	0.423			0.712	0.423	1.052	0.588	44.412
A	19	X	2	W	84	86	170.34	170.36	196.10	196.10	12.5		0.512	0.490			0.512	0.490	0.852	0.663	44.434
A	19	X	2	W	92	94	170.42	170.44	196.18	196.18	12.3		0.606	0.485			0.606	0.485	0.946	0.657	44.456
A	19	X	2	W	100	102	170.5	170.52	196.26	196.26	13.0		0.458	0.483			0.458	0.483	0.798	0.656	44.478
A	19	X	2	W	108	110	170.58	170.6	196.34	196.34	16.8	X									44.499
A	19	X	2	W	116	118	170.66	170.68	196.42	196.42	14.7		0.739	0.786			0.739	0.786	1.079	0.995	44.521
A	19	X	2	W	124	126	170.74	170.76	196.50	196.50	11.7	X									44.543
A	19	X	2	W	134	136	170.84	170.86	196.60	196.60	14.4		0.735	0.690			0.735	0.690	1.075	0.888	44.571
A	19	X	3	W	1	2	171.01	171.02	196.77	196.76	15.5	X									44.616
A	19	X	3	W	9	10	171.09	171.1	196.85	196.85	13.4		0.990	0.948			0.990	0.948	1.330	1.178	44.638
A	19	X	3	W	17	18	171.17	171.18	196.93	196.93	16.1										44.660
A	19	X	3	W	41	42	171.41	171.42	197.17	197.16	13.5										44.725
A	19	X	3	W	49	50	171.49	171.5	197.25	197.24	13.3		1.235	1.084			1.235	1.084	1.575	1.330	44.747
A	19	X	3	W	57	58	171.57	171.58	197.33	197.32	14.4		0.781	1.214			0.781	1.214	1.121	1.476	44.769
A	19	X	3	W	65	66	171.65	171.66	197.41	197.40	14.8		0.659	0.545			0.659	0.545	0.999	0.725	44.791
A	19	X	3	W	73	74	171.73	171.74	197.49	197.49	14.0		0.704	0.891			0.704	0.891	1.044	1.113	44.813
A	19	X	3	W	81	82	171.81	171.82	197.57	197.57	11.9		0.434	0.473			0.434	0.473	0.774	0.644	44.835
A	19	X	3	W	89	90	171.89	171.9	197.65	197.65	15.4		0.427	0.384			0.427	0.384	0.767	0.544	44.857
A	19	X	3	W	97	98	171.97	171.98	197.73	197.73	16.6		0.526	0.678			0.526	0.678	0.866	0.874	44.879
A	19	X	3	W	105	106	172.05	172.06	197.81	197.80	15.0		0.406	0.519			0.406	0.519	0.746	0.696	44.901
A	19	X	3	W	113	114	172.13	172.14	197.89	197.88	14.3		0.495	0.715			0.495	0.715	0.835	0.916	44.923
A	19	X	3	W	121	122	172.21	172.22	197.97	197.96	10.6		0.503	0.707			0.503	0.707	0.843	0.907	44.944
A	19	X	3	W	129	130	172.29	172.3	198.05	198.04	11.4		0.607	0.636			0.607	0.636	0.947	0.827	44.966
A	19	X	3	W	137	138	172.37	172.38	198.13	198.13	10.2		0.460	0.515			0.460	0.515	0.800	0.691	44.988
A	19	X	3	W	145	146	172.45	172.46	198.21	198.21	11.7		0.457	0.338			0.457	0.338	0.797	0.492	45.010
A	19	X	4	w	4	6	172.54	172.56	198.30	198.30	7.8		0.567	0.622			0.567	0.622	0.907	0.811	45.036
B	20	X	1	W	1	3	172.31	172.33	198.32	198.32	10.6		0.424	0.456			0.424	0.456	0.764	0.625	45.042
A	19	X	4	w	12	14	172.62	172.64	198.38	198.38	11.6		0.571	0.600			0.571	0.600	0.911	0.787	45.058

(**Appendix Table 5-1** continued)

Hole	Core	Type	Section	Type	Top (cm)	Bottom (cm)	Top (m CSF-A)	Bottom (m CSF-A)	Depth (rmcd; m revised CCSF-A)	Depth (m adj rmcd; m adj rev CCSF-A)	Coarse Fraction (wt %)	Barren Sample	δ¹³C measured at Bremen (‰, VPDB)	δ¹⁸O measured at Bremen (‰, VPDB)	δ¹³C measured at NOCS (‰, VPDB)	δ¹⁸O measured at NOCS (‰, VPDB)	δ¹³C compiled (‰, VPDB)	δ¹⁸O compiled (‰, VPDB)	δ¹³C adjusted to Cibs (true+0.34)	δ¹⁸O adjusted to Cibs (true+0.1/0.89)	Age (Ma) [WK Age]
B	20	X	1	W	11	13	172.41	172.43	198.42	198.42	5.2		0.318	0.474			0.318	0.474	0.658	0.645	45.069
A	19	X	4	w	20	22	172.7	172.72	198.46	198.46	14.5		0.559	0.633			0.559	0.633	0.899	0.824	45.080
B	20	X	1	W	16	18	172.46	172.48	198.47	198.47	7.6		0.346	0.503			0.346	0.503	0.686	0.678	45.083
B	20	X	1	W	21	23	172.51	172.53	198.52	198.52	5.1		0.447	0.480			0.447	0.480	0.787	0.652	45.096
B	20	X	1	W	26	28	172.56	172.58	198.57	198.57	9.2		0.390	0.513			0.390	0.513	0.730	0.688	45.110
B	20	X	1	W	31	33	172.61	172.63	198.62	198.62	10.9		0.427	0.427			0.427	0.427	0.767	0.592	45.124
B	20	X	1	W	36	38	172.66	172.68	198.67	198.67	5.6		0.341	0.511			0.341	0.511	0.681	0.687	45.137
B	20	X	1	W	41	43	172.71	172.73	198.72	198.72	12.8		0.341	0.395			0.341	0.395	0.681	0.556	45.151
B	20	X	1	W	46	48	172.76	172.78	198.77	198.77	13.5		0.394	0.406			0.394	0.406	0.734	0.568	45.165
B	20	X	1	W	51	53	172.81	172.83	198.82	198.82	10.6										45.179
B	20	X	1	W	56	58	172.86	172.88	198.87	198.87	9.5		0.298	0.504			0.298	0.504	0.638	0.679	45.192
B	20	X	1	W	61	63	172.91	172.93	198.92	198.92	7.2		0.320	0.417			0.320	0.417	0.660	0.581	45.206
B	20	X	1	W	66	68	172.96	172.98	198.97	198.97	6.4		0.375	0.404			0.375	0.404	0.715	0.566	45.220
B	20	X	1	W	71	73	173.01	173.03	199.02	199.02	13.9		0.457	0.373			0.457	0.373	0.797	0.531	45.233
B	20	X	1	W	76	78	173.06	173.08	199.07	199.07	10.6		0.431	0.448			0.431	0.448	0.771	0.615	45.247
B	20	X	1	W	81	83	173.11	173.13	199.12	199.12	10.5		0.557	0.572			0.557	0.572	0.897	0.756	45.261
B	20	X	1	W	86	88	173.16	173.18	199.17	199.17	9.0		0.518	0.509			0.518	0.509	0.858	0.684	45.274
B	20	X	1	W	91	93	173.21	173.23	199.22	199.22	10.7		0.319	0.487			0.319	0.487	0.659	0.660	45.288
B	20	X	1	W	96	98	173.26	173.28	199.27	199.27	10.2		0.470	0.526			0.470	0.526	0.810	0.703	45.302
B	20	X	1	W	101	103	173.31	173.33	199.32	199.32	11.8		0.401	0.360			0.401	0.360	0.741	0.517	45.315
B	20	X	1	W	111	113	173.41	173.43	199.42	199.42	10.7		0.305	0.306			0.305	0.306	0.645	0.457	45.343
B	20	X	1	W	121	123	173.51	173.53	199.52	199.52	9.5		0.376	0.342			0.376	0.342	0.716	0.497	45.370
B	20	X	1	W	126	128	173.56	173.58	199.57	199.57	8.1										45.384
B	20	X	1	W	131	133	173.61	173.63	199.62	199.62	8.5		0.579	0.520			0.579	0.520	0.919	0.696	45.398
B	20	X	1	W	136	138	173.66	173.68	199.67	199.67	5.9		0.461	0.611			0.461	0.611	0.801	0.799	45.411
B	20	X	1	W	141	143	173.71	173.73	199.72	199.72	4.7		0.511	0.641			0.511	0.641	0.851	0.833	45.424
B	20	X	1	W	146	148	173.76	173.78	199.77	199.77	4.8		0.579	0.618			0.579	0.618	0.919	0.807	45.433
B	20	X	2	W	1	3	173.81	173.83	199.82	199.82	4.2		0.571	0.544			0.571	0.544	0.911	0.723	45.441
B	20	X	2	W	6	8	173.86	173.88	199.87	199.87	6.2		0.430	0.555			0.430	0.555	0.770	0.736	45.450
B	20	X	2	W	11	13	173.91	173.93	199.92	199.92	7.4		0.602	0.593			0.602	0.593	0.942	0.778	45.459
B	20	X	2	W	16	18	173.96	173.98	199.97	199.97	6.6		0.434	0.523			0.434	0.523	0.774	0.700	45.467
B	20	X	2	W	21	23	174.01	174.03	200.02	200.02	8.7		0.378	0.434			0.378	0.434	0.718	0.600	45.476
B	20	X	2	W	26	28	174.06	174.08	200.07	200.07	9.2		0.490	0.578			0.490	0.578	0.830	0.762	45.485
B	20	X	2	W	31	33	174.11	174.13	200.12	200.12	7.8		0.568	0.527			0.568	0.527	0.908	0.704	45.493
B	20	X	2	W	36	38	174.16	174.18	200.17	200.17	6.9		0.438	0.479			0.438	0.479	0.778	0.651	45.502
B	20	X	2	W	41	43	174.21	174.23	200.22	200.22	8.2		0.235	0.249			0.235	0.249	0.575	0.392	45.511
B	20	X	2	W	46	48	174.26	174.28	200.27	200.27	7.3		0.351	0.369			0.351	0.369	0.691	0.527	45.519
B	20	X	2	W	51	53	174.31	174.33	200.32	200.32	4.2		0.359	0.382			0.359	0.382	0.699	0.541	45.528
B	20	X	2	W	56	58	174.36	174.38	200.37	200.37	5.9		0.337	0.263			0.337	0.263	0.677	0.408	45.537
B	20	X	2	W	61	63	174.41	174.43	200.42	200.42	7.3		0.466	0.385			0.466	0.385	0.806	0.545	45.545
B	20	X	2	W	66	68	174.46	174.48	200.47	200.47	6.6		0.514	0.378			0.514	0.378	0.854	0.537	45.554
B	20	X	2	W	71	73	174.51	174.53	200.52	200.52	4.8		0.490	0.401			0.490	0.401	0.830	0.563	45.563
B	20	X	2	W	76	78	174.56	174.58	200.57	200.57	5.3		0.431	0.325			0.431	0.325	0.771	0.477	45.571
B	20	X	2	W	81	83	174.61	174.63	200.62	200.62	4.4		0.355	0.359			0.355	0.359	0.695	0.516	45.580
B	20	X	2	W	86	88	174.66	174.68	200.67	200.67			0.329	0.338			0.329	0.338	0.669	0.492	45.589
B	20	X	2	W	91	93	174.71	174.73	200.72	200.72	5.1		0.341	0.346			0.341	0.346	0.681	0.501	45.597
B	20	X	2	W	96	98	174.76	174.78	200.77	200.77	5.5		0.518	0.519			0.518	0.519	0.858	0.695	45.606
B	20	X	2	W	101	103	174.81	174.83	200.82	200.82	8.8		0.294	0.238			0.294	0.238	0.634	0.380	45.615
B	20	X	2	W	106	108	174.86	174.88	200.87	200.87	5.3		0.421	0.361			0.421	0.361	0.761	0.518	45.623
B	20	X	2	W	111	113	174.91	174.93	200.92	200.92	6.1		0.431	0.379			0.431	0.379	0.771	0.538	45.632
B	20	X	2	W	116	118	174.96	174.98	200.97	200.97	5.9		0.374	0.216			0.374	0.216	0.714	0.355	45.641
B	20	X	2	W	121	123	175.01	175.03	201.02	201.02	7.1		0.213	0.300			0.213	0.300	0.553	0.449	45.649
B	20	X	2	W	126	128	175.06	175.08	201.07	201.07	5.4		0.636	0.475			0.636	0.475	0.976	0.646	45.658
B	20	X	2	W	131	133	175.11	175.13	201.12	201.12	4.6		0.280	0.318			0.280	0.318	0.620	0.470	45.667
B	20	X	2	W	136	138	175.16	175.18	201.17	201.17	5.8		0.467	0.372			0.467	0.372	0.807	0.530	45.675
B	20	X	2	W	141	143	175.21	175.23	201.22	201.22	6.8		0.325	0.246			0.325	0.246	0.665	0.389	45.684
B	20	X	2	W	146	148	175.26	175.28	201.27	201.27	20.5		0.352	0.177			0.352	0.177	0.692	0.311	45.692
B	20	X	3	W	1	3	175.31	175.33	201.32	201.32	12.9		0.327	0.311			0.327	0.311	0.667	0.462	45.701
B	20	X	3	W	6	8	175.36	175.38	201.37	201.37	7.2		0.446	0.267			0.446	0.267	0.786	0.412	45.710
B	20	X	3	W	11	13	175.41	175.43	201.42	201.42	5.4		0.361	0.187			0.361	0.187	0.701	0.323	45.718

(**Appendix Table 5-1** continued)

Hole	Core	Type	Section	Type	Top (cm)	Bottom (cm)	Top (m CSF-A)	Bottom (m CSF-A)	Depth (rmcd; m revised CCSF-A)	Depth (m adj rmcd; m adj rev CCSF-A)	Coarse Fraction (wt %)	Barren Sample	$\delta^{13}C$ measured at Bremen (‰, VPDB)	$\delta^{18}O$ measured at Bremen (‰, VPDB)	$\delta^{13}C$ measured at NOCS (‰, VPDB)	$\delta^{18}O$ measured at NOCS (‰, VPDB)	$\delta^{13}C$ compiled (‰, VPDB)	$\delta^{18}O$ compiled (‰, VPDB)	$\delta^{13}C$ adjusted to Cibs (true+0.34)	$\delta^{18}O$ adjusted to Cibs (true+0.1/0.89)	Age (Ma) [WK Age]
B	20	X	3	W	16	18	175.46	175.48	201.47	201.47	5.3		0.419	0.345			0.419	0.345	0.759	0.500	45.727
B	20	X	3	W	21	23	175.51	175.53	201.52	201.52	4.9		0.356	0.203			0.356	0.203	0.696	0.341	45.736
B	20	X	3	W	26	28	175.56	175.58	201.57	201.57	4.8		0.672	0.522			0.672	0.522	1.012	0.699	45.744
B	20	X	3	W	31	33	175.61	175.63	201.62	201.62	4.8		0.445	0.456			0.445	0.456	0.785	0.625	45.753
B	20	X	3	W	36	38	175.66	175.68	201.67	201.67	6.2		0.647	0.495			0.647	0.495	0.987	0.669	45.762
B	20	X	3	W	41	43	175.71	175.73	201.72	201.72	3.8		0.578	0.515			0.578	0.515	0.918	0.691	45.770
B	20	X	3	W	51	53	175.81	175.83	201.82	201.82	5.0		0.450	0.498			0.450	0.498	0.790	0.672	45.788
B	20	X	3	W	56	58	175.86	175.88	201.87	201.87	7.3		0.427	0.455			0.427	0.455	0.767	0.624	45.796
B	20	X	3	W	61	63	175.91	175.93	201.92	201.92	10.1		0.585	0.490			0.585	0.490	0.925	0.663	45.805
B	20	X	3	W	66	68	175.96	175.98	201.97	201.97	5.5		0.469	0.543			0.469	0.543	0.809	0.722	45.814
B	20	X	3	W	71	73	176.01	176.03	202.02	202.02	5.4		0.431	0.337			0.431	0.337	0.771	0.491	45.822
B	20	X	3	W	76	78	176.06	176.08	202.07	202.07	7.4		0.529	0.474			0.529	0.474	0.869	0.645	45.831
B	20	X	3	W	81	83	176.11	176.13	202.12	202.12	5.4		0.628	0.524			0.628	0.524	0.968	0.701	45.840
B	20	X	3	W	86	88	176.16	176.18	202.17	202.17	7.4		0.673	0.443			0.673	0.443	1.013	0.610	45.848
B	20	X	3	W	91	93	176.21	176.23	202.22	202.22	12.5		0.276	0.325			0.276	0.325	0.616	0.478	45.857
B	20	X	3	W	96	98	176.26	176.28	202.27	202.27	8.6		0.170	0.162			0.170	0.162	0.510	0.294	45.866
B	20	X	3	W	101	103	176.31	176.33	202.32	202.32			0.319	0.458			0.319	0.458	0.659	0.627	45.874
B	20	X	3	W	106	108	176.36	176.38	202.37	202.37			0.401	0.334			0.401	0.334	0.741	0.488	45.883
B	20	X	3	W	111	113	176.41	176.43	202.42	202.42	12.9		0.348	0.431			0.348	0.431	0.688	0.597	45.892
B	20	X	3	W	116	118	176.46	176.48	202.47	202.47	11.8		0.448	0.535			0.448	0.535	0.788	0.713	45.900
B	20	X	3	W	121	123	176.51	176.53	202.52	202.52	28.0		0.369	0.357			0.369	0.357	0.709	0.513	45.909
B	20	X	3	W	126	128	176.56	176.58	202.57	202.57			0.499	0.176			0.499	0.176	0.839	0.310	45.918
B	20	X	3	W	131	133	176.61	176.63	202.62	202.62	16.6		0.522	0.421			0.522	0.421	0.862	0.585	45.926
B	20	X	3	W	136	138	176.66	176.68	202.67	202.67	25.7										45.935
B	20	X	3	W	141	143	176.71	176.73	202.72	202.72			0.545	0.263			0.545	0.263	0.885	0.408	45.944
B	20	X	3	W	146	148	176.76	176.78	202.77	202.77	33.2		0.712	0.414			0.712	0.414	1.052	0.578	45.952
B	20	X	4	W	1	3	176.81	176.83	202.82	202.82	22.5		1.377	0.742			1.377	0.742	1.717	0.946	45.961
B	20	X	4	W	6	8	176.86	176.88	202.87	202.87		X									45.970
B	20	X	4	W	11	13	176.91	176.93	202.92	202.92	18.8		1.090	0.596			1.090	0.596	1.430	0.782	45.978
B	20	X	4	W	16	18	176.96	176.98	202.97	202.97	26.8	X									45.987
B	20	X	4	W	21	23	177.01	177.03	203.02	203.02	14.4		0.787	0.738			0.787	0.738	1.127	0.942	45.996
B	20	X	4	W	26	28	177.06	177.08	203.07	203.07	25.5		0.950	0.684			0.950	0.684	1.290	0.881	46.004
B	20	X	4	W	31	33	177.11	177.13	203.12	203.12			0.710	0.673			0.710	0.673	1.050	0.869	46.013
B	20	X	4	W	36	38	177.16	177.18	203.17	203.17	13.6		1.032	0.676			1.032	0.676	1.372	0.872	46.022
B	20	X	4	W	41	43	177.21	177.23	203.22	203.22	20.8		0.826	0.475			0.826	0.475	1.166	0.646	46.030
B	20	X	4	W	46	48	177.26	177.28	203.27	203.27	32.2		0.883	0.547			0.883	0.547	1.223	0.727	46.039
B	20	X	4	W	51	53	177.31	177.33	203.32	203.32	8.4	X									46.048
B	20	X	4	W	56	58	177.36	177.38	203.37	203.37	7.4		0.821	0.703			0.821	0.703	1.161	0.902	46.056
B	20	X	4	W	61	63	177.41	177.43	203.42	203.42	12.3		0.838	0.610			0.838	0.610	1.178	0.798	46.065
B	20	X	4	W	66	68	177.46	177.48	203.47	203.47	30.5		0.969	0.637			0.969	0.637	1.309	0.828	46.074
B	20	X	4	W	71	73	177.51	177.53	203.52	203.52	31.4		0.807	0.572			0.807	0.572	1.147	0.755	46.082
B	20	X	4	W	76	78	177.56	177.58	203.57	203.57	19.4		0.718	0.735			0.718	0.735	1.058	0.938	46.091
B	20	X	4	W	81	83	177.61	177.63	203.62	203.62	12.5		0.826	0.755			0.826	0.755	1.166	0.961	46.099
B	20	X	4	W	86	88	177.66	177.68	203.67	203.67	23.0		1.129	0.689			1.129	0.689	1.469	0.887	46.108
B	20	X	4	W	91	93	177.71	177.73	203.72	203.72	31.8		0.987	0.667			0.987	0.667	1.327	0.862	46.117
B	20	X	4	W	96	98	177.76	177.78	203.77	203.77	35.1		1.083	0.814			1.083	0.814	1.423	1.027	46.125
B	20	X	4	W	101	103	177.81	177.83	203.82	203.82	20.6		0.776	0.517			0.776	0.517	1.116	0.693	46.134
B	20	X	4	W	106	108	177.86	177.88	203.87	203.87	23.5		0.742	0.624			0.742	0.624	1.082	0.813	46.143
B	20	X	4	W	111	113	177.91	177.93	203.92	203.92		X									46.151
B	20	X	4	W	116	118	177.96	177.98	203.97	203.97			0.786	0.729			0.786	0.729	1.126	0.931	46.160
B	20	X	4	W	121	123	178.01	178.03	204.02	204.02		X									46.169
B	20	X	4	W	126	128	178.06	178.08	204.07	204.07			0.562	0.552			0.562	0.552	0.902	0.733	46.177
B	20	X	4	W	131	133	178.11	178.13	204.12	204.12		X									46.186

Appendix Table 5-2 IODP Exp. 320 Site U1333 bulk sediment isotopic composition data

Hole	Core	Type	Section	Type	Top (cm)	Bottom (cm)	Top (m CSF-A)	Bottom (m CSF-A)	Depth (m adj rmcd; m adj rev CCSF-A)	$\delta^{13}C$ measured at Bremen (‰, VPDB)	$\delta^{18}O$ measured at Bremen (‰, VPDB)	Age (Ma) [WK Age]	
B	15	H	5	W	41	43	137.61	137.63	164.48	2.505	-0.387	39.380	
B	15	H	5	W	121	123	138.41	138.43	165.54	2.914	-0.860	39.524	
B	15	H	5	W	141	143	138.61	138.63	165.80	2.434	-1.542	39.557	
B	15	H	CC	W	16	18	139.68	139.7	167.00			39.708	signal too low - insufficient carbonate content
B	16	H	1	W	36	38	141.06	141.08	167.84	2.404	-0.878	39.833	
B	16	H	1	W	76	78	141.46	141.48	168.24	2.459	-1.437	39.909	
B	16	H	1	W	111	113	141.81	141.83	168.62			39.981	signal too low - insufficient carbonate content
B	16	H	2	W	1	3	142.21	142.23	169.13			40.039	signal too low - insufficient carbonate content
B	16	H	2	W	56	58	142.76	142.78	169.73			40.089	signal too low - insufficient carbonate content
B	16	H	2	W	91	93	143.11	143.13	170.10			40.120	signal too low - insufficient carbonate content
B	16	H	2	W	141	143	143.61	143.63	170.65			40.166	signal too low - insufficient carbonate content
B	16	H	3	W	16	18	143.86	143.88	170.91			40.187	signal too low - insufficient carbonate content
B	16	H	3	W	51	53	144.21	144.23	171.25			40.215	signal too low - insufficient carbonate content
B	16	H	3	W	76	78	144.46	144.48	171.49			40.235	signal too low - insufficient carbonate content
B	16	H	3	W	101	103	144.71	144.73	171.73			40.255	signal too low - insufficient carbonate content
B	16	H	4	W	6	8	145.26	145.28	172.42	2.550	-1.333	40.329	signal too low - insufficient carbonate content
B	16	H	4	W	36	38	145.56	145.58	172.88	2.608	-1.298	40.382	
B	16	H	4	W	91	93	146.11	146.13	173.50	2.103	-1.799	40.427	
B	16	H	4	W	141	143	146.61	146.63	173.99	2.202	-1.483	40.463	
B	16	H	5	W	26	28	146.96	146.98	174.30	2.220	-1.346	40.485	
B	16	H	5	W	76	78	147.46	147.48	174.75	1.954	-1.012	40.519	
C	17	H	7	W	21	23	140.31	140.33	166.02			39.581	signal too low - insufficient carbonate content
C	17	H	7	W	46	48	140.56	140.58	166.27	2.249	-2.049	39.609	signal too low - insufficient carbonate content
C	17	H	7	W	61	63	140.71	140.73	166.42	2.302	-1.657	39.625	
C	17	H	CC	W	21	23	141.03	141.05	166.74			39.670	signal too low - insufficient carbonate content

Appendix Table 5-3 IODP Exp. 320 Site U1333 carbonate content data

Hole	Core	Type	Section	Type	Top (cm)	Bottom (cm)	Top (m CSF-A)	Bottom (m CSF-A)	Depth (rmcd; m revised CCSF-A)	Depth (m adj rmcd; m adj rev CCSF-A)	$CaCO_3$ (wt %)	Below Detection Limit	Age (Ma) [WK Age]
B	15	H	4	W	111	113	136.81	136.83	162.82	163.5	39.5		39.213
B	15	H	4	W	146	148	137.16	137.18	163.17	163.9	36.8		39.286
B	15	H	5	W	41	43	137.61	137.63	163.62	164.5	58.2		39.380
B	15	H	5	W	66	68	137.86	137.88	163.87	164.8	28.3		39.425
B	15	H	5	W	96	98	138.16	138.18	164.17	165.2	30.6		39.479
B	15	H	5	W	121	123	138.41	138.43	164.42	165.5	16.1		39.524
B	15	H	5	W	141	143	138.61	138.63	164.62	165.8	13.3		39.557
C	17	H	7	W	6	8	140.16	140.18	165.87	165.9	30.9		39.565
C	17	H	7	W	21	23	140.31	140.33	166.02	166.0	0.5		39.581
C	17	H	7	W	31	33	140.41	140.43	166.12	166.1	2.9		39.592
C	17	H	7	W	41	43	140.51	140.53	166.22	166.2	2.0		39.603
C	17	H	7	W	46	48	140.56	140.58	166.27	166.3	3.8		39.609
C	17	H	7	W	61	63	140.71	140.73	166.42	166.4	11.6		39.625
C	17	H	7	W	65	67	140.75	140.77	166.46	166.5	1.4		39.630
B	15	H	6	W	51	53	139.21	139.23	165.22	166.5	3.6		39.639
B	15	H	6	W	56	58	139.26	139.28	165.27	166.6	1.3		39.647
B	15	H	6	W	61	63	139.31	139.33	165.32	166.6	4.4		39.654
B	15	H	6	W	68	70	139.38	139.4	165.39	166.7		BDL	39.664
C	17	H	CC	W	21	23	141.03	141.05	166.74	166.7	2.6		39.670
B	15	H	CC	W	1	3	139.53	139.55	165.54	166.9	0.1		39.686
B	15	H	CC	W	16	18	139.68	139.7	165.69	167.0	0.5		39.708
B	15	H	CC	W	21	23	139.73	139.75	165.74	167.1		BDL	39.715
B	15	H	CC	W	26	28	139.78	139.8	165.79	167.1		BDL	39.723
B	16	H	1	W	6	8	140.76	140.78	166.77	167.5		BDL	39.787
B	16	H	1	W	26	28	140.96	140.98	166.97	167.7		BDL	39.816
B	16	H	1	W	36	38	141.06	141.08	167.07	167.8		BDL	39.833
B	16	H	1	W	41	43	141.11	141.13	167.12	167.9	8.8		39.842
B	16	H	1	W	51	53	141.21	141.23	167.22	168.0	5.2		39.861
B	16	H	1	W	76	78	141.46	141.48	167.47	168.2	10.2		39.909
B	16	H	1	W	91	93	141.61	141.63	167.62	168.4	6.0		39.938
B	16	H	1	W	111	113	141.81	141.83	167.82	168.6	4.2		39.981
B	16	H	1	W	126	128	141.96	141.98	167.97	168.8	8.0		40.012
B	16	H	1	W	141	143	142.11	142.13	168.12	169.0		BDL	40.028
B	16	H	2	W	1	3	142.21	142.23	168.22	169.1		BDL	40.039
B	16	H	2	W	21	23	142.41	142.43	168.42	169.3		BDL	40.057
B	16	H	2	W	31	33	142.51	142.53	168.52	169.5		BDL	40.066
B	16	H	2	W	33	35	142.53	142.55	168.54	169.5	7.1		40.068
B	16	H	2	W	46	48	142.66	142.68	168.67	169.6	0.8		40.080
B	16	H	2	W	56	58	142.76	142.78	168.77	169.7	0.1		40.089
B	16	H	2	W	76	78	142.96	142.98	168.97	169.9	3.5		40.107
B	16	H	2	W	81	83	143.01	143.03	169.02	170.0	0.2		40.111
B	16	H	2	W	91	93	143.11	143.13	169.12	170.1	0.1		40.120
B	16	H	2	W	108	110	143.28	143.3	169.29	170.3	0.0		40.136
B	16	H	2	W	121	123	143.41	143.43	169.42	170.4	0.0		40.148
B	16	H	2	W	131	133	143.51	143.53	169.52	170.5	0.0		40.157
B	16	H	2	W	141	143	143.61	143.63	169.62	170.6	0.3		40.166
B	16	H	3	W	16	18	143.86	143.88	169.87	170.9	0.0		40.187
B	16	H	3	W	26	28	143.96	143.98	169.97	171.0	0.0		40.195
B	16	H	3	W	31	33	144.01	144.03	170.02	171.1	0.1		40.199
B	16	H	3	W	36	38	144.06	144.08	170.07	171.1	1.0		40.203
B	16	H	3	W	51	53	144.21	144.23	170.22	171.2	0.0		40.215
B	16	H	3	W	66	68	144.36	144.38	170.37	171.4	0.0		40.227
B	16	H	3	W	76	78	144.46	144.48	170.47	171.5	0.0		40.235
B	16	H	3	W	88	90	144.58	144.6	170.59	171.6	-0.1		40.245
B	16	H	3	W	101	103	144.71	144.73	170.72	171.7	1.4		40.255
B	16	H	3	W	121	123	144.91	144.93	170.92	171.9	-0.1		40.271
B	16	H	3	W	136	138	145.06	145.08	171.07	172.1	9.3		40.293
B	16	H	4	W	6	8	145.26	145.28	171.27	172.4	11.5		40.329

(**Appendix Table 5-3** continued)

Hole	Core	Type	Section	Type	Top (cm)	Bottom (cm)	Top (m CSF-A)	Bottom (m CSF-A)	Depth (rmcd; m revised CCSF-A)	Depth (m adj rmcd; m adj rev CCSF-A)	$CaCO_3$ (wt %)	Below Detection Limit	Age (Ma) [WK Age]
B	15	H	4	W	111	113	136.81	136.83	162.82	163.5	39.5		39.213
B	15	H	4	W	146	148	137.16	137.18	163.17	163.9	36.8		39.286
B	15	H	5	W	41	43	137.61	137.63	163.62	164.5	58.2		39.380
B	15	H	5	W	66	68	137.86	137.88	163.87	164.8	28.3		39.425
B	15	H	5	W	96	98	138.16	138.18	164.17	165.2	30.6		39.479
B	15	H	5	W	121	123	138.41	138.43	164.42	165.5	16.1		39.524
B	15	H	5	W	141	143	138.61	138.63	164.62	165.8	13.3		39.557
C	17	H	7	W	6	8	140.16	140.18	165.87	165.9	30.9		39.565
C	17	H	7	W	21	23	140.31	140.33	166.02	166.0	0.5		39.581
C	17	H	7	W	31	33	140.41	140.43	166.12	166.1	2.9		39.592
C	17	H	7	W	41	43	140.51	140.53	166.22	166.2	2.0		39.603
C	17	H	7	W	46	48	140.56	140.58	166.27	166.3	3.8		39.609
C	17	H	7	W	61	63	140.71	140.73	166.42	166.4	11.6		39.625
C	17	H	7	W	65	67	140.75	140.77	166.46	166.5	1.4		39.630
B	15	H	6	W	51	53	139.21	139.23	165.22	166.5	3.6		39.639
B	15	H	6	W	56	58	139.26	139.28	165.27	166.6	1.3		39.647
B	15	H	6	W	61	63	139.31	139.33	165.32	166.6	4.4		39.654
B	15	H	6	W	68	70	139.38	139.4	165.39	166.7		BDL	39.664
C	17	H	CC	W	21	23	141.03	141.05	166.74	166.7	2.6		39.670
B	15	H	CC	W	1	3	139.53	139.55	165.54	166.9	0.1		39.686
B	15	H	CC	W	16	18	139.68	139.7	165.69	167.0	0.5		39.708
B	15	H	CC	W	21	23	139.73	139.75	165.74	167.1		BDL	39.715
B	15	H	CC	W	26	28	139.78	139.8	165.79	167.1		BDL	39.723
B	16	H	1	W	6	8	140.76	140.78	166.77	167.5		BDL	39.787
B	16	H	1	W	26	28	140.96	140.98	166.97	167.7		BDL	39.816
B	16	H	1	W	36	38	141.06	141.08	167.07	167.8		BDL	39.833
B	16	H	1	W	41	43	141.11	141.13	167.12	167.9	8.8		39.842
B	16	H	1	W	51	53	141.21	141.23	167.22	168.0	5.2		39.861
B	16	H	1	W	76	78	141.46	141.48	167.47	168.2	10.2		39.909
B	16	H	1	W	91	93	141.61	141.63	167.62	168.4	6.0		39.938
B	16	H	1	W	111	113	141.81	141.83	167.82	168.6	4.2		39.981
B	16	H	1	W	126	128	141.96	141.98	167.97	168.8	8.0		40.012
B	16	H	1	W	141	143	142.11	142.13	168.12	169.0		BDL	40.028
B	16	H	2	W	1	3	142.21	142.23	168.22	169.1		BDL	40.039
B	16	H	2	W	21	23	142.41	142.43	168.42	169.3		BDL	40.057
B	16	H	2	W	31	33	142.51	142.53	168.52	169.5		BDL	40.066
B	16	H	2	W	33	35	142.53	142.55	168.54	169.5	7.1		40.068
B	16	H	2	W	46	48	142.66	142.68	168.67	169.6	0.8		40.080
B	16	H	2	W	56	58	142.76	142.78	168.77	169.7	0.1		40.089
B	16	H	2	W	76	78	142.96	142.98	168.97	169.9	3.5		40.107
B	16	H	2	W	81	83	143.01	143.03	169.02	170.0	0.2		40.111
B	16	H	2	W	91	93	143.11	143.13	169.12	170.1	0.1		40.120
B	16	H	2	W	108	110	143.28	143.3	169.29	170.3	0.0		40.136
B	16	H	2	W	121	123	143.41	143.43	169.42	170.4	0.0		40.148
B	16	H	2	W	131	133	143.51	143.53	169.52	170.5	0.0		40.157
B	16	H	2	W	141	143	143.61	143.63	169.62	170.6	0.3		40.166
B	16	H	3	W	16	18	143.86	143.88	169.87	170.9	0.0		40.187
B	16	H	3	W	26	28	143.96	143.98	169.97	171.0	0.0		40.195
B	16	H	3	W	31	33	144.01	144.03	170.02	171.1	0.1		40.199
B	16	H	3	W	36	38	144.06	144.08	170.07	171.1	1.0		40.203
B	16	H	3	W	51	53	144.21	144.23	170.22	171.2	0.0		40.215
B	16	H	3	W	66	68	144.36	144.38	170.37	171.4	0.0		40.227
B	16	H	3	W	76	78	144.46	144.48	170.47	171.5	0.0		40.235
B	16	H	3	W	88	90	144.58	144.6	170.59	171.6	-0.1		40.245
B	16	H	3	W	101	103	144.71	144.73	170.72	171.7	1.4		40.255
B	16	H	3	W	121	123	144.91	144.93	170.92	171.9	-0.1		40.271
B	16	H	3	W	136	138	145.06	145.08	171.07	172.1	9.3		40.293
B	16	H	4	W	6	8	145.26	145.28	171.27	172.4	11.5		40.329

Appendix B Data Tables for Chapter 3: Dynamic, large-magnitude CCD changes during the Middle Eocene Climatic Optimum

Appendix Table 5-4 Summary of turbidite occurrence in ODP Leg 154 Cores 929E 10-13R

Position	Feature	Leg	Site	Hole	Core	Sec	Interval (cm)	Section Top (mbsf)	Depth (mbsf)
Top	turbidite	154	929	E	10R	6	50	565.8	566.3
Base	turbidite	154	929	E	10R	6	75	565.8	566.55
Top	slump (?)	154	929	E	11R	2	60	569.4	570
Base	slump (?)	154	929	E	11R	4	60	572.4	573
Top	turbidite	154	929	E	13R	1	109	587.2	588.29
Base	turbidite	154	929	E	13R	1	118	587.2	588.38
Top	turbidite	154	929	E	13R	2	48	588.7	589.18
Base	turbidite	154	929	E	13R	2	54	588.7	589.24
Top	turbidite	154	929	E	13R	2	141	588.7	590.11
Base	turbidite	154	929	E	13R	2	144	588.7	590.14
Top	turbidite	154	929	E	13R	5	80	593.2	594
Base	turbidite	154	929	E	13R	5	85	593.2	594.05
Top	turbidite?	154	929	E	13R	5	145	593.2	594.65
Base	turbidite?	154	929	E	13R	6	5	594.7	594.75

*VCD = visual core description

Appendix Table 5-5 ODP Leg 198 Site 1209 magnetic susceptibility, carbonate content, and coarse fraction data

Site	Hole	Core	Type	Section	Type	Top (cm)	Bottom (cm)	Depth (mbsf)	Depth (rmcd)	Magnetic susceptibility	$CaCO_3$ (wt %)	Coarse Fraction (%)
1209	C	5	H	2	W	120	122	138.7	151.9	3.04E-06	98.82	0.88
1209	C	5	H	2	W	122	124	138.72	151.92	3.18E-06	99.31	0.94
1209	C	5	H	2	W	124	126	138.74	151.94	3.37E-06	99.11	0.90
1209	C	5	H	2	W	126	128	138.76	151.96	3.41E-06	99.04	0.75
1209	C	5	H	2	W	128	130	138.78	151.98	3.54E-06	99.34	0.89
1209	C	5	H	2	W	130	132	138.8	152	3.62E-06	99.47	0.93
1209	C	5	H	2	W	132	134	138.82	152.02	3.56E-06	99.09	0.99
1209	C	5	H	2	W	134	136	138.84	152.04	3.64E-06	99.26	1.04
1209	C	5	H	2	W	136	138	138.86	152.06	3.75E-06	99.22	0.93
1209	C	5	H	2	W	138	140	138.88	152.08	3.87E-06	99.03	0.87
1209	C	5	H	2	W	140	142	138.9	152.1	4.18E-06	98.95	1.05
1209	C	5	H	2	W	142	144	138.92	152.12	4.16E-06	99.39	0.84
1209	C	5	H	2	W	144	146	138.94	152.14	4.03E-06	98.93	0.82
1209	C	5	H	2	W	146	148	138.96	152.16	4.04E-06	98.98	0.74
1209	C	5	H	2	W	148	150	138.98	152.18	4.11E-06	99.08	0.79
1209	C	5	H	3	W	2	4	139.02	152.22	4.15E-06	98.04	0.80
1209	C	5	H	3	W	4	6	139.04	152.24	4.30E-06	97.14	0.86
1209	C	5	H	3	W	6	8	139.06	152.26	4.18E-06	97.31	0.80
1209	C	5	H	3	W	8	10	139.08	152.28	4.09E-06	97.57	0.87
1209	C	5	H	3	W	10	12	139.1	152.3	4.09E-06	96.89	0.86
1209	C	5	H	3	W	12	14	139.12	152.32	4.29E-06	97.57	0.68
1209	C	5	H	3	W	14	16	139.14	152.34	4.45E-06	97.27	0.69
1209	C	5	H	3	W	16	18	139.16	152.36	4.54E-06	96.59	0.78
1209	C	5	H	3	W	18	20	139.18	152.38	4.46E-06	97.48	0.93
1209	C	5	H	3	W	20	22	139.2	152.4	4.28E-06	97.99	1.04
1209	C	5	H	3	W	22	24	139.22	152.42	4.29E-06	97.13	1.11
1209	C	5	H	3	W	24	26	139.24	152.44	4.41E-06	96.89	0.95
1209	C	5	H	3	W	26	28	139.26	152.46	4.54E-06	97.41	0.93
1209	C	5	H	3	W	28	30	139.28	152.48	4.54E-06	97.25	1.22
1209	C	5	H	3	W	30	32	139.3	152.5	4.69E-06	97.08	1.32
1209	C	5	H	3	W	32	34	139.32	152.52	5.33E-06	97.54	1.64
1209	C	5	H	3	W	34	36	139.34	152.54	6.05E-06	96.00	1.74
1209	C	5	H	3	W	36	38	139.36	152.56	6.77E-06	92.79	1.72
1209	C	5	H	3	W	38	40	139.38	152.58	8.27E-06	94.25	2.03
1209	C	5	H	3	W	40	42	139.4	152.6	9.46E-06	92.86	1.90
1209	C	5	H	3	W	42	44	139.42	152.62	1.20E-05	88.34	1.87
1209	C	5	H	3	W	44	46	139.44	152.64	1.46E-05	85.67	1.27
1209	C	5	H	3	W	46	48	139.46	152.66	2.17E-05	77.79	0.87
1209	C	5	H	3	W	48	50	139.48	152.68	2.85E-05	71.20	0.70
1209	C	5	H	3	W	50	52	139.5	152.7	4.10E-05	66.60	0.63
1209	C	5	H	3	W	52	54	139.52	152.72	3.28E-05	74.39	0.55
1209	C	5	H	3	W	54	56	139.54	152.74	2.92E-05	83.95	0.57
1209	C	5	H	3	W	56	58	139.56	152.76	1.92E-05	63.25	0.68
1209	C	5	H	3	W	58	60	139.58	152.78	1.59E-05	91.83	1.02
1209	C	5	H	3	W	60	62	139.6	152.8	1.21E-05	93.15	1.25
1209	C	5	H	3	W	62	64	139.62	152.82	9.74E-06	96.90	1.53
1209	C	5	H	3	W	64	66	139.64	152.84	9.16E-06	94.08	1.51
1209	C	5	H	3	W	66	68	139.66	152.86	8.89E-06	95.19	1.82
1209	C	5	H	3	W	68	70	139.68	152.88	7.96E-06	96.33	2.27
1209	C	5	H	3	W	70	72	139.7	152.9	8.95E-06	96.60	2.07
1209	C	5	H	3	W	72	74	139.72	152.92	1.31E-05	95.65	2.03
1209	C	5	H	3	W	74	76	139.74	152.94	1.29E-05	94.97	1.42
1209	C	5	H	3	W	76	78	139.76	152.96	1.34E-05	92.19	1.07

(**Appendix Table 5-5** continued)

Site	Hole	Core	Type	Section	Type	Top (cm)	Bottom (cm)	Depth (mbsf)	Depth (rmcd)	Magnetic susceptibility	$CaCO_3$ (wt %)	Coarse Fraction (%)
1209	C	5	H	3	W	78	80	139.78	152.98	1.08E-05	92.80	1.15
1209	C	5	H	3	W	80	82	139.8	153	1.01E-05	92.02	1.37
1209	C	5	H	3	W	82	84	139.82	153.02	1.01E-05	98.75	1.39
1209	C	5	H	3	W	84	86	139.84	153.04	1.01E-05	96.21	1.23
1209	C	5	H	3	W	86	88	139.86	153.06	1.22E-05	86.70	1.11
1209	C	5	H	3	W	88	90	139.88	153.08	2.48E-05	76.01	0.69
1209	C	5	H	3	W	90	92	139.9	153.1	2.96E-05	77.61	0.68
1209	C	5	H	3	W	92	94	139.92	153.12	2.59E-05	71.72	0.80
1209	C	5	H	3	W	94	96	139.94	153.14	2.71E-05	75.42	0.54
1209	C	5	H	3	W	96	98	139.96	153.16	3.17E-05	70.71	0.58
1209	C	5	H	3	W	98	100	139.98	153.18	4.95E-05	68.40	0.57
1209	C	5	H	3	W	100	102	140	153.2	5.81E-05	42.31	0.54
1209	C	5	H	3	W	102	104	140.02	153.22	6.12E-05	53.95	0.59
1209	C	5	H	3	W	104	106	140.04	153.24	4.84E-05	67.09	0.63
1209	C	5	H	3	W	106	108	140.06	153.26	3.77E-05	81.78	0.66
1209	C	5	H	3	W	108	110	140.08	153.28	2.08E-05	85.90	0.87
1209	C	5	H	3	W	110	112	140.1	153.3	2.24E-05	83.64	0.87
1209	C	5	H	3	W	112	114	140.12	153.32	2.06E-05	85.50	0.61
1209	C	5	H	3	W	114	116	140.14	153.34	1.97E-05	86.33	0.70
1209	C	5	H	3	W	116	118	140.16	153.36	2.12E-05	81.70	0.59
1209	C	5	H	3	W	118	120	140.18	153.38	2.10E-05	86.06	0.56
1209	C	5	H	3	W	120	122	140.2	153.4	1.91E-05	88.86	0.49
1209	C	5	H	3	W	122	124	140.22	153.42	1.87E-05	88.82	0.52
1209	C	5	H	3	W	124	126	140.24	153.44	2.05E-05	87.31	0.43
1209	C	5	H	3	W	126	128	140.26	153.46	1.84E-05	84.68	0.44
1209	C	5	H	3	W	128	130	140.28	153.48	1.59E-05	88.74	0.49
1209	C	5	H	3	W	130	132	140.3	153.5	1.55E-05	91.37	0.45
1209	C	5	H	3	W	132	134	140.32	153.52	1.40E-05	90.05	0.49
1209	C	5	H	3	W	134	136	140.34	153.54	1.30E-05	92.95	1.19
1209	C	5	H	3	W	136	138	140.36	153.56	1.15E-05	95.68	0.72
1209	C	5	H	3	W	138	140	140.38	153.58	1.08E-05	96.02	0.88
1209	C	5	H	3	W	140	142	140.4	153.6	1.00E-05	94.88	0.94
1209	C	5	H	3	W	142	144	140.42	153.62	9.97E-06	96.51	1.19
1209	C	5	H	3	W	144	146	140.44	153.64	1.07E-05	94.03	1.12
1209	C	5	H	3	W	146	148	140.46	153.66	1.17E-05	95.46	0.91
1209	C	5	H	3	W	148	150	140.48	153.68	1.22E-05	93.83	0.92
1209	C	5	H	4	W	2	4	140.52	153.72	1.29E-05	92.01	0.81
1209	C	5	H	4	W	4	6	140.54	153.74	1.30E-05	91.73	0.70
1209	C	5	H	4	W	6	8	140.56	153.76	1.38E-05	91.68	0.70
1209	C	5	H	4	W	8	10	140.58	153.78	1.36E-05	91.89	0.71
1209	C	5	H	4	W	10	12	140.6	153.8	1.41E-05	91.53	1.01
1209	C	5	H	4	W	12	14	140.62	153.82	1.42E-05	94.56	1.02
1209	C	5	H	4	W	14	16	140.64	153.84	1.30E-05	92.70	1.01
1209	C	5	H	4	W	16	18	140.66	153.86	1.22E-05	95.12	0.94
1209	C	5	H	4	W	18	20	140.68	153.88	1.05E-05	94.11	1.20
1209	C	5	H	4	W	20	22	140.7	153.9	1.02E-05	96.58	1.34
1209	C	5	H	4	W	22	24	140.72	153.92	9.71E-06	95.25	1.36
1209	C	5	H	4	W	24	26	140.74	153.94	9.91E-06	94.53	1.32
1209	C	5	H	4	W	26	28	140.76	153.96	9.80E-06	96.50	1.19
1209	C	5	H	4	W	28	30	140.78	153.98	9.11E-06	95.88	1.14
1209	C	5	H	4	W	30	32	140.8	154	9.13E-06	95.57	1.23
1209	C	5	H	4	W	32	34	140.82	154.02	9.46E-06	96.33	1.25
1209	C	5	H	4	W	34	36	140.84	154.04	9.27E-06	96.90	1.36

(**Appendix Table 5-5** continued)

Site	Hole	Core	Type	Section	Type	Top (cm)	Bottom (cm)	Depth (mbsf)	Depth (rmcd)	Magnetic susceptibility	$CaCO_3$ (wt %)	Coarse Fraction (%)
1209	C	5	H	4	W	36	38	140.86	154.06	9.04E-06	96.09	1.48
1209	C	5	H	4	W	38	40	140.88	154.08	8.59E-06	96.77	1.56
1209	C	5	H	4	W	40	42	140.9	154.1	8.68E-06	96.65	1.37
1209	C	5	H	4	W	42	44	140.92	154.12	8.09E-06	96.46	1.24
1209	C	5	H	4	W	44	46	140.94	154.14	7.54E-06	97.62	1.61
1209	C	5	H	4	W	46	48	140.96	154.16	7.36E-06	97.19	1.57
1209	C	5	H	4	W	48	50	140.98	154.18	7.36E-06	96.41	1.81
1209	C	5	H	4	W	50	52	141	154.2	7.09E-06	98.71	1.73
1209	C	5	H	4	W	52	54	141.02	154.22	6.87E-06	97.49	1.63
1209	C	5	H	4	W	54	56	141.04	154.24	6.53E-06	97.33	1.69
1209	C	5	H	4	W	56	58	141.06	154.26	6.23E-06	98.33	1.68
1209	C	5	H	4	W	58	60	141.08	154.28	6.00E-06	98.15	1.84

Appendix Table 5-6 ODP Leg 207 Site 1260 carbonate content data

Site	Hole	Core	Section	Top	Bot	Depth (mbsf)	Depth (rmcd)	$CaCO_3$ (wt %)	Age (Ma; Westerhold et al., 2014
1260	A	6	1	7	8.5	38.27	38.27	86.60	39.816
1260	A	6	1	17	18.5	38.37	38.37	83.28	39.821
1260	A	6	1	27	28.5	38.47	38.47	75.52	39.825
1260	A	6	1	37	38.5	38.57	38.57	77.74	39.830
1260	A	6	1	47	48.5	38.67	38.67	81.12	39.834
1260	A	6	1	57	58.5	38.77	38.77	81.88	39.839
1260	A	6	1	67	68.5	38.87	38.87	81.08	39.843
1260	A	6	1	77	78.5	38.97	38.97	75.57	39.848
1260	A	6	1	87	88.5	39.07	39.07	74.30	39.852
1260	A	6	1	97	98.5	39.17	39.17	69.20	39.857
1260	A	6	1	107	108.5	39.27	39.27	67.13	39.861
1260	A	6	1	117	118.5	39.37	39.37	63.82	39.866
1260	A	6	1	127	128.5	39.47	39.47	70.62	39.870
1260	A	6	1	137	138.5	39.57	39.57	83.35	39.875
1260	A	6	1	147	148.5	39.67	39.67	81.20	39.879
1260	A	6	2	7	8.5	39.77	39.77	77.00	39.884
1260	A	6	2	17	18.5	39.87	39.87	77.88	39.889
1260	A	6	2	27	28.5	39.97	39.97	78.59	39.893
1260	A	6	2	37	38.5	40.07	40.07	79.67	39.898
1260	A	6	2	47	48.5	40.17	40.17	71.69	39.902
1260	A	6	2	57	58.5	40.27	40.27	79.26	39.907
1260	A	6	2	67	68.5	40.37	40.37	80.43	39.911
1260	A	6	2	77	78.5	40.47	40.47	82.94	39.916
1260	A	6	2	87	88.5	40.57	40.57	63.02	39.920
1260	A	6	2	97	98.5	40.67	40.67	53.97	39.925
1260	A	6	2	107	108.5	40.77	40.77	67.16	39.929
1260	A	6	2	117	118.5	40.87	40.87	79.13	39.934
1260	A	6	2	127	128.5	40.97	40.97	80.97	39.938
1260	A	6	2	137	138.5	41.07	41.07	60.11	39.943
1260	A	6	2	147	148.5	41.17	41.17	50.79	39.947
1260	A	6	3	7	8.5	41.27	41.27	55.17	39.952
1260	A	6	3	17	18.5	41.37	41.37	57.53	39.956
1260	A	6	3	27	28.5	41.47	41.47	73.58	39.961
1260	A	6	3	37	38.5	41.57	41.57	59.36	39.965
1260	A	6	3	47	48.5	41.67	41.67	51.63	39.970
1260	A	6	3	57	58.5	41.77	41.77	51.04	39.974
1260	A	6	3	67	68.5	41.87	41.87	52.79	39.979
1260	A	6	3	77	78.5	41.97	41.97	62.78	39.983
1260	A	6	3	87	88.5	42.07	42.07	77.63	39.988
1260	A	6	3	97	98.5	42.17	42.17	80.82	39.992
1260	A	6	3	107	108.5	42.27	42.27	71.24	39.997
1260	A	6	3	117	118.5	42.37	42.37	57.08	40.001
1260	A	6	3	127	128.5	42.47	42.47	59.67	40.006
1260	A	6	3	137	138.5	42.57	42.57	60.24	40.010
1260	A	6	3	137	138.5	42.57	42.57	61.02	40.010
1260	A	6	3	147	148.5	42.67	42.67	67.90	40.015
1260	A	6	4	7	8.5	42.77	42.77	76.26	40.019
1260	A	6	4	17	18.5	42.87	42.87	83.67	40.024

(**Appendix Table 5-6** continued)

Site	Hole	Core	Section	Top	Bot	Depth (mbsf)	Depth (rmcd)	$CaCO_3$ (wt %)	Age (Ma; Westerhold et al., 2014
1260	A	6	4	27	28.5	42.97	42.97	80.55	40.029
1260	A	6	4	37	38.5	43.07	43.07	75.00	40.033
1260	A	6	4	47	48.5	43.17	43.17	71.73	40.038
1260	A	6	4	57	58.5	43.27	43.27	76.75	40.042
1260	A	6	4	57	58.5	43.27	43.27	77.48	40.042
1260	A	6	4	67	68.5	43.37	43.37	48.14	40.047
1260	A	6	4	67	68.5	43.37	43.37	48.41	40.047
1260	A	6	4	77	78.5	43.47	43.47	51.98	40.051
1260	A	6	4	87	88.5	43.57	43.57	44.07	40.056
1260	A	6	4	97	98.5	43.67	43.67	44.49	40.060
1260	A	6	4	107	108.5	43.77	43.77	44.24	40.065
1260	A	6	4	117	118.5	43.87	43.87	46.26	40.069
1260	A	6	4	127	128.5	43.97	43.97	55.08	40.074
1260	A	6	4	137	138.5	44.07	44.07	60.00	40.078
1260	A	6	4	147	148.5	44.17	44.17	59.21	40.083
1260	A	6	5	7	8.5	44.27	44.27	74.32	40.087
1260	A	6	5	17	18.5	44.37	44.37	72.54	40.092
1260	A	6	5	27	28.5	44.47	44.47	72.03	40.096
1260	A	6	5	37	38.5	44.57	44.57	76.01	40.101
1260	A	6	5	45.5	47	44.655	44.655	75.26	40.105
1260	A	6	5	57	58.5	44.77	44.77	72.15	40.110
1260	A	6	5	67	68.5	44.87	44.87	74.63	40.114
1260	A	6	5	87	88.5	45.07	45.07	77.60	40.124
1260	B	1	4	7	8.5	44.77	44.77	75.03	40.110
1260	B	1	4	17	18.5	44.87	44.87	73.81	40.114
1260	B	1	4	27	28.5	44.97	44.97	70.94	40.119
1260	B	1	4	37	38.5	45.07	45.07	67.68	40.124
1260	B	1	4	47	48.5	45.17	45.17	78.58	40.129
1260	B	1	4	57	58.5	45.27	45.27	77.43	40.134
1260	B	1	4	67	68.5	45.37	45.37	75.44	40.139
1260	B	1	4	77	78.5	45.47	45.47	73.78	40.144
1260	B	1	4	87	88.5	45.57	45.57	73.89	40.150
1260	B	1	4	97	98.5	45.67	45.67	72.35	40.155
1260	B	1	4	117	118.5	45.87	45.87	74.24	40.166
1260	B	1	4	127	128.5	45.97	45.97	72.17	40.172
1260	B	1	5	17	18.5	46.37	46.37	78.00	40.196
1260	B	1	5	27	28.5	46.47	46.47	76.34	40.202
1260	B	1	5	47	48.5	46.67	46.67	74.28	40.214
1260	B	1	5	67	68.5	46.87	46.87	78.81	40.227
1260	B	1	5	77	78.5	46.97	46.97	75.91	40.233
1260	B	1	5	97	98.5	47.17	47.17	83.25	40.245
1260	B	1	5	117	118.5	47.37	47.37	75.36	40.256
1260	B	1	5	147	148.5	47.67	47.67	76.86	40.271
1260	A	7	1	77	78.5	48.27	48.77	82.27	40.334
1260	A	7	1	127	128.5	48.77	49.27	82.10	40.364
1260	A	7	2	57	58.5	49.57	50.07	82.87	40.405
1260	A	7	3	77	78.5	51.27	51.77	86.93	40.494

Appendix Table 5-7 ODP Leg 208 Site 1263 benthic foraminifera isotopic composition, carbonate content, fragmentation, planktic, coarse fraction, and magnetic susceptibility data

Leg	Site	Hole	Type	Core	Section	Type	Top (cm)	Bottom (cm)	Depth (mbsf)	Depth (mcd)	$CaCO_3$ (wt %)	$\delta^{13}C$ (‰ VPDB) *N. truempyii*	$\delta^{18}O$ (‰ VPDB) *N. truempyii*	Fragmentation (%)	Planktic (%)	Coarse Fraction (%)	Magnetic Susceptibility
208	1263	B	H	8	W	2	74	76	114.74	133.08	95.35						
208	1263	B	H	8	W	3	30	32	115.80	134.14	94.45						
208	1263	B	H	8	W	3	120	122	116.70	135.04	92.80						
208	1263	B	H	8	W	4	34	36	117.34	135.68	92.00						
208	1263	B	H	8	W	4	94	96	117.94	136.28	93.00						
208	1263	B	H	8	W	5	4	6	118.54	136.88	92.92						
208	1263	B	H	8	W	5	29	31	118.79	137.13	94.03						
208	1263	B	H	8	W	5	59	61	119.09	137.43	92.91	1.137	0.172	1.28	99.83	2.30	7.88E-06
208	1263	B	H	8	W	5	64	66	119.14	137.48	93.77	1.003	0.963	1.07	99.73	2.55	7.11E-06
208	1263	B	H	8	W	5	69	71	119.19	137.53	93.67	1.185	0.422	0.57	99.65	3.06	6.56E-06
208	1263	B	H	8	W	5	74	76	119.24	137.58	94.39	0.999	0.283	1.11	99.84	2.41	6.41E-06
208	1263	B	H	8	W	5	79	81	119.29	137.63	94.32	0.870	0.146	1.01	99.83	2.47	6.88E-06
208	1263	B	H	8	W	5	84	86	119.34	137.68	92.59	1.062	0.388	1.27	99.35	2.63	7.74E-06
208	1263	B	H	8	W	5	89	91	119.39	137.73	93.45	0.836	0.327	1.03	99.83	2.52	7.60E-06
208	1263	B	H	8	W	5	94	96	119.44	137.78	95.13	1.012	0.290	0.71	100.00	2.79	7.19E-06
208	1263	B	H	8	W	5	99	101	119.49	137.83	92.01	1.095	0.339	1.35	99.67	2.01	8.53E-06
208	1263	B	H	8	W	5	104	106	119.54	137.88	90.62	0.838	0.173	3.07	99.79	0.90	1.45E-05
208	1263	B	H	8	W	5	109	111	119.59	137.93	90.73	0.845	-0.020	3.06	98.94	0.55	1.55E-05
208	1263	B	H	8	W	5	114	117	119.64	137.98	88.12	0.630	-0.265	2.17	99.42	0.88	1.71E-05
208	1263	B	H	8	W	5	119	121	119.69	138.03	88.68	0.860	-0.110	3.30	98.34	0.78	2.19E-05
208	1263	B	H	8	W	5	124	126	119.74	138.08	91.84	0.986	-0.061	2.03	98.76	1.65	1.07E-05
208	1263	B	H	8	W	5	129	131	119.79	138.13	91.30	1.098	0.254	2.03	99.54	1.73	9.37E-06
208	1263	B	H	8	W	5	134	136	119.84	138.18	92.02	0.979	0.093	2.54	100.00	1.60	8.43E-06
208	1263	B	H	8	W	5	139	141	119.89	138.23	92.44	0.930	0.045	1.74	99.61	2.15	7.60E-06
208	1263	B	H	8	W	5	144	146	119.94	138.28	89.43	1.047	0.366	1.38	99.78	2.01	9.59E-06
208	1263	B	H	8	W	5	149	151	119.99	138.33	91.19	1.063	0.124	2.56	99.11	1.11	1.37E-05
208	1263	B	H	8	W	6	4	6	120.04	138.38	92.19	1.004	0.049	1.63	100.00	1.66	9.83E-06
208	1263	B	H	8	W	6	9	11	120.09	138.43	92.32	1.002	0.223	2.84	98.75	1.57	9.73E-06
208	1263	B	H	8	W	6	14	16	120.14	138.48	93.35	0.738	-0.144	2.07	99.16	1.58	9.53E-06
208	1263	B	H	8	W	6	19	21	120.19	138.53	93.94	0.819	-0.035	2.52	100.00	1.70	8.79E-06
208	1263	B	H	8	W	6	24	26	120.24	138.58	91.02	0.733	-0.098	3.16	98.88	1.20	1.12E-05
208	1263	B	H	8	W	6	29	31	120.29	138.63	92.07	0.992	0.186	2.68	99.51		
208	1263	B	H	8	W	6	34	36	120.34	138.68	91.83	1.056	0.201	2.40	99.02		
208	1263	B	H	8	W	6	39	41	120.39	138.73	94.58	1.072	0.260	1.32	99.68		
208	1263	B	H	8	W	6	44	46	120.44	138.78	93.52	1.081	0.189	0.82	99.71		
208	1263	B	H	8	W	6	49	51	120.49	138.83	94.38	0.919	0.263	0.75	99.73		
208	1263	B	H	8	W	6	54	56	120.54	138.88	94.88	1.017	0.091	0.69	99.76		
208	1263	B	H	8	W	6	59	61	120.59	138.93	92.81	1.159	0.483	1.02	100.00		
208	1263	B	H	8	W	6	64	66	120.64	138.98	94.91	0.927	0.097	1.14	99.69		
208	1263	B	H	8	W	6	69	71	120.69	139.03	90.03	1.075	0.159	1.17	99.26		
208	1263	B	H	8	W	6	74	76	120.74	139.08	94.36	1.114	0.069	1.18	100.00		

(**Appendix Table 5-7** continued)

Leg	Site	Hole	Type	Core	Section	Type	Top (cm)	Bottom (cm)	Depth (mbsf)	Depth (mcd)	$CaCO_3$ (wt %)	$\delta^{13}C$ (‰ VPDB) *N. truempyii*	$\delta^{18}O$ (‰ VPDB) *N. truempyii*	Fragmentation (%)	Planktic (%)	Coarse Fraction (%)	Magnetic Susceptibility
208	1263	B	H	8	W	6	79	81	120.79	139.13	94.50	0.872	0.063	0.94	100.00		
208	1263	B	H	8	W	6	84	86	120.84	139.18	91.06	0.902	0.165	1.24	99.12		
208	1263	B	H	8	W	6	89	91	120.89	139.23	93.16	0.941	0.161	1.90	100.00		
208	1263	B	H	8	W	6	94	96	120.94	139.28	92.85	1.082	0.129	1.89	99.57		
208	1263	B	H	8	W	6	99	101	120.99	139.33	92.36	0.978	0.306	1.71	98.29		
208	1263	B	H	8	W	6	104	106	121.04	139.38	94.71	1.144	0.392	1.26	99.51		
208	1263	B	H	8	W	6	129	131	121.29	139.63	93.75						
208	1263	B	H	8	W	7	9	11	121.59	139.93	92.47						
208	1263	B	H	8	W	7	39	41	121.89	140.23	93.60						
208	1263	A	H	14	W	6	29	31	122.68	140.43	88.80						
208	1263	A	H	14	W	6	54	56	122.93	140.68	91.71						
208	1263	A	H	14	W	6	94	96	123.33	141.08	92.84						
208	1263	A	H	14	W	6	139	141	123.78	141.53	92.67						
208	1263	B	H	9	W	1	39	41	122.39	142.34	89.73						
208	1263	B	H	9	W	1	149	151	123.49	143.44	91.05						
208	1263	B	H	9	W	2	120	122	124.70	144.65	92.97						
208	1263	B	H	9	W	3	110	112	126.10	146.05	89.99						
208	1263	B	H	9	W	4	120	122	127.70	147.65	93.64						

Appendix Table 5-8 ODP Leg 154 Site 929 benthic foraminifera, bulk sediment isotopic composition, and carbonate content data

Site	Hole	Core	Type	Section	Type	Top (cm)	Bottom (cm)	Depth (mbsf)	$\delta^{13}C$ (‰ VPDB) Bulk sediment	$\delta^{18}O$ (‰ VPDB) Bulk sediment	$\delta^{13}C$ (‰ VPDB) N. truempyii	$\delta^{18}O$ (‰ VPDB) N. truempyii	$CaCO_3$ (wt %)	AGE (Ma)
929	E	12	R	1	W	15	17	577.65	1.924	-1.919	0.32	-0.16	37.38	39.607
929	E	12	R	1	W	45	48	577.95	1.642	-1.959	0.17	-0.31	66.03	39.615
929	E	12	R	1	W	86	88	578.36	1.722	-2.501	0.44	-0.31	52.44	39.632
929	E	12	R	1	W	115	117	578.65	1.857	-2.256	0.31	-0.01	50.99	39.643
929	E	12	R	2	W	10	12	579.10	2.047	-1.947	0.79	0.02	63.25	39.661
929	E	12	R	2	W	36	38	579.36	2.047	-1.911	0.94	-0.08	64.42	39.672
929	E	12	R	2	W	81	83	579.81	1.800	-2.257	0.69	-0.43		39.690
929	E	12	R	2	W	108	110	580.08	2.199	-1.866	0.69	-0.61	55.29	39.704
929	E	12	R	2	W	131	133	580.31	2.008	-2.162	0.84	-0.57		39.727
929	E	12	R	3	W	3	5	580.53	1.856	-1.993	0.87	-0.25		39.748
929	E	12	R	3	W	35	37	580.85	1.995	-2.178	0.72	-0.38	48.22	39.776
929	E	12	R	3	W	59	60	581.09	2.029	-2.332	0.76	-0.65	40.91	39.795
929	E	12	R	3	W	83	85	581.33	1.937	-2.545	0.63	-0.75		39.810
929	E	12	R	3	W	102	104	581.52	1.855	-2.439	0.80	-0.62	49.00	39.829
929	E	12	R	3	W	129	131	581.79	1.725	-2.386	0.75	-0.39		39.861
929	E	12	R	3	W	139	141	581.89	1.791	-2.203	0.66	-0.45	48.87	39.877
929	E	12	R	3	W	148	150	581.98	1.905	-2.322	0.76	-0.51		39.891
929	E	12	R	4	W	0	2	582.00	1.890	-2.339	0.75	-0.53		39.895
929	E	12	R	4	W	6	8	582.06	2.056	-2.132	0.61	-0.50	45.26	39.904
929	E	12	R	4	W	15	16.5	582.15	1.937	-2.461	0.70	-0.96	34.44	39.918
929	E	12	R	4	W	21	23.5	582.21	1.927	-2.583	0.75	-0.99	14.93	39.930
929	E	12	R	4	W	29	31	582.29	2.124	-2.536	0.61	-0.94		39.979
929	E	12	R	4	W	35.5	37	582.36	2.467	-2.549	0.48	-1.20		40.021
929	E	12	R	4	W	41	43	582.41	2.328	-2.646	0.62	-1.28	32.39	40.052
929	E	12	R	4	W	52	54	582.52	Barren		Barren		1.44	40.121
929	E	12	R	4	W	62	64	582.62	Barren		Barren		0.80	40.188
929	E	12	R	4	W	72	74	582.72	Barren		0.81	-1.25	15.12	40.255
929	E	12	R	4	W	83	85	582.83	1.789	-2.131	0.68	-0.57	31.86	40.369
929	E	12	R	4	W	100	102	583.00	1.742	-2.128	0.47	-0.16	41.48	40.505
929	E	12	R	4	W	109	111	583.09	1.699	-2.044	0.45	-0.09	36.74	40.514
929	E	12	R	4	W	118	120	583.18	1.721	-1.939	0.46	-0.02		40.523
929	E	12	R	4	W	136	138	583.36	1.573	-2.073	0.44	-0.18	24.18	40.541
929	E	12	R	4	W	148	150	583.48	1.647	-1.888	0.35	0.00	45.76	40.553
929	E	12	R	5	W	10	12	583.60	1.732	-1.786	0.36	0.05		40.563
929	E	12	R	5	W	40	42	583.90	1.677	-1.974	0.16	0.00	50.88	40.583
929	E	12	R	5	W	77	79	584.27	1.637	-1.797	0.08	-0.01		40.609
929	E	12	R	5	W	120	122	584.70	1.649	-1.970	0.19	-0.19		40.639
929	E	12	R	6	W	46	48	585.46	1.812	-1.981	0.24	0.00	60.84	40.692
929	E	12	R	6	W	87	89	585.87	1.698	-1.972	0.02	-0.05		40.720
929	E	12	R	6	W	124	126	586.24	1.685	-1.871	-0.07	-0.37	69.60	40.746
929	E	12	R	6	W	147	149	586.47	1.676	-2.113	0.14	-0.07	63.48	40.762
929	E	12	R	7	W	12	14	586.62	1.541	-2.052	0.16	-0.22		40.771
929	E	12	R	CC	W	11	13	586.90	1.572	-2.006	0.25	-0.28	60.07	40.788
929	E	13	R	1	W	14	16	587.35	1.677	-1.841	0.42	-0.07		40.815

(**Appendix Table 5-8** continued)

Site	Hole	Core	Type	Section	Type	Top (cm)	Bottom (cm)	Depth (mbsf)	$\delta^{13}C$ (‰ VPDB) Bulk sediment	$\delta^{18}O$ (‰ VPDB) Bulk sediment	$\delta^{13}C$ (‰ VPDB) N. truempyii	$\delta^{18}O$ (‰ VPDB) N. truempyii	$CaCO_3$ (wt %)	AGE (Ma)
929	E	13	R	1	W	96	98	588.17	1.811	-1.771	0.46	-0.17		40.860
929	E	13	R	2	W	14	16	588.85	1.940	-1.672	0.72	-0.06		40.895
929	E	13	R	2	W	75	77	589.46	1.945	-1.654	0.38	-0.06		40.928
929	E	13	R	3	W	7	9	590.28	1.819	-1.923	0.30	-0.13		40.969
929	E	13	R	3	W	102	104	591.23	1.766	-2.023	0.49	-0.18		41.015
929	E	13	R	4	W	3	5	591.74	1.865	-2.017	0.26	-0.31		41.046
929	E	13	R	4	W	90	92	592.61	1.720	-1.996	0.29	-0.17		41.099
929	E	13	R	5	W	52	54	593.73	1.929	-1.939	0.43	-0.36		41.162
929	E	13	R	5	W	120	122	594.41	1.766	-1.930	0.25	-0.22		41.212
929	E	13	R	6	W	61	63	595.32	1.815	-2.013	0.23	-0.62		41.535

Appendix Table 5-9 ODP Leg 154 Site 929 Age Model

Site 929E Depth (mbsf)	Age Model (Ma)
568.04	39.309
569.00	39.379
569.43	39.422
572.99	39.450
574.03	39.492
574.94	39.534
575.73	39.590
577.77	39.608
580.02	39.698
580.67	39.762
581.06	39.793
581.39	39.814
581.79	39.862
582.21	39.927
582.49	40.099
582.72	40.256
582.83	40.363
582.91	40.496
583.54	40.558
586.49	40.763
587.70	40.836
588.48	40.877
589.18	40.912
589.89	40.952
591.01	41.002
592.51	41.093
593.66	41.157
594.36	41.208
594.60	41.228
594.77	41.499
594.93	41.509
595.23	41.530
595.51	41.545
597.52	41.602
597.97	41.643
599.06	41.737
600.18	41.789
600.59	41.811
601.99	41.902
602.56	41.944
603.17	41.973
603.77	42.014
605.89	42.164

Appendix C Data Tables for Chapter 4: Evidence for hyperthermals in the middle Eocene: the C19r event

Appendix Table 5-10 ODP Leg 114 Site 702 benthic foraminifera isotopic composition data

Site	Hole	Core	Type	Section	Type	Top (cm)	Bottom (cm)	Top Depth (mbsf)	Bottom Depth (mbsf)	$\delta^{13}C$ (‰ VPDB)	$\delta^{18}O$ (‰ VPDB)	Age (Ma)
702	B	10	X	5	W	6	18	88.36	88.48	0.547	0.453	41.655
702	B	10	X	5	W	26	28	88.56	88.58	0.581	0.451	41.668
702	B	10	X	5	W	36	38	88.66	88.68	0.460	0.370	41.676
702	B	10	X	5	W	46	48	88.76	88.78	0.569	0.381	41.685
702	B	10	X	5	W	56	58	88.86	88.88	0.626	0.455	41.694
702	B	10	X	5	W	66	68	88.96	88.98	0.582	0.414	41.702
702	B	10	X	5	W	76	78	89.06	89.08	0.754	0.551	41.711
702	B	10	X	5	W	86	88	89.16	89.18	0.621	0.293	41.720
702	B	10	X	5	W	96	98	89.26	89.28	0.679	0.449	41.728
702	B	10	X	5	W	106	108	89.36	89.38	0.536	0.325	41.737
702	B	10	X	5	W	116	118	89.46	89.48	0.579	0.335	41.746
702	B	10	X	5	W	126	128	89.56	89.58	0.527	0.307	41.754
702	B	10	X	5	W	136	138	89.66	89.68	0.430	0.233	41.763
702	B	10	X	5	W	146	148	89.76	89.78	0.262	0.154	41.772
702	B	10	X	6	W	6	8	89.86	89.88	0.173	0.154	41.780
702	B	10	X	6	W	16	18	89.96	89.98	0.182	0.178	41.789
702	B	10	X	6	W	26	28	90.06	90.08	-0.163	0.009	41.798
702	B	10	X	6	W	36	38	90.16	90.18	-0.072	-0.097	41.806
702	B	10	X	6	W	46	48	90.26	90.28	0.597	0.383	41.815
702	B	10	X	6	W	56	58	90.36	90.38	0.494	0.227	41.824
702	B	10	X	6	W	66	68	90.46	90.48	0.465	0.211	41.832
702	B	10	X	6	W	76	78	90.56	90.58	0.778	0.409	41.841
702	B	10	X	6	W	86	88	90.66	90.68	0.605	0.345	41.850
702	B	10	X	6	W	96	98	90.76	90.78	0.606	0.308	41.858
702	B	10	X	6	W	106	108	90.86	90.88	0.518	0.295	41.867
702	B	10	X	6	W	116	118	90.96	90.98	0.749	0.411	41.875
702	B	10	X	6	W	126	128	91.06	91.08	0.607	0.423	41.884
702	B	10	X	6	W	136	138	91.16	91.18	0.772	0.446	41.893
702	B	10	X	6	W	146	148	91.26	91.28	0.631	0.380	41.901
702	B	10	X	7	W	6	8	91.36	91.38	0.610	0.215	41.910
702	B	10	X	7	W	16	18	91.46	91.48	0.518	0.277	41.919
702	B	10	X	7	W	26	28	91.56	91.58	0.391	0.072	41.927
702	B	11	X	1	W	6	8	91.86	91.88	0.416	-0.193	41.953
702	B	11	X	1	W	16	18	91.96	91.98	0.840	0.574	41.962
702	B	11	X	1	W	26	28	92.06	92.08	0.892	0.584	41.971
702	B	11	X	1	W	36	38	92.16	92.18	0.758	0.473	41.979
702	B	11	X	1	W	46	48	92.26	92.28	0.714	0.441	41.988
702	B	11	X	1	W	56	58	92.36	92.38	0.706	0.555	41.997
702	B	11	X	1	W	66	68	92.46	92.48	0.763	0.651	42.005
702	B	11	X	1	W	76	78	92.56	92.58	0.766	0.623	42.014
702	B	11	X	1	W	86	88	92.66	92.68	0.744	0.643	42.023
702	B	11	X	1	W	96	98	92.76	92.78	0.679	0.581	42.031

(**Appendix Table 5-10** continued)

Site	Hole	Core	Type	Section	Type	Top (cm)	Bottom (cm)	Top Depth (mbsf)	Bottom Depth (mbsf)	$\delta^{13}C$ (‰ VPDB)	$\delta^{18}O$ (‰ VPDB)	Age (Ma)
702	B	11	X	1	W	106	108	92.86	92.88	0.802	0.655	42.040
702	B	11	X	1	W	116	118	92.96	92.98	0.737	0.575	42.049
702	B	11	X	1	W	126	128	93.06	93.08	0.666	0.445	42.057
702	B	11	X	1	W	136	138	93.16	93.18	0.639	0.418	42.066
702	B	11	X	1	W	146	148	93.26	93.28	0.889	0.595	42.075
702	B	11	X	2	W	6	8	93.36	93.38	0.818	0.717	42.083
702	B	11	X	2	W	16	18	93.46	93.48	0.845	0.626	42.092
702	B	11	X	2	W	26	28	93.56	93.58	0.699	0.566	42.101
702	B	11	X	2	W	36	38	93.66	93.68	0.720	0.492	42.109
702	B	11	X	2	W	46	48	93.76	93.78	0.914	0.507	42.118
702	B	11	X	2	W	56	58	93.86	93.88	0.790	0.439	42.127
702	B	11	X	2	W	66	68	93.96	93.98	0.817	0.555	42.135
702	B	11	X	2	W	76	78	94.06	94.08	0.872	0.564	42.144
702	B	11	X	2	W	86	88	94.16	94.18	0.997	0.694	42.153
702	B	11	X	2	W	96	98	94.26	94.28	0.966	0.721	42.161
702	B	11	X	2	W	106	108	94.36	94.38	0.889	0.679	42.170

Appendix Table 5-11 IODP Exp. 342 Site U1408 benthic and planktic foraminifera and bulk sediment isotopic composition and coarse fraction data

Site	Hole	Core	Type	Section	Type	Top (cm)	Bottom (cm)	Midpoint (mbsf)	Depth (Revised CCSF)	Coarse fraction (wt %)	$\delta^{13}C$ (‰ VPDB) Bulk sediment	$\delta^{18}O$ (‰ VPDB) Bulk sediment	$\delta^{13}C$ (‰ VPDB) *M. cressatus*	$\delta^{18}O$ (‰ VPDB) *M. cressatus*	$\delta^{13}C$ (‰ VPDB) *N. truempyii*	$\delta^{18}O$ (‰ VPDB) *N. truempyii*	AGE
1408	C	9	H	5	W	1	3	74.81	78.85	1.3	1.690	-0.810					41.512
1408	C	9	H	5	W	4	6	74.84	78.88	1.1	1.710	-0.750					41.513
1408	C	9	H	5	W	7	9	74.87	78.91	1.5	1.660	-0.780					41.515
1408	C	9	H	5	W	10	12	74.90	78.94	1.9	1.750	-0.740					41.516
1408	C	9	H	5	W	13	15	74.93	78.97	1.8	1.810	-0.720					41.517
1408	C	9	H	5	W	16	18	74.96	79.00	1.6	1.720	-0.680					41.518
1408	C	9	H	5	W	19	21	74.99	79.03	1.5	1.720	-0.720					41.519
1408	C	9	H	5	W	22	24	75.02	79.06	2.0	1.650	-0.770					41.520
1408	C	9	H	5	W	25	27	75.05	79.09	1.5	1.600	-0.830					41.521
1408	C	9	H	5	W	28	30	75.08	79.12	1.0	1.710	-0.710					41.522
1408	C	9	H	5	W	31	33	75.11	79.15		1.690	-0.700					41.523
1408	C	9	H	5	W	34	36	75.14	79.18	2.3	1.780	-0.680					41.524
1408	C	9	H	5	W	37	39	75.17	79.21	1.0	1.660	-0.790					41.525
1408	C	9	H	5	W	40	42	75.20	79.24	0.7	1.660	-0.820					41.526
1408	C	9	H	5	W	43	45	75.23	79.27	0.9	1.650	-0.750					41.527
1408	C	9	H	5	W	46	48	75.26	79.30	0.7	1.470	-1.110					41.528
1408	C	9	H	5	W	49	51	75.29	79.33	1.0	1.620	-0.870					41.529
1408	C	9	H	5	W	52	54	75.32	79.36	0.8	1.660	-0.880					41.530
1408	C	9	H	5	W	55	57	75.35	79.39	0.6	1.600	-0.910					41.531
1408	C	9	H	5	W	58	60	75.38	79.42	0.8	1.600	-0.890					41.533
1408	C	9	H	5	W	61	63	75.41	79.45	0.7	1.700	-0.880					41.534
1408	C	9	H	5	W	64	66	75.44	79.48	1.6	1.710	-0.860					41.535
1408	C	9	H	5	W	67	69	75.47	79.51	1.4	1.620	-0.940					41.536
1408	C	9	H	5	W	70	72	75.50	79.54	0.7	1.690	-0.900					41.537
1408	C	9	H	5	W	73	75	75.53	79.57	0.9	1.640	-0.970					41.538
1408	C	9	H	5	W	76	78	75.56	79.60	1.4	1.610	-1.010					41.539
1408	C	9	H	5	W	79	81	75.59	79.63	1.5	1.510	-0.930					41.540
1408	C	9	H	5	W	82	84	75.62	79.66	1.0	1.680	-0.900					41.541
1408	C	9	H	5	W	85	87	75.65	79.69	1.0	1.660	-0.920					41.542
1408	C	9	H	5	W	88	90	75.68	79.72	1.2	1.680	-0.960					41.543
1408	C	9	H	5	W	91	93	75.71	79.75	1.7	1.520	-0.970					41.544
1408	C	9	H	5	W	94	96	75.74	79.78	0.9	1.570	-0.970					41.545
1408	C	9	H	5	W	97	99	75.77	79.81	1.1	1.600	-1.030					41.546
1408	C	9	H	5	W	100	102	75.80	79.84	1.6	1.620	-0.880					41.547
1408	C	9	H	5	W	103	105	75.83	79.87	2.7	1.670	-0.960					41.548
1408	C	9	H	5	W	106	108	75.86	79.90	2.4	1.550	-1.000					41.549
1408	C	9	H	5	W	109	111	75.89	79.93	1.8	1.650	-0.970					41.551
1408	A	9	H	1	W	52	54	71.32	79.94	1.6	1.700	-0.330	2.924	-1.719	0.240	0.680	41.551
1408	C	9	H	5	W	112	114	75.92	79.96	1.0	1.610	-0.930					41.552
1408	A	9	H	1	W	55	57	71.35	79.97	1.7	1.650	-0.580	2.964	-1.614	0.180	0.710	41.552
1408	C	9	H	5	W	115	117	75.95	79.99	1.0	1.680	-0.880					41.553
1408	A	9	H	1	W	58	60	71.38	80.00	1.3	1.690	-0.430	2.547	-1.633	0.190	0.670	41.553
1408	C	9	H	5	W	118	120	75.98	80.02	0.6	1.630	-0.920					41.554
1408	A	9	H	1	W	61	63	71.41	80.03	0.9	1.700	-0.520	2.873	-1.683	0.170	0.710	41.554
1408	C	9	H	5	W	121	123	76.01	80.05	1.1	1.670	-0.900					41.555
1408	A	9	H	1	W	64	66	71.44	80.06	1.7	1.690	-0.440	2.806	-1.841	0.090	0.660	41.555
1408	C	9	H	5	W	124	126	76.04	80.08	1.3	1.570	-0.930					41.556
1408	A	9	H	1	W	67	69	71.47	80.09	1.0	1.780	-0.480	2.759	-1.706	0.290	0.680	41.556
1408	C	9	H	5	W	127	129	76.07	80.11	0.9	1.670	-0.880					41.557
1408	A	9	H	1	W	70	72	71.50	80.12	1.1	1.680	-0.600	2.330	-1.505	0.200	0.680	41.557
1408	C	9	H	5	W	130	132	76.10	80.14	0.8	1.630	-0.900					41.558
1408	A	9	H	1	W	73	75	71.53	80.15		1.750	-0.470	2.797	-1.435	0.130	0.590	41.558
1408	A	9	H	1	W	76	78	71.56	80.18	1.8	1.730	-0.630	3.720	-1.938	0.332	0.792	41.559

(**Appendix Table 5-11** continued)

Site	Hole	Core	Type	Section	Type	Top (cm)	Bottom (cm)	Midpoint (mbsf)	Depth (Revised CCSF)	Coarse fraction (wt %)	$\delta^{13}C$ (‰ VPDB) *Bulk sediment*	$\delta^{18}O$ (‰ VPDB) *Bulk sediment*	$\delta^{13}C$ (‰ VPDB) *M. cressatus*	$\delta^{18}O$ (‰ VPDB) *M. cressatus*	$\delta^{13}C$ (‰ VPDB) *N. truempyii*	$\delta^{18}O$ (‰ VPDB) *N. truempyii*	AGE
1408	A	9	H	1	W	79	81	71.59	80.21	2.0	1.760	-0.520	3.408	-1.880	0.135	0.656	41.560
1408	A	9	H	1	W	82	84	71.62	80.24	1.8	1.800	-0.520	3.360	-1.924	0.212	0.748	41.561
1408	A	9	H	1	W	85	87	71.65	80.27	2.4	1.790	-0.480	3.846	-2.046	0.125	0.753	41.563
1408	A	9	H	1	W	88	90	71.68	80.30	3.0	1.740	-0.630	3.371	-1.833	0.135	0.580	41.564
1408	A	9	H	1	W	91	93	71.71	80.33	1.8	1.810	-0.490	3.577	-1.774	0.029	0.762	41.565
1408	A	9	H	1	W	94	96	71.74	80.36	1.5	1.780	-0.580	3.257	-1.869	0.122	0.686	41.566
1408	A	9	H	1	W	97	99	71.77	80.39	2.7	1.660	-0.580	3.432	-2.157	0.121	0.728	41.567
1408	A	9	H	1	W	100	102	71.80	80.42	2.4	1.620	-0.660	3.616	-1.956	0.020	0.673	41.568
1408	A	9	H	1	W	103	105	71.83	80.45	2.5	1.690	-0.710	3.033	-1.648	0.197	0.628	41.569
1408	A	9	H	1	W	106	108	71.86	80.48	2.5	1.700	-0.570	3.447	-1.964	0.073	0.656	41.570
1408	A	9	H	1	W	109	111	71.89	80.51	3.3	1.590	-0.670	3.424	-2.016	0.118	0.637	41.571
1408	A	9	H	1	W	112	114	71.92	80.54	3.3	1.650	-0.600	3.147	-2.173	0.114	0.512	41.572
1408	A	9	H	1	W	115	117	71.95	80.57	3.2	1.670	-0.680	3.362	-2.038	0.321	0.686	41.573
1408	A	9	H	1	W	118	120	71.98	80.60	2.5	1.660	-0.570	3.339	-1.998	0.053	0.631	41.574
1408	A	9	H	1	W	121	123	72.01	80.63	2.9	1.650	-0.550	3.458	-2.150	0.043	0.497	41.575
1408	A	9	H	1	W	124	126	72.04	80.66	2.5	1.530	-0.730	3.073	-2.033	0.118	0.551	41.576
1408	A	9	H	1	W	127	129	72.07	80.69	2.8	1.680	-0.600	3.777	-2.128	0.122	0.679	41.577
1408	A	9	H	1	W	130	132	72.10	80.72	2.6	1.670	-0.600	3.335	-1.913	0.130	0.570	41.578
1408	A	9	H	1	W	133	135	72.13	80.75		1.600	-0.570	3.269	-1.980	0.120	0.490	41.579
1408	A	9	H	1	W	136	138	72.16	80.78	2.2	1.650	-0.510	3.412	-2.055	0.083	0.560	41.581
1408	A	9	H	1	W	139	141	72.19	80.81	2.3	1.570	-0.550	3.452	-1.933	0.071	0.527	41.582
1408	A	9	H	1	W	142	144	72.22	80.84	2.2	1.560	-0.590	3.451	-2.028	0.068	0.667	41.583
1408	A	9	H	1	W	145	147	72.25	80.87	2.4	1.600	-0.640	3.216	-1.981	0.104	0.617	41.584
1408	A	9	H	1	W	148	150	72.28	80.90				3.041	-1.954	0.070	0.540	41.585
1408	A	9	H	2	W	1	3	72.31	80.93	2.2	1.630	-0.470	3.095	-1.878	0.186	0.724	41.586
1408	A	9	H	2	W	4	6	72.34	80.96	2.7			3.018	-1.679	0.100	0.695	41.587
1408	A	9	H	2	W	7	9	72.37	80.99	2.5	1.580	-0.600	3.150	-1.859	0.215	0.743	41.588
1408	A	9	H	2	W	10	12	72.40	81.02	2.3	1.540	-0.560	2.927	-1.765	0.129	0.782	41.589
1408	A	9	H	2	W	13	15	72.43	81.05		1.650	-0.560	3.305	-1.842	0.130	0.550	41.590
1408	A	9	H	2	W	16	18	72.46	81.08	2.5	1.560	-0.430	3.634	-2.197	0.193	0.764	41.591
1408	A	9	H	2	W	19	21	72.49	81.11	2.5	1.600	-0.370	3.692	-1.997			41.592
1408	A	9	H	2	W	22	24	72.52	81.14	2.4	1.590	-0.370	3.243	-1.863	0.112	0.791	41.593
1408	A	9	H	2	W	25	27	72.55	81.17	2.0	1.590	-0.360			0.127	0.821	41.594
1408	A	9	H	2	W	28	30	72.58	81.20	1.9	1.540	-0.380	2.883	-1.760	0.047	0.739	41.595
1408	A	9	H	2	W	31	33	72.61	81.23	2.0	1.550	-0.390	3.150	-1.763	0.090	0.766	41.596
1408	A	9	H	2	W	34	36	72.64	81.26	1.8	1.550	-0.380	3.145	-1.877	-0.063	0.765	41.597
1408	A	9	H	2	W	37	39	72.67	81.29	2.0	1.600	-0.330	3.123	-1.451			41.599
1408	A	9	H	2	W	40	42	72.70	81.32	1.9	1.600	-0.340	2.628	-1.751	-0.096	0.857	41.600
1408	A	9	H	2	W	43	45	72.73	81.35	1.3	1.630	-0.330			-0.022	0.737	41.601
1408	A	9	H	2	W	46	48	72.76	81.38	0.9	1.620	-0.400	2.239	-1.947	-0.001	0.614	41.602
1408	A	9	H	2	W	49	51	72.79	81.41	0.9	1.670	-0.310	2.773	-1.644			41.603
1408	A	9	H	2	W	52	54	72.82	81.44	1.3	1.570	-0.410	3.020	-1.644	0.082	0.698	41.604
1408	A	9	H	2	W	55	57	72.85	81.47	1.0	1.650	-0.360	2.982	-1.888	0.113	0.873	41.605
1408	A	9	H	2	W	58	60	72.88	81.50	1.1	1.600	-0.420	3.023	-1.460	0.035	0.768	41.606
1408	A	9	H	2	W	61	63	72.91	81.53	1.0	1.610	-0.240	2.753	-1.765	-0.088	0.573	41.607
1408	A	9	H	2	W	64	66	72.94	81.56	1.5	1.620	-0.400	2.750	-1.799			41.608
1408	A	9	H	2	W	67	69	72.97	81.59	1.5	1.630	-0.330	3.378	-1.701	0.006	0.852	41.609
1408	A	9	H	2	W	70	72	73.00	81.62	1.2	1.630	-0.380	3.128	-1.688	0.037	0.786	41.610
1408	A	9	H	2	W	73	75	73.03	81.65	2.5	1.620	-0.310	3.432	-1.803	0.041	0.844	41.611
1408	A	9	H	2	W	76	78	73.06	81.68	1.6	1.610	-0.530	3.252	-1.830	-0.102	0.801	41.612
1408	A	9	H	2	W	79	81	73.09	81.71	1.1	1.590	-0.440	3.187	-1.998	0.039	0.823	41.613
1408	A	9	H	2	W	82	84	73.12	81.74	2.1	1.570	-0.480	2.913	-1.634	0.130	0.767	41.614
1408	A	9	H	2	W	85	87	73.15	81.77	1.9	1.590	-0.480	3.373	-1.748	0.125	0.774	41.615
1408	A	9	H	2	W	88	90	73.18	81.80	1.6	1.550	-0.390	3.366	-1.744	0.101	0.760	41.617

(**Appendix Table 5-11** continued)

Site	Hole	Core	Type	Section	Type	Top (cm)	Bottom (cm)	Midpoint (mbsf)	Depth (Revised CCSF)	Coarse fraction (wt %)	$\delta^{13}C$ (‰ VPDB) *Bulk sediment*	$\delta^{18}O$ (‰ VPDB) *Bulk sediment*	$\delta^{13}C$ (‰ VPDB) *M. cressatus*	$\delta^{18}O$ (‰ VPDB) *M. cressatus*	$\delta^{13}C$ (‰ VPDB) *N. truempyii*	$\delta^{18}O$ (‰ VPDB) *N. truempyii*	AGE
1408	A	9	H	2	W	91	93	73.21	81.83	1.3	1.610	-0.380	3.043	-1.705	0.010	0.778	41.618
1408	A	9	H	2	W	94	96	73.24	81.86	1.9	1.550	-0.470	3.414	-1.915	0.033	0.809	41.619
1408	A	9	H	2	W	97	99	73.27	81.89	1.9	1.570	-0.550	2.320	-2.009	0.058	0.736	41.620
1408	A	9	H	2	W	100	102	73.30	81.92	2.1	1.560	-0.520			0.018	0.685	41.621
1408	A	9	H	2	W	103	105	73.33	81.95	2.3	1.520	-0.570			0.030	0.631	41.622
1408	A	9	H	2	W	106	108	73.36	81.98	2.0	1.560	-0.630			-0.030	0.550	41.623
1408	A	9	H	2	W	109	111	73.39	82.01	2.2	1.520	-0.630			-0.034	0.613	41.624
1408	A	9	H	2	W	112	114	73.42	82.04	2.2	1.460	-0.700			-0.085	0.637	41.625
1408	A	9	H	2	W	115	117	73.45	82.07	2.4	1.350	-0.640	2.647	-1.706			41.626
1408	A	9	H	2	W	118	120	73.48	82.10	2.9	1.250	-0.750	2.626	-1.905	-0.202	0.428	41.627
1408	A	9	H	2	W	121	123	73.51	82.13	2.9	1.290	-0.620	2.835	-1.997	-0.227	0.455	41.628
1408	A	9	H	2	W	124	126	73.54	82.16		1.200	-0.750	2.706	-1.724			41.629
1408	A	9	H	2	W	127	129	73.57	82.19	4.9	1.240	-0.700	2.473	-1.877	-0.196	0.484	41.630
1408	A	9	H	2	W	130	132	73.60	82.22	8.8	1.190	-0.660	2.630	-1.844	-0.244	0.433	41.631
1408	A	9	H	2	W	133	135	73.63	82.25	10.8	1.230	-0.645	2.951	-2.082	-0.276	0.319	41.632
1408	A	9	H	2	W	136	138	73.66	82.28	5.7	1.200	-0.720	1.969	-1.809	-0.182	0.323	41.633
1408	A	9	H	2	W	139	141	73.69	82.31	6.3	1.280	-0.610	2.743	-1.929	0.044	0.062	41.635
1408	A	9	H	2	W	142	144	73.72	82.34	7.0	1.310	-0.750	2.774	-1.927	-0.186	0.425	41.636
1408	A	9	H	2	W	145	147	73.75	82.37	5.3	1.380	-0.660	3.075	-2.449	-0.144	0.396	41.637
1408	A	9	H	2	W	148	150	73.78	82.40	2.8	1.520	-0.710	2.696	-1.770	-0.109	0.421	41.638
1408	A	9	H	3	W	1	3	73.81	82.43	3.4	1.380	-0.790	2.824	-1.979	-0.149	0.392	41.639
1408	A	9	H	3	W	4	6	73.84	82.46	3.4	1.400	-0.740	2.792	-2.025	0.000	0.513	41.640
1408	A	9	H	3	W	7	9	73.87	82.49	4.1	1.330	-0.910	2.940	-1.990	-0.018	0.548	41.641
1408	A	9	H	3	W	10	12	73.90	82.52	3.6	1.440	-0.650	3.379	-1.989	-0.009	0.511	41.642
1408	A	9	H	3	W	13	15	73.93	82.55	2.9	1.500	-0.680	2.919	-1.871	-0.044	0.581	41.643
1408	A	9	H	3	W	16	18	73.96	82.58	1.8	1.650	-0.610	2.335	-1.667	-0.066	0.632	41.644
1408	A	9	H	3	W	19	21	73.99	82.61	2.1	1.590	-0.630	2.707	-1.893	-0.061	0.668	41.645
1408	A	9	H	3	W	22	24	74.02	82.64	2.3	1.520	-0.730	2.976	-1.261	-0.138	0.524	41.646
1408	A	9	H	3	W	25	27	74.05	82.67	2.2	1.610	-0.690	3.058	-1.570	0.030	0.637	41.647
1408	A	9	H	3	W	28	30	74.08	82.70	2.8	1.570	-0.720	2.893	-1.910	-0.016	0.752	41.648
1408	A	9	H	3	W	31	33	74.11	82.73	2.7	1.600	-0.680	2.907	-1.570	-0.003	0.613	41.649
1408	A	9	H	3	W	34	36	74.14	82.76	3.7	1.530	-0.790	2.809	-1.766	-0.122	0.631	41.650
1408	A	9	H	3	W	37	39	74.17	82.79		1.480	-0.700	2.917	-1.783	-0.160	0.410	41.651
1408	A	9	H	3	W	40	42	74.20	82.82	3.5	1.470	-0.690	3.136	-1.836	-0.129	0.563	41.653
1408	A	9	H	3	W	43	45	74.23	82.85	3.9	1.350	-0.630	2.288	-1.576	-0.091	0.664	41.654
1408	A	9	H	3	W	46	48	74.26	82.88	4.1	1.260	-0.650	2.765	-1.917	-0.190	0.357	41.655
1408	A	9	H	3	W	49	51	74.29	82.91	4.7	1.240	-0.700	2.746	-1.968	-0.057	0.403	41.656
1408	A	9	H	3	W	52	54	74.32	82.94	4.7	1.160	-0.590	2.401	-1.668	-0.202	0.436	41.657
1408	A	9	H	3	W	55	57	74.35	82.97	4.6	1.150	-0.640	2.899	-1.727	-0.219	0.329	41.658
1408	A	9	H	3	W	58	60	74.38	83.00	5.8	1.050	-0.610	2.922	-1.918	-0.159	0.618	41.659
1408	A	9	H	3	W	61	63	74.41	83.03	5.9	1.060	-0.580	2.958	-2.033	-0.140	0.438	41.660
1408	A	9	H	3	W	64	66	74.44	83.06	5.2	1.110	-0.640	3.055	-1.701	-0.208	0.521	41.661
1408	A	9	H	3	W	67	69	74.47	83.09	3.9	1.100	-0.670	3.345	-2.145	-0.144	0.590	41.662
1408	A	9	H	3	W	70	72	74.50	83.12	3.3	1.140	-0.650	2.352	-1.430	-0.086	0.555	41.663
1408	A	9	H	3	W	73	75	74.53	83.15	3.0	1.220	-0.670	2.771	-1.755	-0.145	0.627	41.664
1408	A	9	H	3	W	76	78	74.56	83.18	2.8	1.340	-0.620	2.848	-1.667	-0.095	0.601	41.665
1408	A	9	H	3	W	79	81	74.59	83.21	2.1			2.900	-2.214	-0.090	0.470	41.666
1408	A	9	H	3	W	82	84	74.62	83.24	0.5	1.560	-0.620	2.633	-1.778	-0.103	0.453	41.667
1408	A	9	H	3	W	85	87	74.65	83.27	1.1	1.580	-0.330	2.998	-2.178	-0.091	0.724	41.668
1408	A	9	H	3	W	88	90	74.68	83.30	1.2	1.510	-0.420	2.858	-1.792	-0.105	0.637	41.669
1408	A	9	H	3	W	91	93	74.71	83.33	1.6	1.540	-0.690	2.696	-1.978	-0.065	0.716	41.671
1408	C	10	H	1	W	88	90	79.18	83.35						-0.060	0.410	41.671
1408	A	9	H	3	W	94	96	74.74	83.36	1.7	1.590	-0.420	2.906	-1.786	0.014	0.838	41.672
1408	C	10	H	1	W	91	93	79.21	83.38	1.5	1.530	-0.500	3.090	-1.812	-0.080	0.580	41.672

(**Appendix Table 5-11** continued)

Site	Hole	Core	Type	Section	Type	Top (cm)	Bottom (cm)	Midpoint (mbsf)	Depth (Revised CCSF)	Coarse fraction (wt %)	$\delta^{13}C$ (‰ VPDB) Bulk sediment	$\delta^{18}O$ (‰ VPDB) Bulk sediment	$\delta^{13}C$ (‰ VPDB) M. cressatus	$\delta^{18}O$ (‰ VPDB) M. cressatus	$\delta^{13}C$ (‰ VPDB) N. truempyii	$\delta^{18}O$ (‰ VPDB) N. truempyii	AGE
1408	A	9	H	3	W	97	99	74.77	83.39		1.640	-0.310	2.698	-1.859	0.030	0.630	41.673
1408	C	10	H	1	W	94	96	79.24	83.41	1.6	1.570	-0.370			-0.030	0.600	41.673
1408	A	9	H	3	W	100	102	74.80	83.42	2.5	1.620	-0.220	3.335	-1.759	-0.003	0.742	41.674
1408	C	10	H	1	W	97	99	79.27	83.44	1.6	-0.110	-2.890	3.259	-1.793	-0.030	0.520	41.674
1408	A	9	H	3	W	103	105	74.83	83.45	1.7	1.660	-0.340	3.078	-1.717	0.010	0.826	41.675
1408	C	10	H	1	W	100	102	79.30	83.47	1.4	1.610	-0.340	2.993	-1.596	-0.030	0.600	41.675
1408	A	9	H	3	W	106	108	74.86	83.48				2.897	-1.494	-0.123	0.875	41.676
1408	C	10	H	1	W	103	105	79.33	83.50	1.7	1.610	-0.340	2.713	-1.836	-0.160	0.480	41.677
1408	A	9	H	3	W	109	111	74.89	83.51	1.7	1.590	-0.330	3.177	-1.502	0.020	0.729	41.677
1408	C	10	H	1	W	106	108	79.36	83.53	1.9	1.580	-0.350	3.270	-1.883	0.050	0.660	41.678
1408	A	9	H	3	W	112	114	74.92	83.54	2.0	1.590	-0.290	2.545	-1.058	0.083	0.821	41.678
1408	C	10	H	1	W	109	111	79.39	83.56	1.9	1.550	-0.400	2.539	-0.130	0.000	0.690	41.679
1408	A	9	H	3	W	115	117	74.95	83.57	2.4	1.550	-0.410	2.995	-1.444	0.036	0.840	41.679
1408	C	10	H	1	W	112	114	79.42	83.59	1.5	1.690	-0.270			0.050	0.700	41.680
1408	C	10	H	1	W	115	117	79.45	83.62	2.0	1.650	-0.400	2.788	-1.634	-0.100	0.430	41.681
1408	C	10	H	1	W	118	120	79.48	83.65	1.6	1.610	-0.550	2.968	-1.478	-0.030	0.650	41.682
1408	C	10	H	1	W	121	123	79.51	83.68	2.1	1.640	-0.370	2.709	-1.351	0.050	0.600	41.683
1408	C	10	H	1	W	124	126	79.54	83.71	2.1			3.542	-1.695	0.070	0.630	41.684
1408	C	10	H	1	W	127	129	79.57	83.74	1.5	1.600	-0.370	2.820	-1.504	0.020	0.640	41.685
1408	C	10	H	1	W	130	132	79.60	83.77	2.3	1.520	-0.460	2.990	-1.527	0.050	0.610	41.686
1408	C	10	H	1	W	133	135	79.63	83.80	2.8	1.520	-0.410	2.987	-1.552	0.010	0.610	41.687
1408	C	10	H	1	W	136	138	79.66	83.83	3.0	1.450	-0.460	3.057	-1.819	-0.050	0.600	41.688
1408	C	10	H	1	W	139	141	79.69	83.86	2.9	1.470	-0.500	2.484	-1.255	0.100	0.580	41.689
1408	C	10	H	1	W	142	144	79.72	83.89	3.0	1.460	-0.540	2.897	-1.707	-0.160	0.570	41.690
1408	C	10	H	1	W	145	147	79.75	83.92	2.9	1.440	-0.550	3.235	-1.895			41.691
1408	C	10	H	1	W	148	150	79.78	83.95	3.5	1.440	-0.610	2.754	-1.699	-0.180	0.550	41.692
1408	C	10	H	2	W	1	3	79.81	83.98	3.3	1.340	-0.610	2.266	-1.317	-0.070	0.250	41.693
1408	C	10	H	2	W	4	6	79.84	84.01	3.4	1.330	-0.600	2.790	-1.835	-0.080	0.530	41.695
1408	C	10	H	2	W	7	9	79.87	84.04	3.4			2.589	-1.886	-0.120	0.370	41.696
1408	C	10	H	2	W	10	12	79.90	84.07	3.6	1.300	-0.510	3.113	-2.215	-0.120	0.390	41.697
1408	C	10	H	2	W	13	15	79.93	84.10	4.5	1.340	-0.580	2.857	-2.075	-0.130	0.430	41.698
1408	C	10	H	2	W	16	18	79.96	84.13	3.7	1.300	-0.620	2.843	-1.737	-0.050	0.410	41.699
1408	C	10	H	2	W	19	21	79.99	84.16	3.4	1.310	-0.610	2.651	-1.906	-0.160	0.390	41.700
1408	C	10	H	2	W	22	24	80.02	84.19	3.2	1.330	-0.620	2.514	-1.692	-0.130	0.380	41.701
1408	C	10	H	2	W	25	27	80.05	84.22	3.2	1.310	-0.660	3.249	-1.927	-0.040	0.390	41.702
1408	C	10	H	2	W	28	30	80.08	84.25	2.8	1.310	-0.670	2.593	-2.040	-0.170	0.320	41.703
1408	C	10	H	2	W	31	33	80.11	84.28	3.2	1.380	-0.650	3.190	-2.082	0.000	0.360	41.704
1408	C	10	H	2	W	34	36	80.14	84.31	2.1	1.480	-0.680	2.519	-1.865	-0.120	0.360	41.705
1408	C	10	H	2	W	37	39	80.17	84.34	1.9	1.460	-0.730	2.777	-1.639	0.050	0.450	41.706
1408	C	10	H	2	W	40	42	80.20	84.37	2.2	1.520	-0.720	2.477	-2.030	0.060	0.450	41.707
1408	C	10	H	2	W	43	45	80.23	84.40	2.4			2.630	-2.205			41.708
1408	C	10	H	2	W	46	48	80.26	84.43	1.8	1.670	-0.630	3.019	-1.846	-0.050	0.420	41.709
1408	C	10	H	2	W	49	51	80.29	84.46	2.7	1.640	-0.650	2.811	-2.036	0.020	0.370	41.710
1408	C	10	H	2	W	52	54	80.32	84.49	2.4	1.710	-0.580	2.848	-1.743	-0.010	0.420	41.711
1408	C	10	H	2	W	55	57	80.35	84.52	1.8	1.710	-0.690	2.722	-1.583	-0.030	0.440	41.713
1408	C	10	H	2	W	58	60	80.38	84.55	2.8	1.830	-0.550	2.869	-1.772	0.100	0.490	41.714
1408	C	10	H	2	W	61	63	80.41	84.58	1.9	1.750	-0.620	2.957	-2.102	0.100	0.490	41.715
1408	C	10	H	2	W	64	66	80.44	84.61	1.9	1.810	-0.530	2.804	-1.710	0.040	0.510	41.716
1408	C	10	H	2	W	67	69	80.47	84.64	2.2	1.790	-0.480	3.339	-1.666	0.100	0.550	41.717
1408	C	10	H	2	W	70	72	80.50	84.67	2.2	1.930	-0.730	2.841	-1.409	0.120	0.610	41.718
1408	C	10	H	2	W	73	75	80.53	84.70	1.9	1.720	-0.450	3.003	-1.857	0.090	0.580	41.719
1408	C	10	H	2	W	76	78	80.56	84.73	2.6	1.730	-0.510	3.367	-1.827	0.120	0.570	41.720
1408	C	10	H	2	W	79	81	80.59	84.76	3.0	1.740	-0.550	2.686	-1.773	0.070	0.600	41.721
1408	C	10	H	2	W	82	84	80.62	84.79	3.0	1.660	-0.470	2.938	-1.478	0.050	0.550	41.722

(**Appendix Table 5-11** continued)

Site	Hole	Core	Type	Section	Type	Top (cm)	Bottom (cm)	Midpoint (mbsf)	Depth (Revised CCSF)	Coarse fraction (wt %)	$\delta^{13}C$ (‰ VPDB) Bulk sediment	$\delta^{18}O$ (‰ VPDB) Bulk sediment	$\delta^{13}C$ (‰ VPDB) M. cressatus	$\delta^{18}O$ (‰ VPDB) M. cressatus	$\delta^{13}C$ (‰ VPDB) N. truempyii	$\delta^{18}O$ (‰ VPDB) N. truempyii	AGE
1408	C	10	H	2	W	85	87	80.65	84.82	3.4	1.610	-0.550	2.412	-1.436	-0.010	0.460	41.723
1408	C	10	H	2	W	88	90	80.68	84.85	3.5	1.640	-0.430	3.294	-1.685	0.120	0.580	41.724
1408	C	10	H	2	W	91	93	80.71	84.88	3.9	1.430	-0.480	2.840	-1.537	0.050	0.640	41.725
1408	C	10	H	2	W	94	96	80.74	84.91	4.0	1.510	-0.590	2.923	-1.885	-0.060	0.630	41.726
1408	C	10	H	2	W	97	99	80.77	84.94	4.6	1.370	-0.510	2.522	-1.432	0.130	0.630	41.727
1408	C	10	H	2	W	100	102	80.80	84.97	3.7	1.430	-0.390	2.802	-2.022	0.000	0.750	41.728
1408	C	10	H	2	W	103	105	80.83	85.00	3.5	1.480	-0.370	3.144	-1.822			41.729
1408	C	10	H	2	W	106	108	80.86	85.03	3.5	1.450	-0.380	2.871	-1.759	0.050	0.650	41.730
1408	C	10	H	2	W	109	111	80.89	85.06	3.5	1.440	-0.400	2.995	-1.687	-0.040	0.440	41.732
1408	C	10	H	2	W	112	114	80.92	85.09	3.5	1.440	-0.330	2.778	-1.822	0.060	0.570	41.733
1408	C	10	H	2	W	115	117	80.95	85.12	2.6	1.580	-0.360	2.916	-1.338	0.010	0.620	41.734
1408	C	10	H	2	W	118	120	80.98	85.15	1.5	1.410	-0.510	2.508	-1.681	-0.010	0.640	41.735
1408	C	10	H	2	W	121	123	81.01	85.18	1.8	1.750	-0.020	2.782	-1.581	-0.070	0.640	41.736
1408	C	10	H	2	W	124	126	81.04	85.21	1.5			2.858	-1.648	-0.080	0.560	41.737
1408	C	10	H	2	W	127	129	81.07	85.24	1.2	1.480	-0.850	2.948	-1.958	-0.080	0.610	41.738
1408	C	10	H	2	W	130	132	81.10	85.27	1.7	1.500	-0.770	2.870	-1.856	0.000	0.620	41.739
1408	C	10	H	2	W	133	135	81.13	85.30	2.0	1.540	-0.760	2.608	-1.836	-0.010	0.610	41.740
1408	C	10	H	2	W	136	138	81.16	85.33	2.3	1.580	-0.710	3.238	-1.623	0.030	0.670	41.741
1408	C	10	H	2	W	139	141	81.19	85.36	1.6	1.600	-0.620	2.824	-1.483	0.010	0.760	41.742
1408	C	10	H	2	W	142	144	81.22	85.39	2.0	1.590	-0.740	2.639	-1.290	0.120	0.590	41.743
1408	C	10	H	2	W	145	147	81.25	85.42	2.0	1.630	-0.810	3.130	-1.728	0.120	0.600	41.744
1408	C	10	H	2	W	148	150	81.28	85.45	2.3	1.620	-0.760	3.079	-1.584	0.130	0.410	41.745

Appendix Table 5-12 IODP Exp. 342 Site U1408 fragmentation, BFAR, and % Planktic data

Site	Hole	Core	Type	Section	Type	Top (cm)	Bottom (cm)	Midpoint (mbsf)	Depth (Revised CCSF)	Frag. (%)	P/(P+B)	BFAR	Age (Ma)
1408	A	9	H	1	W	52	54	71.32	79.94	1.69	0.98	0.11	41.551
1408	A	9	H	1	W	55	57	71.35	79.97	2.48	0.99	0.10	41.552
1408	A	9	H	1	W	58	60	71.38	80.00	3.75	0.98	0.12	41.553
1408	A	9	H	1	W	61	63	71.41	80.03	5.26	0.97	0.08	41.554
1408	A	9	H	1	W	64	66	71.44	80.06	2.30	0.99	0.07	41.555
1408	A	9	H	1	W	67	69	71.47	80.09	5.94	0.98	0.08	41.556
1408	A	9	H	1	W	70	72	71.50	80.12	4.82	0.99	0.15	41.557
1408	A	9	H	1	W	76	78	71.56	80.18	2.47	0.98	0.09	41.559
1408	A	9	H	1	W	82	84	71.62	80.24	2.68	0.99	0.09	41.561
1408	A	9	H	1	W	91	93	71.71	80.33	2.52	0.98	0.09	41.565
1408	A	9	H	1	W	100	102	71.80	80.42	1.75	0.99	0.08	41.568
1408	A	9	H	1	W	106	108	71.86	80.48	1.52	0.99	0.12	41.570
1408	A	9	H	1	W	115	117	71.95	80.57	1.20	1.00	0.12	41.573
1408	A	9	H	1	W	121	123	72.01	80.63	1.15	0.99	0.12	41.575
1408	A	9	H	1	W	130	132	72.10	80.72	1.04	0.99	0.14	41.578
1408	A	9	H	1	W	136	138	72.16	80.78	1.31	0.99	0.14	41.581
1408	A	9	H	1	W	142	144	72.22	80.84	1.59	0.99	0.08	41.583
1408	A	9	H	2	W	1	3	72.31	80.93	1.12	0.99	0.12	41.586
1408	A	9	H	2	W	7	9	72.37	80.99	0.80	0.99	0.14	41.588
1408	A	9	H	2	W	16	18	72.46	81.08	1.04	0.99	0.14	41.591
1408	A	9	H	2	W	22	24	72.52	81.14	1.42	0.99	0.15	41.593
1408	A	9	H	2	W	31	33	72.61	81.23	1.93	0.99	0.08	41.596
1408	A	9	H	2	W	40	42	72.70	81.32	2.08	0.98	0.11	41.600
1408	A	9	H	2	W	43	45	72.73	81.35	4.03	0.97	0.08	41.601
1408	A	9	H	2	W	46	48	72.76	81.38	8.36	0.98	0.07	41.602
1408	A	9	H	2	W	49	51	72.79	81.41	5.38	0.99	0.06	41.603
1408	A	9	H	2	W	52	54	72.82	81.44	2.09	0.99	0.05	41.604
1408	A	9	H	2	W	58	60	72.88	81.50	3.29	0.99	0.09	41.606
1408	A	9	H	2	W	64	66	72.94	81.56	3.26	0.99	0.08	41.608
1408	A	9	H	2	W	73	75	73.03	81.65	2.43	0.99	0.08	41.611
1408	A	9	H	2	W	79	81	73.09	81.71	2.86	0.99	0.06	41.613
1408	A	9	H	2	W	88	90	73.18	81.80	1.78	0.98	0.10	41.617
1408	A	9	H	2	W	97	99	73.27	81.89	0.99	0.99	0.07	41.620
1408	A	9	H	2	W	103	105	73.33	81.95	0.94	0.99	0.08	41.622
1408	A	9	H	2	W	112	114	73.42	82.04	0.98	0.99	0.10	41.625
1408	A	9	H	2	W	121	123	73.51	82.13	1.05	1.00	0.14	41.628
1408	A	9	H	2	W	130	132	73.60	82.22	1.03	0.99	0.09	41.631
1408	A	9	H	2	W	133	135	73.63	82.25	1.31	0.99	0.05	41.632
1408	A	9	H	2	W	139	141	73.69	82.31	1.13	0.99	0.05	41.635
1408	A	9	H	2	W	145	147	73.75	82.37	1.04	0.99	0.12	41.637
1408	A	9	H	3	W	1	3	73.81	82.43	1.75	0.99	0.09	41.639
1408	A	9	H	3	W	7	9	73.87	82.49	1.02	0.99	0.14	41.641
1408	A	9	H	3	W	13	15	73.93	82.55	1.67	0.99	0.18	41.643
1408	A	9	H	3	W	16	18	73.96	82.58	4.28	0.99	0.10	41.644
1408	A	9	H	3	W	22	24	74.02	82.64	2.12	0.99	0.06	41.646
1408	A	9	H	3	W	25	27	74.05	82.67	1.73	1.00	0.09	41.647
1408	A	9	H	3	W	28	30	74.08	82.70	1.25	0.99	0.10	41.648
1408	A	9	H	3	W	37	39	74.17	82.79	0.88	1.00	0.00	41.651
1408	A	9	H	3	W	43	45	74.23	82.85	0.37	0.99	0.09	41.654
1408	A	9	H	3	W	52	54	74.32	82.94	0.55	1.00	0.06	41.657
1408	A	9	H	3	W	58	60	74.38	83.00	0.81	0.99	0.11	41.659
1408	A	9	H	3	W	64	66	74.44	83.06	0.90	1.00	0.05	41.661
1408	A	9	H	3	W	70	72	74.50	83.12	0.82	1.00	0.11	41.663
1408	A	9	H	3	W	76	78	74.56	83.18	1.03	0.99	0.07	41.665
1408	A	9	H	3	W	79	81	74.59	83.21	1.73	0.99	0.07	41.666

(**Appendix Table 5-12** continued)

Site	Hole	Core	Type	Section	Type	Top (cm)	Bottom (cm)	Midpoint (mbsf)	Depth (Revised CCSF)	Frag. (%)	P/(P+B)	BFAR	Age (Ma)
1408	A	9	H	3	W	82	84	74.62	83.24	5.97	0.94	0.09	41.667
1408	A	9	H	3	W	85	87	74.65	83.27	3.11	0.99	0.06	41.668
1408	A	9	H	3	W	91	93	74.71	83.33	3.71	0.99	0.09	41.671
1408	A	9	H	3	W	100	102	74.80	83.42	1.86	0.99	0.00	41.674
1408	A	9	H	3	W	103	105	74.83	83.45	3.03	0.99	0.11	41.675
1408	A	9	H	3	W	106	108	74.86	83.48	1.19	0.99	0.14	41.676
1408	A	9	H	3	W	109	111	74.89	83.51	1.79	1.00	0.09	41.677
1408	A	9	H	3	W	112	114	74.92	83.54	1.61	0.99	0.00	41.678
1408	A	9	H	3	W	115	117	74.95	83.57	1.66	0.99	0.11	41.679
1408	C	10	H	1	W	88	90	79.18	83.35	6.21	1.00	0.03	41.671
1408	C	10	H	1	W	91	93	79.21	83.38	2.57	0.99	0.09	41.672
1408	C	10	H	1	W	112	114	79.42	83.59	2.32	0.98	0.08	41.680
1408	C	10	H	1	W	118	120	79.48	83.65	2.11	1.00	0.03	41.682
1408	C	10	H	1	W	124	126	79.54	83.71	1.40	0.99	0.11	41.684
1408	C	10	H	1	W	127	129	79.57	83.74	1.98	0.99	0.06	41.685
1408	C	10	H	1	W	133	135	79.63	83.80	0.86	0.99	0.10	41.687
1408	C	10	H	1	W	139	141	79.69	83.86	1.06	1.00	0.06	41.689
1408	C	10	H	1	W	145	147	79.75	83.92	0.89	1.00	0.13	41.691
1408	C	10	H	2	W	4	6	79.84	84.01	0.63	0.99	0.08	41.695
1408	C	10	H	2	W	13	15	79.93	84.10	0.71	0.99	0.11	41.698
1408	C	10	H	2	W	19	21	79.99	84.16	0.75	1.00	0.05	41.700
1408	C	10	H	2	W	25	27	80.05	84.22	0.50	1.00	0.05	41.702
1408	C	10	H	2	W	34	36	80.14	84.31	1.30	0.99	0.08	41.705
1408	C	10	H	2	W	40	42	80.20	84.37	1.93	0.99	0.10	41.707
1408	C	10	H	2	W	49	51	80.29	84.46	1.92	0.99	0.13	41.710
1408	C	10	H	2	W	55	57	80.35	84.52	2.18	0.99	0.08	41.713
1408	C	10	H	2	W	58	60	80.38	84.55	2.92	0.99	0.07	41.714
1408	C	10	H	2	W	61	63	80.41	84.58	2.66	0.99	0.10	41.715
1408	C	10	H	2	W	64	66	80.44	84.61	2.17	0.99	0.10	41.716
1408	C	10	H	2	W	73	75	80.53	84.70	1.20	0.99	0.10	41.719
1408	C	10	H	2	W	79	81	80.59	84.76	1.48	1.00	0.07	41.721
1408	C	10	H	2	W	88	90	80.68	84.85	0.88	1.00	0.16	41.724
1408	C	10	H	2	W	94	96	80.74	84.91	1.06	0.99	0.10	41.726
1408	C	10	H	2	W	103	105	80.83	85.00	1.13	0.99	0.11	41.729
1408	C	10	H	2	W	109	111	80.89	85.06	1.19	1.00	0.04	41.732
1408	C	10	H	2	W	115	117	80.95	85.12	1.93	1.00	0.06	41.734
1408	C	10	H	2	W	121	123	81.01	85.18	2.32	1.00	0.05	41.736

List of References

Expedition 320/321 Scientists, 2010. Site U1333. *In* Pälike, H., Lyle, M., Nishi, H., Raffi, I., Gamage, K., Klaus, A., and the Expedition 320/321 Scientists, *Proc. IODP,* 320/321: Tokyo (Integrated Ocean Drilling Program Management International, Inc.), edited.

Agnini, C., E. Fornaciari, I. Raffi, R. Catanzariti, H. Pälike, J. Backman, and D. Rio (2014), Biozonation and biochronology of Paleogene calcareous nannofossils from low and middle latitudes, Newsl Stratigr, 47(2), 131-181.

Anagnostou, E., E. H. John, K. M. Edgar, G. L. Foster, A. Ridgwell, G. N. Inglis, R. D. Pancost, D. J. Lunt, and P. N. Pearson (2016), Changing atmospheric CO_2 concentration was the primary driver of early Cenozoic climate, Nature, 533(7603), 380-384.

Armstrong McKay, D. I., T. Tyrrell, and P. A. Wilson (2016), Global carbon cycle perturbation across the Eocene-Oligocene climate transition, Paleoceanography, n/a-n/a, doi: 10.1002/2015PA002818.

Bailey, I., G. M. Hole, G. L. Foster, P. A. Wilson, C. D. Storey, C. N. Trueman, and M. E. Raymo (2013), An alternative suggestion for the Pliocene onset of major northern hemisphere glaciation based on the geochemical provenance of North Atlantic Ocean ice-rafted debris, Quaternary Sci Rev, 75, 181-194.

Beerling, D. J., and D. L. Royer (2011), Convergent Cenozoic CO_2 history, Nature Geoscience, 4(7), 418-420.

Bemis, B. E., H. J. Spero, J. Bijma, and D. W. Lea (1998), Reevaluation of the oxygen isotopic composition of planktonic foraminifera: Experimental results and revised paleotemperature equations, Paleoceanography, 13(2), 150-160.

Berggren, W. A. (1995), A revised Cenozoic geochronology and chronostratigraphy, Geochronology Time Scales and Gobal Stratigraphic Correlation, SEPM Special Publication No. 54, 129-212.

Berggren, W. A., and P. N. Pearson (2005), A revised tropical to subtropical Paleogene planktonic foraminiferal zonation, The Journal of Foraminiferal Research, 35(4), 279-298.

Berner, R. A., A. C. Lasaga, and R. M. Garrels (1983), The carbonate-silicate geochemical cycle and its effect on atmospheric carbon dioxide over the past 100 million years, Am. J. Sci, 283(7), 641-683.

Bijl, P. K., A. J. P. Houben, S. Schouten, S. M. Bohaty, A. Sluijs, G. J. Reichart, J. S. Sinninghe Damsté, and H. Brinkhuis (2010), Transient Middle Eocene Atmospheric CO2 and Temperature Variations, Science, 330(6005), 819-821, doi: 10.1126/science.1193654.

Bohaty, S. M., and J. C. Zachos (2003), Significant Southern Ocean warming event in the late middle Eocene, Geology, 31(11), 1017-1020, doi: 10.1130/g19800.1.

Bohaty, S. M., J. C. Zachos, and M. L. Delaney (2012), Foraminiferal Mg/Ca evidence for Southern Ocean cooling across the Eocene-Oligocene transition, Earth and Planetary Science Letters, 317, 251-261.

Bohaty, S. M., J. C. Zachos, F. Florindo, and M. L. Delaney (2009), Coupled greenhouse warming and deep-sea acidification in the middle Eocene, Paleoceanography, 24(2), PA2207.

Borrelli, C., and M. E. Katz (2015), Dynamic deep-water circulation in the northwestern Pacific during the Eocene: Evidence from Ocean Drilling Program Site 884 benthic foraminiferal stable isotopes ($\delta^{18}O$ and $\delta^{13}C$), Geosphere, doi: 10.1130/ges01152.1.

Boscolo Galazzo, F., E. Thomas, and L. Giusberti (2015), Benthic foraminiferal response to the Middle Eocene Climatic Optimum (MECO) in the South-Eastern Atlantic (ODP Site 1263), Palaeogeography, Palaeoclimatology, Palaeoecology, 417, 432-444.

Boscolo Galazzo, F., L. Giusberti, V. Luciani, and E. Thomas (2013), Paleoenvironmental changes during the Middle Eocene Climatic Optimum (MECO) and its aftermath: The benthic foraminiferal record from the Alano section (NE Italy), Palaeogeography, Palaeoclimatology, Palaeoecology, 378(0), 22-35.

Boscolo Galazzo, F., E. Thomas, M. Pagani, C. Warren, V. Luciani, and L. Giusberti (2014), The middle Eocene climatic optimum (MECO): A multiproxy record of paleoceanographic changes in the southeast Atlantic (ODP Site 1263, Walvis Ridge), Paleoceanography, doi: 10.1002/2014PA002670.

Bowen, G. J., B. J. Maibauer, M. J. Kraus, U. Röhl, T. Westerhold, A. Steimke, P. D. Gingerich, S. L. Wing, and W. C. Clyde (2015), Two massive, rapid releases of carbon during the onset of the Palaeocene-Eocene thermal maximum, Nature Geosci, 8(1), 44-47, doi: 10.1038/ngeo2316

Bralower, T. J., S. I. Premoli, and M. J. Malone (2002), Proc. ODP, Init. Repts., 198: College Station, TX (Ocean Drilling Program), doi:10.2973/odp.proc.ir.198.2002.

Bralower, T. J., S. I. Premoli, and M. J. Malone (2003), Leg 198, Proceedings of the Ocean Drilling Program: Initial reports, 198, 148.

Bralower, T. J., S. I. Premoli, and M. J. Malone (2005), Data report: Paleocene-early Oligocene calcareous nannofossil biostratigraphy, ODP Leg 198 Sites 1209, 1210, and 1211 (Shatsky Rise, Pacific Ocean), paper presented at Proc. ODP, Sci. Results.

Broecker, W. S. (1971), Calcite accumulation rates and glacial to interglacial changes in ocean mixing, edited, The Late Cenozoic Ages, Yale University Press.

Broecker, W. S., and E. Clark (1999), CaCO3 size distribution: A paleocarbonate ion proxy?, Paleoceanography, 14(5), 596-604.

Brown, J. H., J. F. Gillooly, A. P. Allen, V. M. Savage, and G. B. West (2004), Toward a metabolic theory of ecology, Ecology, 85(7), 1771-1789.

Burgess, C. E., P. N. Pearson, C. H. Lear, H. E. G. Morgans, L. Handley, R. D. Pancost, and S. Schouten (2008), Middle Eocene climate cyclicity in the southern Pacific: Implications for global ice volume, Geology, 36(8), 651-654.

Calvert, S. E., and T. F. Pedersen (1993), Geochemistry of recent oxic and anoxic marine sediments: implications for the geological record, Marine geology, 113(1), 67-88.

Ciesielski, P. F., and Y. Kristoffersen (1988), *Proc. ODP, Init. Repts.,* 114: College Station, TX (Ocean Drilling Program), 483–548, edited.

Clement, B. M., and E. A. Hailwood (1991), Magnetostratigraphy of sediments from Sites 701 and 702. *In* Ciesielski, P.F., Kristoffersen, Y., et al., *Proc. ODP, Sci. Results,* 114: College Station, TX (Ocean Drilling Program), 359–366, edited.

Colosimo, A. B., T. J. Bralower, and J. C. Zachos (2006), Evidence for lysocline shoaling at the Paleocene/Eocene thermal maximum on Shatsky Rise, northwest Pacific, paper presented at Proceedings of the Ocean Drilling Program, Scientific Results, Ocean Drilling Prog. College Station, TX.

Coxall, H. K., and P. A. Wilson (2011), Early Oligocene glaciation and productivity in the eastern equatorial Pacific: Insights into global carbon cycling, Paleoceanography, 26(2), PA2221, doi: 10.1029/2010pa002021.

Coxall, H. K., P. A. Wilson, H. Pälike, C. H. Lear, and J. Backman (2005), Rapid stepwise onset of Antarctic glaciation and deeper calcite compensation in the Pacific Ocean, Nature, 433(7021), 53-57.

Cramer, B. S., J. D. Wright, D. V. Kent, and M. P. Aubry (2003), Orbital climate forcing of δ13C excursions in the late Paleocene–early Eocene (chrons C24n–C25n), Paleoceanography, 18(4).

Cramer, B. S., J. R. Toggweiler, J. D. Wright, M. E. Katz, and K. G. Miller (2009), Ocean overturning since the Late Cretaceous: Inferences from a new benthic foraminiferal isotope compilation, Paleoceanography, 24(4).

Cui, Y., L. R. Kump, A. J. Ridgwell, A. J. Charles, C. K. Junium, A. F. Diefendorf, K. H. Freeman, N. M. Urban, and I. C. Harding (2011), Slow release of fossil carbon during the Palaeocene-Eocene Thermal Maximum, Nature Geoscience, 4(7), 481-485.

Curry, W. B., N. J. Shackleton, and C. Richter (1995), Leg 154, Proceedings ODP, Initial Reports, 154, 421-442.

D'Haenens, S., A. Bornemann, P. Claeys, U. Röhl, E. Steurbaut, and R. P. Speijer (2014), A transient deep-sea circulation switch during Eocene Thermal Maximum 2, Paleoceanography, doi: 10.1002/2013PA002567.

Dawber, C. F., and A. K. Tripati (2011a), Element/Calcium ratios in middle Eocene samples of Oridorsalis umbonatus from Ocean Drilling Program Site 1209, Climate of the Past Discussions, 7, 3795-3821.

Dawber, C. F., and A. K. Tripati (2011b), Constraints on glaciation in the middle Eocene (46-37 Ma) from Ocean Drilling Program (ODP) Site 1209 in the tropical Pacific Ocean, Paleoceanography, 26(2), PA2208.

Dawber, C. F., and A. K. Tripati (2012a), Relationships between bottom water carbonate saturation and element/Ca ratios in coretop samples of the benthic foraminifera Oridorsalis umbonatus, Biogeosciences, 9(8), 3029-3045.

Dawber, C. F., and A. K. Tripati (2012b), Exploring the controls on element ratios in middle Eocene samples of the benthic foraminifera Oridorsalis umbonatus, Climate of the Past, 8(6), 1957-1971.

Dawber, C. F., A. K. Tripati, A. S. Gale, C. MacNiocaill, and S. P. Hesselbo (2011), Glacioeustasy during the middle Eocene? Insights from the stratigraphy of the Hampshire Basin, UK, Palaeogeography, Palaeoclimatology, Palaeoecology, 300(1), 84-100.

DeConto, R. M., D. Pollard, P. A. Wilson, H. Pälike, C. H. Lear, and M. Pagani (2008), Thresholds for Cenozoic bipolar glaciation, Nature, 455(7213), 652-656.

DeConto, R. M., S. Galeotti, M. Pagani, D. Tracy, K. Schaefer, T. Zhang, D. Pollard, and D. J. Beerling (2012), Past extreme warming events linked to massive carbon release from thawing permafrost, Nature, 484(7392), 87-91.

Delaney, M. L., and E. A. Boyle (1988), Tertiary paleoceanic chemical variability: Unintended consequences of simple geochemical models, Paleoceanography, 3(2), 137-156, doi: 10.1029/PA003i002p00137.

Dickens, G. R. (2003), Rethinking the global carbon cycle with a large, dynamic and microbially mediated gas hydrate capacitor, Earth and Planetary Science Letters, 213(3), 169-183.

Dickens, G. R. (2011), Down the rabbit hole: Toward appropriate discussion of methane release from gas hydrate systems during the Paleocene-Eocene thermal maximum and other past hyperthermal events, Climate of the Past, 7(3), 831-846.

Dickens, G. R., J. R. O'Neil, D. K. Rea, and R. M. Owen (1995), Dissociation of oceanic methane hydrate as a cause of the carbon isotope excursion at the end of the Paleocene, Paleoceanography, 10(6), 965-971.

Diester-Haass, L., and R. Zahn (1996), Eocene-Oligocene transition in the Southern Ocean: History of water mass circulation and biological productivity, Geology, 24(2), 163-166.

Dutton, A., K. C. Lohmann, and R. M. Leckie (2005), Insights from the Paleogene tropical Pacific: Foraminiferal stable isotope and elemental results from Site 1209, Shatsky Rise, Paleoceanography, 20(3).

Dymond, J., E. Suess, and M. W. Lyle (1992), Barium in deep-sea sediment: A geochemical proxy for paleoproductivity, Paleoceanography, 7(2), 163-181.

Edgar, K. M., H. Pälike, and P. A. Wilson (2013), Testing the impact of diagenesis on the delta O-18 and delta C-13 of benthic foraminiferal calcite from a sediment burial depth transect in the equatorial Pacific, Paleoceanography, 28(3), 468-480, doi: Doi 10.1002/Palo.20045.

Edgar, K. M., P. A. Wilson, P. F. Sexton, and Y. Suganuma (2007), No extreme bipolar glaciation during the main Eocene calcite compensation shift, Nature, 448(7156), 908-911.

Edgar, K. M., P. A. Wilson, P. F. Sexton, S. Gibbs, A. P. Roberts, and R. D. Norris (2010), New biostratigraphic, magnetostratigraphic and isotopic insights into the Middle Eocene Climatic Optimum in low latitudes, Palaeogeography, Palaeoclimatology, Palaeoecology, 297(3), 670-682.

Eldrett, J. S., I. C. Harding, P. A. Wilson, E. Butler, and A. P. Roberts (2007), Continental ice in Greenland during the Eocene and Oligocene, Nature, 446(7132), 176-179.

Emiliani, C. (1954), Temperatures of Pacific bottom waters and polar superficial waters during the Tertiary, Science, 119(3103), 853-855.

Epstein, S., R. Buchsbaum, H. A. Lowenstam, and H. C. Urey (1953), Revised carbonate-water isotopic temperature scale, Geological Society of America Bulletin, 64(11), 1315-1326.

Erbacher, J., D. C. Mosher, M. J. Malone, D. Berti, K. L. Bice, H. Bostock, H. J. Brumsack, T. Danelian, A. Forster, and F. Heidersdorf (2004), Leg 207 Summary, Proceedings of the Ocean Drilling Program. Initial Results, 207, 1-89.

Erez, J. (1978), Vital effect on stable-isotope composition seen in foraminifera and coral skeletons.

Faure, G. (1977), Principles of isotope geology, John Wiley and Sons, Inc., New York, NY.

Galeotti, S., S. Krishnan, M. Pagani, L. Lanci, A. Gaudio, J. C. Zachos, S. Monechi, G. Morelli, and L. J. Lourens (2010), Orbital chronology of Early Eocene hyperthermals from the Contessa Road section, central Italy, Earth and Planetary Science Letters, 290(1-2), 192-200.

Gillooly, J. F., J. H. Brown, G. B. West, V. M. Savage, and E. L. Charnov (2001), Effects of size and temperature on metabolic rate, science, 293(5538), 2248-2251.

Gradstein, F. M., J. Ogg, George, M. Schmitz, and G. Ogg (2012), The Geologic Time Scale 2012 2-Volume Set, elsevier.

Greenwood, D. R., and S. L. Wing (1995), Eocene continental climates and latitudinal temperature gradients, Geology, 23(11), 1044-1048, doi: 10.1130/0091-7613(1995)023<1044:ECCALT>2.3.CO;2.

Griffith, E., M. Calhoun, E. Thomas, K. Averyt, A. Erhardt, T. J. Bralower, M. W. Lyle, A. Olivarez-Lyle, and A. Paytan (2010), Export productivity and carbonate

accumulation in the Pacific Basin at the transition from a greenhouse to icehouse climate (late Eocene to early Oligocene), Paleoceanography, 25(26), 3212.

Grossman, E. L. (1987), Stable isotopes in modern benthic foraminifera; a study of vital effect, The Journal of Foraminiferal Research, 17(1), 48-61.

Hain, M. P., D. M. Sigman, J. A. Higgins, and G. H. Haug (2015), The effects of secular calcium and magnesium concentration changes on the thermodynamics of seawater acid/base chemistry: Implications for Eocene and Cretaceous ocean carbon chemistry and buffering, Global Biogeochemical Cycles.

Hancock, H. J., and G. R. Dickens (2006), Carbonate dissolution episodes in Paleocene and Eocene sediment, Shatsky Rise, west-central Pacific, paper presented at Proceedings of the Ocean Drilling Program. Scientific Results, Texas A&M University.

Hay, W. W., et al. (1999), Alternative global Cretaceous paleogeography, Evolution of the Cretaceous ocean-climate system, 1.

Holbourn, A., W. Kuhnt, M. E. Schulz, and H. Erlenkeuser (2005), Impacts of orbital forcing and atmospheric carbon dioxide on Miocene ice-sheet expansion, Nature, 438(7067), 483-487.

Hönisch, B., et al. (2012), The Geological Record of Ocean Acidification, Science, 335(6072), 1058-1063, doi: 10.1126/science.1208277.

Houben, A. J. P., C. A. van Mourik, A. Montanari, R. Coccioni, and H. Brinkhuis (2012), The Eocene–Oligocene transition: Changes in sea level, temperature or both?, Palaeogeography, Palaeoclimatology, Palaeoecology, 335–336, 75-83.

Hsü, K. J., and J. L. LaBrecque (1986), Vol 73, Init. Repts., DSDP, 73: Washington (U.S. Govt. Printing Office), 495-512.

Huber, M. (2002), Straw Man 1: A preliminary view of the tropical Pacific from a global coupled climate model simulation of early Paleogene climate, Proceedings of the Ocean Drilling Program, Initial Reports. Ocean Drilling Program, College Station TX.

Huber, M., and L. C. Sloan (2001), Heat transport, deep waters, and thermal gradients: Coupled simulation of an Eocene greenhouse climate, Geophys. Res. Lett, 28(18), 3481-3484.

Inglis, G. N., A. Farnsworth, D. Lunt, G. L. Foster, C. J. Hollis, M. Pagani, P. E. Jardine, P. N. Pearson, P. J. Markwick, and A. M. Galsworthy (2015), Descent toward the Icehouse: Eocene sea surface cooling inferred from GDGT distributions, Paleoceanography, 30(7), 1000-1020.

IPCC (2013), Climate Change 2013: The Physical Science Basis. Contribution of Working Group I to the Fifth Assessment Report of the Intergovernmental Panel on Climate Change [Stocker, T.F., D. Qin, G.-K. Plattner, M. Tignor, S.K. Allen, J. Boschung, A. Nauels, Y. Xia, V. Bex and P.M. Midgley (eds.)]. Cambridge University Press, Cambridge, United Kingdom and New York, NY, USA, 1535 pp., edited.

Jansen, J. H. F., S. J. Van der Gaast, B. Koster, and A. J. Vaars (1998), CORTEX, a shipboard XRF-scanner for element analyses in split sediment cores, Marine Geology, 151(1), 143-153.

Jovane, L., F. Florindo, R. Coccioni, J. Dinarés-Turell, A. Marsili, S. Monechi, A. P. Roberts, and M. Sprovieri (2007), The middle Eocene climatic optimum event in the Contessa Highway section, Umbrian Apennines, Italy, Geological Society of America Bulletin, 119(3-4), 413-427.

Katz, M. E., D. R. Katz, J. D. Wright, K. G. Miller, D. K. Pak, N. J. Shackleton, and E. Thomas (2003), Early Cenozoic benthic foraminiferal isotopes: Species reliability and interspecies correction factors, Paleoceanography, 18(2), doi: 10.1029/2002pa000798.

Katz, M. E., K. G. Miller, J. D. Wright, B. S. Wade, J. V. Browning, B. S. Cramer, and Y. Rosenthal (2008), Stepwise transition from the Eocene greenhouse to the Oligocene icehouse, Nature Geoscience, 1(5), 329-334.

Kelly, D. C., J. C. Zachos, T. J. Bralower, and S. A. Schellenberg (2005), Enhanced terrestrial weathering/runoff and surface ocean carbonate production during the recovery stages of the Paleocene-Eocene thermal maximum, Paleoceanography, 20(4).

Kennett, J. P., and L. D. Stott (1991), Abrupt deep sea warming, paleoceanographic changes and benthic extinctions at the end of the Paleocene, Nature, 353, 225-229.

Kim, S. T., and J. R. O'Neil (1997), Equilibrium and nonequilibrium oxygen isotope effects in synthetic carbonates, Geochimica et Cosmochimica Acta, 61(16), 3461-3475.

Kirtland Turner, S. (2014), Pliocene switch in orbital-scale carbon cycle/climate dynamics, Paleoceanography, 29(12), 1256-1266, doi: 10.1002/2014PA002651.

Kirtland Turner, S., and A. Ridgwell (2013), Recovering the true size of an Eocene hyperthermal from the marine sedimentary record, Paleoceanography, 2013PA002541, doi: 10.1002/2013pa002541.

Kirtland Turner, S., P. F. Sexton, C. D. Charles, and R. D. Norris (2014), Persistence of carbon release events through the peak of early Eocene global warmth, Nature Geoscience, doi: 10.1038/ngeo2240.

Komar, N., R. E. Zeebe, and G. R. Dickens (2013), Understanding long-term carbon cycle trends: The late paleocene through the early eocene, Paleoceanography, 2013PA002520, doi: 10.1002/palo.20060.

Kurtz, A. C., L. R. Kump, M. A. Arthur, J. C. Zachos, and A. Paytan (2003), Early Cenozoic decoupling of the global carbon and sulfur cycles, Paleoceanography, 18(4).

Laskar, J., A. Fienga, M. Gastineau, and H. Manche (2011a), La2010: a new orbital solution for the long-term motion of the Earth, Astronomy & Astrophysics, 532, A89.

Laskar, J., M. Gastineau, J. B. Delisle, A. Farrés, and A. Fienga (2011b), Strong chaos induced by close encounters with Ceres and Vesta, Astronomy & Astrophysics, 532, L4.

Laskar, J., P. Robutel, F. Joutel, M. Gastineau, A. C. M. Correia, and B. Levrard (2004), A long-term numerical solution for the insolation quantities of the Earth, Astronomy & Astrophysics, 428(1), 261-285.

Lauretano, V., K. Littler, M. Polling, J. C. Zachos, and L. J. Lourens (2015), Frequency, magnitude and character of hyperthermal events at the onset of the Early Eocene Climatic Optimum, Clim. Past, 11(10), 1313-1324, doi: 10.5194/cp-11-1313-2015.

Le, J., and N. Shackleton (1992), Carbonate dissolution fluctuations in the western equatorial Pacific during the late Quaternary, Paleoceanography, 7(1), 21-42.

Lear, C. H., H. Elderfield, and P. A. Wilson (2000), Cenozoic Deep-Sea Temperatures and Global Ice Volumes from Mg/Ca in Benthic Foraminiferal Calcite, Science, 287(5451), 269-272, doi: 10.1126/science.287.5451.269.

Lear, C. H., Y. Rosenthal, H. K. Coxall, and P. A. Wilson (2004), Late Eocene to early Miocene ice sheet dynamics and the global carbon cycle, Paleoceanography, 19(4).

Lear, C. H., T. R. Bailey, P. N. Pearson, H. K. Coxall, and Y. Rosenthal (2008), Cooling and ice growth across the Eocene-Oligocene transition, Geology, 36(3), 251-254.

Leon-Rodriguez, L., and G. R. Dickens (2010), Constraints on ocean acidification associated with rapid and massive carbon injections: The early Paleogene record at ocean drilling program site 1215, equatorial Pacific Ocean, Palaeogeography, Palaeoclimatology, Palaeoecology, 298(3–4), 409-420, doi: 10.1016/j.palaeo.2010.10.029.

Leon-Rodriguez, L., and G. R. Dickens (2013), Data report: stable isotope composition of Eocene bulk carbonate at Sites U1331, U1332, and U1333, paper presented at Proc. IODP Volume.

Littler, K., U. Röhl, T. Westerhold, and J. C. Zachos (2014), A high-resolution benthic stable-isotope record for the South Atlantic: Implications for orbital-scale changes in Late Paleocene–Early Eocene climate and carbon cycling, Earth and Planetary Science Letters, 401(0), 18-30.

Lourens, L. J., A. Sluijs, D. Kroon, J. C. Zachos, E. Thomas, U. Röhl, J. Bowles, and I. Raffi (2005), Astronomical pacing of late Palaeocene to early Eocene global warming events, Nature, 435(7045), 1083-1087.

Luciani, V., L. Guisberti, C. Agnini, E. Fornaciari, D. Rio, D. Spofforth, and H. Pälike (2010), Ecological and evolutionary response of Tethyan planktonic foraminifera to the middle Eocene climatic optimum (MECO) from the Alano section (NE Italy), Palaeogeography, Palaeoclimatology, Palaeoecology, 292(1), 82-95.

Lunt, D. J., A. Ridgwell, A. Sluijs, J. C. Zachos, S. Hunter, and A. Haywood (2011), A model for orbital pacing of methane hydrate destabilization during the Palaeogene, Nature Geoscience, 4(11), 775-778.

Lyle, M. W. (2003), Neogene carbonate burial in the Pacific Ocean, Paleoceanography, 18(3), 1059.

Lyle, M. W., and J. Backman (2013), Data report: calibration of XRF-estimated CaCO3 along the Site U1338 splice, In Pälike, H., Lyle, M., Nishi, H., Raffi, I., Gamage, K., Klaus, A., and the Expedition 320/ 321 Scientists, Proc. IODP, 320/321: Tokyo (Integrated Ocean Drilling Program Management International, Inc.), doi: doi:10.2204/iodp.proc.320321.205.2013.

Lyle, M. W., P. A. Wilson, and T. R. Janecek (2002a), Leg 199 Summary, in Lyle, M., et al., Proceedings of the Ocean Drilling Program, Initial reports, 199, 1-89.

Lyle, M. W., P. A. Wilson, and T. R. Janecek (2002b), Site 1218, Proceedings of the Ocean Drilling Program, Initial Reports, 199.

Lyle, M. W., A. Olivarez Lyle, J. Backman, and A. K. Tripati (2005), Biogenic sedimentation in the Eocene equatorial Pacific--The stuttering greenhouse and Eocene carbonate compensation depth, Proceedings of the Ocean Drilling Program, Scientific Results Volume 199, 199, 1-35.

Lyle, M. W., J. Barron, T. J. Bralower, M. Huber, A. O. Lyle, A. C. Ravelo, D. K. Rea, and P. A. Wilson (2008), Pacific Ocean and Cenozoic evolution of climate, Reviews of Geophysics, 46(2), RG2002-[2047].

Mann, M. E., and J. M. Lees (1996), Robust estimation of background noise and signal detection in climatic time series, Climatic Change, 33(3), 409-445, doi: 10.1007/BF00142586.

Markwick, P. J. (1998), Fossil crocodilians as indicators of Late Cretaceous and Cenozoic climates: implications for using palaeontological data in reconstructing palaeoclimate, Palaeogeography, Palaeoclimatology, Palaeoecology, 137(3), 205-271.

Martini, E. (1971), Standard Tertiary and Quaternary calcareous nannoplankton zonation, A. Farinacci (Ed.), Proc. II Plankt. Conf. Roma 1970. Tecnoscienza, Roma, 2, 739–785.

McInerney, F. A., and S. L. Wing (2011), The Paleocene-Eocene Thermal Maximum: A perturbation of carbon cycle, climate, and biosphere with implications for the future, Annual Review of Earth and Planetary Sciences, 39, 489-516.

Merico, A., T. Tyrrell, and P. A. Wilson (2008), Eocene/Oligocene ocean de-acidification linked to Antarctic glaciation by sea-level fall, Nature, 452(7190), 979-982.

Miller, K. G., J. D. Wright, and R. G. Fairbanks (1991), Unlocking the ice house: Oligocene-Miocene oxygen isotopes, eustasy, and margin erosion, Journal of Geophysical Research: Solid Earth, 96(B4), 6829-6848.

Miller, K. G., J. T. R., K. M. E., and K. D. J. (1987), Abyssal circulation and benthic foraminiferal changes near the Paleocene/Eocene boundary, Paleoceanography, 2(6), 741--761, doi: 10.1029/PA002i006p00741.

Moebius, I., O. Friedrich, and H. D. Scher (2014), Changes in Southern Ocean bottom water environments associated with the Middle Eocene Climatic Optimum (MECO), Palaeogeography, Palaeoclimatology, Palaeoecology.

Moebius, I., O. Friedrich, K. M. Edgar, and P. F. Sexton (2015), Episodes of intensified biological productivity in the subtropical Atlantic Ocean during the termination of the Middle Eocene Climatic Optimum (MECO), Paleoceanography, n/a-n/a, doi: 10.1002/2014PA002673.

Moore Jr, T. C., R. D. Jarrard, A. Olivarez Lyle, and M. W. Lyle (2008), Eocene biogenic silica accumulation rates at the Pacific equatorial divergence zone, Paleoceanography, 23(2), PA2202.

Moran, K., et al. (2006), The Cenozoic palaeoenvironment of the Arctic Ocean, Nature, 441(7093), 601-605, doi: Doi 10.1038/Nature04800.

Norris, R. D., D. Kroon, and A. Klaus (1998), Leg 171B Summary Proceedings of the Ocean Drilling Program, Initial Reports 171B.

Norris, R. D., P. A. Wilson, and P. Blum (2014a), Paleogene Newfoundland sediment drifts, Proc. IODP, 342: College Station, TX (Integrated Ocean Drilling Program).

Norris, R. D., et al. (2014b), Site U1408. In Norris, R.D., Wilson, P.A., Blum, P., and the Expedition 342 Scientists, Proc. IODP, 342: College Station, TX (Integrated Ocean Drilling Program), doi: doi:10.2204/iodp.proc.342.101.2014.

Norris, R. D., et al. (2014c), Proc. IODP, 342: College Station, TX (Integrated Ocean Drilling Program).

Nunes, F., and R. D. Norris (2006), Abrupt reversal in ocean overturning during the Palaeocene/Eocene warm period, Nature, 439(7072), 60-63.

ODSN (2011), ODSN (Ocean Drilling Stratigraphic Network), available at: http://www.odsn.de, last access: 12 May 2015.

Ogg, J. G. (2012), Chapter 5 - Geomagnetic Polarity Time Scale, in The Geologic Time Scale, edited by F. M. Gradstein, J. G. O. D. Schmitz and G. M. Ogg, pp. 85-113, Elsevier, Boston.

Ogg, J. G., and L. Bardot (2001), Aptian through Eocene magnetostratigraphic correlation of the Blake Nose Transect (Leg 171B), Florida continental margin, paper presented at Proceedings of the Ocean Drilling Program, Scientific Results.

Olivarez Lyle, A., and M. W. Lyle (2002), Determination of biogenic opal in pelagic marine sediments: a simple method revisited, paper presented at Proceedings of the Ocean Drilling Program, Initial Reports.

Olivarez Lyle, A., and M. W. Lyle (2005), Organic carbon and barium in Eocene sediments: Possible controls on nutrient recycling in the Eocene equatorial Pacific Ocean, paper presented at Proc. Ocean Drill. Program Sci. Results.

Olivarez Lyle, A., and M. W. Lyle (2006), Missing organic carbon in Eocene marine sediments: is metabolism the biological feedback that maintains end-member climates?, Paleoceanography, 21(2).

Pagani, M. (2005), Marked Decline in Atmospheric Carbon Dioxide Concentrations During the Paleogene, Science, 309, 600-603, doi: 10.1126/science.1110063.

Pagani, M., J. C. Zachos, K. H. Freeman, B. Tipple, and S. M. Bohaty (2005), Marked decline in atmospheric carbon dioxide concentrations during the Paleogene, Science, 309(5734), 600-603.

Pagani, M., M. Huber, Z. Liu, S. M. Bohaty, J. Henderiks, W. Sijp, S. Krishnan, and R. M. DeConto (2011), The role of carbon dioxide during the onset of Antarctic glaciation, Science, 334(6060), 1261-1264.

Paillard, D., L. Labeyrie, and P. Yiou (1996), Macintosh program performs time-series analysis, Eos, Transactions American Geophysical Union, 77(39), 379-379.

Pälike, H., and F. Hilgen (2008), Rock clock synchronization, Nature Geoscience, 1(5), 282-282, doi: Doi 10.1038/Ngeo197.

Pälike, H., J. Frazier, and J. C. Zachos (2006), Extended orbitally forced palaeoclimatic records from the equatorial Atlantic Ceara Rise, Quaternary Sci Rev, 25(23-24), 3138-3149, doi: Doi 10.1016/J.Quascirev.2006.02.011.

Pälike, H., M. W. Lyle, H. Nishi, I. Raffi, K. Gamage, and A. Klaus (2010), and the Expedition 320/321 Scientists, 2010. Proc. IODP, 320/321: Tokyo (Integrated Ocean Drilling Program Management International, Inc.).

Pälike, H., et al. (2012), A Cenozoic record of the equatorial Pacific carbonate compensation depth, Nature, 488(7413), 609-614, doi: 10.1038/nature11360.

Pälike, H., R. D. Norris, J. O. Herrle, P. A. Wilson, H. K. Coxall, C. H. Lear, N. J. Shackleton, A. K. Tripati, and B. S. Wade (2006), The heartbeat of the Oligocene climate system, Science, 314(5807), 1894-1898.

Panchuk, K., A. Ridgwell, and L. R. Kump (2008), Sedimentary response to Paleocene-Eocene Thermal Maximum carbon release: A model-data comparison, Geology, 36(4), 315-318, doi: 10.1130/G24474A.1.

Park, R., and S. Epstein (1960), Carbon isotope fractionation during photosynthesis, Geochimica et Cosmochimica Acta, 21(1-2), 110-126.

Pascher, K. M., C. J. Hollis, S. M. Bohaty, G. Cortese, R. M. McKay, H. Seebeck, N. Suzuki, and K. Chiba (2015), Expansion and diversification of high-latitude radiolarian assemblages in the late Eocene linked to a cooling event in the southwest Pacific, Clim. Past, 11(12), 1599-1620, doi: 10.5194/cp-11-1599-2015.

Paytan, A., and M. Kastner (1996), Benthic Ba fluxes in the central Equatorial Pacific, implications for the oceanic Ba cycle, Earth and Planetary Science Letters, 142(3), 439-450.

Pearson, P. N. (2012), Oxygen isotopes in foraminifera: Overview and Historical review, Paleontological Society Papers, 18, 1-38.

Pearson, P. N., and W. P. Chaisson (1997), Late Paleocene to middle Miocene planktonic foraminifer biostratigraphy of the Ceara Rise, paper presented at Proceedings of the Ocean Drilling Program. Scientific results, Ocean Drilling Program.

Pearson, P. N., and M. R. Palmer (2000), Atmospheric carbon dioxide concentrations over the past 60 million years, Nature, 406(6797), 695-699.

Pearson, P. N., P. W. Ditchfield, J. Singano, K. G. Harcourt-Brown, C. J. Nicholas, R. K. Olsson, N. J. Shackleton, and M. A. Hall (2001), Warm tropical sea surface temperatures in the Late Cretaceous and Eocene epochs, Nature, 413(6855), 481-487.

Penman, D. E., B. Hönisch, R. E. Zeebe, E. Thomas, and J. C. Zachos (2014), Rapid and sustained surface ocean acidification during the Paleocene-Eocene Thermal Maximum, Paleoceanography.

Peterson, L., and J. Backman (1990), Late Cenozoic carbonate accumulation and the history of the carbonate compensation depth in the western equatorial Indian Ocean, paper presented at Proc. ODP Sci. Res.

Petrizzo, M. R., I. Premoli Silva, and P. Ferrari (2005), Data report: Paleogene planktonic foraminifer biostratigraphy, ODP Leg 198 holes 1209A, 1210A, and 1211A (Shatsky Rise, northwest Pacific Ocean), paper presented at Proceedings of the Ocean Drilling Program: Scientific Results.

Ridgwell, A. (2007), Interpreting transient carbonate compensation depth changes by marine sediment core modeling, Paleoceanography, 22(4), PA4102, doi: 10.1029/2006PA001372.

Ridgwell, A., and D. N. Schmidt (2010), Past constraints on the vulnerability of marine calcifiers to massive carbon dioxide release, Nature Geoscience, 3(3), 196-200.

Röhl, U., and L. J. Abrams (2000), High resolution, downhole, and nondestructive core measurements from sites 999 and 1001 in the Caribbean Sea: Application to the LPTM.

Röhl, U., T. Westerhold, T. J. Bralower, and J. C. Zachos (2007), On the duration of the Paleocene Eocene thermal maximum (PETM), Geochemistry, Geophysics, Geosystems, 8(12), 1-13.

Rosman, K. J. R., and P. D. P. Taylor (1998), Isotopic compositions of the elements 1997 (Technical Report), Pure and Applied Chemistry, 70(1), 217-235.

Savian, J. F., et al. (2014), Enhanced primary productivity and magnetotactic bacterial production in response to middle Eocene warming in the Neo-Tethys Ocean, Palaeogeography, Palaeoclimatology, Palaeoecology, 414(0), 32-45.

Scher, H. D., and M. L. Delaney (2010), Breaking the glass ceiling for high resolution Nd isotope records in early Cenozoic paleoceanography, Chemical Geology, 269(3), 329-338.

Scher, H. D., S. M. Bohaty, J. C. Zachos, and M. L. Delaney (2011), Two-stepping into the icehouse: East Antarctic weathering during progressive ice-sheet expansion at the Eocene-Oligocene transition, Geology, 39(4), 383-386, doi: Doi 10.1130/G31726.1.

Scher, H. D., S. M. Bohaty, B. W. Smith, and G. H. Munn (2014), Isotopic interrogation of a suspected late Eocene glaciation, Paleoceanography, 2014PA002648, doi: 10.1002/2014PA002648.

Schrag, D. P., D. J. DePaolo, and F. M. Richter (1995), Reconstructing past sea surface temperatures: Correcting for diagenesis of bulk marine carbonate, Geochimica et Cosmochimica Acta, 59(11), 2265-2278.

Sexton, P. F., and S. Barker (2012), Onset of 'Pacific-style'deep-sea sedimentary carbonate cycles at the mid-Pleistocene transition, Earth and Planetary Science Letters, 321, 81-94.

Sexton, P. F., P. A. Wilson, and R. D. Norris (2006a), Testing the Cenozoic multisite composite d18O and d13C curves: New monospecific Eocene records from a single locality, Demerara Rise (Ocean Drilling Program Leg 207), Paleoceanography, 21(2).

Sexton, P. F., P. A. Wilson, and P. N. Pearson (2006b), Microstructural and geochemical perspectives on planktic foraminiferal preservation:,"glassy" versus "frosty", Geochemistry, Geophysics, Geosystems, 7, Q12P19.

Sexton, P. F., R. D. Norris, P. A. Wilson, H. Pälike, T. Westerhold, U. Röhl, C. T. Bolton, and S. Gibbs (2011), Eocene global warming events driven by ventilation of oceanic dissolved organic carbon, Nature, 471(349-352).

Sghibartz, C., H. Pälike, P. A. Wilson, K. M. Edgar, and G. L. Foster (unpublished), Site U1333 Benthic foraminifera Stable Isotope dataset from the late Eocene and Early Oligocene.

Shackleton, N. J., and J. P. Kennett (1975), Paleotemperature history of the Cenozoic and the initiation of Antarctic glaciation: oxygen and carbon isotope analyses in DSDP Sites 277, 279, and 281, Initial reports of the deep sea drilling project, 29, 743-755.

Shackleton, N. J., W. B. Curry, C. Richter, and T. J. Bralower (1997), Proceedings of the Ocean Drilling Program, Scientific Results, 154.

Sluijs, A., R. E. Zeebe, P. K. Bijl, and S. M. Bohaty (2013), A middle Eocene carbon cycle conundrum, Nature Geoscience, 6(6), 429-434, doi: Doi 10.1038/Ngeo1807.

Sluijs, A., G. J. Bowen, H. Brinkhuis, L. J. Lourens, and E. Thomas (2007), The Palaeocene-Eocene Thermal Maximum super greenhouse: biotic and geochemical signatures, age models and mechanisms of global change, Deep Time Perspectives on Climate Change: Marrying the Signal From Computer Models and Biological Proxies, 323-347.

Sluijs, A., S. Schouten, M. Pagani, M. Woltering, H. Brinkhuis, J. S. Damsté, G. R. Dickens, M. Huber, G. J. Reichart, and R. Stein (2006), Subtropical Arctic Ocean

temperatures during the Palaeocene/Eocene thermal maximum, Nature, 441(7093), 610-613.

Speijer, R. P., C. Scheibner, P. Stassen, and A. M. M. Morsi (2012), Response of marine ecosystems to deep-time global warming: A synthesis of biotic patterns across the Paleocene-Eocene thermal maximum (PETM), Austrian Journal of Earth Sciences, 105(1), 6-16.

St John, K. (2008), Cenozoic ice-rafting history of the central Arctic Ocean: Terrigenous sands on the Lomonosov Ridge, Paleoceanography, 23(1), PA1S05.

Stap, L., A. Sluijs, E. Thomas, and L. J. Lourens (2009), Patterns and magnitude of deep sea carbonate dissolution during Eocene Thermal Maximum 2 and H2, Walvis Ridge, southeastern Atlantic Ocean, Paleoceanography, 24(1).

Stap, L., L. J. Lourens, E. Thomas, A. Sluijs, S. M. Bohaty, and J. C. Zachos (2010), High-resolution deep-sea carbon and oxygen isotope records of Eocene Thermal Maximum 2 and H2, Geology, 38(7), 607-610.

Stoll, H. M., and D. P. Schrag (2000), High-resolution stable isotope records from the Upper Cretaceous rocks of Italy and Spain: Glacial episodes in a greenhouse planet?, Geological Society of America Bulletin, 112(2), 308-319, doi: 10.1130/0016-7606(2000)112<308:hsirft>2.0.co;2.

Stott, L. D., J. P. Kennett, N. J. Shackleton, and R. M. Corfield (1990), 48. The evolution of Antarctic surface waters during the Paleogene: inferences from the stable isotopic composition of planktonic foraminifers, ODP leg 113, Proc Ocean Drilling Project Sci Results, 113, 849-863.

Suganuma, Y., and J. G. Ogg (2006), Campanian through Eocene magnetostratigraphy of sites 1257–1261, ODP leg 207, Demerara rise (Western Equatorial Atlantic), paper presented at Proc. Ocean Drill. Program Sci. Results.

Takata, H., R. Nomura, A. Tsujimoto, B. K. Khim, and I. K. Chung (2013), Abyssal benthic foraminifera in the eastern equatorial Pacific (IODP exp 320) during the Middle Eocene, Journal of Paleontology, 87(6), 1160-1185.

Thomas, D., T. J. Bralower, and C. E. Jones (2003), Neodymium isotopic reconstruction of late Paleocene–early Eocene thermohaline circulation, Earth and Planetary Science Letters, 209(3), 309-322.

Thomas, E. (2006), An ocean view of the early Cenozoic Greenhouse World, Oceanography, 19(4).

Thomas, E. (2007), Cenozoic mass extinctions in the deep sea: What perturbs the largest habitat on Earth?, Geological Society of America Special Papers, 424, 1-23, doi: 10.1130/2007.2424(01).

Thomas, E., and N. J. Shackleton (1996), The Paleocene-Eocene benthic foraminiferal extinction and stable isotope anomalies, Geological Society, London, Special Publications, 101(1), 401-441.

Thomas, E., and J. C. Zachos (2000), Was the late Paleocene thermal maximum a unique event?, GFF, 122(1), 169-170.

Tjallingii, R., U. Röhl, M. Kölling, and T. Bickert (2007), Influence of the water content on X-ray fluorescence core-scanning measurements in soft marine sediments, Geochemistry, Geophysics, Geosystems, 8(2).

Toffanin, F., C. Agnini, D. Rio, G. Acton, and T. Westerhold (2013), Middle Eocene to early Oligocene calcareous nannofossil biostratigraphy at IODP Site U1333 (equatorial Pacific), Micropaleontology, 59(1), 69-82.

Tripati, A. K., and H. Elderfield (2005), Deep-sea temperature and circulation changes at the Paleocene-Eocene thermal maximum, Science, 308(5730), 1894-1898.

Tripati, A. K., J. Backman, H. Elderfield, and P. Ferretti (2005), Eocene bipolar glaciation associated with global carbon cycle changes, Nature, 436(7049), 341-346.

Tripati, A. K., M. L. Delaney, J. C. Zachos, L. D. Anderson, D. C. Kelly, and H. Elderfield (2003), Tropical sea-surface temperature reconstruction for the early Paleogene using Mg/Ca ratios of planktonic foraminifera, Paleoceanography, 18(4).

Van Andel, T. H. (1975), Mesozoic/cenozoic calcite compensation depth and the global distribution of calcareous sediments, Earth and Planetary Science Letters, 26(2), 187-194.

Voigt, J., E. C. Hathorne, M. Frank, H. Vollstaedt, and A. Eisenhauer (2015), Variability of carbonate diagenesis in equatorial Pacific sediments deduced from radiogenic and stable Sr isotopes, Geochimica et Cosmochimica Acta(0).

Wade, B. S., P. N. Pearson, W. A. Berggren, and H. Pälike (2011), Review and revision of Cenozoic tropical planktonic foraminiferal biostratigraphy and calibration to the geomagnetic polarity and astronomical time scale, Earth-Science Reviews, 104(1-3), 111-142, doi: Doi 10.1016/J.Earscirev.2010.09.003.

Walker, J. C. G., P. B. Hays, and J. F. Kasting (1981), A negative feedback mechanism for the long-term stabilization of the Earth's surface temperature, Journal of Geophysical Research: Oceans, 86(C10), 9776-9782, doi: 10.1029/JC086iC10p09776.

Westerhold, T., and U. Röhl (2006), 15. Data Report: Revised Composite Depth Records for Shatsky Rise Sites 1209, 1210, and 1211.

Westerhold, T., and U. Röhl (2013), Orbital pacing of Eocene climate during the Middle Eocene climate optimum and the chron C19r event – missing link found in the tropical western Atlantic, Geochemistry, Geophysics, Geosystems, n/a-n/a, doi: 10.1002/2013gc004960.

Westerhold, T., U. Röhl, H. K. McCarren, and J. C. Zachos (2009), Latest on the absolute age of the Paleocene Eocene Thermal Maximum (PETM): new insights from exact stratigraphic position of key ash layers + 19 and - 17, Earth and Planetary Science Letters, 287(3), 412-419.

Westerhold, T., U. Röhl, T. Frederichs, S. M. Bohaty, and J. C. Zachos (2015), Astronomical calibration of the geological timescale: closing the middle Eocene gap, Climate of the Past Discussions, 11(3).

Westerhold, T., U. Röhl, H. Pälike, R. Wilkens, P. A. Wilson, and G. Acton (2014), Orbitally tuned timescale and astronomical forcing in the middle Eocene to early Oligocene, Clim. Past, 10, 955-973.

Westerhold, T., U. Röhl, J. Laskar, I. Raffi, J. Bowles, L. J. Lourens, and J. C. Zachos (2007), On the duration of magnetochrons C24r and C25n and the timing of early Eocene global warming events: Implications from the Ocean Drilling Program Leg 208 Walvis Ridge depth transect, Paleoceanography, 22(2).

Westerhold, T., et al. (2011), Revised composite depth scales and integration of IODP Sites U1331–U1334 and ODP Sites 1218–1220, Proceedings of the Integrated Ocean Drilling Program, 320/321, doi: 10.2204/iodp.proc.320321.201.2012.

Witkowski, J., S. M. Bohaty, K. McCartney, and D. M. Harwood (2012), Enhanced siliceous plankton productivity in response to middle Eocene warming at Southern Ocean ODP Sites 748 and 749, Palaeogeography, Palaeoclimatology, Palaeoecology, 326, 78-94.

Witkowski, J., S. M. Bohaty, K. M. Edgar, and D. M. Harwood (2014), Rapid fluctuations in mid-latitude siliceous plankton production during the Middle Eocene Climatic Optimum (ODP Site 1051, western North Atlantic), Marine Micropaleontology, 106(0), 110-129.

Yamamoto, Y., H. Fukami, and Y. Toshitsugu (2015), Paleomagnetic study of IODP Sites U1403, U1408, and U1410: updated magnetostratigraphies for the intervals recovered by advanced piston coring, paper presented at Exp. 342 Post Cruise Meeting, Utah.

Zachos, J. C., J. R. Breza, and S. W. Wise (1992), Early Oligocene ice-sheet expansion on Antarctica: Stable isotope and sedimentological evidence from Kerguelen Plateau, southern Indian Ocean, Geology, 20(6), 569-573, doi: 10.1130/0091-7613(1992)020<0569:EOISEO>2.3.CO;2.

Zachos, J. C., G. R. Dickens, and R. E. Zeebe (2008), An early Cenozoic perspective on greenhouse warming and carbon-cycle dynamics, Nature, 451(7176), 279-283.

Zachos, J. C., M. Pagani, L. C. Sloan, E. Thomas, and K. Billups (2001a), Trends, rhythms, and aberrations in global climate 65 Ma to present, Science, 292(5517), 686-693.

Zachos, J. C., N. J. Shackleton, J. S. Revenaugh, H. Pälike, and B. P. Flower (2001b), Climate response to orbital forcing across the Oligocene-Miocene boundary, Science, 292(5515), 274-278, doi: Doi 10.1126/Science.1058288.

Zachos, J. C., H. McCarren, B. Murphy, U. Röhl, and T. Westerhold (2010), Tempo and scale of late Paleocene and early Eocene carbon isotope cycles: Implications for the origin of hyperthermals, Earth and Planetary Science Letters, 299(1), 242-249.

Zachos, J. C., M. W. Wara, S. Bohaty, M. L. Delaney, M. R. Petrizzo, A. Brill, T. J. Bralower, and I. Premoli-Silva (2003), A transient rise in tropical sea surface temperature during the Paleocene-Eocene Thermal Maximum, Science, 302(5650), 1551-1554, doi: Doi 10.1126/Science.1090110.

Zachos, J. C., D. Kroon, P. Blum, J. Bowles, P. Gaillot, T. Hasegawa, E. C. Hathorne, D. A. Hodell, D. C. Kelly, and J. H. Jung (2004), Leg 208 Summary, Proceedings ODP, Initial Reports, 208, 1-112.

Zachos, J. C., et al. (2005), Rapid Acidification of the Ocean During the Paleocene-Eocene Thermal Maximum, Science, 308(5728), 1611-1615, doi: 10.1126/science.1109004.

Zeebe, R. E. (2012), LOSCAR: Long-term Ocean-atmosphere-Sediment CArbon cycle Reservoir Model v2. 0.4, Geosci. Model Dev., 5, 149-166, doi: 10.5194, edited, gmd-5-149-2012.

Zeebe, R. E. (2013), What caused the long duration of the Paleocene-Eocene Thermal Maximum?, Paleoceanography, 28(3), 440-452, doi: 10.1002/palo.20039.

Zeebe, R. E., and J. C. Zachos (2007), Reversed deep-sea carbonate ion basin gradient during Paleocene-Eocene thermal maximum, Paleoceanography, 22(3).

Zeebe, R. E., A. Ridgwell, and J. C. Zachos (2016), Anthropogenic carbon release rate unprecedented during the past 66 million years, Nature Geoscience, 9(4), 325-329.

Zhang, Y. G., M. Pagani, Z. H. Liu, S. M. Bohaty, and R. DeConto (2013), A 40-million-year history of atmospheric CO2, Philosophical Transactions of the Royal Society A: Mathematical, Physical and Engineering Sciences, 371(2001), 20130096.